Interactions Between Radio-loud Active Galaxies and Their Environments

Joanna Louise Goodger

Submitted to the University of Hertfordshire
in partial fulfillment of the requirements
of the degree of Doctor of Philosophy

August 20, 2010

Abstract

In this dissertation, I present my work on the behaviour of different features of radio-loud active galaxies to investigate how energy is transferred from their jets to the environment. To this end, I have studied the knots in the jet in Centaurus A, the radio and X-ray emission from the lobes of the FR II radio galaxies 3C 353 and Pictor A, and the gas properties of a sample of galaxy groups some of which host radio-loud active galaxies.

Using new and archival multi-frequency radio and X-ray data for Centaurus A obtained over almost 20 years with the Very Large Array and with *Chandra*, I have measured the X-ray and radio spectral indices, radio and X-ray flux density variations, polarisation variations and proper motions of the jet knots. I used these measurements to constrain the likely knot formation mechanisms and particle acceleration processes within this jet and compared my results with the variations detected in the properties of the knots in M 87. I found that none of the knots are a result of impulsive particle acceleration and that those knots that are detected in both X-ray and radio are likely due to collisions between the jet and an obstacle, while the radio only knots, the majority of which are moving, are likely due to compressions of the fluid flow.

Using six frequencies of new and archival radio data and new *XMM-Newton* observations of 3C 353, I show that inverse-Compton emission is detected in the lobes of this source. By combining this X-ray inverse-Compton emission with the radio synchrotron emission, I have constrained the electron population and the magnetic field energy density in the lobes of this radio galaxy. I have argued that the variations in the X-ray/radio ratio in the brighter lobe requires a changing magnetic field strength. I have extended this work using a statistical analysis of the X-ray and radio emission to show that the observed small-scale variation in surface brightness cannot be reproduced by simple combinations of the electron energy distribution and the magnetic field strength. I therefore suggest that the changes in surface brightness that give rise to the filamentary structures seen in the lobes are probably due to strong spatial variations of the magnetic field strength.

Finally, I present a study of galaxy groups observed with *XMM-Newton* in which I measure temperature and surface brightness profiles to examine whether radio-source heating makes radio-loud groups hotter and more luminous than radio-quiet groups. I compare my measurements with previous luminosity-temperature relationships and conclude that there is a significant difference in the gas properties of radio-loud and radio-quiet groups.

Acknowledgements

I am eternally gratefully to a great number of people for their support and encouragement during the past three years in particular. These have been the hardest years of my life so far, but with your support, I made it in one piece and it was worth it. Firstly, I want to thank my supervisors, Martin Hardcastle and Judith Croston, who have always been there for me, to answer the stupid questions, and the big ones, and to instruct me in both the science and the techniques involved in this work. They're better supervisors than I could have hoped for and I hope to continue to know them for years to come.

I also do not think that I would have come this far without my friends. The girls back in Totton have always encouraged me to do the best I can and I know that even now they are proud of me, as are my friends from QM who are always there when I need to get away from Hatfield and my thesis. Nic and Rosie, Pratik and Paz, Emsal, Evrim and Sam; they have all been there to share a pint and listen to my woes. And at UH, I have made more good friends that have picked me up and pushed me onwards when I've been down and blue; to my friends in the STRI (particularly the G^2) - I thank you too.

But of course, I would not have got this far without my parents, John and Gwen, my brothers, Paul and Mark, and my Nan who have always been there. I know that they are proud of me, and I hope that they always will be.

Lastly and most importantly, I want to thank Steve. He's my rock and my life line and without him, I wouldn't be the person that I am today.

Contents

For my Family

Past, Present and Future

Chapter 1

Introduction

Active galaxies are some of the most powerful objects in the Universe but the question of how these galaxies transport the energy generated in their cores to the systems where they live has motivated generations of astronomers and the mechanisms involved are largely unknown. The work in this thesis works towards answering these energy transfer questions by considering the energetics of the various features of radio galaxies.

After a brief historical overview of the discovery of active galaxies and the development of this area of astronomy over the last century, I will introduce the radiation processes that reveal the structure of these exotic objects. Next, in Section 1.3, I will describe the features of radio galaxies, as determined from radio observations, before moving on to describe the observations in other wave bands and what they have told us about active galaxies. In Section 1.4, I will present the current models for unifying the menagerie of active galaxies before discussing the effect of active galaxies on their environments and vice versa in Section 1.5. Finally, in Section 1.6, I outline the aims of this work, specifying the questions about energy transfer that I intend to answer in this thesis and I outline the structure of this dissertation.

1.1 A Brief History of Active Galaxies

Since Edwin Hubble determined the existence of galaxies outside our own Milky Way (Hubble 1936), we have pondered their formation, their evolution and their structure.

Shortly after Hubble's discovery, Seyfert (1943) obtained optical spectra of the centre of bright 'extragalactic nebulae', now known as spiral galaxies, and noted the presence of high-excitation emission lines, namely H, He, O and N lines, in some of these objects and not in others; those galaxies with strong, broad-line emission lines were later classified as 'Seyfert class 1 galaxies' (Sy1) (Khachikian & Weedman 1974), while those without these broad lines were classed 'Seyfert class 2 galaxies' (Sy2). Narrow-line emission lines were detected in both classes of Seyfert galaxy.

Either these objects had different core structures, or there was something within the Sy1 obscuring our view of the regions emitting the broad lines. More information about their cores was required to resolve these issues.

Over a decade later, radio observations began to flood in on all sorts of objects and in 1955, the Third Cambridge Catalogue (3C; Edge et al. 1959) of radio sources at 158 MHz was released including observations of some of Seyfert's galaxies. This was shortly followed by the revised catalogue of 199 sources observed at 178 MHz (3CR; Bennett 1962). Many of these previously unresolved 'radio stars' were associated with external galaxies and star-like objects of high redshift, known as quasars (Schmidt 1963). These radio interferometry catalogues revealed extended structures for many of the radio sources and eventually led to a dozen or so descriptions of extended radio objects such as double-lobed and single-lobed, X-shaped and Y-shaped, bridged and plumed, wide-angled and narrow-angled tail radio galaxies (Leahy & Williams 1984). The properties of these radio galaxies will be discussed further in Section 1.3.1.

The quasi-stellar objects (QSOs) identified by Schmidt (1963) had no detectable extended emission and appeared star-like except that their spectra showed broad emission lines with a considerable redshift suggesting 'activity' similar to Seyfert galaxies in the cores of distant galaxies. These QSOs were subsequently classed as radio-loud (RLQs) and radio-quiet (RQQs) quasars, depending on whether they had nuclear (or extended) radio emission. All these quasars had optical broad-line and narrow-line emission lines, strong optical continuum emission dominated by a 'big blue bump' and strong nuclear X-ray emission. In addition to RLQs, a class of variable objects was also established named Blazars, which included two subclasses: Optically Violent Variable quasars (OVV), which in addition to the lines and strong emission classically associated with quasars, include an optical component which can vary by $\Delta m \sim 0.1$ mag in a time period as short as a day; and BL Lac objects (named after the prototype of the class, BL Lacertae) which also have an optically varying component, but without any optical lines (Antonucci & Ulvestad 1985, and references therein). How these point-like sources fitted in with the extended sources and radio-quiet galaxies was a matter of great debate for quite some time.

Meanwhile in the X-ray regime, the first cosmic X-ray source (Scorpius X-1) was discovered (Giacconi et al. 1962), prompting the birth of X-ray astronomy, which developed over the next decade from high atmosphere balloons carrying instruments to the *EINSTEIN* space observatory in 1978. Observations of active galaxies in the X-ray regime reveal a bright X-ray core, indicating the presence of hot gas or, if non-thermal in origin, very energetic particle acceleration in the central regions of active galaxies (see Section 1.2). X-ray observations have proved to be vital in determining the structure of active galaxies on all scales and will be discussed in depth in Section 1.3.4.

1.2 Radiation Mechanisms

In order to determine what is causing the various observational properties of active galaxies, it is important to identify the radiation mechanisms at work and the wave bands in which we can detect them.

1.2.1 Synchrotron Emission

Synchrotron emission is emitted from a relativistic, charged particle in a magnetic field. As it spirals around the magnetic field, it undergoes centripetal acceleration and loses energy at a rate given by

$$\frac{dE}{dt} = -\frac{4}{3}\sigma_T c\gamma^2 \frac{B^2}{2\mu_0} \tag{1.1}$$

for a particle with a Lorentz factor of γ, which is related to the particle's total energy by $E = \gamma m_e c^2$. The magnetic field strength is B, σ_T is the Thompson cross-section and μ_0 is the permeability of the vacuum (e.g. Longair 1994).

An individual electron of mass m_e and charge e in a uniform magnetic field, emits synchrotron radiation over a broad range of frequencies, narrowly peaked at a critical frequency, ν_c given by Longair (1994) as

$$\nu_c = \gamma^2 \frac{eB}{2\pi m_e} \tag{1.2}$$

In radio galaxies, we observe the synchrotron emission from a population of electrons with a range of Lorentz factors. The loss time-scale for synchrotron emitting particles is given by $E/(dE/dt)$, which is proportional to γ^{-1} (and E^{-1}) so an X-ray emitting electron loses energy $\sim 10^5$ times faster than a radio-emitting electron and protons of a given energy lose their energy $\sim 10^6$ times slower than electrons.

In the radio, the spectrum can often be approximated by a power-law; for this to be possible, the electrons must also have a power-law distribution in energy. If we therefore assume that the electron energy spectrum is given by $N(E) = N_0 E^{-p}$ in the range E_{min} – E_{max}, then the total emissivity for the population emitting synchrotron radiation is given by

$$J(\nu) = \int_{E_{min}}^{E_{max}} j(\nu) N(E) dE = \int_{E_{min}}^{E_{max}} j(\nu) N_0 E^{-p} dE \tag{1.3}$$

where $j(\nu)$ is the emissivity for a single electron, which is a function of critical frequency. By substituting equations for E derived from Equation (1.2), and assuming that the synchrotron spectrum is narrowly peaked, we find that the total emissivity is dependent on the magnetic field strength and the electron energy distribution:

$$J_{syn}(\nu) \propto N_0 \nu^{-\frac{p-1}{2}} B^{\frac{p+1}{2}} \tag{1.4}$$

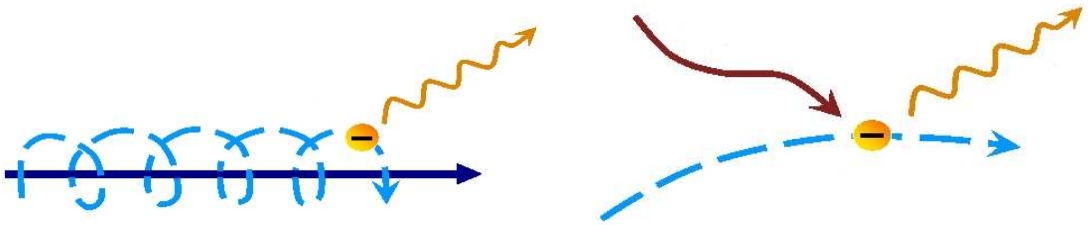

Figure 1.1: Diagrams of the synchrotron emission (left) and inverse-Compton emission (right) mechanisms. The magnetic field lines are shown in a blue solid line, the path of the electron in dashed cyan, incident low-energy photons by the red wave and the higher-energy photons in yellow wave.

In order to determine the effects of magnetic field strength and the electron energy spectrum on the synchrotron emission detected from the jets, lobes and hotspots of radio galaxies, we require additional information as they cannot be separated using just the radio synchrotron emission, as Equation (1.4) shows.

The shape of the synchrotron emission spectrum is often characterised by the spectral index, α, which is defined in terms of the flux density, $S(\nu) \propto S_0 \nu^{-\alpha}$.

1.2.2 Inverse-Compton Scattering

Compton scattering occurs when a photon collides with a particle and imparts some of its energy to the particle. If the particle has sufficient energy already, the photon will gain energy from the collision; this is inverse-Compton (iC) scattering. The relativistic particles in radio galaxies have enough energy to up scatter photons to X-ray energies. In this thesis I am interested in iC scattering within the lobes.

Within radio galaxies, there are many sources of photons which may be scattered to X-ray energies; the radio synchrotron photons (SSC: synchrotron self-Compton emission), the cosmic microwave background radiation (iC/CMB), photons from the central AGN (NIC: nuclear iC emission) and starlight from the host galaxy (iC/SL: stellar iC emission). The first two sources of scattered light are relatively easy to calculate as the source photon fields are close to isotropic with respect to the electrons in the lobes. With NIC, the photons come from only the direction of the core so the photon field is anisotropic with respect to the electrons in the lobe, and with iC/SL, the photon field is also anisotropic as the photon density at a particular position within the lobe depends on the distribution of the stellar population of the galaxy.

Following the discussion of Hardcastle et al. (1998), in the case of SSC and iC/CMB, we can assume an isotropic distribution of photons of energy ϵ_i scattering off a population of relativistic

electrons which have the iC spectral emissivity given by Rybicki & Lightman (1979):

$$j_{iC}(\nu_f) = \frac{3\pi\epsilon_f N\sigma_T F(\epsilon_i)}{\gamma^2\epsilon_i} f(x) \tag{1.5}$$

where N is the number density of electrons, F is the photon number intensity ($F = n(\epsilon_i)c/4\pi$, where $n(\epsilon_i)$ is the photon number density), ϵ_i and ϵ_f are the initial and scattered photon energies and $f(x) = 2x\ln(x) + x + 1 - 2x^2$ where $x = \epsilon_f/4\gamma^2\epsilon_i$.

If we further assume that the lobe is a sphere and thus use the relationship between the average photon density and the local photon production rate, $\dot{n}$ (Band & Grindlay 1985), we find that the photon number density for synchrotron photons is

$$n_{SSC}(\nu_i)d\nu_i = \frac{3}{4c} R \frac{J(\nu_i)d\nu_i}{h\nu_i} \tag{1.6}$$

where R is the radius of the emitting region and $J(\nu_i)$ is the synchrotron emissivity at ν_i. The total emissivity is then given by:

$$J_{SSC}(\nu_f) = \frac{9}{16} m_e^2 c^4 \nu_f \sigma_T R \int_{E_{min}}^{E_{max}} \int_{\nu_{min}}^{\nu_{max}} \frac{N(E)J(\nu_i)}{E^2\nu_i^2} f(x) d\nu_i dE \tag{1.7}$$

where $N(E)$ is the electron number density as a function of energy, which takes the form of a power-law (Section 1.2.1).

The iC/CMB follows the same arguments where the photon number density of the CMB photons is given by

$$n_{CMB}(\nu_i)d\nu_i = \frac{8\pi\nu_i^2 d\nu_i}{c^3(e^{\frac{h\nu_i}{kT}} - 1)} \tag{1.8}$$

which leads to an total emissivity for the iC scattering of CMB photons of

$$J_{CMB}(\nu_f) = 6\pi h m_e^2 c^4 \nu_f \sigma_T \int_{E_{min}}^{E_{max}} \int_{\nu_{min}}^{\nu_{max}} \frac{N(E)\nu_i}{E^2(e^{\frac{h\nu_i}{kT}} - 1)} f(x) d\nu_i dE \tag{1.9}$$

These expressions for iC scattering are the basis of the *synch* code designed by Hardcastle et al. (1998) and used by me in Chapter 3 to estimate the change in magnetic field strength within the lobes of 3C 353 required to produce the observed enhancement in the X-ray emission. This is possible as iC scattering depends on the electron number density and not on the magnetic field strength.

The NIC and iC/SL radiation fields are anisotropic so are much more complicated to calculate. Brunetti et al. (1997) argue that there may be a significant contribution to the extended X-ray emission from the iC scattering of IR-optical photons from a central quasar by the low-energy electron population. They derived expressions for anisotropic iC scattering of photons from a hidden quasar and found that the first indication that this is a dominant source of iC photons would be asymmetry in the observed X-ray emission from the lobes; if the radio axis were inclined to the sky, the more distant lobe would be more luminous. I have used the method of Brunetti et al. to model NIC in the lobes in this work.

In order to estimate the starlight photon density, it is necessary to estimate the distribution of various star spectral types, which can be done using observational constraints on the spectral energy distribution (SED) for the host galaxy. Croston et al. (2009) estimated the starlight photon density for Centaurus A (NGC 5128, hereafter Cen A) by deprojecting the V-band surface brightness of van den Bergh (1976) using the method of Mellier & Mathez (1987) to find the photon density at a given distance. They then defined a spectral energy distribution for the galaxy using previous measurements and normalised it to the V-band data. They could thus model iC scattered emissivity for the starlight using the *synch* code. These iC model predictions for the jet in Cen A, which is the object studied in Chapter 5, are shown in Figure 1.2 with the limits from observations in the radio and X-ray (Hardcastle et al. 2007b; Goodger et al. 2010) and TeV (Aharonian et al. 2009). This plot illustrates the contributions from each of the photon fields to the predicted iC X-ray emission and TeV γ-ray emission.

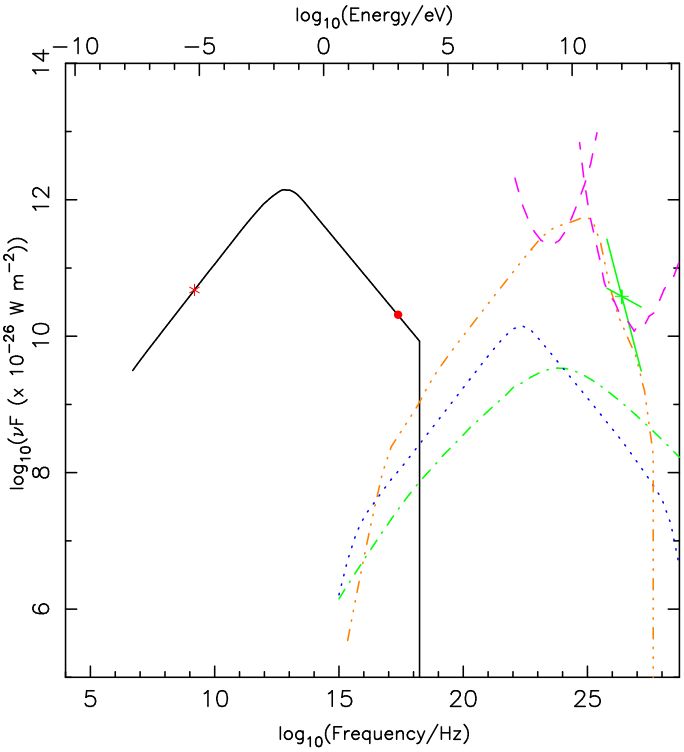

Figure 1.2: Synchrotron and iC scattering flux predictions as a function of frequency for the jet in Cen A. Shown in black is the synchrotron emission, orange shows the iC-scattered starlight. Blue shows the iC scattered CMB and green is the synchrotron self-Compton prediction (SSC). The red data points are the radio and X-ray constraints on the emission from the jet from Hardcastle et al. (2007b); Goodger et al. (2010). The green bowtie is the TeV measurement from HESS (Aharonian et al. 2009). The pink lines show the sensitivity curves for Fermi (lower energy; after 1 year's operation) and a reference design for the Cherenkov Telescope Array (CTA) (higher energy; 50 hour exposure) (Hardcastle, private communication).

1.2.3 Thermal Emission

In addition to the synchrotron radiation and iC scattering, we also detect thermal emission from the central regions of active galaxies and the hot intracluster medium. Thermal emission includes blackbody radiation, bremsstrahlung and line emission from the collisional excitation and de-excitation of heavy elements. These mechanisms are shown diagrammatically in Figure 1.3.

Thermal bremsstrahlung is due to the random thermal motions of particles. In thermal equilibrium, the collisions between electrons and the Coulomb field of ions cause them to decelerate and emit photons. The emissivity of the particles depends mainly on the particle density and less so on the velocity, and therefore temperature. The emissivity of a single ion is given by:

$$\epsilon_{brem}(\nu) = \frac{32\pi}{3}\frac{2\pi}{3}^{1/2} Z^2 g(\nu, T, Z) n_i n_e m_e c^2 r_e^3 \left(\frac{m_e c^2}{kT}\right)^{1/2} e^{\frac{-h\nu}{kT}} \tag{1.10}$$

where Z is the charge of the emitting ions, m_e is the mass of an electron and r_e is the classical electron radius. n_e and n_i are the number densities of the electrons and ions. T is the temperature of the gas, k is the Boltzmann constant, h is the Planck constant, and $g(\nu, T, Z)$ is the Gaunt factor which corrects for quantum mechanical effects.

Whereas the synchrotron emission and iC scattering from the features investigated in this work can be modelled by power laws, the thermal spectrum of a hot gas is much more complicated and requires detailed models of the line emission processes. Throughout this work, I have used two models of the thermal emission (Figure 1.4); *mekal*, which combines bremsstrahlung emission with the line emission from several heavy elements based on the work by Mewe et al. (1985, 1986) and Liedahl et al. (1995), and *apec*, the Astrophysical Plasma Emission Code, which utilises the Astrophysical Plasma Emission Database, and outputs plasma spectral models which include di-electronic and radiative recombination followed by cascades, as well as collisional excitation and de-excitation, two-photon emission, radiative recombination, and relativistic bremsstrahlung (Smith et al. 2001). For consistency with previous work, I used the *mekal* thermal models for the majority of the work in this thesis; however, in Chapter 6 I use the *apec* model as I aim to measure the temperatures to the best that I can and the *apec* model includes superior data on the energy transitions within the gas. Using *apec* only significantly affects the transitions at higher temperatures so our conclusions would be unchanged by the slight differences between these models.

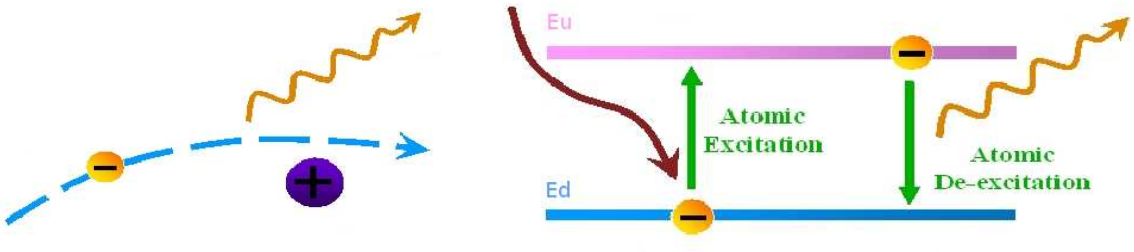

Figure 1.3: Diagrams of the bremsstrahlung emission mechanism (left) and line-excitation and de-excitation (right). As in Figure 1.1, in the left panel the path of the electron is shown by the dashed cyan line, the incident low-energy photons is shown by the red wave and the higher-energy X-ray photon by the orange wave. In the right panel, the movement of the electron between the upper energy level (pink) and the lower energy level (cyan) is shown by the green lines.

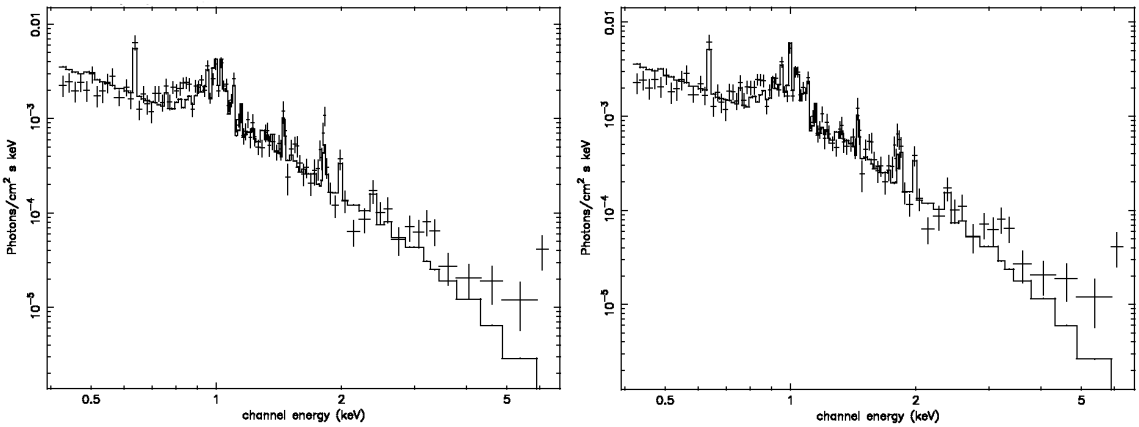

Figure 1.4: Thermal predictions for X-ray emission using the *mekal* model (left panel) and the *apec* model (right panel). The data plotted is the MOS1 *XMM-Newton* data for NGC 533. The temperature of the hot gas in this group is ~ 1.21 keV, with a fixed Galactic absorption of $n_H = 3.01 \times 10^{20}\,\mathrm{cm}^{-1}$ and a redshift of $z = 0.0181$.

1.3 Observational Constraints on the Structure of Active Galaxies

As discussed in Section 1.1, as technology advanced in all frequencies from radio to gamma-ray, the information on active galaxies increased until there were well over a dozen classifications of active galaxy.

Using the 3CR catalogue, Fanaroff & Riley classified radio galaxies according to their morphology into those galaxies which were core-brightened – classed Fanaroff Riley class I (FRI) – and those that were edge brightened – classed Fanaroff Riley class II (FRII). Examples of these classifications are shown in Figure 1.5. Fanaroff & Riley discovered that the difference in morphology was correlated with the luminosity; FRI typically have $L_{178\,MHz} < 5 \times 10^{24}\,\mathrm{W\,Hz^{-1}\,sr^{-1}}$ and FRII have higher luminosities. The FR I/FR II dichotomy has been the standard split for the population of radio galaxies for that past 40 years and so the discussion in the following sections uses these classes. It has since been found that the FR I/FR II luminosity split also depends on the host galaxy magnitude (Ledlow & Owen 1996) and the environment (see Section 1.5).

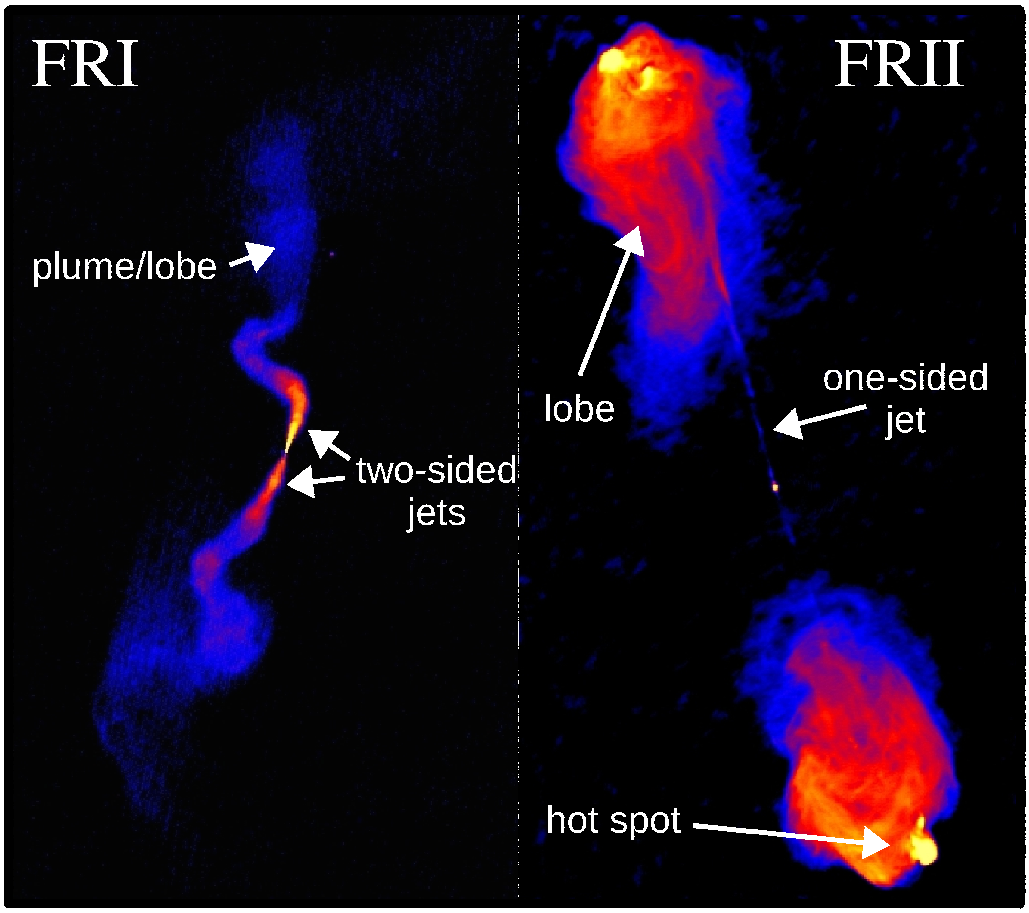

Figure 1.5: Examples of the two Fanaroff & Riley classes of active galaxies. 3C 31 (left) is classified as class I and 3C 405 (Cygnus A; right) is a class II radio galaxy. Images were taken at the VLA in 1.4 GHz.

However, shortly afterwards Hine & Longair (1979) were studying the optical emission from these 3CR radio galaxies and came up with a classification scheme similar to that of Seyfert galaxies, dividing radio galaxies into those with weak and those with strong emission lines. Radio galaxies with strong emission lines were defined as being class A (high-excitation radio galaxies, HERGs), which included galaxies with narrow-line emission (NLRGs) and galaxies with broad-line emission lines, stronger forbidden lines and weaker Fe II lines (BLRGs). Those radio galaxies with weaker, lower-excitation lines were defined as being class B (low-excitation radio galaxies, LERGs). This population split is discussed further in Section 1.4 as we require multi-frequency data to further analyse these populations.

1.3.1 Radio Emission

At radio frequencies, we predominantly detect synchrotron emission from the jets and from the extended emission of radio galaxies and radio-loud quasars which indicates that the particles within these features are moving relativistically. As the work in this thesis focuses mainly on radio galaxies and their environments, in this section I shall introduce the standard model for radio galaxies and the observational evidence for this picture, and then I shall discuss the observations in other frequency bands and how they have contributed to the models of radio galaxies. The structures revealed in different wave bands vary greatly so a multi-frequency approach to studying AGN is vital. To emphasise this, Figure 1.6 shows our closest active galaxy, Cen A in radio, IR, optical, UV and X-ray regimes.

Cores and Jets

The term *core* refers to the central parsec-scale region, which is unresolved in most cases and generally coincident with the centre of the host galaxy. In giga-hertz radio frequencies, the spectrum is inverted or flat with $\alpha < 0$ and is thought to be dominated by emission from the synchrotron-emitting, self-absorbed bases of jets. Observations of the core regions obtained using Very Long Baseline Interferometry (VLBI) showed apparent superluminal motions in the small-scale jets of active galaxies, which suggested highly relativistic jet material at these scales affected by relativistic beaming (e.g. Pearson 1996).

If we define the bulk relativistic Doppler factor, $D = 1/\Gamma(1 - \beta cos\theta)$, then the observed luminosity, S_{obs} within a jet is enhanced or suppressed depending on the velocity of the blob and the viewing angle; $S_{obs} = S_{em}D^{\delta}$, where S_{em} is the emitted luminosity and $\delta = 3 + \alpha$ (α is the synchrotron spectral index; Lind & Blandford 1985). If a blob is moving towards the observer, then the luminosity is enhanced by this relativistic beaming, and if it is moving away, then the luminosity is suppressed (e.g. Phinney 1985). In a jet, the Doppler index $\delta = 2 + \alpha$, as it can be modelled as many blobs producing a continuous flow. A change in the Doppler factor due to a change in the direction of motion or the velocity of the blob will affect the observed flux. These effects are therefore discussed in Chapter 5 where I present work on the jet of Cen A.

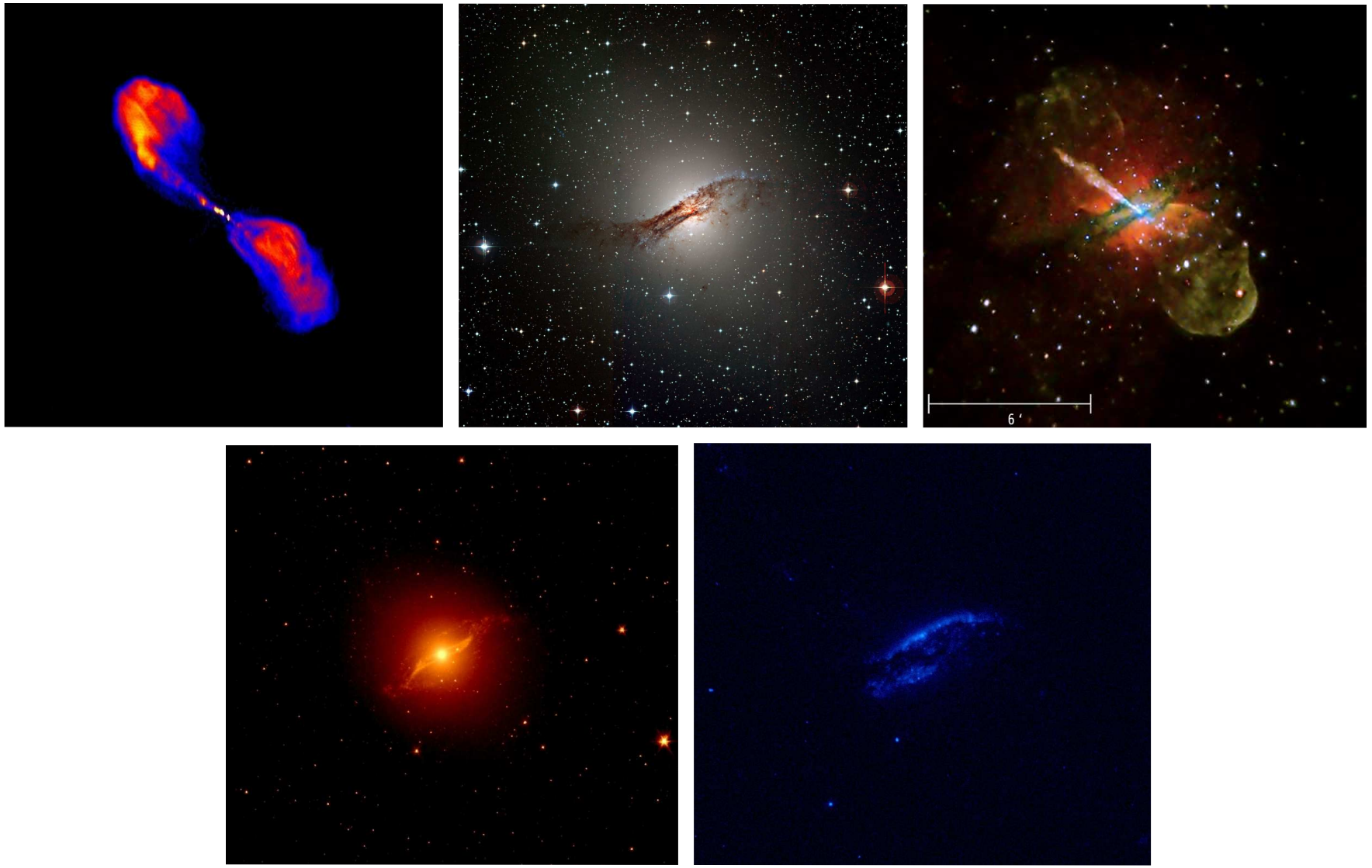

Figure 1.6: Multi-frequency observations of Cen A. The radio image (top left) was taken at 1.4 GHz with the VLA in multiple configurations (A, B, BnC, CnD). The optical image (top centre) was taken with the Wide Field Imager at the MPG/ESO 2.2-m telescope at La Silla, Chile (Credit; ESO). The X-ray image (top right) was taken with *Chandra* and shows low-energy X-rays in red, intermediate-energy X-rays in green and the highest-energy X-rays in blue (Kraft et al. 2003). The IR image (bottom left) was taken at 3.6 μm with *Spitzer* (Quillen et al. 2006) and the UV image (bottom right) is from GALEX.

The larger kpc-scale jets of radio galaxies can be split into two types (Bridle 1982; Bridle & Perley 1984). Type I jets have wide opening angles ($5^\circ - 30^\circ$) and magnetic fields which lie perpendicular to the jet axis. These jets are mostly found in FR Is where they are typically two-sided and fade with distance from the core. FR IIs generally have Type II jets which are one-sided (Muxlow & Garrington 1991) and extend to kpc scales with a brighter hot spot on the jet side (Laing 1989). The polarisation observations suggest that Type II jets have magnetic fields which lie parallel to the jet axis and do not fade with distance. These jets are mostly knotty and have a difference in brightness of at least a factor of 4 between the jet and fainter counterjet due to relativistic beaming.

Both of these types of jet are highly relativistic at parsec scales but at larger distances, the jets of FR Is are thought to decelerate to sub-relativistic, transonic speeds; this is suggested by their two-sided and symmetric nature on larger scales (Laing et al. 1999). A likely reason for this deceleration is entrainment of thermal particles from the environment; an initially laminar jet emerges from the core, but downstream the region becomes turbulent resulting in velocity shear, entrainment and deceleration of the fluid (e.g. Bicknell 1984; Laing & Bridle 2002). The larger opening angles of these Type I jets, and their apparent brightening and flaring also supports these models of less efficient energy transport in FR Is.

In these turbulent FR I jets, we often see compact regions of brighter material – knots – along the jet that are also seen in the optical through to the X-ray regime. The synchrotron loss timescales are comparable to or shorter than the light-travel time from the nucleus in these observation bands, which suggests that these knots are regions of in situ particle acceleration. This particle acceleration affects the energy being transferred along the jet and into the lobe material. These knots are the topic of interest in Chapter 5 where I present work which investigates the temporal behaviour of the knots in multiple frequencies to determine the particle acceleration mechanisms at work in the jet knots of Cen A. One such particle acceleration mechanism is reconfinement of the jet which would cause brightening and flaring at the base of the jet (e.g. Sanders 1983), but compressions and collisions with obstacles as well as impulsive particle acceleration processes, such as magnetic field reconnection, may also be active further along the jet.

The more powerful FR II jets, however, remain collimated much longer and are much narrower, which means that they are less well understood as they have only recently been resolved transversely. Early results suggest that the jets are edge brightened (e.g. Swain et al. 1998) but as they remain relativistic (Hardcastle et al. 2009b), they are not entraining material like the FR I jets so can transport energy efficiently to hotspots where they terminate.

The hotspots are compact, flat-spectrum ($0.5 < \alpha < 0.7$) regions at the 'working surface' of the jet (Blandford & Rees 1974). In higher resolution radio images, multiple components have been detected in the hotspots with the jet terminating at the *primary* hotspot (Laing 1982). It has been suggested that the other *secondary* hotspots may be the result of a precessing jet where the secondary hotspots are previous impacts (e.g. Blundell & Rawlings 2001) or deflections of the primary impact of off clouds or a previous cocoon wall (Lonsdale & Barthel 1986; Williams & Gull 1985).

Extended Lobe Emission

The term ‘lobe’ is a broad term used to describe a variety of extended radio emission. In the Fanaroff-Riley classification, low-power FR I jets often, but not in all cases, disperse into extended, diffuse linear regions called plumes; however, the jets of FR II travel into the external medium, pushing it outwards disrupting the surrounding gas and causing a cocoon to form around the jet, which fills with synchrotron-emitting electrons.

As the lobes interact directly with the surrounding material, the structure of the lobes depends on the environment and on the jet power. Where a plume bends away from the jet axis, the lobe is referred to as a tail. Objects called wide-angle tail radio galaxies (WATs) have twin, FR II-style (Type II) jets that abruptly flare into long, often bent, plumes and tails. If these jets are light, the shape of these tails may be due to the motion of the host or cluster environment, as these are often brightest cluster galaxies (Hardcastle et al. 2005). Narrow-angle tail radio galaxies (NATs) are also detected in clusters; however, the large proper motion of the host galaxy means that ram pressure exerted by the intracluster medium causes the lobes to be bent back behind the galaxy, away from the direction of motion, so the radio galaxy may appear to have only one tail.

Between the lobes, close to the core, there may be a faint, diffuse region which fills the gap between the lobes. This region is referred to as a *bridge*. Within the lobes and the bridge there may also be poorly defined, diffuse regions within the low surface-brightness regions which are referred to as *haloes*, and in some cases the lobe material broadens away from the jet axis and produces *wings*. Examples of these morphologies are shown in Figure 1.7.

We detect radio lobes via the synchrotron emission process so the effects of magnetic field strength and the distribution of the radiating particle energies cannot be separated. By assuming that the energy density of each of these fields is the same – an equipartition model – then we can estimate the minimum total energy of the radio source (e.g. Leahy 1991). Assuming equal filling factors in magnetic fields and radiating particles, equipartition is given by

$$\frac{B^2}{2\mu_0} = (1+\kappa)\int_{E_{min}}^{E_{max}} EN(E)dE \tag{1.12}$$

where κ is the proton to electron energy ratio. Burbidge (1956) showed that the minimum energy condition is very close to the equipartition condition so assuming equipartition produces a reasonable estimate. However, in order to test this assumption, we require independent measurements of the magnetic field strength which cannot be made with just the radio synchrotron emission. X-ray observations of the lobes have proved vital to this problem and are discussed in Section 1.3.4.

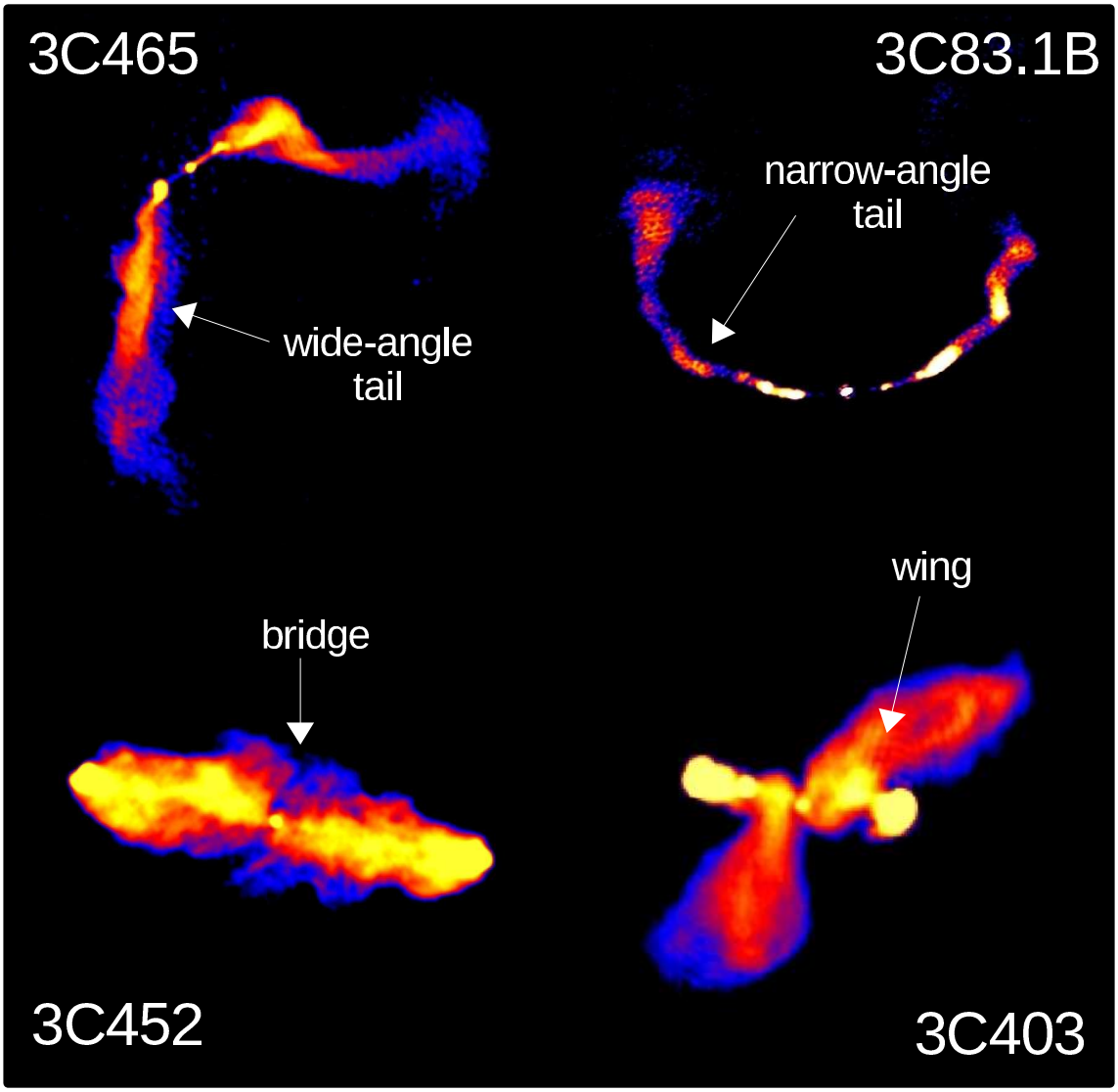

Figure 1.7: Examples of the different radio descriptions used; top left is 3C 465, a wide-angle tailed galaxy (WAT), top right is 3C 83.1B, which is a narrow-angle tailed galaxy (NAT), bottom left is 3C 452, which is a good example of a bridged galaxy, and bottom right is 3C 403, which has wings on both lobes and is thus described as a X-shaped radio galaxy.

1.3.2 UV and Optical Emission

The hosts of powerful radio galaxies are generally elliptical and giant elliptical galaxies, typically residing in groups and clusters. The less powerful active galaxies, such as Seyfert galaxies, are found in spiral galaxies suggesting that there is a link between the host properties and the generation of radio sources; despite having an AGN, only small galaxy-scale radio features are typically detected in spiral galaxies (e.g. HCG 6764; Hota & Saikia 2006; Croston et al. 2008b); however, an FR I double radio source has been detected in the spiral galaxy 0313–192 (Keel et al. 2006).

Studies of the host properties have shown that the hosts of FR Is tend to be more optically luminous that those of FR IIs (Lilly & Prestage 1987; Owen & Laing 1989), which may indicate higher dust extinction in FR IIs (Gonzalez-Serrano et al. 1993); this might affect the fuelling of the central AGN. Govoni et al. (2000) found that the elliptical hosts of AGN tend to be bluer than the corresponding population of field elliptical galaxies, which suggest that the AGN host ellipticals may be undergoing current or recent star formation. These optical correlations relating the host properties to the AGN activity are consistent with a model where galaxy mergers trigger AGN activity (Heckman et al. 1986). This is also supported by the evolution of the global star formation rate in the Universe (Madau et al. 1996) which shows a marked similarity to the evolution of the co-moving number density of powerful radio sources (Dunlop & Peacock 1990), thus suggesting that the triggering of quasar/jet activity is intimately linked with the evolution of the general galaxy population. There are still many uncertainties concerning the nature of merger triggering such as the types of merger or interaction involved and at what stage the jets are triggered. It is also unclear whether there are multiple radio outbursts as the galaxies build up during mergers and ultimately, how radio galaxies fit into the overall galaxy evolution models. The study of circumnuclear starburst regions has therefore become very important for determining whether mergers are triggering AGN activity and starbursts; however, due to the small scales of these starburst regions, removing the jet and other activity-related components from the central optical emission is difficult (see Tadhunter et al. 2005, and references therein).

The strong spectral lines detected in Seyfert galaxies, HERGs (NLRGs and BLRGs), and quasars indicate that there are multiple regions emitting in optical bands originating from the central few parsecs of the AGN. The narrow lines have widths corresponding to several hundred kilometres per second, suggesting an origin in a region of low-density gas. However, the widths of the broad-line emission lines indicate velocities of the order of 10^4 km s^{-1} and the lack of forbidden emission lines suggests a much denser region where collisional de-excitation is more likely than the spontaneous de-excitation which produces forbidden lines (Rees et al. 1989; Dumont et al. 1998; Ferland et al. 1992). These narrow-line and broad-line regions (NLR and BLR respectively) are within a few tens of parsecs of the centre of the AGN, and are directly detected in Seyfert galaxies as they are not dominated by jet-related synchrotron emission like more powerful radio galaxies.

Observations of the environments of active galaxies show that more powerful radio galaxies (FR IIs) prefer poorer clusters and lower power radio galaxies (FR Is) prefer groups of galaxies (Prestage & Peacock 1988; Hill & Lilly 1991). In either case, the likelihood of a galaxy merger is higher than in the field. This is thought to explain why although nearly all nearby galaxies have a super-massive black hole (SMBH) in their cores, only $\sim 10\%$ are active (Kormendy 2001). The activity of SMBH may also be controlled by the availability of fuel; mergers can provide abundant cold material that can be accreted as can cooling flows in the centres of clusters and groups, but it has been suggested that some active galaxies accrete hot gas, which is not supplied during merger events (Allen et al. 2006; Hardcastle et al. 2007a; Tasse et al. 2008). This is discussed further in Section 1.4.3.

The mass of the central SMBH has been shown to tightly correlate with the stellar bulge component of the host (e.g. Kormendy & Richstone 1995; Ferrarese & Merritt 2000; Marconi & Hunt 2003), which suggest that the properties of the host and the black hole are linked. It has thus been suggested that they co-evolve until either all the gas has been consumed (e.g. Archibald et al. 2002) or the central AGN is powerful enough to drive the remaining gas out of the galaxy (e.g. Silk & Rees 1998; Fabian 1999). Using the Sloan Digital Sky Survey (SDSS), Best et al. (2005) confirmed these relationships and determined that although the fraction of active AGNs is related to the stellar and black hole masses, the dominant mechanism for triggering AGN activity is mergers and interactions between galaxies, which are more common in groups and poor clusters.

Although we do not detect lobe emission from active galaxies in optical wave bands, optical jets have been known for nearly a hundred years; the jet in M 87 was first detected before it was even identified as a galaxy (Curtis 1918). Other bright optical jets have been discovered with ground-based observations (3C273; Greenstein & Schmidt 1964, 3C66B; Butcher et al. 1980), but since the launch of the *Hubble Space Telescope* (*HST*), ~ 40 more optical jets have been detected (Jester 2003). The multi-band detections suggest that we are detecting optical synchrotron emission with an optical spectral index of 0.6 – 1.6 (Stawarz et al. 2003), which indicates a spectral break (as $\alpha_{opt} > \alpha_{rad}$). The length of optical jets of FR Is is generally much shorter than those of FR IIs (Butcher et al. 1980; Stawarz et al. 2003) but they are all longer than the light travel times of the optical synchrotron emitting electrons, which gives further support to a model involving an in situ particle acceleration process along the jet.

Observations in the ultraviolet band are difficult so this band is not often used in studies of AGN. As mergers are thought to trigger activity within the AGN, UV bright galaxies may indicate increased star formation from a merger, but this does not immediately identify the galaxy as an AGN.

1.3.3 Infra-red Emission

Early infra-red (IR) observations of active galaxies focused on optically selected Seyfert galaxies and revealed an excess referred to as the 'infra-red bump' in these objects (Harper & Low 1973; Telesco & Harper 1980). High resolution IR imaging of the central kpc of active galaxies has since revealed that this central emission is likely due to the thermal emission of dust from central disks in many AGN (e.g. Brookes et al. 2006). Only in the radio-loud sources has non-thermal infra-red emission been detected at kpc-scale distances from the core; this was quickly associated with the jet synchrotron emission (Edelson & Malkan 1986). The central, larger-scale dust disks are likely due to recent mergers; the kpc-scale disk in Cen A is attributed to the collision between a small gas-rich spiral and a larger elliptical galaxy (Baade & Minkowski 1954; Quillen et al. 2006).

The IR emission from more distant AGN is likely from the unresolved core but is thought to be contaminated with non-thermal synchrotron IR from the jet bases. The dust also absorbs large amounts of light from the central AGN reducing their apparent brightness. By comparing the IR emission to other core related emission (in Optical, UV and X-ray), Cleary et al. (2007) and Hardcastle et al. (2009b) have shown that the IR luminosity is correlated with the total and core radio emission and that BLRGs lie above this correlation and LERGs lie below, which suggests that the non-thermal emission is more important in BLRGs than in NLRGs and LERGs. Hardcastle et al. (2009b) also compared the IR emission with the X-ray emission as the IR can tell us the luminosity of a heavily obscured AGN. This is discussed further in the next section.

1.3.4 X-ray Emission

Many active galaxies are hosted by galaxies in clusters and groups, so the X-ray picture of many radio galaxies is dominated by thermal emission from hot gas in the system. The hot gas emits thermal bremsstrahlung and line emission, which can be fitted using the models discussed in Section 1.2.3. The early detections of this hot environment and the corresponding pressure measurements, allowed estimates of the internal lobe pressure to be made by assuming pressure balance (e.g. Worrall & Birkinshaw 2000; Hardcastle & Worrall 2000). However, these measurements may be overestimated by a order of magnitude due to iC scattering (e.g. Brunetti et al. 1999). The difference in these estimates of the internal lobe pressure could arise from a departure from the equipartition condition or from a dominant relativistic population of protons. Earlier observations suggested that the lobes iC scatter photons from the CMB (Feigelson et al. 1995; Tashiro et al. 1998, 2001; Hardcastle et al. 2002a; Isobe et al. 2002), the synchrotron emitted photons from the electron population (Hardcastle et al. 2002a) and to a lesser extent, photons from the nucleus (Brunetti et al. 1997) into the X-ray regime so that the contribution of this X-ray emission has to be excluded while measuring the external environment pressures. This was later confirmed with the superior sensitivity and spatial resolution of *Chandra*.

Basic physics principles dictate that as an FR II jet pushes into the environment at supersonic speeds, the ram pressure of the external environment pushes back maintaining a balance; however, the transverse expansion of the lobes is not so clear. As described by Scheuer (1974), if the lobes are overpressured with respect to the environment, the transverse expansion would be controlled by the pressure difference; this expansion could be supersonic and would then produce a bow shock around the source (Model A by Scheuer 1974). If the lobe is in pressure balance with the environment, then the transverse expansion will be subsonic while the linear expansion may continue supersonically (Model C). In order to distinguish between these lobe expansion models we need to understand more about the particle content and the behaviour of the lobes.

Bright X-ray thermal emission has been detected from the edges of the radio lobes in Cen A (Croston et al. 2009) and NGC 3801 (Croston et al. 2007), which indicates shock heating of the gas surrounding the radio lobes. In Cen A, we also detect synchrotron emission due to the linear expansion of the inner south-west lobe accelerating the surrounding gas to X-ray emitting energies.

As suggested in Section 1.2, the radio synchrotron emission and the X-ray iC emission can be used to constrain the electron energy distribution and magnetic field strengths. We can also use these constraints to test the equipartition condition by adjusting the magnetic field strength of the models until the predicted X-ray emission agrees with the X-ray observations. This technique is used with the emission from 3C 353 in Chapter 3 and was used by Croston et al. (2005b) to estimate the magnetic field strengths of FR II radio galaxies and quasars. They show that the majority are close to equipartition or slightly electron dominated.

The external pressures of the intracluster medium can be determined from the surface brightness profile and an estimate of the temperature of the group or cluster of galaxies, which can in turn be converted into density, pressure and entropy profiles (see Section 1.5). If the external pressures are greater than the internal ones, then we would not see extended structures as their expansion would be suppressed and they would collapse. This suggests that the lobes are either in pressure balance or overpressured with respect to the environment. The expected effect of an AGN on other gas properties is discussed in Section 1.5.

The jet knots discussed in Section 1.3.4, also emit synchrotron emission in X-rays, which suggest that they are also regions of in situ particle acceleration. Although offsets have been detected between the radio and X-ray knots of distant radio galaxies, attributed to downstream advection of synchrotron emitting electrons, higher resolution radio images show that there are radio counterparts which are unresolved in previous images (Hardcastle et al. 2003). The fact that we detect X-ray synchrotron emission from these regions indicates that these are areas of current particle acceleration as the synchrotron loss timescales are of the order of tens of years. The particle acceleration mechanisms that could accelerate particles to these X-ray emitting energies are investigated in Chapter 5.

We also detect X-rays from the central regions of active galaxies as a bright point source and it is the X-ray spectrum from these core regions that differentiates AGN from star-burst galaxies. This X-ray emission is due to non-thermal emission from the jets and from a corona of hot electrons (e.g. Shapiro et al. 1976; Sunyaev & Truemper 1979). In radio-quiet active galaxies, we detect only the corona-related X-ray emission, whereas in LERGs, we only detect the jet-related emission. We can also detected absorbed X-ray emission from obscured AGN, where the corona-related emission is absorbed and we detect the jet-related emission only. Examples of the spectra of radio galaxies with and without the central absorbed component are shown in Figure 1.8.

By comparing the absorbed and unabsorbed components of these X-ray cores with the central emission in radio, optical and IR (see Section 1.3.3), Hardcastle et al. (2009b) have shown that the galaxies with absorbed components tend to be associated with the radio bright NLRGs and BLRGs whereas those without the absorbed hard X-ray component are associated with low-excitation radio galaxies. This also suggests that the jet origin is outside of the torus (Hardcastle et al. 2006a). The implications of these properties are discussed in Section 1.4.3.

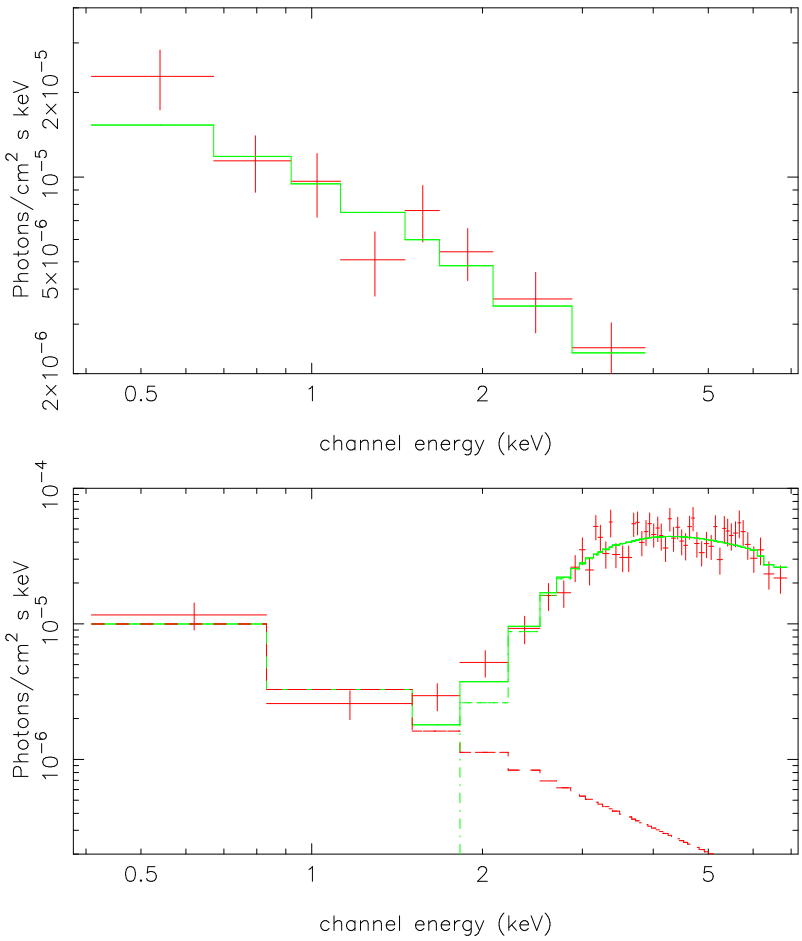

Figure 1.8: Examples of the X-ray spectra of the low-excitation radio galaxy (LERG) PKS 1839-48 (top panel) and the narrow-line, high-excitation radio galaxy (NLRG) PKS 0213-13 (bottom panel) by Mingo et al. in prep. The additional absorbed component in the NLRG indicates the presence of the torus.

1.3.5 Gamma-ray Emission

Astronomy in the γ-ray regime is only now being realised so that there are few γ-ray detections of AGN. The *Fermi* Large Area Telescope (LAT) has detected high-energy (MeV/GeV) γ-rays from M87 (Abdo et al. 2009) and from the giant radio lobes of Cen A (Cheung & Fermi-LAT collaboration 2010), and more recently, the H.E.S.S. (High Energy Stereoscopic System) experiment (Aharonian et al. 2006), has detected very high energy (VHE) TeV γ-rays from M87 (Aharonian et al. 2003, 2006) and from Cen A (Aharonian et al. 2009). It is however, unclear where exactly these γ-rays originate.

Hardcastle et al. (2009a) used *WMAP* 408 MHz – 90 GHz radio data to constrain the high-frequency radio spectra of the giant lobes of Cen A, which allowed them to estimate the TeV iC emission from the lobes. They show that TeV emission is only likely from the northern lobe as the emission is best fit with a continuous injection model that leaves the maximum energy of the emitting particles unconstrained. The Fermi-LAT Collaboration (2010) resolved TeV emission from the giant lobes of Cen A which they interpreted as iC scattered relic radiation from the CMB and IR-Optical extragalactic background light (EBL) at higher energies (Georganopoulos et al. 2008).

Several other possible mechanisms have been proposed for the production of VHE γ-rays, particularly in Cen A. Kraft et al. (2001) have detected more than 200 X-ray point sources in the vicinity of Cen A, but source ensembles, such as the sum of the contributions from supernova remnants (SNRs) or planetary nebula (PNe), require an unrealistic number of sources to produce γ-rays (Aharonian et al. 2009). Hadronic models (Reimer et al. 2004) suggested that the protons or $\mu^{\pm}$ and $\pi^{\pm}$ created in the inner jet could emit synchrotron radiation at these energies, and Stawarz et al. (2006) suggested that $e^{\pm}$ created in the immediate vicinity of the SMBH might iC scatter nuclear starlight photons to these γ-ray energies. Both of these models are consistent with the HESS detection. Another suggestion is that the particles in the shock of the southwest inner radio lobe, or in the kpc-scale jet, that are accelerated to the TeV energies and that emit X-ray synchrotron radiation could be iC scattering photons into the γ-ray regime (Croston et al. 2009).

1.3.6 Summary of Active Galaxy Characteristics

Throughout Section 1.3 I have presented the observational evidence for the features associated with active galaxies and here I summarise the current picture of active galaxies and the outstanding questions that are relevant to this thesis.

The Central AGN

The central AGN consists of a SMBH of mass greater than 10^6 $M_\odot$ (Woltjer 1959), which radiates vast amounts of energy as it efficiently accretes material (Salpeter 1964; Lynden-Bell 1969). The accreted material may form a disk (e.g. Shapiro et al. 1976; Sunyaev & Truemper 1979), or it may accrete directly onto the SMBH (Bondi accretion; Bondi 1952). The jets, if present, probably originate at or near the SMBH although the precise mechanism is not well understood. The jets radiate via iC scattering of the nuclear photons as well as by the synchrotron emission process. Synchrotron and iC emission mechanisms were discussed in Section 1.2. We also detect a corona of hot gas close to the SMBH that Compton scatters optical and IR nuclear photons into the X-ray regime.

Centralised Cold Structures

Surrounding the central engine, there may be a torus of optically thick, neutral gas and dust normally at the same orientation as the accretion disk. Tori are generally seen in IR due to thermal emission by the gas and dust; however, the absorption of soft X-ray and optical emission also reveals dusty disks (see Figure 1.6).

In AGN with accretion disks and tori, between them lies the broad-line region (BLR), a collection of gas clouds, highly ionised in the inner reaches and in a low-ionisation state further out, and surrounding the torus is the narrow-line region (NLR); these regions are discussed in Section 1.3.2 and are inferred from optical spectra. These gas clouds are photoionised by high-energy photons from the accretion disk. All these features exist within the central few parsecs of some AGN, but not all (see Section 1.4.3); these features consist of cold material and thus indicate accretion of cold gas.

Jets

We do not see jets in all active galaxies; however those that are detected can broadly be classed as low-powered, FR I-type jets that decelerate as they move into the surrounding gas and entrain material, and more powerful, FR II-type jets that do not decelerate (see Section 1.3.1). FR I-type jets tend to be turbulent, with knots of bright material where the jet plasma is re-accelerated. Knots are less often seen in FR II-type jets; they are generally fainter so less is known about these knots. The specific particle acceleration mechanisms that produce these jet knots are unclear, although there are plenty of suggestions. Impulsive particle acceleration mechanisms such as small-scale magnetic field reconnection would cause short-lived flaring of jet knots. In Chapter 5 I also investigate longer-lived particle acceleration mechanisms such as adiabatic compression, shocks due to collisions between the jet material and an obstacle such as Wolf-Rayet stars or molecular clouds (Hardcastle et al. 2003), reconfinement of the jet plasma (e.g. Sanders 1983) and enhancements due

purely to relativistic beaming. The confinement mechanism for the jet itself is not well understood but these issues are beyond the scope of this thesis.

At the end of the jets in FR II-type jets, we observe bright hot spots, which are likely the result of the jet encountering the wall of cocoon produced during the expansion. There have been various mechanisms proposed for the location and number of hot spots detected including a precessing beam and deflections off of clouds in the area (Lonsdale & Barthel 1986; Williams & Gull 1985).

Lobes

The appearance of the lobes is largely due to the power of the jet and the environment into which it is expanding. The expansion is generally subsonic as it moves away from the core, remaining in pressure balance with the environment. In FR II lobes, the lobes are generally in pressure balance or overpressured so the expansion heats the surrounding gas. If the expansion is supersonic, such as in Cen A, it can cause a strong shock (Croston et al. 2009). In FR I lobes, the shape of the lobes is generally dependent on the interaction with the environment resulting in more diffuse, plume-like lobes. The models for the expansion of the lobes depend mainly on the minimum energy condition, which is often approximated by the equipartition condition, so the energy densities of the magnetic fields and particles within the lobes are important factors. Croston et al. (2005b) found that the lobes in 70% of the 33 classical double radio galaxies and quasars in their sample were in equipartition or slightly electron dominated. However, in FR I lobes, the internal pressure due to relativistic electrons is insufficient to balance the external pressure (Morganti et al. 1988; Hardcastle et al. 1998). The most plausible origin of the required additional internal pressure is either material that has been entrained and heated, or magnetic dominance of the lobe (Croston et al. 2003, 2008a). In Chapter 3 I examine the emission from the lobes of the FR II source 3C 353 to determine whether this source is in equipartition and also whether the emission is dependent on the magnetic field, the particle energy, or both.

Within the lobes we see filamentary structures that suggest that the lobe material is not uniformly distributed throughout the lobes [e.g. Fornax A (Ekers et al. 1983; Fomalont et al. 1989); Hercules A (Dreher & Feigelson 1984); and Cygnus A (Perley et al. 1984)] . An example of the filamentary structure seen in 3C 310 is shown in Figure 1.9. These structures may be due to projection effects, where a denser, brighter string of material is seen as a bright arc but the features of the lobe material that cause this enhancement are not well understood. In Chapter 4, I use the radio and X-ray emission from different regions of the lobes to determine whether the emission is related and I test whether the emission can be produced using models where the electron energy density and the magnetic field change by different amounts.

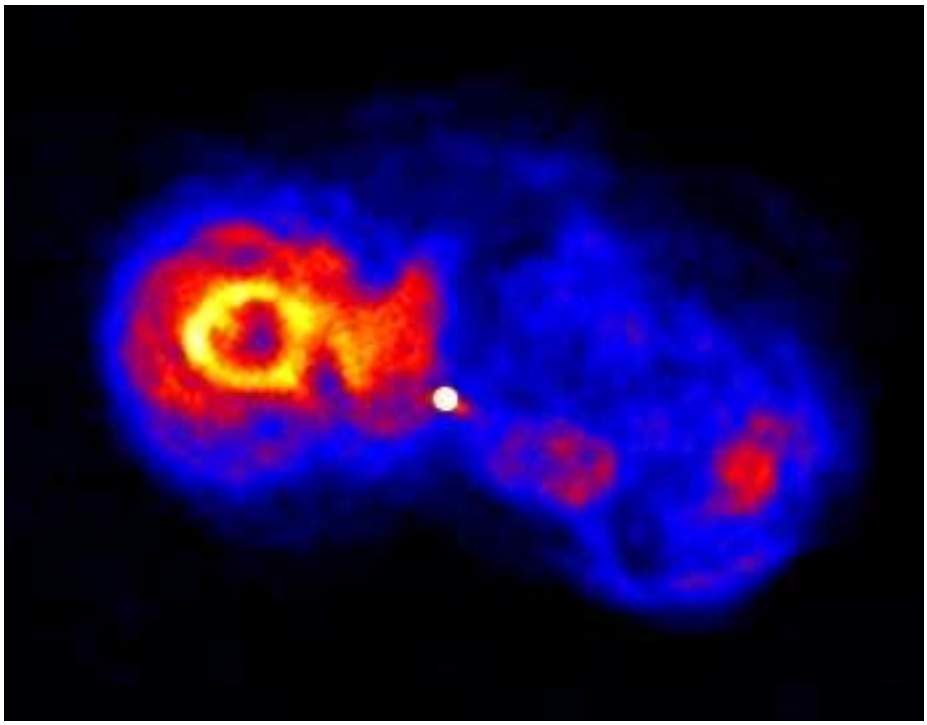

Figure 1.9: Radio image of 3C 310 showing filamentary lobe structure.

1.4 Unification of Active Galaxies

As already discussed, AGN have a variety of characteristics that allow us to classify them based on their radio morphology and broad-band spectra. Initial attempts to combine these objects into a single unified model started with a model by Scheuer & Readhead (1979) where they argued radio-quiet QSOs and flat-spectrum radio quasars were the same object, just viewed at different angles. However, the common occurrence of low-brightness emission surrounding flat-spectrum quasars means this picture is not viable as the unaligned quasars would not be radio-quiet (Perley et al. 1980). Orr & Browne (1982) went further and linked core-dominated and lobe-dominated radio-loud quasars (CDRLQs and LDRLQs) also using projection and the effects of relativistic beaming. They showed that observing a quasar directly down the jet resulted in a core-dominated, radio-loud quasar with a flat spectrum. Quasars observed at angles to the jet axis would thus be classed as lobe-dominated, steep-spectrum, radio-loud quasars. Concurrently, Antonucci & Miller (1985) were developing a model for Seyfert galaxies suggesting that Sy1 and Sy2 galaxies have the same structures and that the observed differences are due to an optically thick disk obscuring the broad-line emission lines in Sy2 objects. This also required an argument for the viewing angle determining whether the disk obscured all of the BLR emission. These models of unification were the first steps towards radio galaxy and quasar unified models using the observing angle and relativistic beaming to group objects (Barthel 1989). Eventually these models evolved to a scheme where the central AGN is a consistent feature with additional features, such as accretion disks, tori and jets, due to the environment and accretion mode.

1.4.1 Radio Loudness

The population of AGN can be split into radio-loud and radio-quiet active galaxies depending on their luminosity at 1.4 GHz (greater or less than $\sim 10^{25}\,\mathrm{W\,Hz^{-1}}$, e.g. Sadler et al. 2002). At lower luminosities, the radio source population is dominated by emission from other sources such as star-burst galaxies although there are still some AGN. The galaxies presented in this thesis are all radio-loud by this definition.

The presence of a powerful jet is believed to be the cause of this split and although samples of active galaxies can become contaminated with star-burst galaxies, the radio brightness and jet power should be a continuum down to a limit determined where the galaxy is no longer active and, as discussed in Section 1.3.2, this activity is dependent on the host and the large-scale environment.

1.4.2 Fanaroff-Riley Subclasses

The Fanaroff-Riley dichotomy describes the morphological differences between galaxies, which are related to the jet power but not directly to the structure of the central AGN. It is more likely that the behaviour of the extended lobe emission is dependent on the host and large-scale environment (Bicknell 1995). This is supported by a correlation between the FR I/FR II divide in luminosity and the optical luminosity so that this FR I/FR II luminosity split is closely linked to the break in the radio luminosity function (RLF) (Ledlow & Owen 1996).

The majority of the early work on the RLF focused on its evolution and the contributions from starburst galaxies, and flat and steep-spectrum objects (Jackson & Wall 1999). However, Kaiser & Best (2007) considered the FR classes which include both flat and steep-spectrum objects and used dynamical models (e.g. Falle 1991; Kaiser & Alexander 1997) and the synchrotron emission from the radio lobes of FR II sources (Kaiser et al. 1997; Blundell et al. 1999; Manolakou & Kirk 2002) to develop a model which unifies FR IIs with the 'standard' turbulent FR Is by suggesting that all objects have an FR II (Type II) jet in their centres, which flares when it reaches a lower density point in the environment and undergoes reconfinement of the jet. In FR Is, the weaker jet reaches pressure balance and the dense external material replaces the lobe material, eventually reaching the jet flow, at which point, the jet becomes unstable and turbulent, begins entraining material and expands into the extended linear plumes. In FR IIs, the jets are stronger and thus maintain relativistic speeds and continue to be overpressured, thus protecting the jet flow from the ambient material. These lobes eventually reach a pressure balance but by then they have achieved the well known rounded shape of classic FR II lobes. Kaiser & Best also calculated the limiting jet power ($\mathcal{Q}_{min} = 3.3 \times 10^{37}$ W), which is consistent with the dividing line for the FR classes found by Rawlings & Saunders (1991).

Although most FR Is have low-excitation optical spectra and the majority of FR IIs have high-excitation optical spectra, there are also low-excitation FR IIs (e.g. Jackson & Rawlings 1997; Chiaberge et al. 2002; Hardcastle et al. 2004) and high-excitation FR Is (e.g. Blundell & Rawlings

2001). This suggests that although the large-scale lobe structure can adequately be explained as due to the jet power and environment, it is still clear that there is a more physical difference in the core AGN of some active galaxies.

1.4.3 High and Low Excitation Galaxies

If active galaxies are divided up into those with and without high-excitation emission lines, the story of their evolution and the similarities in their structures becomes more elegant. As mentioned in Section 1.3, Hine & Longair (1979) defined two classes of active galaxy, those with 'weak' line emission (low-excitation radio galaxies; LERGs) and those with 'strong' emission lines (high-excitation radio galaxies; HERGs).

The presence of high-excitation emission lines in HERGs indicates the presence of BLRs and NLRs in these objects and the absorbed X-ray emission suggests accretion disks too. In order for these features to be present, the SMBH must be efficiently accreting cold material ($T \sim 1000\,\mathrm{K}$) from a relatively thin accretion disk (Hardcastle et al. 2007a). If the HERG has a jet, then we detect NLRGs, BLRGs and Quasars at increasing viewing angles, and if there is only a weak jet, we detect Sy2 then Sy1s as the angle increases. The standard model for accretion in these objects is that angular momentum is lost through viscosity, which itself produces energy that is radiated away in a quasi-blackbody spectrum that peaks in the optical/UV bands (Shakura & Sunyaev 1973). The OVV objects also fit into this unification scheme as beamed core-dominated radio-loud quasars (CDRLQs) which are optically varying (Urry & Padovani 1995).

The lack of strong emission lines in LERGs suggests that they do not have BLRs or NLRs within their cores and their unabsorbed X-ray spectra and lack of strong mid-IR emission suggest they have no tori or accretion disks either (Hardcastle et al. 2009b). Hardcastle et al. suggest that the unabsorbed X-ray emission as well as the strongly correlated optical and radio emission indicate a jet origin. They go further to suggest that the lack of structure in the core of LERGs could be due to accretion of hot gas; if the accreting material is hot, then the disk would be geometrically thick to the extent that it would be almost spherical around the SMBH and would Bondi accrete onto the SMBH (Hardcastle et al. 2007a). Hardcastle et al. also showed that the NLRGs (and by association the BLRGs and RLQs) cannot be fuelled in this manner. This is consistent with models of advection-dominated accretion flows (ADAFs) where the energy generated through the viscous nature of the accreting material is advected rather than radiated away, which suggests that LERGs should be less luminous than the HERGs counterparts (Narayan 2005). The problem with this model is that the hot gas would be cooling radiatively which might result in a thin disk of cold material around the SMBH as well, which would lead to the formation of structures which are not seen. The BL Lac objects also fit into this picture as the beamed LERG population (Browne 1983; Urry & Padovani 1995).

This picture is also supported by Baldi & Capetti (2008) who compared UV and optical emission to detect evidence of recent star formation. They found evidence of recent star formation in HERGs but not in LERGs suggesting that recent mergers have triggered star formation and power the AGN by supplying cold gas. This is also the conclusion of work by Herbert et al. (2010) who compared the 4000Å break strength of radio galaxies at $z \sim 0.5$. They found that the LERGs and HERGs have different star-formation histories, with LERGs having no evidence for recent, cold-gas-powered star formation.

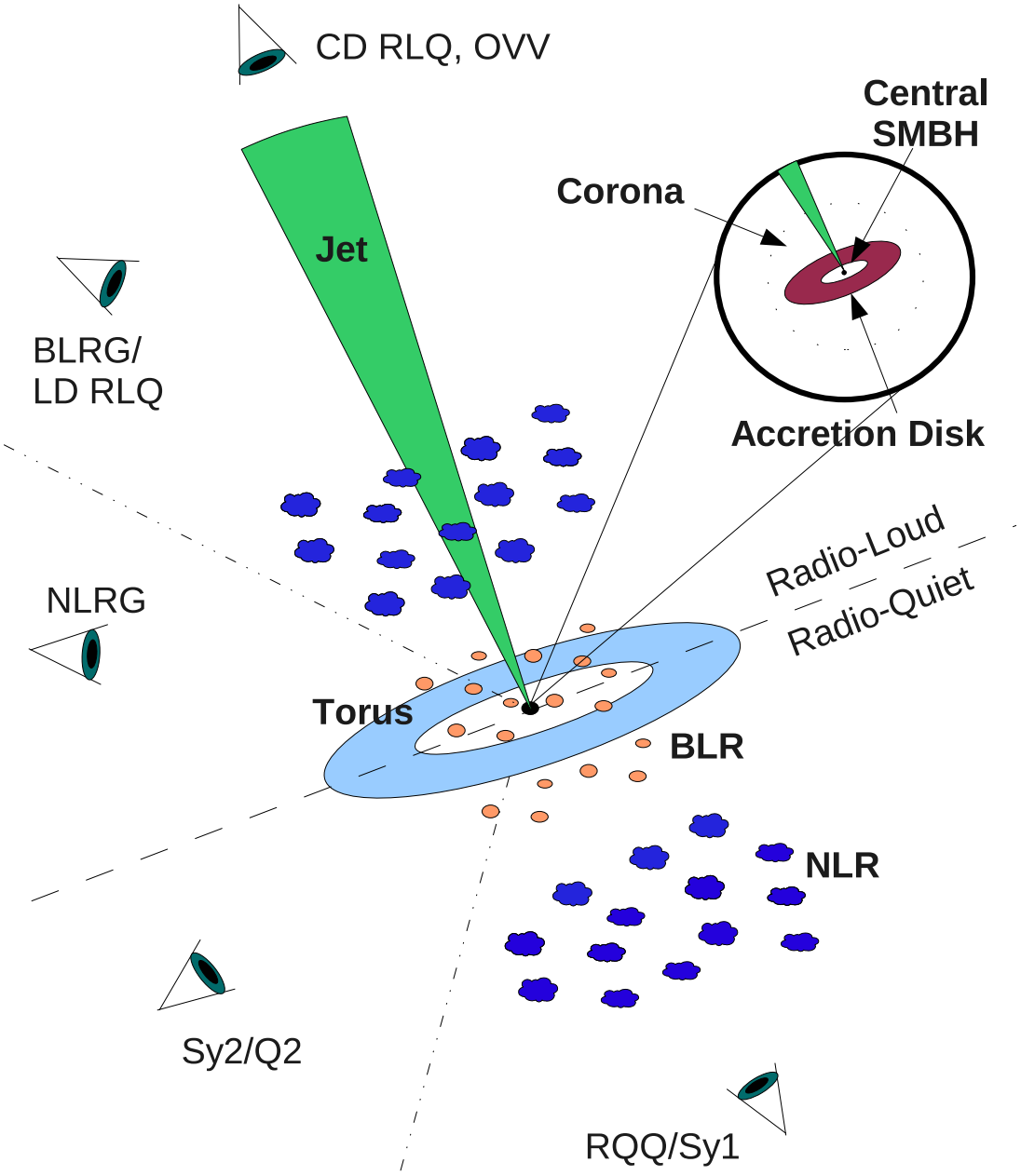

Figure 1.10: Diagram showing the features of AGN and the unification of radio-loud HERGs and radio-quiet active galaxies by viewing angle. LERGs are not shown as their structure suggests that they do not contain a torus, NLR, BLR or central accretion disk.

1.5 Environments of Radio Galaxies: Groups and Clusters

The division between defining a group and a cluster is a vague one but generally a group has less than 50 member galaxies within a diameter of 1 – 2 Mpc, while clusters have many more (up to ~ 1000) members and have typical sizes of 3 – 4 Mpc (Sarazin 1986).

In addition to the member galaxies, groups and clusters have an abundance of hot intergalactic gas at temperatures of 10^7 – 10^8 K; clusters tend to have temperatures of $kT > 2.0$ keV ($T \sim 2.3 \times 10^7$ K). This intracluster medium (ICM) is detected in the X-ray as thermal bremsstrahlung and atomic line emission. The ICM also Compton scatters the CMB so that clusters are seen as shadows in CMB maps through the Sunyaev-Zel'dovich (SZ) effect (see Carlstrom et al. (2002) for a review). The velocities of the galaxies within the system are in the range 800 – 1000 km s^{-1} suggesting that there is also a large amount of dark matter within groups and clusters giving the system a mass of 10^{14} to 10^{15} M$_\odot$.

In the X-ray regime, the surface brightness of these systems peaks in the centre and decreases with radius. Traditionally, a hydrostatic isothermal model has been used to describe the surface brightness profile, assuming that both the hot gas and the galaxies are in hydrostatic equilibrium and isothermal. The model is defined in gas density, n, by (e.g. Birkinshaw & Worrall 1993) as

$$n(r) = n_0 \left(1 + \frac{r^2}{r_c^2}\right)^{-3\beta/2} \tag{1.13}$$

where r_c is the core radius and β, in isothermal systems, is the ratio of the specific energy of the hot gas;

$$\beta \equiv \nu m_p \sigma^2 / kT_{gas} \tag{1.14}$$

where ν is the mean molecular weight, m_p is the mass of a proton, σ is the one-dimensional velocity dispersion, and T_{gas} is the temperature of the intergroup medium. In non-isothermal systems, β is just a measure of the slope of the density profile at large radii.

In some cases, the gas density profile may be complex so a projected double-β model is required (Croston et al. 2008a), which is defined as the projected line-of-sight sum of two β models in gas density:

$$n(r) = n_0 \left[\left(1 + \frac{r^2}{r_{c,in}^2}\right)^{-3\beta_{in}/2} + N \left(1 + \frac{r^2}{r_c^2}\right)^{-3\beta/2} \right] \tag{1.15}$$

where N is the relative normalisation of the two β models. In clusters, where the velocity dispersion is relatively high, there can be some change in the temperature without significantly changing the shape of the surface brightness profile; however, in groups, the gas must be fairly isothermal for the β model to be a good fit. Several other models also provide adequate fits to the real data, in particular fitting centrally peaked profiles. These include a double-β model, which consists of a β model for $r < r_{cut}$ and another for $r > r_{cut}$ with normalisations and β values that assure the gas density is continuous (Pratt & Arnaud 2002), a modified double-β model (the KBB model by

Pratt & Arnaud 2002), which includes the factor ξ that determines the degree to which the profile is peaked, and a modified single-β model (the AB model by Pratt & Arnaud 2002) that is able to fit central cusps; instead of the N_0 factor in Equation (1.13), the normalisation is $A(r/r_c)^{-\alpha}$. The complicated structures in the density profiles due to cavities, bubbles or shocks within the hot gas, will reduce the quality of the fit but some models can improve the fit to the central structures as can deprojecting the profile (Croston et al. 2006).

Observations of the temperature profiles of the hot gas in these systems show that in many of these systems, the temperature drops at large radii and may drop towards the core, so that an isothermal model is not a good representation. However, if we consider a point r_{cool} at which the cooling time, t_{cool}, is the same as the age of the system, t_a, then the weight of the gas at larger radii is balanced by the thermal pressure of the gas within this radius. As the gas radiates by thermal bremsstrahlung, the central gas cools. To maintain the pressure balance at r_{cool}, the gas density within this radius must increase resulting in a flow of material inwards. This is a cooling flow and this picture is largely consistent with the observed temperature profiles; however, the central temperatures are only a factor of 2 – 3 less than at larger radii (Allen et al. 2001; Vikhlinin et al. 2005). The X-ray surface brightness profiles observed with *ROSAT* were highly peaked with steep temperature gradients towards the centre, which implies a higher rate of cooling that was inconsistent with the mass deposition rates for colder gas required to produce the observed star formation and line emission (see Fabian 1994, and references therein). Later observations with *Chandra* and *XMM-Newton* showed that the cold gas mass deposition rates were overestimated in the earlier results and that the minimum temperature of the multi-phase gas within the cluster appears to only cool to approximately 1/3 of the outer cluster temperatures; the emission lines expected from cooling through lower temperatures are not seen (e.g. Peterson et al. 2003; Sakelliou et al. 2002).

Most groups and clusters are dominated by a central ‘brightest cluster galaxy’ (BCG) which is typically a giant elliptical, but some have several large galaxies in the core, which may in the future coalesce into a massive BCG. In models of hierarchical galaxy formation (e.g. White & Rees 1978), eventually all the galaxies in the group or cluster would coalesce into a high-luminosity, super-massive galaxy. In this scenario, the galaxies form when gas condenses at the centre of dark matter haloes. The main problem with this theory is that it predicts a broad halo mass distribution that, given a constant mass-to-light ratio, would produce more high- and low-luminosity galaxies than are observed as shown in the luminosity function in Figure 1.11 (Croton et al. 2006).

One solution to explain the lack of super-massive galaxies, also provides a explanation for cool cores detected in the X-ray gas, only cooling to 1/3 of the temperature of the outer regions. If there is an active galaxy within the central regions of the group or cluster, AGN feedback could heat the gas within the centre preventing it reaching cold temperatures and also quenching star formation, as the gas would not be able to cool enough to condense into stars. AGN feedback could thus explain the lack of high-luminosity, high-mass galaxies (Croton et al. 2006; Bower et al. 2006). At the

other end of the scale, feedback from supernovae may be energetic enough to explain the lack of low-luminosity, low-mass galaxies by expelling the intergalactic gas from smaller galaxies and thus quenching their star formation (Benson et al. 2003).

The presence of an AGN in the centre of the group or cluster should also affect other gas properties such as the entropy. Entropy determines the structure of the IGM and records the thermodynamic history of the system's gas, so an AGN in the centre of the group or cluster may therefore explain the observed excess entropy of the gas (Ponman et al. 1999). A radio-loud AGN in the centre of a group or cluster could transfer energy from the core to radii of a few Mpc, steepening the entropy profile, and multiple periods of activity would accumulate energy to the levels detected, thus increasing the entropy beyond the predictions of simple hierarchical formation and evolution. As discussed in the review of clusters by Voit (2005), the entropy of a system is defined as

$$K = \frac{k_B T}{\mu m_p \rho_g^{2/3}} \tag{1.16}$$

The quantity K is the constant of proportionality in the equation of state $P = K\rho_g^{5/3}$ for an adiabatic monatomic gas and is directly related to the standard thermodynamic entropy per particle, $s = k_B \ln K^{3/2} + s_0$, where s_0 is a constant that depends only on fundamental constants and the mixture of particle masses. The gas density and temperature profiles are thus manifestations of the entropy

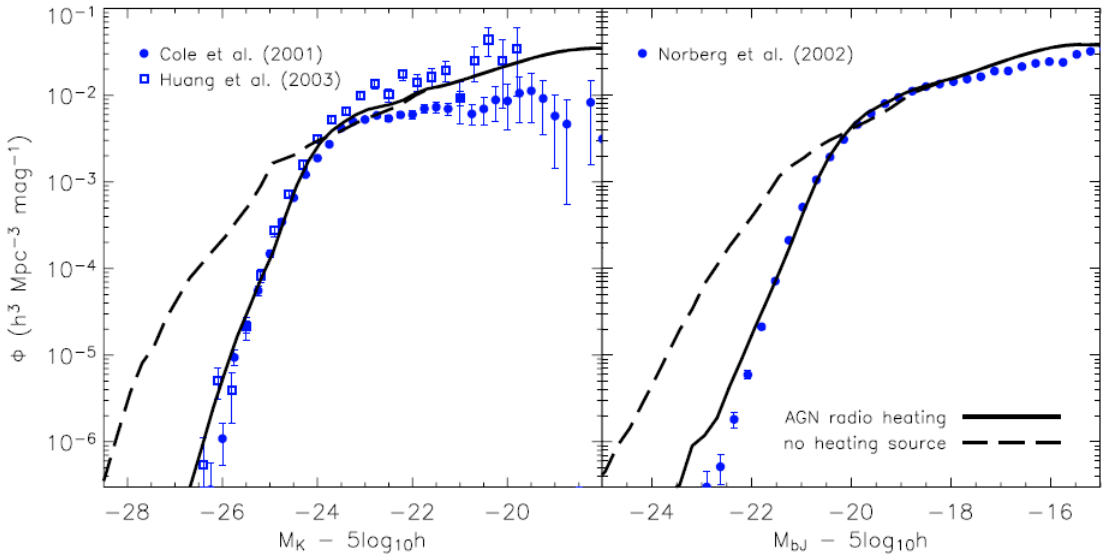

Figure 1.11: Galaxy luminosity functions in the *K* (left) and b_J (right) photometric bands, plotted with and without radio mode feedback (solid and long-dashed lines respectively) as modelled by Croton et al. (2006). Symbols indicate observational results by Cole et al. (2001), Huang et al. (2003) and Norberg et al. (2002) as listed in each panel. As discussed by Croton et al., the inclusion of AGN heating produces a good fit to the data; without this heating source their model over predicts the luminosities of massive galaxies by about two magnitudes and fails to reproduce the sharp bright-end cut-offs in the observed luminosity functions.

distribution of the system. As high entropy gas floats and low-entropy gas sinks in the system, the entropy directly affects the structure of the IGM.

If the material is accreting smoothly, then the entropy gain depends on whether the material is preheated as it crosses an 'entropy shock' into the cluster. If the material is cold the gain is just due to the entropy shock, but if the material is hot, then there is also a component related to the preheating of the material (e.g. Knight & Ponman 1997; Tozzi & Norman 2001). Following the arguments of Voit (2005), in the first case, the entropy profile depends on the mass accretion history and the profiles should be self similar with respect to K_{200}, which is where the entropy is 200 times the critical entropy of the Universe. If the material is hot, then the profiles break from self-similarity and the core is isentropic. In reality the material is accreted in lumps of different densities, not smoothly, so the lumps mix with the ICM of the main halo resulting in a complex shell of shocks as the material falls into the cluster. However, numerical simulations produce self-similar entropy profiles as expected from the scaling properties of hierarchical structure formation (Navarro et al. 1995; Kaiser 1986).

In keeping with the temperature and density profiles, the entropy distribution decreases towards the core; however, the profile is flatter than expected for self-similar clusters (Voit & Ponman 2003). This supports AGN heating in the central regions. However, recent *Chandra* observations of groups, suggest that AGN heating is at kpc distances from the core rather than from the very core; Jetha et al. (2007) found no difference in the central entropy profiles of radio-loud and radio-quiet groups and we would expect an isentropic core at the level of the entropy floor in radio-loud groups with heating. The entropy floor level is thought to be due to pre-heating; non-gravitational heating of the ICM prior to cluster collapse (Ponman et al. 1999).

Although other mechanisms are capable of transferring sufficient energy to the cluster gas to counterbalance cooling cores, the impact of radio galaxies is clearly important; however a detailed analysis of these processes is beyond the scope of this work. Departures from self-similarity indicate additional physics at work in the cores of clusters and groups so in Chapter 6 I investigate the relationship between luminosity and temperature for different populations of groups.

1.6 The Aims of This Thesis

In this thesis, I present work primarily using radio and X-ray data, to investigate the processes involved in transporting energy from the cores of active galaxies to their environments. In particular, I address the following outstanding questions:

- What are the properties of magnetic fields in FR IIs?
- How do the magnetic fields and electron energy distribution affect the lobe energy densities?
- What is the nature of jet knots in FR Is?
- What is the in-situ particle acceleration process at work within FR I jets?
- What is the internal structure of FR I jets like?
- How do active galaxies in groups affect their environments?

In the next Chapter, I discuss the challenges of reducing radio and X-ray data, outlining the standard techniques that I have used in this thesis. In Chapter 3, I present work using the X-ray and radio emission from the lobes of FR II active galaxies with the aim of relating the changes in the surface brightness to the changes in the electron energy spectrum and the magnetic field strength of the emitting material. I also consider the energies of the electron and magnetic field densities to find out where the energy is stored in the lobes. This work was accepted for publication in the Monthly Notices of the Royal Astronomical Society (MNRAS) in 2008 (Goodger et al. 2008).

In Chapter 4, I extend this work to look at the smaller scale changes in the lobe emission to infer the differences within the lobe that produce the filamentary structure seen in many radio galaxies. This work was submitted to MNRAS in February 2010.

I have also worked on the X-ray and radio emission from the jet of Cen A to investigate how the jet fluid is re-accelerated and how the energy is transferred to the lobes. In Chapter 5, I present this work on the jet knots, where I used the temporal changes of the emission to determine the particle acceleration mechanisms at work in this jet. This work was published in 2010 in the Astrophysical Journal (Goodger et al. 2010).

Then in Chapter 6, I examine the X-ray properties of a sample of galaxy groups to investigate whether the presence of a radio-loud galaxy affects the gas properties following up the initial work by Croston et al. (2005a).

Finally, I summarise the conclusions of this work and draw them together to discuss the implications to the current theories of galaxy formation and evolution in Chapter 7.

Throughout this work I use a cosmology in which $H_0 = 70\,\mathrm{km\,s^{-1}\,Mpc^{-1}}$, $\Omega_m = 0.3$ and $\Omega_\Lambda = 0.7$. I define the spectral index such that flux density, $S \propto \nu^{-\alpha}$ and the photon index as $\Gamma = 1 + \alpha$. The errors in this work are 1σ errors unless otherwise stated.

Chapter 2

Data Reduction Processes

Throughout this work, I have used radio and X-ray data to probe the energetics and dynamics of radio galaxies and their interactions with their environments. The radio data were taken at the NRAO Very Large Array (VLA) in New Mexico, USA, and at the NCRA Giant Meterwave Radio Telescope (GMRT) in Pune, India. The X-ray data were observed with the *XMM-Newton* and the *Chandra* space telescopes. In this Chapter I review the standard techniques used to overcome the challenges of radio and X-ray data reduction.

2.1 Radio Data Reduction

The standard method for radio data reduction using the Astronomical Image Processing System (AIPS) developed by the National Radio Astronomy Observatory (NRAO), involves calibrating the raw data in flux, phase and polarisation. The raw data consist of a FITS (Flexible Image Transport System) file containing an entry for the amplitude and phase for each 'visibility' for each integration, for each baseline, for each polarisation. The recorded visibility function, $V_\nu(\overline{r_1}, \overline{r_2})$, is related to the radio brightness, $I(\nu)$, of the target by a Fourier transform;

$$V_\nu(\overline{r_1}, \overline{r_2}) = \int\int I_\nu(s) e^{-2\pi i s(\overline{r_1}-\overline{r_2})/c} d\Omega \tag{2.1}$$

where $(\overline{r_1} - \overline{r_2})$ is the separation of the antennas and dS is related to the distance to the target, R, by $ds = |\overline{R}|^2 d\Omega$ (Clark 1999). These visibilities are used in the method described below. A typical fits file contains hundreds of thousands of observed visibilities.

When these uv data are read into AIPS, the order in which the objects were observed as well as the number of visibilities per object can be viewed using *listr* in 'scan' mode. These data are then calibrated using the following techniques.

2.1.1 Phase and Flux Calibration

If the atmosphere were homogeneous and plane-parallel to the Earth's surface and the array of antennas, the atmosphere would affect each antenna equally. The differences in the path length of the radio waves can be calculated and an additional time delay can then be introduced in the electronics so that the signal arrives at the correlator at the same time.

However, because of the curvature of the Earth's surface and the motion of the Earth through space, the height of the antennas changes as does the position of the source in the sky, so that the path length of the radio waves through the atmosphere changes with time and elevation. In the troposphere, there is a dry component and a wet component, both of which delay the radio waves via refraction. The ionosphere is a magneto-active plasma so delays the signal via refraction but also rotates the plane of polarisation (see Section 2.1.3). The signal is also absorbed and re-emitted by these layers in the atmosphere thus affecting the observed flux density of the source.

To correct for these delays and the reduction of the flux density, we observe calibrators throughout the observation run. A flux calibrator is observed at the beginning (and/or the end) of the run followed by a phase calibrator which is observed alternately with the target. These calibrators are observed as they have known flux densities that are not strongly variable, they have accurate positions and they are isolated, small-diameter radio sources (mostly core-dominated, radio-loud quasars; CDRLQs) so that they can be treated as constant flux point sources. The differences between the amplitude and phase of the observed data and the known data can be used to calculate an initial correction to the phase and amplitude of the source.

The phase calibrator is used to correct the amplitude and phase over time, compensating for the changing atmospheric effects (refraction, absorption and rotation of the plane of polarisation) and the change in the path length and time delays of the incident radio waves due to the elevation of the source. The flux calibrator is then used to correct for differences between the real flux density of the source and the observed flux density.

Once the corrections have been determined, we use the command *getjy* to scale the phase calibrator solutions to the absolute flux using the flux calibrator's gain solutions and then apply these combined adjustments to the target using *clcal*. The uv data shown in Figure 2.1 demonstrated the effect of these calibration steps on the raw data. It also shows the quality of the final data with the radio-frequency interference (RFI) removed by flagging.

2.1.2 Bandpass Calibration

When the bandwidth is comparable to the observing frequency, assuming a mean flux density over the bandwidth introduces radial smearing away from the pointing centre. This effect is also known as 'chromatic aberration'. This is particularly evident at low frequencies so in Chapter 3 where I use

multi-frequency observations of 3C 353, the data were bandpass calibrated. To reduce bandwidth smearing, we use channels to divide up the bandwidth, which are then calibrated per antenna, per time, to a constant level using a small subset of channels in a single antenna, where there is little RFI. The differences in gain, which is a combination of amplitude and phase, between the observed values and that of the calibration subset are calculated and applied to the channels to correct for the frequency dependence of the gain. This is done using the AIPS tool *bpass*. The data are then flagged for RFI before being spectrally averaged using the tool *splat* to reduce the number of channels to a more manageable number and reduce the effect of any remaining RFI. This calibration is performed before flux- and phase-calibration when required.

2.1.3 Polarisation Calibration

Polarisation at the VLA is detected using circular polarisation detectors whereas during the reduction and analysis of the data, we use the Stokes parameters; I, the total intensity, Q and U the linear polarisation parameters and V, the circular polarisation. During the conversion to these parameters within the antennas, a small amount of right-circular polarisation shows up in the left-circular polarisation channel and vice versa. This 'leakage' term can be calculated by observing a calibrator that is preferably unpolarised so that the value in the cross-hand channels is the sum of the two leakage terms. This is accomplished using the task *pcal* in AIPS.

The variation of the target's parallactic angle is known, so the discrepancy between the measured polarisation and the known polarisation of the calibrator indicates the polarisation of the instrument, offset by a constant amount due to the actual polarisation of the source. This also corrects for the rotation of the plane of polarisation due to the ionosphere. We observe a target of known polarisation and use the AIPS tool *rldif* to establish the absolute value for the source and correct for the constant offset.

The polarisation of 3C 353 was studied by Swain (1996) so polarisation calibration was not required in the work presented in Chapter 3. However, in Chapter 5, we use the polarisation of the jet knots of Cen A as an indication of shock behaviour so polarisation calibration was carried out.

2.1.4 Self-Calibration and Imaging

The calibrated data can then be used to create a map of the target by applying a Fourier transform to the uv data. We can improve on the quality of the map using the 'CLEAN' algorithm (Högbom 1974) which deconvolves the brightest point in this map with a point source, then the next brightest, for a given number of iterations.

This cleaned map is then used to 'self-calibrate' the uv data initially in phase so that more exact corrections can be calculated. In the previous calibration steps, calibrators were used to estimate

the corrections required to adjust the observed visibilities to the true values of the source. However, these calibrators are not at the same position in the sky as the target, and they were observed at different times. To improve on the accuracy of the corrections to the phase and the amplitude of the target data, we use a map of the target, with the estimated corrections applied to make a better model for the target.

By combining these phase self-calibrations with increasingly cleaner maps, the corrections are improved and the real structure is revealed. Once these corrections show no further improvement, self-calibration of the amplitude and phase is applied as this also corrects the flux density. This can result in the loss of accurate absolute flux calibration if too many iterations are applied.

2.1.5 Baseline Calibration

In some cases it is necessary to calibrate the baselines as the distances between the antennas are not accurately known. The previous assumption that the gains needed to calibrate each baseline are simply the geometric products of the gains of the two antennas involved in the baseline is no longer valid, so a single gain cannot be determined for each antenna and used to calibrate all baselines to that antenna. This is particularly important for very high dynamic range so was utilised in the reduction of the Cen A data in Chapter 5.

We use the AIPS tool *blcal* to correct for this; the uv data is divided by the best model produced after self-calibrating the data thereby estimating the baseline-based errors. These corrections are then applied during another calibration step or by using *split* setting the *blver* keyword to 1.

2.2 X-ray Data Reduction

In this work, I used *XMM-Newton* and *Chandra* data; however, I only had to reduce data from *XMM-Newton* as the work I did with *Chandra* data was part of a collaboration and the data were already reduced when I received them. In the following Sections I outline the basic steps for reducing *Chandra* data and *XMM-Newton* data. I then describe the methods of producing images and spectra from these data. Finally I discuss the challenges of analysing the spectra and removing background contamination.

X-ray data were recorded as events so an *events* file contains information on the position, energy and time of each photon received by the instrument. The information of the location of the detection allows us to make images while the energy information allows us to extract spectra. The raw detections are processed using a pipeline that is instrument specific so the steps included are summarised in the next two sections for *Chandra* and *XMM-Newton* data.

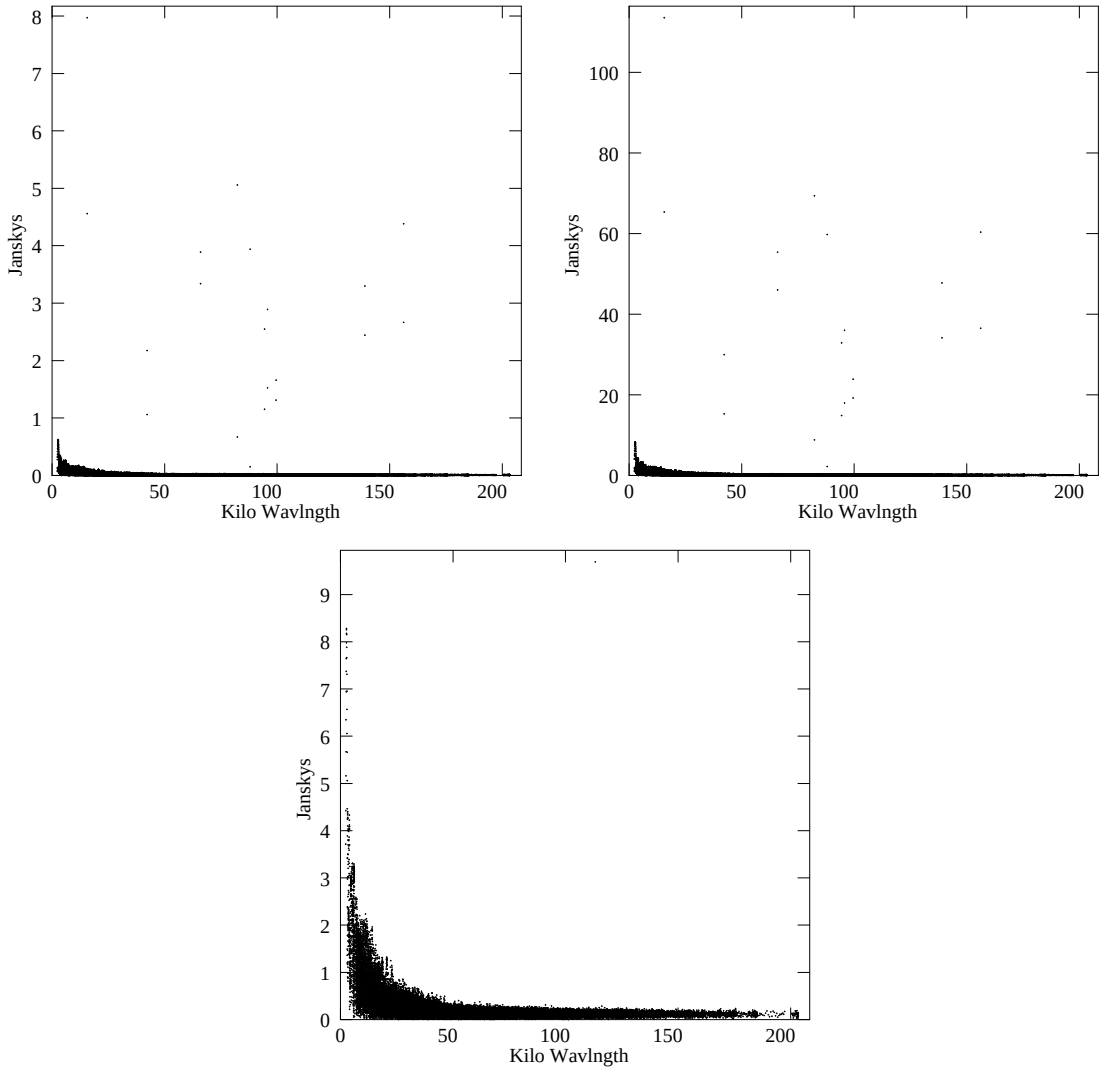

Figure 2.1: Illustrating the radio data reduction process using L-band (1.4 GHz) data for 3C 353. The raw uv data is shown in the top left panel, the top right panel shows that flux and phase calibrated data, and in the bottom panel is the final, flagged data. The most evident difference made during the calibration steps is to adjust the amplitude range from 0 – 8 Jy to 0 – 100 Jy. The flagging processes removes the spurious data so the 'true' data were plotted in the bottom panel.

2.2.1 Calibrating *Chandra* Data

The *Chandra* observations used in this work were taken with the AXAF CCD Imaging Spectrometer (ACIS) instrument. The Standard Data Processing (SDP) of these data is split into several levels, the first of which are automatically performed by the *Chandra* X-ray Center. Level 0 converts the raw telemetry into FITS files and at level 1, an instrument correction is applied to produce the events files. Level 2 filters the events file to good time intervals (GTIs) and produces a candidate list.

Using the events file produced at level 1, the data are cleaned of spurious events. Using the tool *acis_run_hotpix*, hot pixels, afterglow events, and pixels with bright bias are identified and the information is stored in a file that is applied to the events file using the *acis_process_events* tool; afterglow events are those where a cosmic ray has interacted with the CCD leaving a residual charge. The final step in this basic pipeline is to flag and remove streaks where a significant amount of charge is randomly deposited along pixel rows as they are read out. These data are automatically flagged for ACIS observations at level 1 and can then be removed at level 2. This can be done manually for other chips using the tool *destreak*.

Spectra are extracted from these *Chandra* data using the CIAO tools developed by the *Chandra* X-ray Center. In Chapter 5, where the X-ray spectra of the jet knots in Cen A are analysed, the tools *specextract* and *psextract* were used for extended and compact sources respectively. The response files are calculated during both of these tasks. The importance of these response files is discussed further in Section 2.2.4.

In Chapter 4, I use energy filtered events files to examine the relationship between the X-ray and radio emission from the lobes of Pictor A (Pic A) and 3C 353. As I relate the X-ray counts in a region directly to the radio surface brightness, I used images of the data rather than spectra. These images were from a single observation so the 'image' is the events file. However, in Chapter 5, I use 10 separate observations of Cen A, so the images were exposure corrected at an appropriate energy and then combined, weighting according to the value of the exposure map (Hardcastle et al. 2007b).

2.2.2 Calibrating *XMM-Newton* Data

XMM-Newton data consists of three events files, one for the PN camera and one for each of the MOS cameras. The *XMM-Newton* data reduction in this work was done using SAS version 7.0.0. and the following standard method.

On receipt of an *XMM-Newton* X-ray dataset, the standard EPIC, MOS and PN pipelines and the standard filters #XMMEA_EA and #XMMEA_EP were applied to calibrate the dataset and remove hot pixels and out-of-field events from the events list. As standard, the MOS cameras were filtered to include single, double, triple and quadruple events corresponding to compact events (PATTERN$\leq$ 12), while the PN dataset was filtered to include only single and double events (PATTERN$\leq$ 4). I

made histograms of the events for each camera in order to identify flares, which were excluded from the analysis by removing the sections of the observation which had high count rates.

Using the SAS tool *evselect* we can extract the spectrum of any region of the image including the response files required for further analysis (see Section 2.2.4). To make an image of the data, the datasets were energy filtered to include energies between 0.3 and 5.0 keV, unless stated otherwise, before using *evselect* to generate images. When we combined the images, we accounted for the chip gaps and livetime variations between the cameras by initially scaling the MOS images by the ratio between the countrate for the PN image to the countrate of each MOS image, before combining the three images linearly. Next, we combined the exposure maps for each camera and divided the combined image by the total livetime. The combined, scaled image was then divided by the combined, scaled exposure map thus removing the chip gaps from the final image. The images produced at each step are shown in Figure 2.2. These exposure corrected maps are not corrected for vignetting as the particle background would be scaled up at the edges of the image which is not realistic.

2.2.3 X-ray Imaging

As described above, the process for producing images is slightly different for each instrument. However, once the data have been combined and the chip-gaps have been removed by scaling, the point sources, which are unrelated to target object so are usually selected for exclusion from the spectral analysis, can be removed from the images with the CIAO tool *dmfilth*, filling in the gaps using the countrate of a nearby region of the same size. The final image can then be Gaussian smoothed with various sized kernels to highlight the different features.

While the data are read off of the chips, X-rays are collected on the CCD that have incorrect positions, known as ‘out of time events’ (OTEs). Because the chip is being read, these OTE are

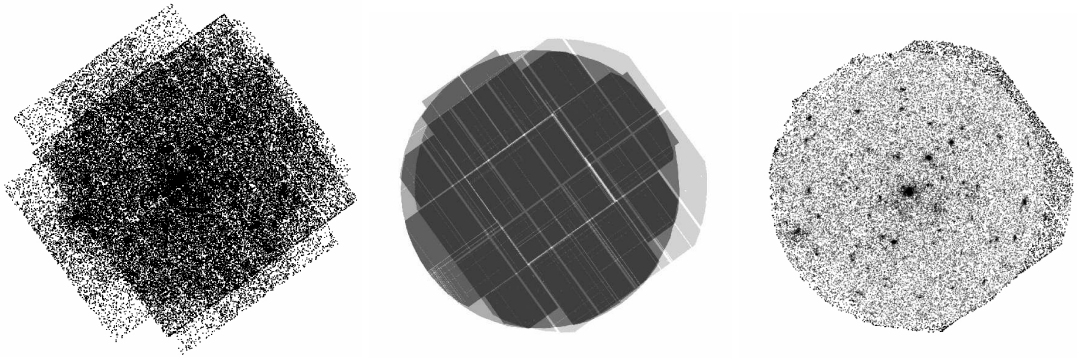

Figure 2.2: An example of the image correcting process using NGC 5322 data. In the left panel is the scaled, combined camera image, in the middle panel is the corresponding scaled and combined exposure map, and on the right is the chip-gap corrected, combined image.

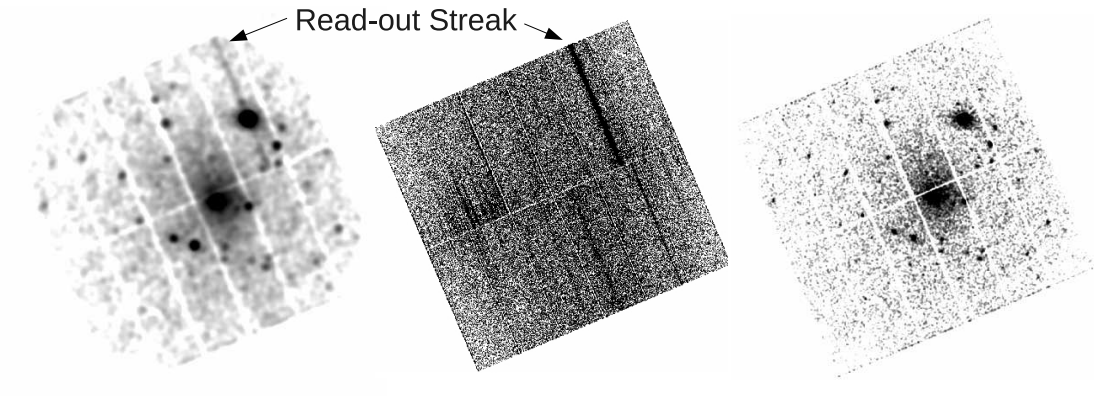

Figure 2.3: An example of the contamination by out of time events (OTEs) in images of the NGC 5129 *XMM-Newton* data. In the left panel is the contaminated pn camera image, in the middle panel is the raw OTE image, and on the right is the OTE corrected, pn camera image. The read-out streak is visible in the first two images towards the top right corner of the images.

allocated to the wrong row on the CCD (RAWY). They thus have the wrong energy correction applied during the data reduction process. These events broaden the spectral features and can be seen in images as a strip of wrongly reconstructed event positions in RAWY. This 'read-out streak' is shown in *XMM-Newton* data in Figure 2.3. The fraction of OTEs depends on the instrument and the observation mode as it is dependent on the integration and read-out times. The fraction of OTEs in *Chandra* data is much less than in *XMM-Newton* data so affects only observations of bright point sources; however, in *XMM-Newton* data where the fraction is higher, it can be relevant for observations of extended sources too.

In full-frame (FFW) mode on *XMM-Newton*, the fraction of OTEs is significant in the pn data at $6.3\,\%$ while in extended full-frame (EFF) the effect is only $2.3\,\%$. The MOS cameras are negligibly affected. These OTEs are subtracted from the images by creating an image of the OTE by giving all the events a random y coordinate during the pn pipeline, and scaling it by the appropriate percentage.

2.2.4 Generating Spectra

We generate source and background spectra separately using the tools described above, but for each dataset we also calculate response files (for each camera for *XMM-Newton* and for the appropriate detector for *Chandra*). A 'Redistribution Matrix File' (RMF) and an 'Auxiliary Response File' (ARF) are generated so we can characterise the response of the detector and thus simulate an output spectrum as observed by the cameras. A response function is calculated as a product of the RMF and the ARF. The RMF calculates the detector response at each position on the chip and therefore corrects for instrument effects specific to the spectrum and the ARF calculates an effective area curve as a function of energy taking into account the telescope's effective area, the filter transmission, the CCD quantum efficiency, the region and pattern selections, the fraction of the PSF in the

region and the OTEs' smearing. These files are linked to the extracted spectra so these effects can be accounted for during the spectral fitting process. The extracted spectra are also grouped into bins typically containing 20 counts using *fungroup* so that the errors on the values in each bin obey Gaussian statistics and to smooth the spectra to aid fitting.

2.2.5 Spectral Fitting

In this work, the spectral fitting was performed using XSPEC, an X-ray spectral fitting package developed by NASA's High Energy Astrophysics Science Archive Research Center (HEASARC). The grouped data are read into XSPEC complete with information on the background spectrum, the detector response (RMF file) and the effective area (ARF file). The background spectrum is discussed in the next Section. If the target is extended or near the edge of the image, then vignetting becomes important and the spectra are weighted accordingly. If the source region is small and compact, then this may not be a significant effect.

XSPEC allows users to fit the data with multiple models constructed from individual components so that many spectral contributions can be individually fitted. For example, emission from the cores of AGN can be fitted with an absorbed power-law model, which would take account of the synchrotron from the bases of the jet, and emission from the hot X-ray gas in the environment may be fitted with thermal model as discussed in Section 1.2. Different components can be allocated different values of absorption taking account of absorption from the local environment or from foreground Galactic absorption. This control allows us to test various combinations of theoretical components and thus determine what the target's spectrum is actually showing us.

2.2.6 Background Contamination

The source spectrum extracted from these data are contaminated by background emission from a variety of sources, the significance of which depends on the target's position on the image.

Other sources of contamination are much harder to quantify and during this thesis the widely accepted 'best' methods for taking account of these factors has changed. In general, if the source region is small and centralised on the chip, then the particle background and instrument noise does not vary significantly across the region of interest and a *local* background subtraction method can be applied. This was the case in the analysis of the core of 3C 353 (Chapter 3) and for the jet knots in Cen A (Chapter 5). A background region, which is positioned close to the source region, is used to measure the background contamination from local environment and from the Galactic medium.

In more extended sources, such as the groups studied in Chapter 6 and the merging cluster in Chapter 3, the contamination from particle background and instrument noise varied significantly and a *double* subtraction method was required (Arnaud et al. 2002; Croston et al. 2008a). A model of

the expected particle and instrument spectrum is measured and subtracted from the source spectrum in addition to the local background contamination, which is still found using a local background region. The details of how the model spectrum was measured in each situation is described in the relevant chapters.

Where there was a significant contribution from OTEs, this was also scaled and subtracted from the source spectrum at this stage. Once the extracted spectra had been background subtracted, the final spectra were binned to 20 counts per channel in most cases; however, in the cases where there was an abundance of good data, the spectra were binned to 50 counts per channel. With the *XMM-Newton* data we ignored the first 20 channels in the MOS data and the first 50 in the pn data as these channels typically have energies less than 0.4 keV, which is below the response of the cameras. Similarly, in the *Chandra* data we ignored the first 28 channels (up to 0.4 keV). We then used XSPEC to fit models to the extracted spectra between energies of ~ 0.4 keV and ~ 8.0 keV. Above this range, the telescope sensitivity drops off as the energy increases, and the sensitivity to non-X-ray events also drops off, but not necessarily at the same rate so that the signal to noise decreases.

Chapter 3

The FR II Radio Galaxy 3C 353

In this Chapter I present work on the FR II radio galaxy 3C 353 and its environment. This work was accepted for publication in the Monthly Notices of the Royal Astronomical Society (MNRAS) in 2008 (Goodger et al. 2008). I used multi-frequency radio data with X-ray data to analyse the spatially changing emission on lobe-wide scales to better understand the role that the electron population and the magnetic fields play in controlling the radio synchrotron and X-ray iC emission.

3.1 Introduction

Extended X-ray emission from the lobes of powerful, FR II radio galaxies and quasars is thought to be produced by iC scattering of the CMB (Feigelson et al. 1995; Hardcastle et al. 2002a) and of IR photons from the core (Brunetti, Setti, & Comastri 1997). Although the synchrotron self-Compton emission from the lobes can also be modelled, it is negligible compared to the iC emission from other populations except in the very smallest lobes (Hardcastle et al. 2002a). These radiation mechanisms are described in detail in Section 1.2. Recent studies of the integrated X-ray properties of radio lobes have been carried out for large samples (Croston et al. 2005b; Kataoka & Stawarz 2005), showing that the CMB is the dominant photon population in most cases. Combining an iC/CMB model for the lobe X-ray emission with information obtained from radio synchrotron emission provides a method of constraining the electron population and magnetic field energy density, which cannot be accomplished using radio data alone. Unlike the jets, the lobe material is not moving relativistically so there are no beaming effects to consider during this analysis (e.g. Mackay 1973). Understanding the contributions of the electron densities of the synchrotron and iC emitting electron populations and the magnetic field allows us to estimate directly the total energy in the radio source, and thus the amount of energy that can be transferred to the environment, without assuming equipartition (see Section 1.3.6), and also allows us to investigate the distribution of internal energy within the source.

In 2005, Hardcastle & Croston carried out a spatially resolved X-ray iC study of the bright X-ray and radio source Pic A. They used the variation of the X-ray/radio ratio across the lobes to investigate the variation in electron distribution and magnetic field strength throughout the source. They found that variations in either component alone could not explain the observed X-ray and radio properties of the lobe. Similar spatially resolved X-ray studies of other bright FR II radio galaxies are needed to follow up these results. Here I report on observations of the radio galaxy 3C 353.

3C 353 is a FR II radio galaxy associated with the cluster Zw 1718.1-0108. Although it is one of the brightest extragalactic sources in the sky at low frequencies, it is relatively poorly studied, presumably due to its low declination and low Galactic latitude. Swain (1996) observed 3C 353 at four radio frequencies with the VLA and published a study of the polarisation variation across the jets, which favoured a spine-sheath model (Swain, Bridle, & Baum 1998). Their VLA observations revealed filamentary structure within the lobes making 3C 353 an excellent target for a spatially resolved study of electron distribution and magnetic fields. X-ray emission from the cluster associated with 3C 353 was first detected by Iwasawa et al. (2000) in *ASCA GIS* and *ROSAT HRI* images. The radio source resides in a giant elliptical galaxy on the edge of the cluster, which Iwasawa et al. found to be bright in the X-ray with a luminous point source coinciding with the radio galaxy's core. Iwasawa et al. determined global cluster temperatures and used optical observations to identify the cluster's members. They confirmed a redshift of $z = 0.0304$ for 3C 353, a redshift of $z = 0.028$ for three bright member galaxies, and used the velocity distribution to confirm 3C 353 as a member of the same system. The angular scale is thus 1 arcsec = 0.61 kpc.

In this Chapter, I use new *XMM-Newton* X-ray observations and radio observations from the VLA and the GMRT to investigate the nature of the electron distribution and the magnetic fields in the lobes and hotspots of 3C 353. I also determine the cluster temperature, density and pressure profiles and examine the cluster's interaction with the lobes of 3C 353.

3.2 Data

I used a combination of new and archival radio data and new *XMM-Newton* X-ray data to examine the broad-spectrum electron energy distribution of 3C 353. These radio data extend to lower frequencies than have been studied previously, whilst these X-ray data have greatly improved sensitivity and resolution compared to the *ASCA* data of Iwasawa et al. (2000). These X-ray and radio data were reduced using the standard methods presented in Chapter 2 and summarised for each frequency in this Section including the additional techniques required to reduce these lower frequency and multi-channel data.

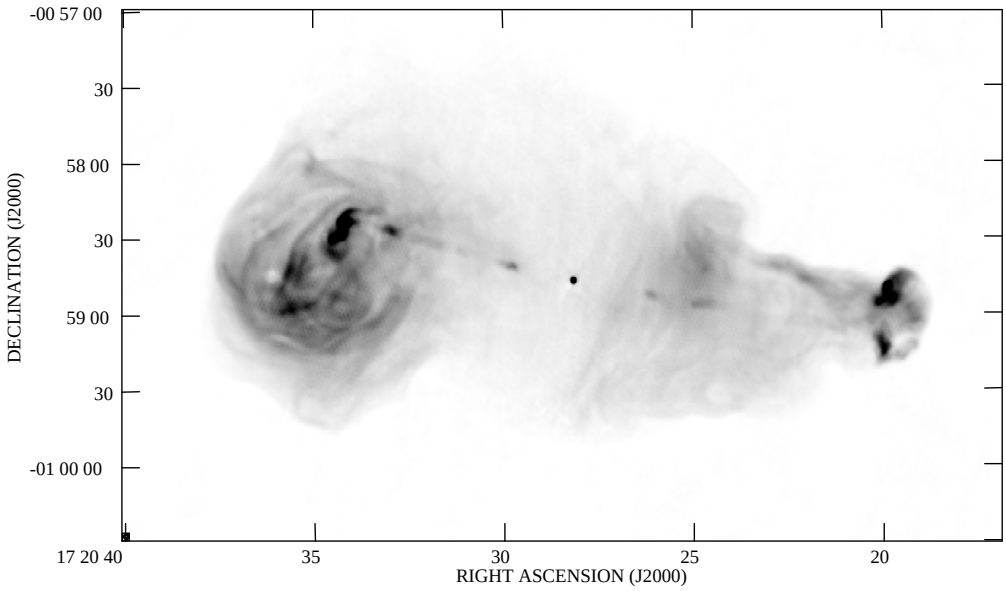

Figure 3.1: 1.67 GHz total intensity radio image of 3C 353 at 1.8 arcsec resolution

3.2.1 Radio

I obtained VLA observations at 1.67 GHz and 4.8 GHz from the VLA archive as well as previously unpublished observations at 327 MHz taken at the VLA and at 615 MHz taken at the GMRT in 2006. I also obtained images of 3C 353 at 74 MHz and 8.4 GHz from my collaborators. All these radio data were reduced in the standard way using AIPS (see Chapter 2). The radio observations are summarized in Table 3.1 and Fig. 3.1 shows an example of the image quality achieved. Fig 3.2 shows the radio contours at 327 MHz, 615 MHz, 1.67 GHz and 4.8 GHz.

4 Band; 74 MHz, 4 m

The 74-MHz observations used are those discussed by Kassim et al. (2007) and the reduction is described in that paper. In addition to bandpass-, flux- and phase- calibration, they emphasise the need for RFI excision and introduce ‘field-based’ phase calibration to include the changing column density of the ionosphere across the relatively large field of the 74 MHz image.

P Band; 327 MHz, 91 cm

These 327 MHz observations of 3C 353 were taken at the VLA on the 27th May 2006 using the nearby Pie Town antenna of the Very Large Baseline Array (VLBA) to increase the long baselines of these A configuration data by a factor of two. I carefully monitored the Pie Town antenna during the calibration steps to ensure that the long baselines survived.

Initial bandpass calibration using 3C 286 resulted in smooth phase and amplitude variation across all channels. As a flux calibrator, 3C286 is slightly resolved at this frequency. If the fractional bandwidth is great enough that the intrinsic visibility of 3C 286 varies across the pass band, a model is required (http://lwa.nrl.navy.mil/tutorial/tutorial.html). At 327 MHz with the Pie Town antenna, I found that this effect is negligible so 3C 286 was used as the flux calibrator without a model, effectively treated as a point source. 3C 286 was used to calibrate the phase across all baselines. The resultant calibrated dataset was flagged to remove noise then spectrally averaged using the AIPS task *splat*, averaging every 4 channels to reduce the number of channels to 6, whilst producing a single source dataset. The calibrated data included baselines up to 80 kλ, twice what would have been achieved with only the A configuration.

The B-configuration dataset was bandpass calibrated using 3C 286 to calibrate the channel gains, then flux calibrated using 3C 286 and phase calibrated with 1416+067. After flagging and phase cross-calibrating with the A-configuration dataset, the datasets were merged and a multi-facet deep-cleaned map of 106 fields was produced. The dynamic range of the final map is 580:1 with a resolution of 6.7×2.9 arcsec.

620 MHz, 48 cm

These 620 MHz observations were taken at the GMRT on 19th July 2006. The two observing frequencies (upper and lower sidebands) were calibrated separately. Preliminary bandpass calibration was performed using 3C 286 followed by flagging and one iteration of *flgit* to remove RFI from all sources (*flgit* uses user-defined values of sigma and scatter allowance to automatically remove RFI from the general trend of the data). This flagged dataset was then bandpass- and flux-calibrated before being manually flagged and another iteration of *flgit* applied. The dataset was spectrally averaged into a multi-source dataset, cutting the number of channels from 128 to 6, whilst applying the bandpass calibration. This dataset was finally flux- and phase-calibrated before 3C 353 was *split* into a single-source file. The flux and phase calibrator used was 1743-038. One iteration of phase self-calibration was performed before the data from the two observing frequencies were split into individual channels and recombined using the tool *dbcon* to a single dataset containing all of the averaged channels. This combined dataset was phase self-calibrated twice more and the final image has resolution 7.50×4.41 arcsec and dynamic range $590:1$.

L Band; 1.67 GHz, 22 cm

Observations from the VLA using A-, B- and C-configurations were flux- and phase-calibrated separately using NRAO 530 as the phase calibrator. Due to the allocation of the observing frequencies in the C-configuration dataset, the data at the two frequencies were split and recombined using *dbcon* to match the frequency allocations of the A- and B-configuration datasets. Once combined, the

data were phase self-calibrated and deep cleaned, with 100,000 iterations of *clean* applied. The final image had a resolution of 1.7 $\times$ 1.4 arcsec and a dynamic range of $500:1$.

C Band; 4.8 GHz, 6.3 cm

For maximum *uv* coverage, I used VLA observations in the B-, C- and D-configurations, each of which were phase- and flux-calibrated and flagged. I combined two epochs of D-configuration observations to increase the signal to noise.

The final combined dataset was phase and amplitude self-calibrated, normalising the gain. There was no significant reduction in the maximum flux when compared to phase-only self-calibration, but the image quality was improved. The final image had a resolution 2.24×1.81 arcsec and a dynamic range of 1180:1.

X Band; 8.4 GHz, 3.6 cm

The X band images of 3C 353 were kindly provided by Alan Bridle. The deep cleaned images have a dynamic range of 2500:1 and a resolution of 1.30×1.30 arcsec. The details of the reduction are described by Swain (1996).

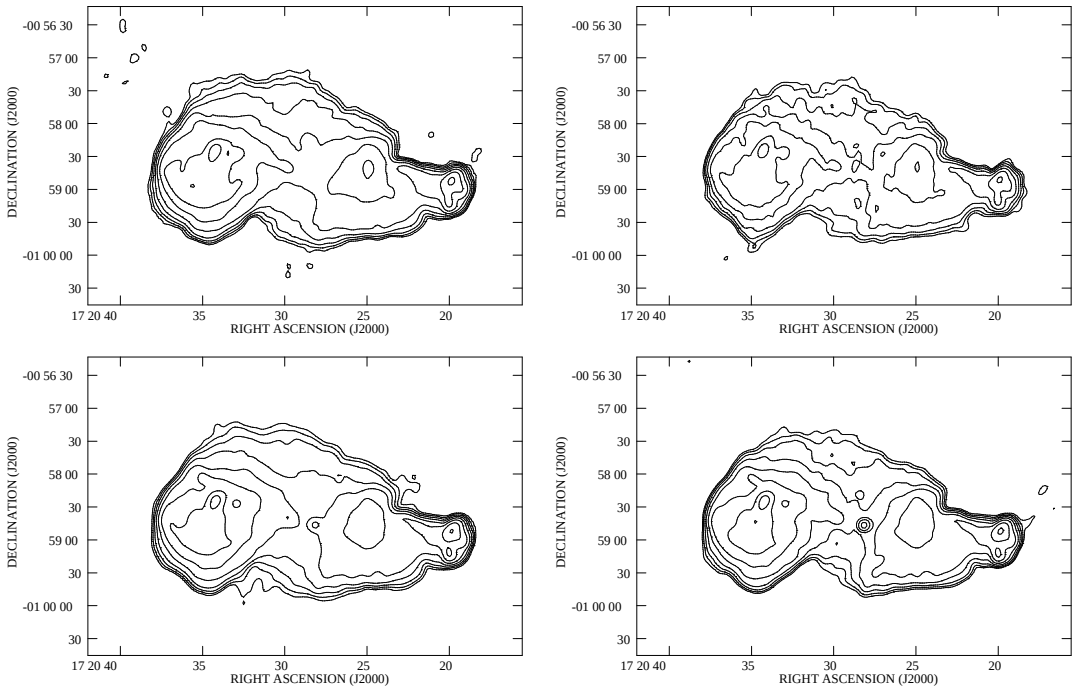

Figure 3.2: Radio contour images of 3C 353 at 327 MHz (top left), 615 MHz (top right), 1.67 GHz (bottom left) and 4.8 GHz (bottom right) all convolved to 7.5×7.5 arcsec resolution. The contour levels are at $5\sigma\times$(1,2,4,...) mJy/beam where $5\sigma = 0.0106$ mJy/beam for 327 MHz, 0.0113 mJy/beam for 620 MHz, 0.0045 mJy/beam for 1.67 GHz and 0.0017 mJy/beam for 4.8ĠHz

Table 3.1: Radio Observation Details

Band	Frequency (MHz)	Telescope:Config.	Date	Duration (s)	Band Width (MHz)	Phase Calibrator	Dynamic Range	Res. (arcsec)
4	73.8	VLA	07/03/1998	7740	1.3	3C 405	2090:1	25.0×25.0
P	327.3	VLA:A+PT	27/05/2006	25660	3.125	3C 286	580:1	6.75×2.92
		VLA:B	04/10/1998	3010	0.098	1416+067		
-	620.5	GMRT	19/07/2006	19847	16.0	1743-038	590:1	6.41×4.27
L	1665/1678	VLA:A	19/05/1968	20710	12.5	NRAO 530	500:1	1.78×1.44
		VLA:B	14/08/1968	6640	25.0	NRAO 530		
		VLA:C	16/09/1985	1441	50.0	1741-038		
C	4848/4898	VLA:B	14/08/1986	6799	50.0	NRAO 530	1180:1	2.24×1.81
		VLA:C	22/08/1985	1679	50.0	1741-038		
		VLA:D	15/11/1993	532	50.0	1730-130		
		VLA:D	28/09/1984	3360	50.0	1725+044		
X	8440/8452	VLA:BCnD	13/03/1994		12.5		2500:1	1.30×1.30

3.2.2 X-ray

I observed 3C 353 on the 25th August 2006 and 17th February 2007 with *XMM-Newton* EPIC MOS 1, MOS 2 and pn cameras. The initial observation (Set 1) from 25th August 2006 yielded 39 522 s and 39 525 s for MOS 1 and MOS 2 respectively and 34 042 s for the pn camera, whereas the second observation on the 17th February 2007 (Set 2) was for 10 473 s and 10 487 s for MOS 1 and MOS 2 and 5 653 s for pn. The pn camera was in Extended Full Frame mode for both observations and the MOS cameras were in Full Frame mode.

The datasets were initially processed using SAS version 7.0.0.and the standard method described in Chapter 2. Set 1 MOS datasets were free from flare events whilst the pn dataset was filtered with a count threshold of 2 counts per second to remove a small flare event at the end of the observation. In Set 2, all cameras were affected by flaring; the MOS and pn datasets were filtered with count rate thresholds of 0.3 and 0.7 counts per second respectively. As only 1510 seconds remained of the pn data, this data set was excluded from further analysis. The net livetimes for Sets 1 and 2 were 44 039 for MOS 1 and MOS 2 and 26 052 for pn.

The MOS and pn datasets were energy filtered to include energies between 0.5 and 5 keV before generating images from the filtered events files. The combined exposure-corrected image was Gaussian smoothed with a kernel of 10.4 arcsec to highlight the clusters and radio lobes using the CIAO command *aconvolve*.

X-ray spectra were extracted using *especget*, a script that combines the *evselect*, *arfgen* and *rmfgen* commands in SAS, from regions defined to examine the emission from the northern and southern sub-cluster regions, and the east and west lobes. As the core and lobes are small regions near the pointing centre, so that vignetting is not important, I used local background subtraction. However, for the cluster, vignetting needs to be considered. The filtered events files were weighted using *evigweight* before spectra were extracted using a double subtraction method, (e.g. Arnaud et al. 2002). Background template files for the field of view were made using files created by Read & Ponman (2003) and scaled to the same particle background level as these observations. A local background region away from the galaxy and the cluster was defined using DS9. A template background spectrum was subtracted from the source spectrum events file to account for instrument and particle noise before a local background region was used to subtract residual background emission due to the differences in the Galactic/extragalactic background levels of the source and scaled background datasets. Due to the low signal to noise of Set 2, only Set 1 could be used in the double subtraction method applied to the cluster. The spectra were then binned to 20 counts per channel after background subtraction, ignoring the first 20 channels for the MOS cameras and the first 50 channels for the pn camera, which correspond to energies below 0.4 keV.

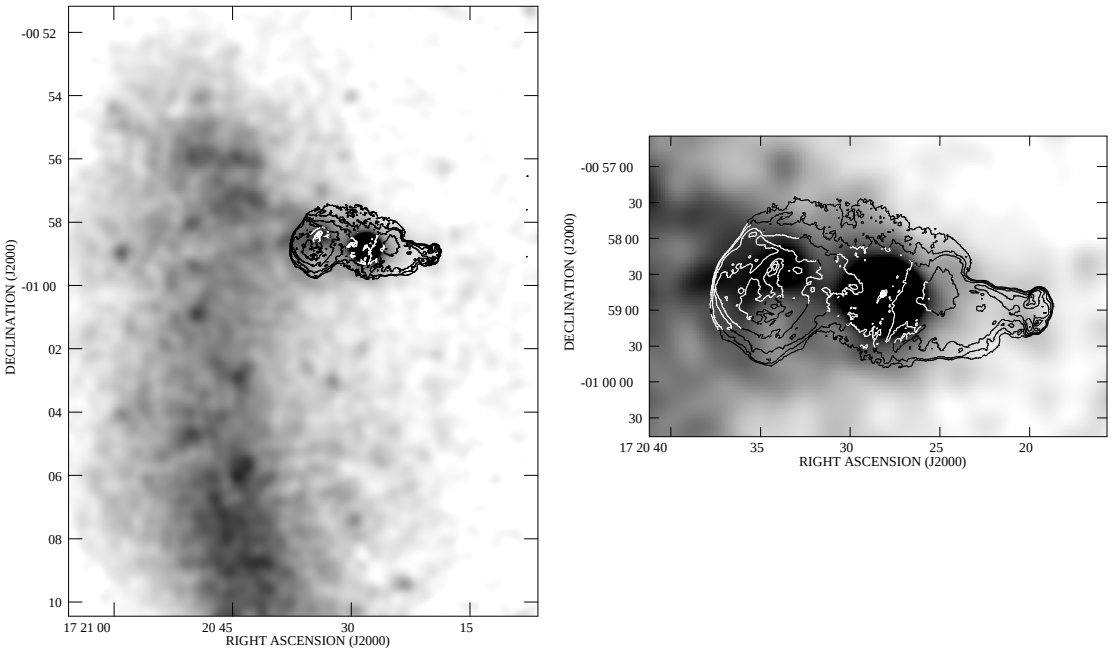

Figure 3.3: Radio contours of 3C 353 at 1.67 GHz with a 0.3-7.0 keV *XMM-Newton* image (MOS 1, MOS 2 + pn) of the X-ray emission from the radio lobes and the cluster Zw 1718.1-0108 (left) Gaussian smoothed with a kernel of 10.4 arcsec; the same image zoomed in to show the iC emission from the lobes (right).

3.3 Results

In this Section I discuss the results of the X-ray spectral fitting and radio flux density measurements. X-ray fitting was carried out using XSPEC v 11.3 in the energy range 0.3 – 7.0 keV. Where thermal models were fitted I used a redshift of 0.03.

3.3.1 Absorbing Column Density

The column density towards 3C 353 is uncertain. Iwasawa et al. (2000) adopt a value of 1.0×10^{21} cm^{-2} based on the H I measurements of Dickey & Lockman (1990). However, they note that the visual extinction in the direction of 3C 353 would correspond to a column density of a factor ~ 2 higher. From the Galactic dust measurements of Schlegel et al. (1998) I estimate an A_V of 1.4 mag, which would correspond to a column density of $\sim 2.6 \times 10^{21}$ for standard Galactic gas/dust ratios. The true value is likely to lie somewhere between these extremes.

I therefore used these new data to estimate a column density directly. I extracted spectra for bright point sources around 3C 353 using local background regions. In Set 1 there were 5 point sources bright enough for spectroscopy. I fitted power-law models with free absorption to these sources and found a weighted mean $N_H = (1.64 \pm 0.07) \times 10^{21}$cm^{-2}. As this is consistent with the range estimated above, I adopt the mean value in the analysis that follows. The X-ray point sources are not shown in Fig. 3.3 and were excluded from the cluster spectra as was the emission from the radio galaxy.

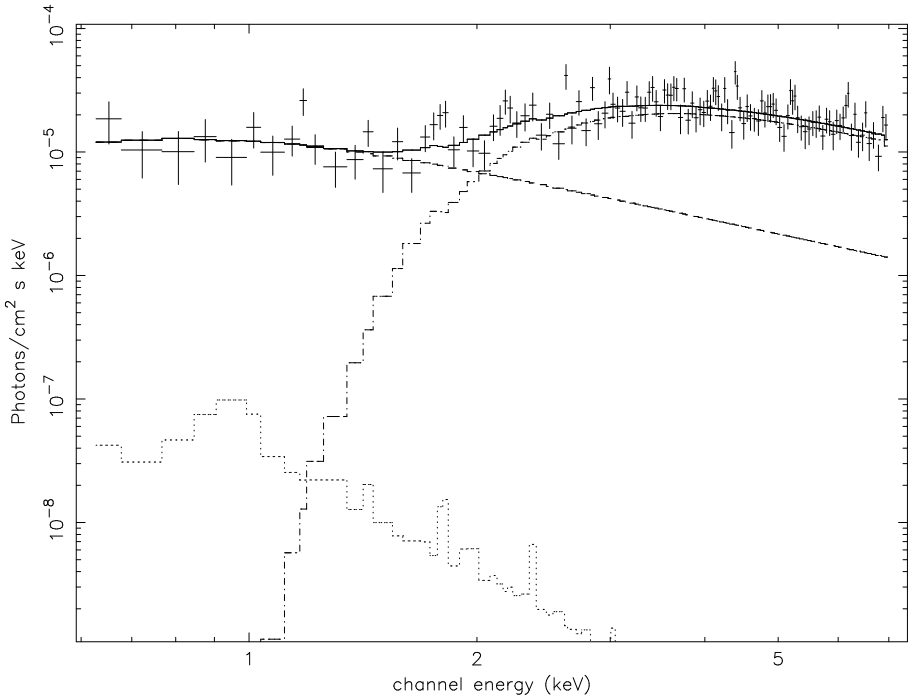

Figure 3.4: X-ray spectrum of the nucleus in the energy range 0.3–7.0 keV. The model plotted is the dual power-law + thermal model as described in Section 3.3.2. For clarity only the pn data are plotted.

3.3.2 The Nucleus

In the X-ray, the nuclear region was defined with a radius of 40 arcsec to include as many nuclear photons as possible while excluding the X-ray emission from the radio lobes. The background was estimated from a local background region positioned above the radio galaxy so as not to include any emission related to the radio galaxy. In the radio, the nuclear region was much smaller, so was adjusted in each dataset to be a close fit to the nuclear emission. The peak intensity was determined using the AIPS task *jmfit* for each frequency, the results of which are shown in Table 3.2.

I initially attempted to fit single power-law and thermal models to the spectrum; however, the fits were poor ($\chi^2 = 466.6$ for 259 degrees of freedom (d.o.f.) and $\chi^2 = 2242.5$ for 259 d.o.f. respectively). I therefore fitted a model which has been shown (Hardcastle et al. 2006a) to provide a good fit to the nuclear X-ray emission from narrow-line radio galaxies, consisting of a power-law component at Galactic absorption (see Section 3.3.1), a second power-law component with redshifted intrinsic absorption and a $kT = 1$ keV thermal component. The best fitting model had $\chi^2 = 268$ for 237 d.o.f. The core spectrum is shown in Figure 3.4. The photon indices of the unabsorbed and absorbed power-law components were $\Gamma = 1.5 \pm 0.1$ and 1.3 ± 0.3 respectively, and the intrinsic column density was $6.1 \pm 0.6 \times 10^{22}$ cm^{-2}. The unabsorbed X-ray component has a 1 keV luminosity density of 1.86×10^{16} W Hz^{-1} sr^{-1}, whereas the absorbed X-ray component with the absorption removed and extrapolated to include energies from 2–10 keV has a luminosity of 2.82×10^{42} erg s^{-1}. I discuss the interpretation of the nuclear emission in Section 3.4.1.

Table 3.2: Radio Core Fluxes

Band	Frequency (MHz)	Flux (Jy)	Luminosity ($\mathrm{W\,Hz^{-1}\,sr^{-1}}$)
P	327.3/329.6	0.097	1.5×10^{22}
-	620.5/633.3	0.089	1.4×10^{22}
L	1665/1678	0.116	1.8×10^{22}
C	4848/4898	0.140	2.2×10^{22}
X	8440/8452	0.149	2.3×10^{22}

The errors on these flux densities are dominated by the intrinsic error on the flux calibration, which is of the order of a few per cent for the frequencies used in this work.

3.3.3 Lobe Properties

By considering the X-ray emission from regions encompassing the East and West lobes but excluding the hotspots and the core, I extracted spectra from the combined X-ray dataset using local background regions which I fitted with both thermal emission models and power laws. Assuming a circularly symmetric model for the core, I determined that ~ 6 per cent of the counts in the East lobe spectra are from the core whereas the core counts account for a quarter of those in the West lobe spectra. Using the *XMM-Newton* calibration files, I determined the fraction of the core spectrum expected to be scattered into the West lobe region to be 4 per cent of the total core emission, and so I included a fixed component in the West lobe spectral fit consisting of the best-fitting core model with a normalisation fixed at 0.04 times that of the core. The details of the core spectrum are given in Section 3.3.2. Due to the low signal to noise of Set 2, the West lobe was undetected in this dataset and so the spectra were extracted from Set 1 only.

The background emission from the cluster environment is the primary contributor to the uncertainty in the lobe flux densities. To best take account of this variation I used a truncated annular background region for the East lobe where the lobe appears to interact with the cluster. I investigated the effect of using local background regions above and below the galaxy; the best fitting power-law models gave consistent photon indices but led to an increase of a factor of 2 in the flux density of the East lobe. These background regions only take account of the emission from one of the two sub-clusters while a truncated annular background region is a more accurate measure of the cluster's contribution. For the West lobe, a local background region located to the south of the galaxy, at a similar distance from the brightest cluster emission took account of the emission from the southern sub-cluster sufficiently to allow a good fit to the spectra.

The power-law model gave better fits than the thermal model for both lobes with $\chi^2 = 39.6$ for 34 d.o.f for the East lobe and $\chi^2 = 23.1$ for 24 d.o.f for the west lobe. The photon indices were $\Gamma = 1.9 \pm 0.4$ and $\Gamma = 1.2 \pm 0.6$ respectively, corresponding to $\alpha = 0.9 \pm 0.4$ and $\alpha = 0.2 \pm 0.6$.

Figure 3.5 shows the best-fitting power-law model for the East and West lobe X-ray data. The low frequency radio spectral index, measured between 327 MHz and 1.67 GHz, is ~ 0.7 for both lobes, so that the X-ray spectral indices of both lobes are consistent with an iC/CMB scattering model. I discuss the nature of the lobes in Section 3.4.2.

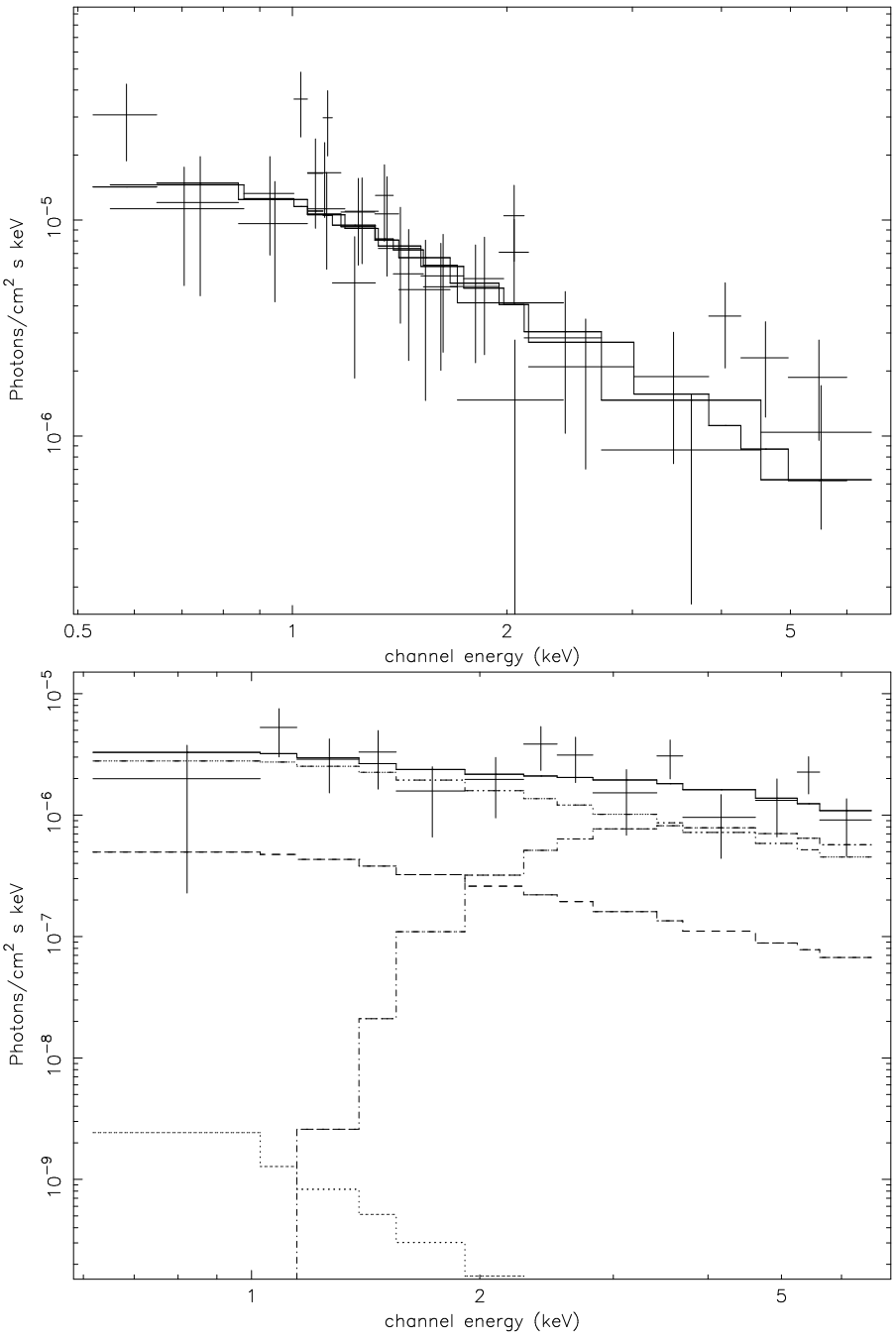

Figure 3.5: X-ray spectra for the East (top panel) and West (bottom panel) lobes in the energy range 0.3–7.0 keV. The East lobe shows the MOS 1, MOS 2 and pn cameras with the power-law model while the West lobe shows only the pn data for clarity with the dual power-law + thermal contribution from the core as well as the best-fitting power-law model from the lobe emission as described in Section 3.3.3.

3.3.4 The Nature of the Hotspots

Both the East and West hotspots are clearly detected in all radio frequencies. The West hotspot is undetected in the X-ray; however, the East hotspot has an X-ray counterpart 6.5 ± 0.8 arcsec (4.0 ± 0.5 kpc) from the centre of the radio hotspot. This has too low signal to noise for spectral analysis to be performed, with only 60 counts between 0.3 and 7.0 keV. The same feature was detected in *Chandra* observations (Kataoka et al. 2008) with an offset of 4.6 ± 0.5 arcsec. A jet knot was also detected in the vicinity of the East X-ray hotspot suggesting that the difference in the offset measurements could be due to contamination from this knot.

The iC analysis performed on the lobes cannot be applied here as the electron populations responsible for any iC X-ray and radio synchrotron emission reside in different regions. X-ray hotspots in radio galaxies of similar radio luminosity to 3C 353 are generally thought to be produced by synchrotron emission, and so this is likely to be the dominant emission process for this X-ray hotspot as well. The offsets measured between the X-ray and radio hotspots are consistent with what is seen in some other sources (Hardcastle et al. 2002a, 2007b; Erlund et al. 2007).

3.3.5 Cluster Characterisation

Unfortunately, the southernmost section of the southern sub-cluster extends beyond the field of view of the *XMM-Newton* cameras; however, a comparison to the *ASCA* image of Iwasawa et al. (2000) shows that the peak of the X-ray surface brightness is included in these data.

I extracted spectra from the northern and southern sub-clusters using a double subtraction method with annular local background regions. The northern and southern sub-cluster regions are shown in Fig. 3.6. Thermal models fitted using *mekal* in XSPEC give acceptable fits ($\chi^2 = 258$ for 175 d.o.f and $\chi^2 = 544$ for 490 d.o.f for the northern and southern sub-clusters respectively) with $kT = 3.3 \pm 0.3$ keV for the northern sub-cluster and $kT = 4.0 \pm 0.5$ keV for the southern sub-cluster both fitted with an absorption of $N_H = 1.6 \times 10^{21}$ cm^{-2}. The best-fitting models are shown in Figure 3.7. Iwasawa et al. (2000) determined the temperature of the combined sub-clusters to be $kT = 4.3 \pm 0.2$ keV using a Galactic absorption of $N_H = 1.0 \times 10^{21}$ cm^{-2} whereas when the upper limit (1.6×10^{21}cm^{-2}) was used, the temperature dropped to 3.94 ± 0.21 keV which is consistent with the mean temperature of the cluster. The difference in temperature of ~ 1 keV supports the idea that the two sub-clusters are originally separate components undergoing a merger. Taking a north-south slice through the cluster using rectangular regions of 208×104 arcsec from 17:20:50.074, -00:53:13.77 (Fig. 3.8), there is no sudden rise in temperature where the sub-clusters meet and therefore no evidence for a shock and no increase in surface brightness, indicating a non-violent interaction between these components.

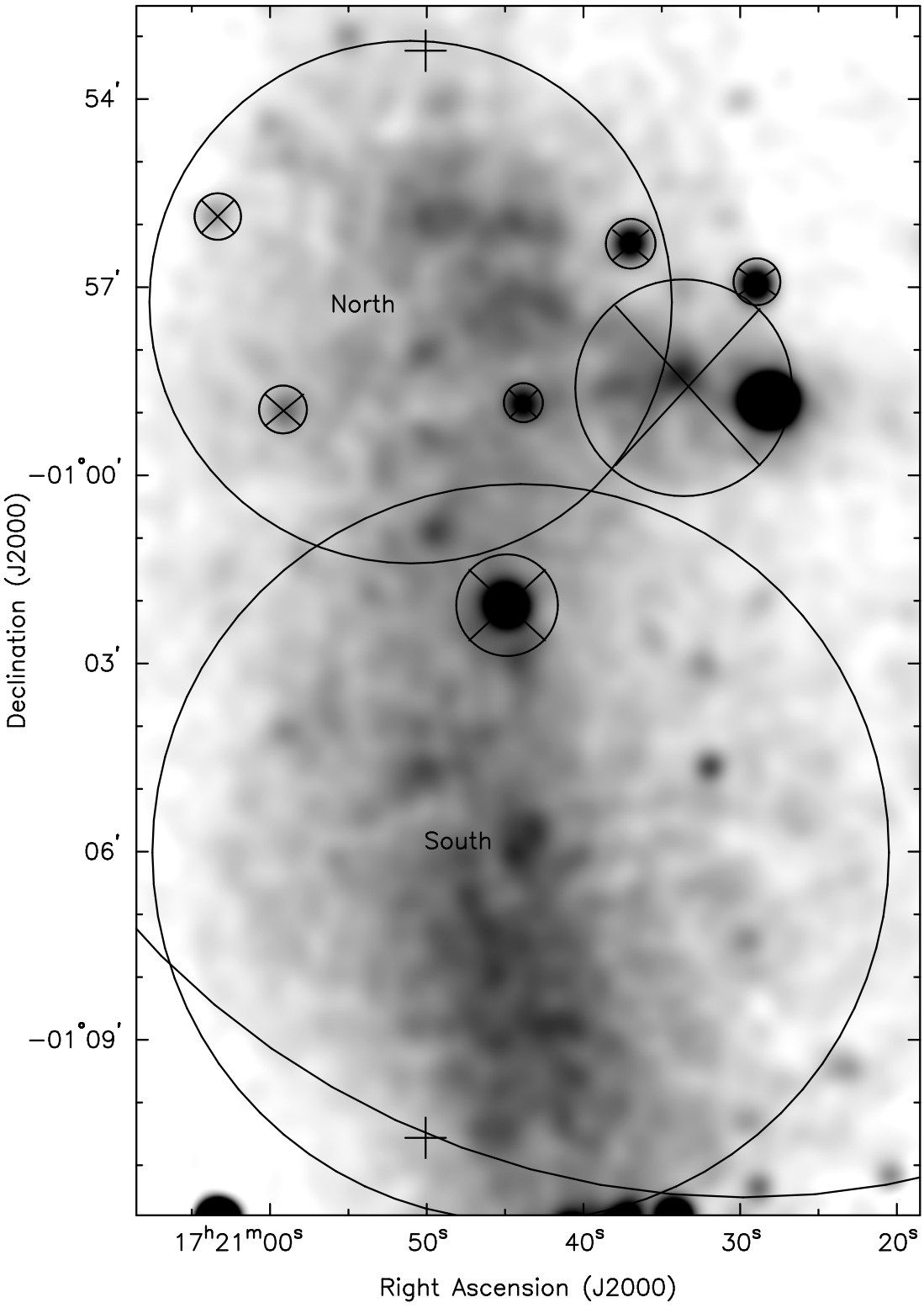

Figure 3.6: Northern and southern sub-cluster regions from which spectra were extracted to determine the sub-cluster global temperatures. The crossed regions are those which were excluded from the analysis and include the X-ray point sources and 3C 353. The crosses indicate the limits of the slice used. The inner edge of a large annular region masking the edge of the camera can be seen at the bottom of the image.

A thermal model was fitted to annular regions in the northern and southern sub-clusters. The results are shown in Table 3.3. The residual local background was accounted for using regions in a relatively source free area of the field of view. Using an annular background region gave consistent temperatures for both sub-clusters. The northern sub-cluster shows a linear increase in temperature with radius with a best fit of $T(r) = 0.010r + 1.528$ keV while the southern sub-

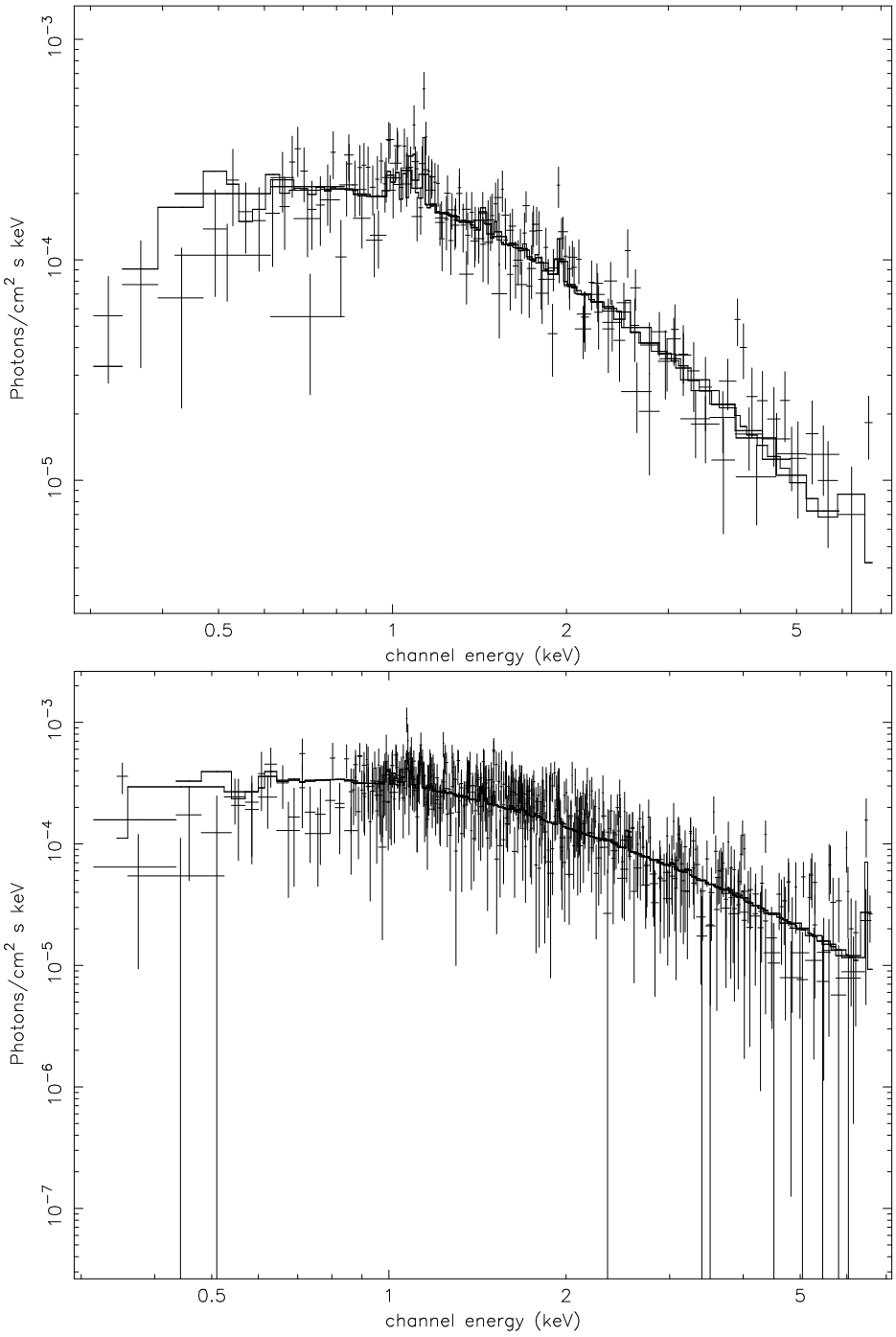

Figure 3.7: X-ray spectra for the northern (top panel) and southern (bottom panel) sub-clusters in the energy range 0.3–7.0 keV. The MOS 1, MOS 2 and pn cameras datasets are shown in each case with the best-fitting thermal model as described in Section 3.3.5.

cluster is isothermal within the errors. 3C 353's East lobe lies at a radius of 250 – 350 arcsec from the centre of the northern sub-cluster but it may also be affected by the southern sub-cluster. The annular temperature at this radius ($kT = 3.5 \pm 0.5$ keV) is consistent with the global northern sub-cluster temperature ($kT = 3.3 \pm 0.3$ keV) as well as the temperature measured by the slice at this radius ($kT = 3.9 \pm 0.6$ keV). I therefore adopt a temperature of 3.5 ± 0.5 keV for the environment of 3C 353.

As 3C 353 interacts mainly with the northern sub-cluster and as the southern sub-cluster is not fully covered within the *XMM-Newton* field of view, surface brightness and pressure profiles were constructed for the northern sub-cluster only. To determine the centre of the northern sub-cluster I used a centroiding routine for each of the *XMM-Newton* cameras. Annular regions were used to extract a surface brightness profile, excluding the chip gaps, X-ray point sources, emission from 3C 353 and from the southern sub-cluster and the position of the missing chip in the MOS 1 camera. An annular region was used to account for the residual local background emission. The surface brightness profiles for each camera were fitted with a model consisting of a β model convolved with the *XMM-Newton* PSF based on the on-axis parametrisation described in the *XMM-Newton* CCF files XRT1_XPSF_0006.CCF, XRT2_XPSF_0007.CCF and XRT3_XPSF_0007.CCF before being fitted with a β model (Fig. 3.9).

I examined the annuli in quadrants to highlight any density variation in a north-south or east-west direction. The northern quadrants and the south-east quadrant were consistent. I excluded the south-west quadrant from the final profile to ensure that X-ray emission from the radio galaxy, and any local disturbances in the cluster gas, were removed. The resulting surface brightness profiles were consistent for all cameras. The joint best-fitting model, for all cameras, had a core radius of 194 arcsec and $\beta = 0.35$. Considering a 1σ confidence interval for 2 interesting parameters, β was unconstrained (though I consider values below 0.35 and above 0.9 unrealistic), whereas the core radius of the northern sub-cluster was limited to between 184 and 412 arcsec. I discuss the results of this section in Section 3.4.3.

Table 3.3: Temperature profiles for the northern and southern sub-clusters

Northern			Southern		
Radius (arcsec)	kT (keV)	χ^2/d.o.f.	Radius (arcsec)	kT (keV)	χ^2/d.o.f.
0 – 50	1.8 ± 0.3	29/19	0 – 75	5.2 ± 0.7	537/348
50 – 100	2.2 ± 0.3	121/65	75 – 150	4.2 ± 0.3	638/444
100 – 150	2.8 ± 0.4	130/102	150 – 200	4.7 ± 0.4	250/167
150 – 250	3.5 ± 0.3	129/108	200 – 250	4.9 ± 0.5	296/183
250 – 350	3.5 ± 0.5	286/172			

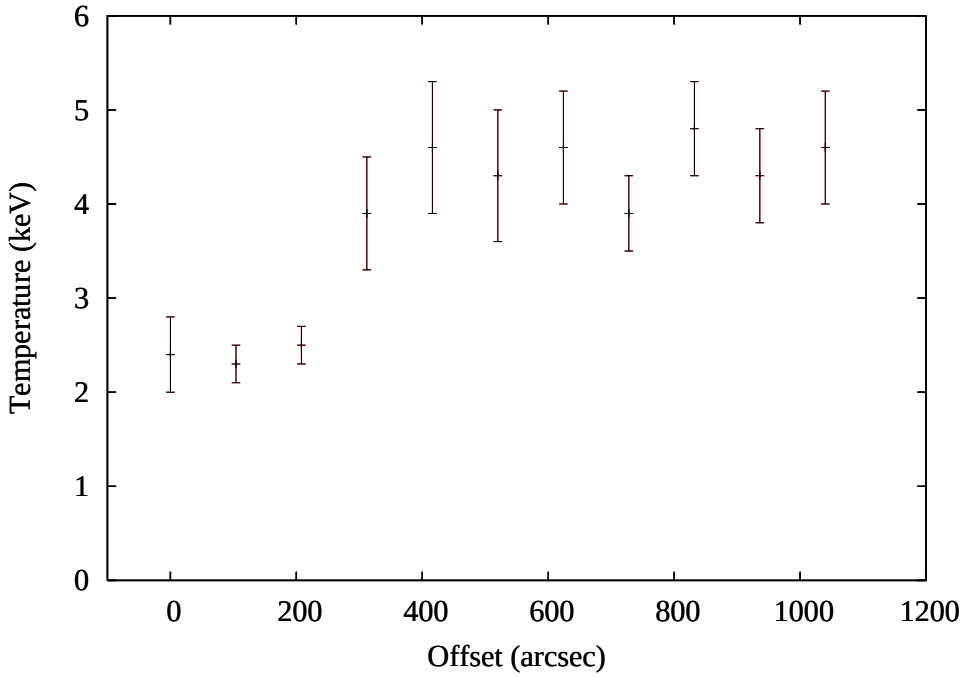

Figure 3.8: Temperature variation of north-south slice through cluster with rectangular regions of 208×104 arcsec from a zero of offset at 17:20:50.074, -00:53:13.77.

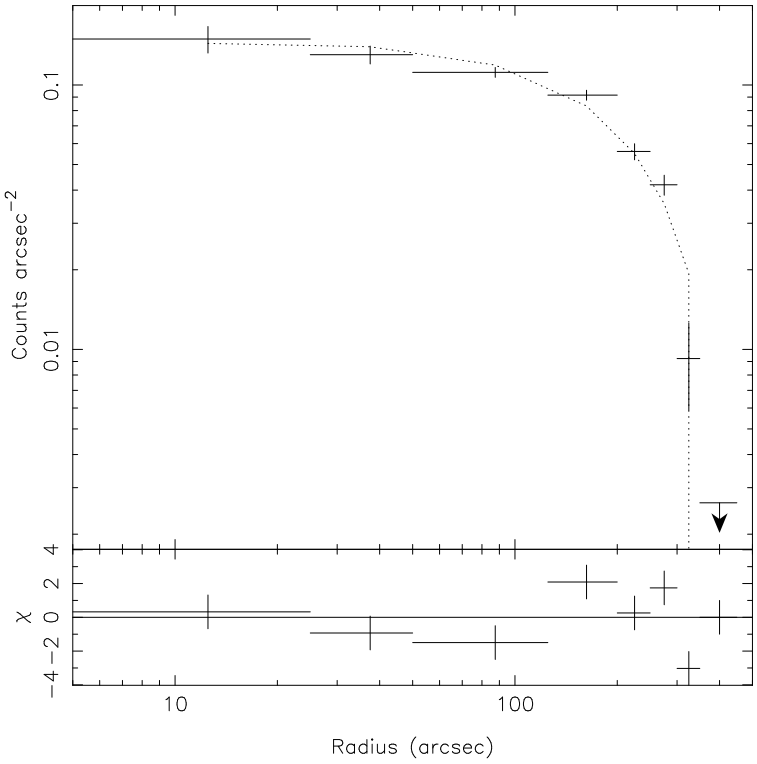

Figure 3.9: Surface brightness profile for the northern sub-cluster showing the pn dataset with the best fitting β model which has $\beta = 0.35$ and core radius 194 arcsec.

3.4 Discussion

3.4.1 The Nature of the Core

The double-peaked nuclear X-ray spectrum, consisting of a heavily absorbed component and a second component with only Galactic absorption, is typical of what is observed in narrow-line radio galaxies (NLRG) (e.g. Sambruna, Eracleous, & Mushotzky 1999; Grandi, Malaguti, & Fiocchi 2006; Belsole, Worrall, & Hardcastle 2006; Hardcastle, Evans, & Croston 2006a). However, when I plot the unabsorbed luminosity of the heavily absorbed nuclear component in 3C 353 against its 178-MHz total radio luminosity, as done by Hardcastle et al. (2006a) (their figure 3, shown in Figure 3.10), I find that 3C 353 lies almost 1 order of magnitude below the correlation they determined for NLRGs: that is, 3C 353 is overluminous in the radio for its X-ray luminosity or underluminous in the X-ray for its radio luminosity, and lies closer to the region of the plot occupied by low-excitation radio galaxies (LERGs). By contrast, the unabsorbed component is consistent with the correlation found by Hardcastle et al. between unabsorbed X-ray luminosity and nuclear 5-GHz radio emission from LERGs.

The optical emission-line classification of 3C 353 is uncertain. Laing et al. (1994) use the ratio of the flux in the [O III] line to that in the Hα to distinguish between the NLRGs and LERGs. The best published optical spectrum of 3C 353 is that of Simpson et al. (1996), and their quoted line fluxes clearly place 3C 353 below the [O III]/Hα cutoff of 0.2 proposed by Laing et al: thus by this definition 3C 353 would be a LERG. However, if the line fluxes are corrected for reddening using values determined from the Schlegel, Finkbeiner, & Davis (1998) dust maps (see Section 3.3.1), then the emission-line ratio rises to 0.17 ± 0.02, where the errors are derived from the normal 10 per cent errors of Simpson et al. and are almost certainly too low: within the errors I cannot say whether 3C 353 should be classed as a LERG or NLRG. The nature of 3C 353's nucleus both in the optical and in the X-ray remains ambiguous.

3.4.2 Lobe Emission and Properties

Using the method of Croston et al. (2005b), the X-ray observations were compared to the predictions of an iC model, based on synchrotron modelling of the radio datasets using SYNCH (Hardcastle et al. 1998). The broad-band spectra for the lobes are shown in Figure 3.11. The measured 1-keV flux densities of the East and West lobes are 11.6 ± 1.6 nJy and 2.7 ± 1.0 nJy respectively. The equipartition magnetic field strengths for the East and West lobes are 0.89 nT and 0.84 nT respectively, while if I assume that all the X-ray emission is iC in origin then the measured flux densities correspond to magnetic field strengths of 0.44 ± 0.06 nT and 0.68 ± 0.2 nT. Therefore, while the weakly detected West lobe has a measured magnetic field strength within errors of the predicted equipartition value, the East lobe's measured magnetic field strength is smaller than the predicted equipartition value by a factor ~ 2 so that $B_{obs}/B_{eq} \simeq 0.4$. The West lobe's measured magnetic

field strength is also consistent with a substantial departure from equipartition. This implies that the lobes of 3C 353 are electron dominated, which is not unusual considering the range of field strengths in the sample of Croston et al. (2005b). This factor would be reduced for 3C 353 if the lobes were not in the plane of the sky.

The measured magnetic field strengths in the lobe correspond to internal pressures of $3.4 \pm 0.6 \times 10^{-13}$ Pa and $1.9 \pm 0.2 \times 10^{-13}$ Pa for the East and West lobes respectively. (If the alternative local background regions discussed in Section 3.3.3 were used, the magnetic field strengths would be reduced by ~ 0.1 nT and the internal pressure of the East lobe would double, but this does not affect my conclusions.)

Using the radio datasets, I constructed a spectral index map between the 1.67-GHz and 327-MHz images, Figure 3.12. It revealed a variation of $\Delta\alpha \sim 0.2$ across both lobes. Within the radio luminous region of the East lobe, excluding the hotspots, the spectral index is roughly constant, $\alpha = 0.66 \pm 0.01$ despite the filamentary structure seen in Figure 3.1, whereas in the West lobe, $\alpha = 0.63 \pm 0.01$ excluding the hotspot. I note that the radio lobes do not appear to be entirely

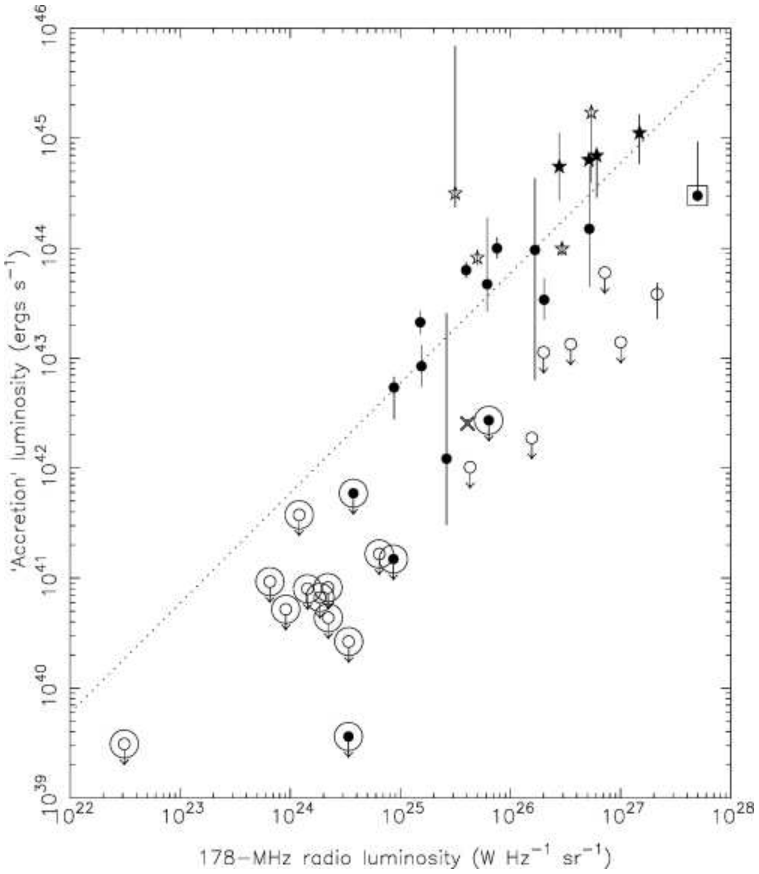

Figure 3.10: X-ray luminosity of the accretion-related component as a function of 178-MHz total radio luminosity for LERGs (open circles), NLRGs (filled circles), BLRGs (open stars) and quasars (filled stars) as presented in Hardcastle et al. (2006b) with the position 3C 353 indicated by the cross.

separate, and thus consider the region in between the radio luminous lobes, north and south of the core to be an inter-lobe region, which cannot be unambiguously associated with either lobe. This inter-lobe region has a relatively steep spectrum of $\alpha = 0.75 \pm 0.01$ whereas the hotspot in both lobes exhibits a flatter spectrum of $\alpha = 0.60 \pm 0.01$. Figure 3.12 shows the spectral index map between 1.67 GHz and 327 MHz with contours from the 327-MHz map.

The X-ray/radio ratio was determined for the hotspot, lobe and inter-lobe regions, using the high signal to noise of the X-ray data set. The 327 MHz radio map of resolution 7.0×7.0 arcsec was used with the convolved, exposure corrected X-ray map of energies 0.3 to 7.0 keV. The X-ray/radio ratio was found to be a factor of 4 greater in the steep inter-lobe region than in the flat, hotspot regions. If the magnetic field strength and the number densities of both the iC and synchrotron emitting electron are constant across the lobe, the X-ray/radio ratio would also be constant, but this is not what is seen in 3C 353. Similar results have been seen in other radio galaxies, notably 3C 452 (Isobe et al. 2002) and Pictor A (Hardcastle & Croston 2005). Hardcastle & Croston considered the following three models to explain the varying X-ray/radio ratio:

(i) Some other emission process could boost the X-ray emission in the inner regions;

(ii) The central regions contain more low-energy electrons relative to the outer regions;

(iii) The magnetic field strength varies as a function of position.

A contribution from the core was included in the X-ray spectral analysis which also takes account of the contribution of the unabsorbed X-ray emission associated with the jet and the absorbed X-ray emission from the accretion disk. Emission from the core cannot therefore boost the X-ray emission in the inner regions. The spectral fits show no evidence for a contamination of the lobe spectra by galaxy-scale thermal emission. Neither could a boost be due to the galaxy's proximity to the cluster as local background regions were used to account for any thermal emission from the sub-clusters. For iC scattering of nuclear photons to be the dominant process, the core bolometric luminosity needs to be at least 10^{38} W. This is not unrealistic, however modelling the lobe surface brightness for this scenario using the results of Brunetti (2000) as described by Hardcastle et al. (2002a) and with 3C 353 in the plane of the sky, reveals a gradient across the lobe which is not observed in either the X-ray image nor the X-ray/radio ratio. Using the spectral energy distributions of Haas et al. (2004), I deduced a typical IR spectrum for 3C 353 by scaling a dual power-law fit to the spectral energy distribution of 3C 33. 3C 33 was chosen as it has a similar luminosity and is classified as a NLRG/FR II. The IR spectrum was normalised by the ratio of low-frequency radio luminosities of the two sources. The predicted flux density for the nuclear iC emission is 6.5×10^{-12} Jy at 1 keV, which is a factor of ~ 700 fainter than the predicted iC/CMB emission and the observed flux density (4.4 and 11.6 nJy respectively). Thus I can rule out model (i).

If I consider the magnetic field to be constant at the measured lobe averaged magnetic field strength of 0.39 nT and apply an iC model to the lobes, I find the emission at 327 MHz traces

electrons with $\gamma \simeq 4000$ whilst the measured iC emission traces electrons at $\gamma \simeq 1000$. As the critical frequency for synchrotron emission goes as γ^2, I find that a variation in the X-ray/radio ratio of a factor of 4 requires a variation in the spectral index between 10 MHz and 327 MHz of ~ 0.5. Even if the equipartition magnetic field strength of 0.89 nT is assumed so that the 327 MHz emission traces electrons of $\gamma \simeq 3000$, the observed spectral index variation requires a factor ~ 1.2 variation in the X-ray/radio ratio which is still much lower than observed. This is also the case with Pic A (Hardcastle & Croston 2005); a variation in the low-energy electron densities alone (model ii) cannot explain the variation of X-ray/radio ratio across the lobe.

Alternatively, if I assume constant electron densities for both the synchrotron and iC emission electrons and also that the magnetic field strength does not vary along the line of sight, I find that the observed variation in the X-ray/radio ratio then requires a variation in the magnetic field of at most a factor of 2.5. For a given frequency, this means the spectral index observed at low frequencies, between 1.67 GHz and 327 MHz, for regions of high X-ray/radio ratio should correspond to the spectral index between 3.5 GHz and 825 MHz for low X-ray/radio ratio regions. I consider the spectral indices between 4.8 GHz and 1.67 GHz to limit the spectral indices of the low X-ray/radio ratio regions and find that they exceed the upper limit predicted by the observed X-ray/radio ratio. From this comparison, I cannot rule out the possibility that a varying magnetic field alone could be responsible for the observed variations in the X-ray/radio ratio and the spectral indices. I therefore considered a colour-colour diagram using the method of Katz-Stone et al. (1993). In their study of Cygnus A, they argue that a single curve on a colour-colour diagram is consistent with a homogeneous distribution of relativistic electrons together with varying the magnetic field strength across the source. The colour-colour diagram for 3C 353, shown in Figure 3.13, has a similar single curve and so is consistent with this picture. In Pic A, Hardcastle & Croston (2005) argued that the detailed positional variations of radio spectra and radio/X-ray ratio were not consistent with such a model, but these data for 3C 353 are not good enough to rule it out here.

I conclude that a varying electron spectrum alone cannot account for the observed variation in X-ray/radio ratio in the lobes of 3C 353 but that a magnetic field strength that varies by a factor of ~ 2.5 throughout the lobes can explain it. Similar conclusions were reached by Hardcastle & Croston (2005) in their study of Pic A.

3.4.3 The Cluster-Lobe Interaction

The surface brightness profile was converted to a pressure profile using the method of Birkinshaw & Worrall (1993), so that the radio lobe pressures determined with SYNCH could be directly compared to the external pressure from the cluster at the position of the radio galaxy. The centre of the East lobe lies ~ 280 arcsec from the centre of the northern sub-cluster. At this radial distance where the temperature of the environment is taken as 3.5 ± 0.5 keV, the external pressure is much greater than the internal pressure of the lobes (see Figure 3.14). As FR II radio galaxies are expected to

be in pressure balance or over pressured, either 3C 353 is not in the plane of the cluster or there is an additional contribution to the pressure from non-radiating particles such as hot thermal or relativistic protons in the lobes. Previous studies of FR II radio galaxies in groups and clusters have shown that pressure balance can usually be achieved without additional protons (e.g. Croston et al. 2005b; Hardcastle et al. 2002a; Belsole et al. 2004). I therefore assume that 3C 353 is not in the plane of the cluster and using the East lobe, determine that 3C 353 requires a shift in radial position corresponding to ~ 600 arcsecs to be in pressure balance with the northern sub-cluster (here I used the best estimate of the lobe pressure from Section 3.4.2). This places 3C 353 ~ 510 kpc either in front or behind the centre of the cluster. At this position, the West lobe's internal pressure is also consistent with the external pressure. The position of 3C 353 with respect to the pressure profile is shown in Figure 3.14. At this distance from the cluster, the external pressures seen by the lobes are different by a factor of ~ 1.8, which may help to explain the difference in appearance of the lobes, the East having a spherical appearance whilst the West lobe is elongated with hotspots at the outer edge.

3.4.4 Additional Features of Note

In addition to the usual radio-lobe structure, the East lobe of 3C 353 contains a dark circular region of unknown origin at 17:20:36.088, -00:58:44.15 (Figure 3.1). Detectable in all radio frequencies except 74 MHz (presumably due to its low resolution), the measured fluxes in this region are a factor of 100 above the rms background but are a factor of 2 fainter than the surrounding lobe emission. The X-ray image shows no sign of any feature in this region and neither does the Digital Sky Survey (DSS). As the emission is independent of frequency I can rule out an foreground absorber and the required geometry is unrealistic for an obstruction in the lobe. Without further information I am unable to identify this feature.

Iwasawa et al. (2000) included optical observations of the cluster region centred on 3C 353 taken with the University of Hawaii 2.2 m telescope in their analysis of Zw 1718.1-0108. They identified three additional massive galaxies, none of which reside in the northern sub-cluster (Figure 7.2). Deeper optical observations would help to establish whether there are any galaxies associated with the northern sub-cluster and whether 3C 353 is the dominant member of this sub-cluster despite its position at the edge.

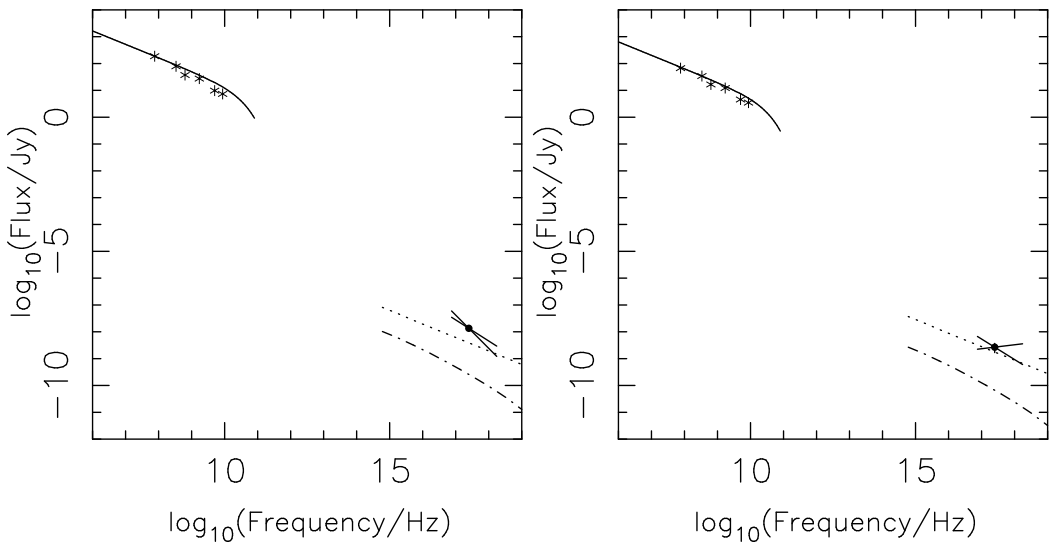

Figure 3.11: Broad-band spectrum for the East (left) and West (right) lobes of 3C 353 . A synchrotron emission model (solid line) is fitted to the radio data (asterisks). The measured X-ray flux is represented by the dot with the bowtie indicating the error. The dotted line shows the iC X-ray flux prediction and the dash-dotted line shows the predicted synchrotron self-Compton emission, both with the equipartition magnetic field strength.

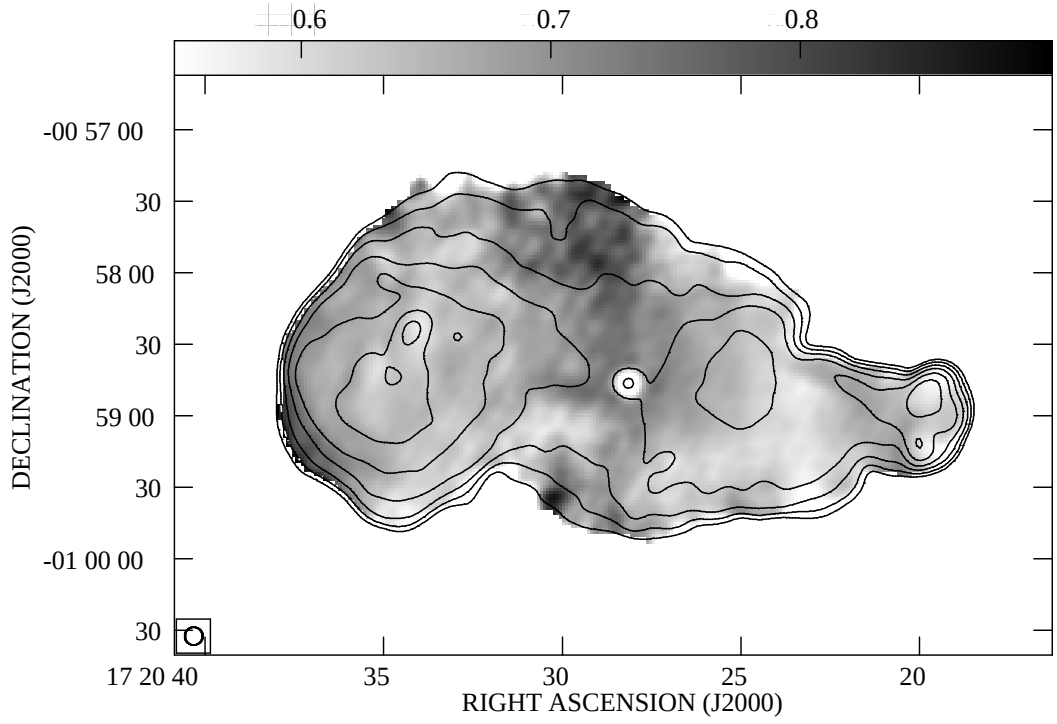

Figure 3.12: Spectral index map between 1.67 GHz and 327 MHz with radio contours at 327 MHz for levels of $0.01\times$(1,2,4,...) mJy/beam. The beam size (7.0 arcsec) is shown by the circle in the bottom left corner.

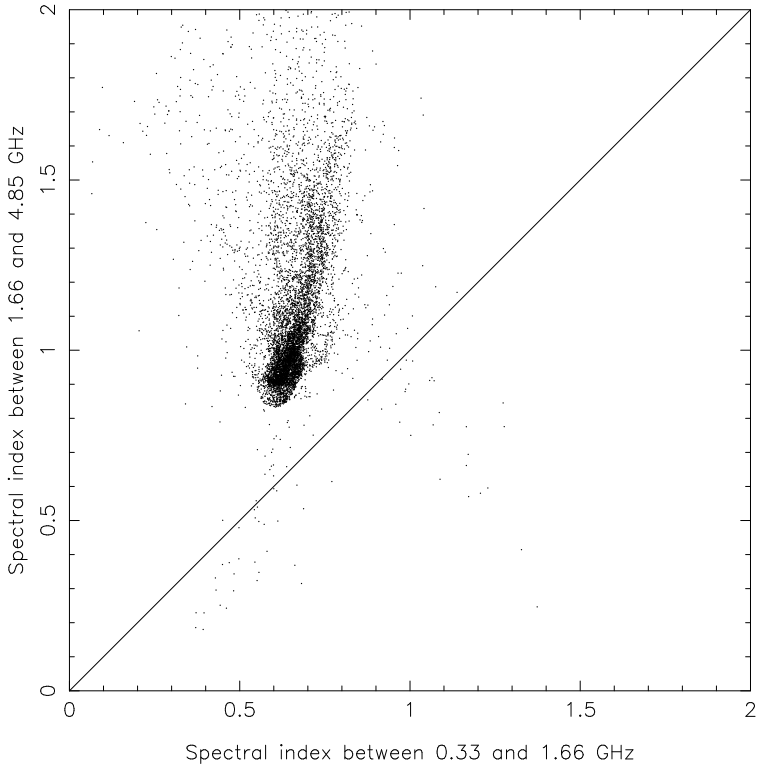

Figure 3.13: Colour-colour diagram for 3C 353 made at 7 arcsec resolution.

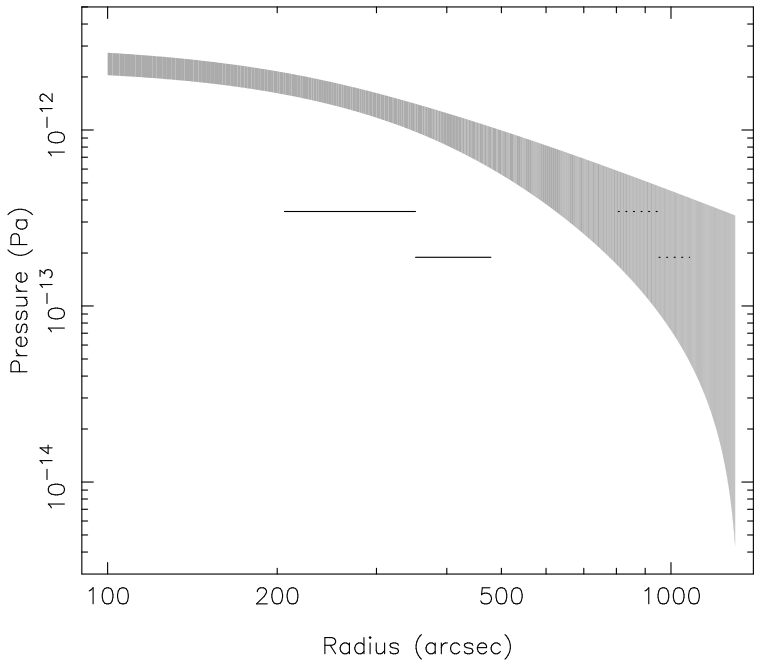

Figure 3.14: Pressure profile for the northern sub-cluster shown by the greyed in region, with the measured pressure of the lobes of 3C 353 at the projected distance (solid line) and at the position with the radial shift applied to where the East lobe is in pressure balance with the sub-cluster (dashed line). The measured iC emission was used to determine the pressure within each lobe. The temperature of the cluster at the radial distance of 3C 353 was used.

3.5 Summary and Conclusions

The results can be summarized as follows:

- By fitting an iC model to the lobes, I found the East lobe to be electron dominated and the West lobe to be consistent (within the large errors) with equipartition.
- I determined that a variation in the electron spectrum cannot account for the varying X-ray and radio emission alone, but that a change in the magnetic field strength across the lobes is required.
- I have obtained a good X-ray spectrum of the nucleus of 3C 353. Both the X-ray and optical properties of this source are ambiguous but it appears to lie in a region of parameter space in between those normally occupied by narrow-line and low-excitation radio galaxies.
- I have detected an X-ray counterpart for the East hotspot offset by 4.0 ± 0.5 kpc.
- The northern and southern sub-clusters were found to be isothermal with a temperature difference of ~ 1 keV supporting a model in which they are two originally separate components undergoing a merger with no evidence for a violent interaction.

Chapter 4

Radio Galaxy Filaments

Shortly after the work in Chapter 3 was published, our results were confirmed by Kataoka et al. (2008) using *Chandra* X-ray data. In this Chapter, I use their X-ray data for 3C 353 as well as previously published data for Pic A (Hardcastle & Croston 2005) to investigate the small-scale variations in the radio and X-ray emission using a new, point-to-point statistical method. This work was submitted to MNRAS in February 2010.

4.1 Introduction

As discussed in Chapter 3, spatial comparisons of the radio and X-ray emission from the lobes of radio galaxies give us insight into the spectral behaviour of the electron population and the effect of the magnetic field on the energy of the lobes.

The proximity of 3C 353 and Pic A means that we clearly detect radio filaments of brighter material within their lobes. This lobe filamentary structure is detected in many other radio galaxies [e.g. Fornax A (Ekers et al. 1983; Fomalont et al. 1989); Hercules A (Dreher & Feigelson 1984); and Cygnus A (Perley et al. 1984)]. From these previous radio observations, we know that these filaments are seen in a range of shapes; some resemble vortices, many resemble shock fronts and others form 'triangles' (Fornax A) and 'mushrooms' (3C 353). As the filaments are much brighter than the surrounding lobe material, they are likely to be overpressured, and they are also highly polarised (van Breugel & Fomalont 1984; Swain et al. 1998; Perley et al. 1997). Perley et al. (1997) writing about Pic A, discuss the required enhancements in the magnetic field and the electron density for the observed fractional brightness enhancement of 20%. They state that the B-field would have to be a factor of 5 stronger in the filaments or the electron density would have to be an order of magnitude higher. Either would make these features overpressured with respect to the inter-filament regions. These filaments may be interpreted as a simple projection effect in shell-like structures caused by shocks and turbulence (e.g. Cygnus A; Perley et al. 1984), spherical waves (e.g. Hercules

A; Mason et al. 1988), or the filling of bubbles of tenuous gas confined by surrounding magnetic fields and a hot ambient medium (e.g. 3C 310; van Breugel & Fomalont 1984).

Previous 3-dimensional (3D) magnetohydrodynamic (MHD) simulations have considered the influence of the environment on the jet (Tregillis et al. 2004; O'Neill et al. 2005) and the interaction between the expanding cocoon and the environment (Krause & Alexander 2007); however, recent 2.5 dimensional MHD simulations of the jet-environment interaction reveal complicated pressure and density structure which suggests that there are turbulent magnetic fields within the jet cocoon (Gaibler et al. 2009). The filamentary structures that manifest in these simulations are overpressured and overdense, which is consistent with the observations mentioned previously. Unfortunately, a study of the small-scale behaviour has not yet been carried out, concentrating instead on the effect of poloidal and toroidal fields on the turbulence at the cocoon's edge.

To understand the nature of these filaments, we require an iC detection. In most of the galaxies where we detect radio filaments, the thermal bremsstrahlung of the environment dominates the iC (e.g. Cygnus A, Centaurus A, M87, and Hercules A) and in the cases of Fornax A and Centaurus B, they cannot be efficiently observed with the present generation of X-ray telescopes due to their large angular size. As previously mentioned, there are X-ray iC/CMB detections of the lobes in Pic A and 3C 353; however, the X-ray iC/CMB emission from the radio filaments is not directly identifiable by eye in the *Chandra* or *XMM-Newton* X-ray observations limiting the analysis by Hardcastle & Croston (2005) and Goodger et al. (2008) to characterisation of the global variations.

In this work I present point-to-point comparisons of the radio synchrotron and X-ray iC emission from the lobes using a statistical method developed to rule out particular relationships between the radio and X-ray emission which does not require detections of the individual filaments. Instead, I statistically investigate whether the radio and X-ray emission is correlated; it is this correlation that can constrain the energy densities of the electrons and magnetic fields. I initially determine whether the radio synchrotron and X-ray iC emission from Pic A and 3C 353 are correlated (Sections 4.3 and 4.4) using the X-ray and radio data from previous published work (Section 4.2). I then simulate the observed X-ray data using a 'linear' model describing a situation where the observed changes in emission are due to changes in the electron population with a constant magnetic field strength (Section 4.5.1), and a 'scaling' model, where the energy density of the magnetic field scales linearly with the energy density of electron population (Section 4.5.2). By comparing these simulated data with the observed correlations, I constrain the physical conditions within the filamentary structure of the lobes. The implications of this constraint are discussed in Section 4.6.

Table 4.1: Radio Observation Details

Galaxy	Frequency (MHz)	Config.	Date	Duration (s)	Band Width (MHz)
Pic A	1446/1496	A	03/10/1987	3600	3.125
		A	01/10/1987	360	12.5
		AnB	03/07/1986	4680	12.5
		BnC	02/10/1986	4680	12.5
		CnD	01/02/1987	2880	12.5
3C 353	1665/1385	A	19/05/1968	20710	12.5
		B	14/08/1968	6640	25.0
		C	16/09/1985	1441	50.0

4.2 Data

I used radio and X-ray observations of Pic A and 3C 353 in this work, all of which have been previously published. Our radio data were taken at the NRAO Very Large Array (VLA) and I make use of *Chandra* observations for X-ray measurements as I require sufficient spatial resolution to detect the filaments with good statistics. The details of these radio and X-ray data are summarised in Tables 4.1 and 4.2 respectively.

4.2.1 Pic A

The radio observations of Pic A used in this work were first presented by Perley et al. (1997) and kindly provided by R. Perley. I used the 1.5 GHz images in this work, which were presented in Hardcastle & Croston (2005) (resolution 7.0×7.0 arcsec). The X-ray data used are the combination of three observations taken in 2000 and 2002 (ObsIDs 346, 3090 and 4369). I used images in the energy range 0.4 – 7.0 keV to measure the X-ray flux density in Pic A.

4.2.2 3C 353

I used the 1.67 GHz radio data for 3C 353 observed at the VLA (as described in Chapter 3 with resolution 1.78×1.44 arcsec, and a 90 ks *Chandra* observation taken in 2007 (presented by Kataoka et al. 2008) for this statistical study (ObsIDs 7886 and 8565). I used images in the energy range 0.4 – 8.0 keV to measure the X-ray flux density in 3C 353.

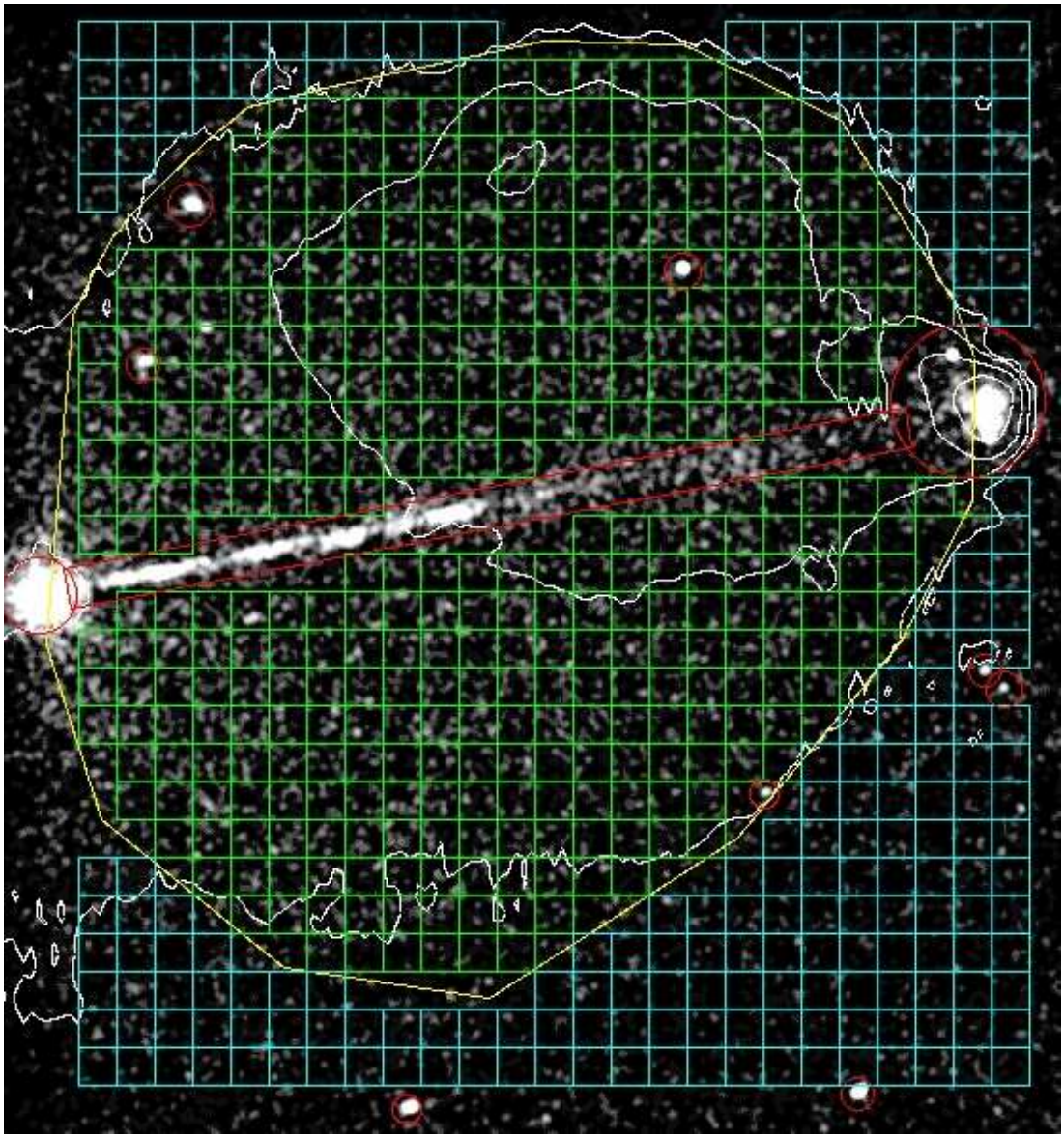

Figure 4.1: X-ray data of the west lobe for Pic A in the energy band 0.4 – 7.0 keV smoothed with a Gaussian with a kernel of 3 pixels (1.5 arcsec) with the source grid regions shown in green, the excluded regions shown in red and the background regions shown in cyan. The edge of Pic A is defined in yellow. The background value was determined using the average of all the background regions (cyan). The white contours show the 1.4 GHz radio emission at 0.007, 0.038, 0.212, 1.166 and 6.412 Jy beam^{-1} (resolution 0.492 arcsec).

Table 4.2: X-ray Observation Details

Galaxy	Date	ObsID	Livetime (s)	Filtered Livetime (s)
Pic A	18/01/2000	346	25737	25737
	17/09/2002	3090	46959	36351
	22/09/2002	4369	49126	49126
3C 353	04/07/2007	7886	71811	70400
	04/07/2007	8565	18179	17900

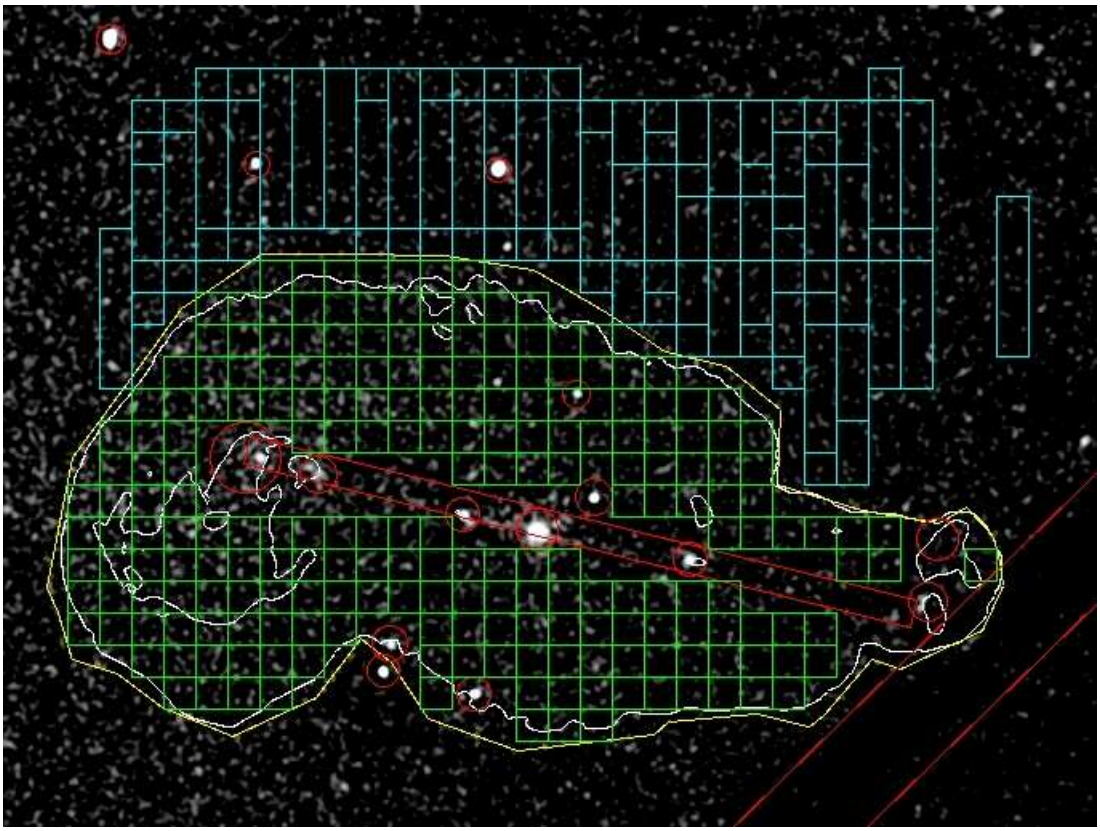

Figure 4.2: X-ray data for 3C 353 in the energy band 0.4 – 8.0 keV smoothed with a Gaussian with a kernel of 3 pixels (1.5 arcsec) with the source grid regions shown in green, the excluded regions shown in red and the extended local background regions in cyan. The edge of 3C 353 is defined in yellow. Each source region (green) is matched with an extended background regions (cyan) at the most similar distance from the centre of the Northern sub-cluster as defined in Chapter 3. The white contours show the 1.4 GHz radio emission at 0.001, 0.011 and 0.110 Jy beam^{-1} (resolution 0.492 arcsec).

4.3 Method

As I cannot identify the filaments directly in our X-ray data, I chose to perform a statistical test on the radio and X-ray emission to determine whether the emission was correlated and if there was a simple relationship between the radio flux density and the X-ray counts. I did this by constructing a grid of regions over the entire radio galaxy, measuring the background-subtracted X-ray counts and radio flux density in each region, and plotting these variables against each other.

The first step in this analysis was to determine the best size for the regions; I required tens of net counts per region after local background subtraction and I also needed enough regions to establish the correlation with good statistics. With this number of net counts, I could use Gaussian statistics to estimate the error on these source grid regions. I found that a grid size of 20×20 pixels ($6.9\,\mathrm{kpc}^2$ for Pic A and $6.0\,\mathrm{kpc}^2$ for 3C 353) was large enough to resolve the filaments so the measurements are independent, had sufficient net counts per bin for a significant detection and gave enough regions across the source to perform adequate statistics. The trends for different region sizes did not change significantly (Figure 4.3). The grid regions for 3C 353 are shown in Figure 4.2 and for Pic A in Figure 4.1, both colour-coded as described below.

Using the radio image as a guide, I defined a generous outline (shown in yellow) around the galaxy to separate the source and the background grid regions (green and cyan respectively). Any grid region that included a contribution from either a point source or a chip gap was excluded from this analysis as were the grid regions which lay on the galaxy's boundary, as these contained a contribution from both the source and the background (shown in red). I also masked out the jet, core and hotspots as I was only interested in the variation of emission from the lobes.

The X-ray counts were calculated using CIAO 4.1 and the task *dmstat*. To account for background emission, I used an average of all the background grid regions for Pic A as its X-ray background is relatively uniform across these data, and I used local background regions located to the north of the galaxy for 3C 353 as it is located on the edge of a merging cluster and thus has a complicated background.

For 3C 353, for each lobe region the background grid region used is the one with the most similar distance from the centre of the northern sub-cluster (as defined in Chapter 3) to that of the source grid region. This background grid region was then extended to the north so that its area was five times that of the source grid region to reduce the error on the background X-ray emission. We considered using the closest edge region to the source grid region, but as there is a gradient in the background emission, approximately parallel to the major axis of 3C 353, due to thermal emission from the sub-cluster, using the closest edge region to the source grid region resulted in some net counts being underestimated in the East lobe and others in the West lobe being overestimated. The overall trend of these data was not significantly affected by the choice of background (Figure 4.4). As I used an average of all the background grid regions for Pic A, the X-ray error was already sufficiently low and thus required no further averaging.

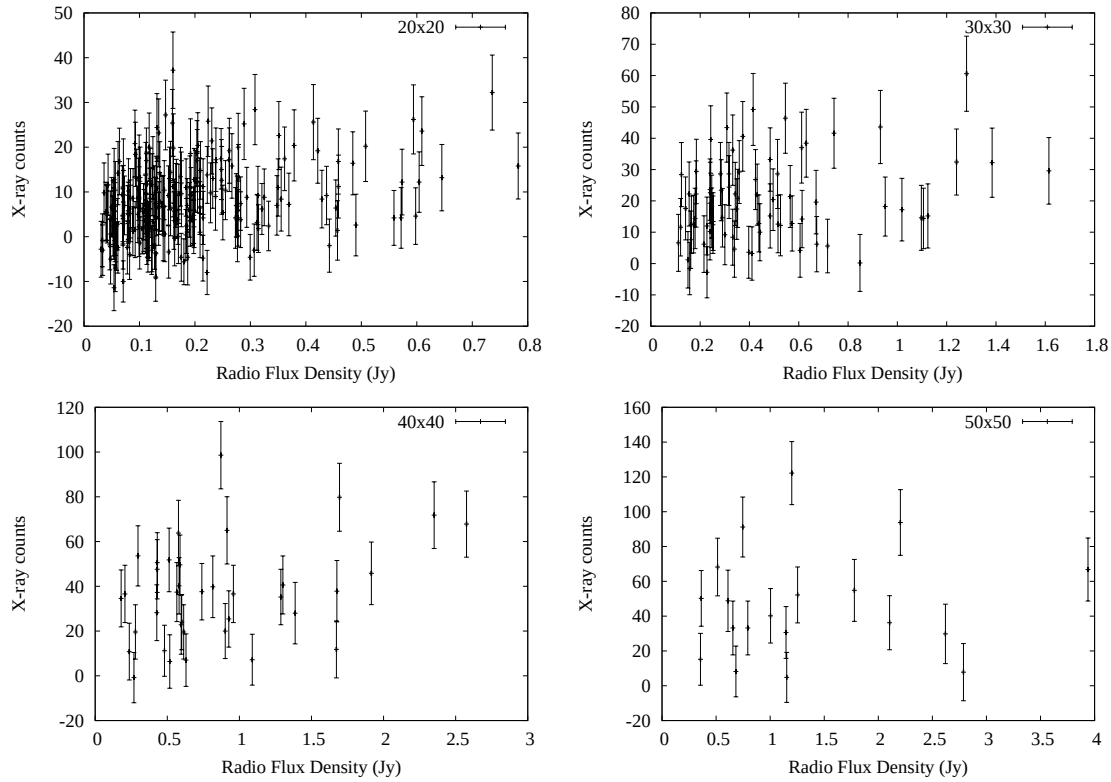

Figure 4.3: Comparison of the effect of grid size on the trend of 3C 353.

The corresponding radio flux densities were found using software based on the *funtools* package to determine the flux from the same source and background regions that I used in the X-ray analysis. The error on the radio flux density is negligible and depends only on the image noise (~ 1.8 mJy beam^{-1} and ~ 0.3 mJy beam^{-1} for Pic A and 3C 353 respectively), which is relatively constant across the radio image.

4.4 Correlation Results

The observed X-ray counts and radio flux densities for 3C 353 and Pic A are plotted against each other in Figure 4.5. At first glance, there is no obvious correlation between the X-ray and radio emission for either galaxy, and a Spearman rank test also suggests that the probability of a correlation is low with correlation coefficients of $\rho = 0.11$ and $\rho = 0.32$ for Pic A and 3C 353 respectively. Using the standard significance test ($z = \rho\sqrt{N-1}$), I find that for Pic A, these data are not significantly correlated ($z = 2.11$) but for 3C 353 I find $z = 4.72$, indicating a significant correlation between the X-ray and radio emission for 3C 353. The apparent high-X-ray count branch at low radio surface brightnesses ($S_R < 0.06$ Jy) in our Pic A data (shown in purple in Figure 4.8) is due to a known change in the X-ray/radio ratio across this region, which is discussed in Hardcastle & Croston (2005). Omitting this additional component in our distribution would result in even less correlation in these data.

I now know that these data are formally correlated; the question is what the nature of this correlation is. I therefore simulated data assuming first a linear relation and then a scaling model as described in the following Section, to compare with the observations.

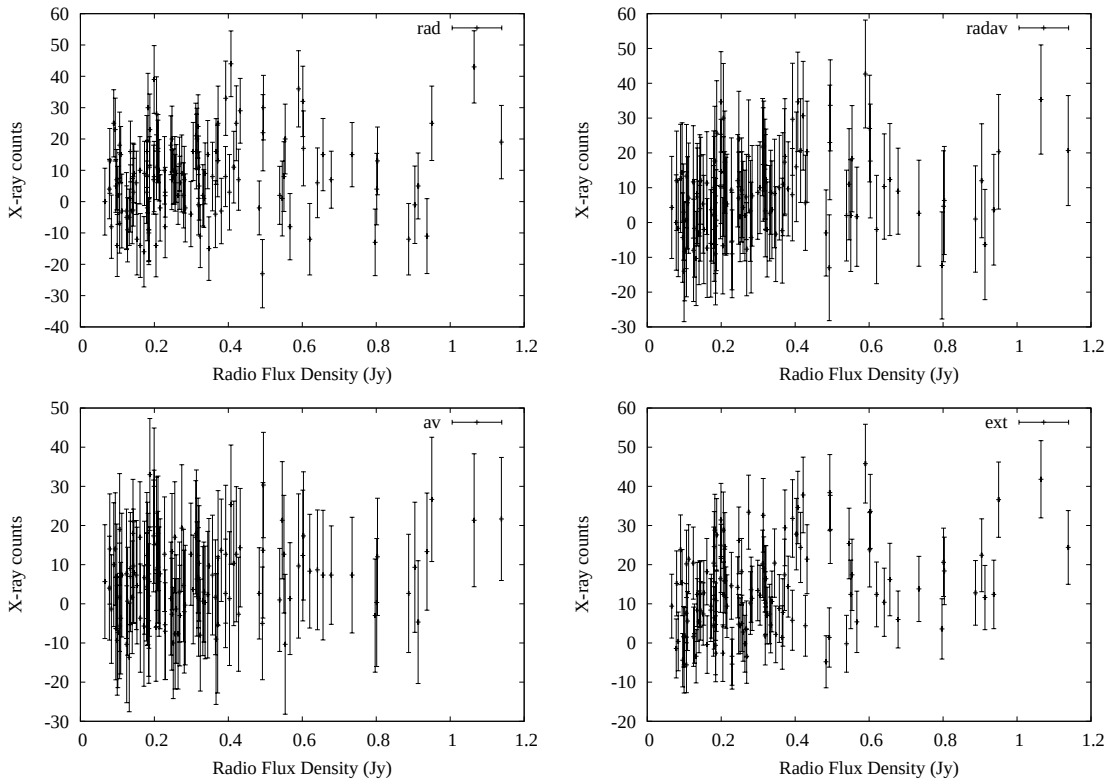

Figure 4.4: Comparison of the effect of background choice on the trend of the data for 3C 353. Using one background region at the most similar distance from the centre of the Northern subcluster is shown top left (rad), using the average of the three region at the most similar distance from the Northern subcluster is shown top right (radav). Using the closest three regions is shown bottom right (av) and the method opted for is shown bottom left; selecting a region with the most similar distance from the Northern subcluster, which is north of the galaxy, and extending the region north to five times the size of the source region (ext).

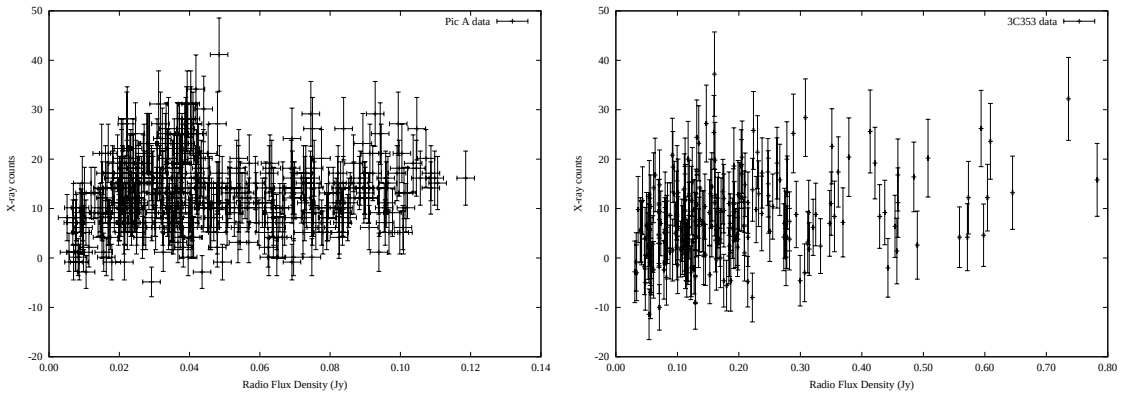

Figure 4.5: Comparison of the observed X-ray counts against radio flux density for Pic A (left panel) and 3C 353 (right panel).

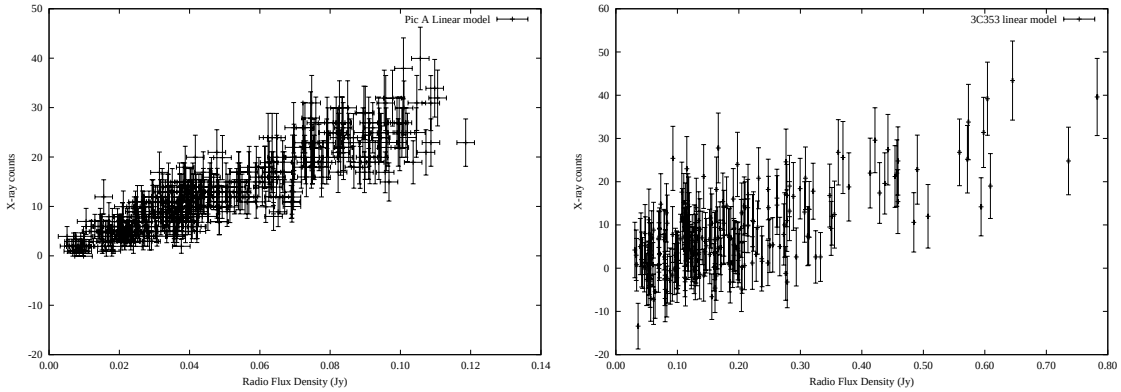

Figure 4.6: Examples of the linearly-related simulated X-ray counts plotted against radio flux density for Pic A (left panel) and 3C 353 (right panel).

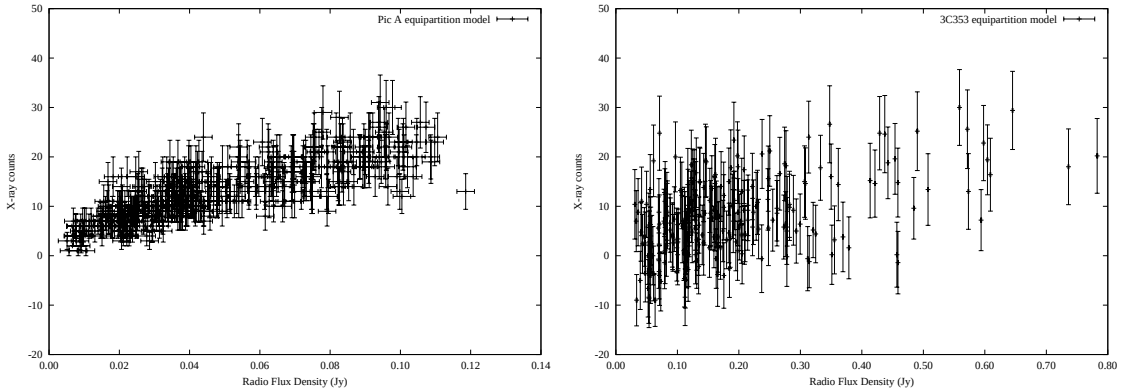

Figure 4.7: Examples of the scaling model simulated X-ray counts against radio flux density for Pic A (left panel) and 3C 353 (right panel).

4.5 Simulations

In this Section I consider the most physically plausible models to test: a linear relationship and a linearly-scaling relationship.

I would expect a linear relationship between the radio and X-ray emission if the radio features were due to changes in the electron energy spectrum and not due to changes in the magnetic field strength. This assumes the filaments are present in the X-ray data, even though they are individually undetected in our data. It is not necessary to know the magnetic field strength in the lobes or filaments as I can assume that it is a constant.

In a linearly-scaling relationship, I am modelling a situation where the magnetic- and electron-energy densities are changing in step ($U_B = CU_E$) as would be the case if the changes in the radio emission were due to changes in both the electron population and the magnetic field strength. The expressions for the radio synchrotron and X-ray iC emission were rearranged to determine how the expected X-ray emission behaves for a given radio flux in this scenario (Section 4.5.2). By testing this scenario, I can evaluate the extent to which the spatially changing emission is due to the electron population.

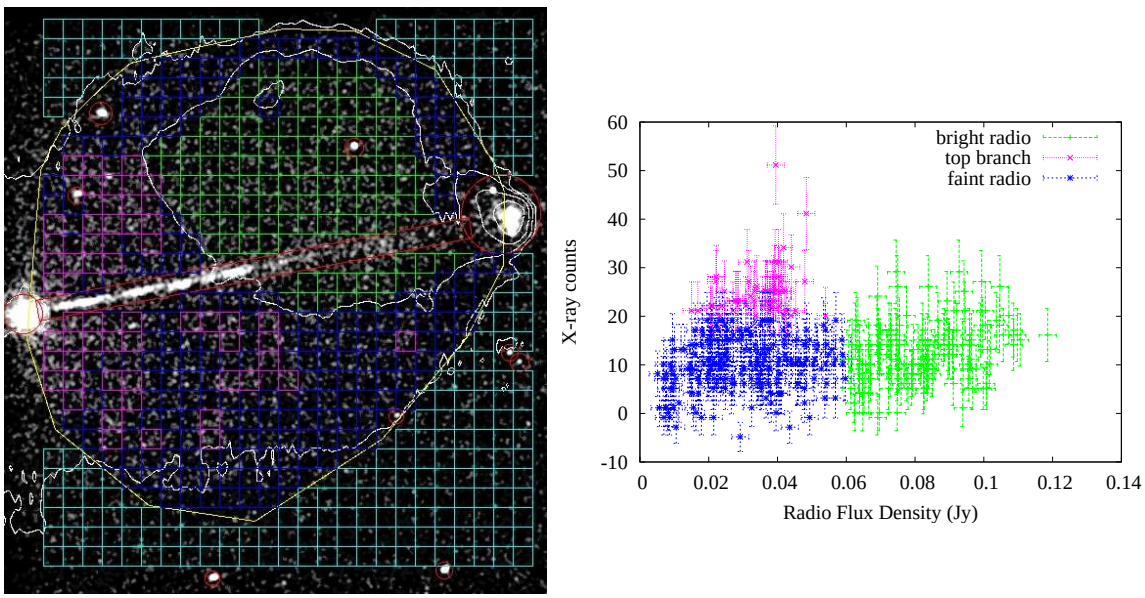

Figure 4.8: The high X-ray surface brightness region in the Pic A are shown in purple on both the map (left) and the scatter plot (right), while the low X-ray surface brightness regions are shown in blue and the remaining bright radio surface brightness regions, which surround the hotspot in the map are shown in green.

4.5.1 A Linear Relationship

In the linear relationship model, I used the ratio of observed X-ray counts to observed radio flux density as the constant of proportionality between the radio and X-ray emission. I accumulated the X-ray counts and radio flux density for all of the source grid regions to determine a global X-ray/radio ratio of 269.81 ± 0.72 counts/Jy for Pic A and 41.49 ± 0.01 counts/Jy for 3C 353. These ratios were then used to simulate the X-ray counts from the radio flux density of the observed data.

To simulate the expected X-ray counts accurately, I introduced scatter to the source and background counts using a Gaussian distribution as an approximation to the Poisson statistics due to the large number of counts. Examples of these linearly related simulated data, for both Pic A and 3C 353, are shown in Figure 4.6. I repeated this simulation of the X-ray data 100 000 times for each galaxy and performed a Spearman rank test for each simulation to obtain a distribution for the correlation coefficients for this model. By comparing this distribution of the correlation coefficients with the value for our observed data ($\rho = 0.12$ for Pic A and $\rho = 0.32$ for 3C 353), I determined the probability of the simulation reproducing the correlation measured in our observed data.

I found that we would expect our observed data to be linearly correlated as weakly as observed or more so at most 1/1000 of the time for 3C 353 allowing us to rule out a linear relationship between the observed radio and X-ray to 99.9% confidence for 3C 353. However, for Pic A the lowest value of ρ produced in 100 000 simulations was 0.698, so I can confidently rule out a linear relationship for these Pic A data.

4.5.2 Linearly Scaling Energy Densities

I also simulated the X-ray counts on the basis of a model in which the emitting material has scaling magnetic and electron energy densities, $U_B = CU_E$, so that the changes in radio surface brightness are due to changes in both the electron population and the magnetic field strength. In this scenario, we would expect the radio synchrotron and the X-ray iC emission to change in the same direction, but not to the same extent.

As is well known from the theory of synchrotron emission (see Section 1.2, e.g. Longair 1994), the radio synchrotron emission is affected by both the electron population and the magnetic field; $J_{r,syn} \propto N_0\, B^{(p+1)/2}$. The X-ray iC emission is only affected by the electron population as the CMB is constant across the radio structure, $J_{XiC} \propto N_0$ (Equation (1.9)).

In this model, we assume the magnetic energy density, $U_B = B^2/2\mu_0$, is proportional to the electron energy density, $U_E = \int EN(E)dE$, so $B^2 \propto N_0$, and we can substitute this condition into the expression for radio synchrotron emission and eliminate the magnetic field strength from the relationship: $J_{rsyn} \propto N_0^{(p+5)/4}$. This can then be rearranged and substituted into the X-ray iC relationship so that the X-ray iC emission is related to the radio synchrotron emission as $J_{XiC} \propto J_{rsyn}^{4/(p+5)}$. In this work I have used $p = 2$ so that $J_{XiC} \propto J_{rsyn}^{4/7}$.

I applied the same scattering to this simulated data as in the linear relationship simulations, and I normalised these simulated data to the total observed X-ray counts. I found that the distribution of correlation coefficients drops below the value from our observations in 5% of these simulations for 3C 353 and never in 100 000 simulations for Pic A. This model can therefore only be ruled out with high confidence for Pic A.

In reality there is likely to be some curvature in the synchrotron spectrum. The high-frequency radio spectral index of the lobes Pic A is $\alpha = 0.85$ (Perley et al. 1997) while the overall spectral index of the iC X-ray emission from the lobes is $\alpha = 0.5 - 0.6$ (Hardcastle & Croston 2005) so that spectral curvature is clearly present in this source. These values suggest that the effective values of p range from 2 in the low-energy electrons to ~ 3 at much higher energies. I have therefore tested a model where $p = 3$ so that $J_{XiC} \propto J_{rsyn}^{1/2}$ using our Pic A data and the observed relationship could still not be reproduced in 100 000 simulations. In order to test curvature models in general, we would require a model for the electron energy spectrum which would need to be evaluated at every point in the lobe: such detailed modelling is beyond the scope of this work.

4.6 Discussion

With this new statistical analysis, we have shown that the radio and X-ray emission is significantly correlated in 3C 353 (greater than 3σ) and with a 2σ significance in Pic A. This is not entirely unexpected as the geometry of the lobes means that, if there is isotropic emission per unit volume, the surface brightness would be brighter in the center of the lobes and would fade away towards the edges. The precise distribution of electrons in the lobes is unknown so a purely geometry-based model is difficult to define; however, the observed correlation will contain a contribution due to the geometry, so that the observed correlation due to the filamentary structure is weaker than the total correlation observed. Similarly, any large-scale variation in the X-ray/radio ratio due to varying large-scale magnetic field strengths would be expected to strengthen the observed correlation. Therefore, the contribution to the observed correlation of any underlying relationship between the X-ray counts and radio flux density would strengthen the observed correlation.

My simulations of a linear relationship between the radio flux density and the X-ray counts represent changes in the surface brightness as being due to a changing electron energy spectrum with a constant magnetic field strength. I have determined that the observed correlation between radio flux density and X-ray counts is weaker than would be expected in this model in either the West lobe of Pic A, with a null hypothesis probability less than 1/100 000, or in the lobes of 3C 353 (probability less than 1/1000). I can therefore confidently rule out this linearly related model for both galaxies to greater than 99.9% confidence. I also simulated a scaling relationship between the electron population and the magnetic field. These simulated data reproduced the observed correlation in 5% of the simulations for 3C 353 but never in 100 000 simulations for Pic A. This relationship represents a physical model where the changes in the emission are due to changes in both the

electron population and the magnetic field strength. Taken together, the simulation results suggest that the filaments are likely due to strong spatial variation of the magnetic field strength alone. Although we could contrive of a model where there are two separate electron populations with different energy ranges superposed on top of each other along the line of sight, or a model where the magnetic field and electron energy densities are related in a complicated manner that precisely reproduces the observed correlation, these models are currently unrealistic and inexplicable.

On larger scales, earlier work on Pic A and 3C 353 (Hardcastle & Croston 2005; Goodger et al. 2008, respectively) led to the argument that the observed spatial variation in the radio/X-ray ratio could not be attributed to changes in the electron energy spectrum alone; we required spatial variation in the large-scale magnetic field strength in the lobes as well. However, in both cases the *global* energy density of the sources was dominated by the electrons, with the energy density in the magnetic field being a factor of a few lower (see Chapter 3).

Given that these new results imply strong variation of the magnetic field strength from point to point in the lobe, and therefore along any given line of sight in the lobe, we must interpret the constraints on the magnetic field from our earlier work as applying to the *average* magnetic field strength in the source. That is, the mean energy density in magnetic field falls below that in electrons, but there are regions of the lobe, seen in synchrotron emission as filaments, where it can be significantly higher. Similarly, the large-scale spatial variation in magnetic field strength reported in our earlier papers is a variation in the mean rather than being related to the small-scale variation implied by the filaments.

The strong point-to-point variation of the magnetic field implied by our preferred model will have implications for spectral ageing in the radio lobes. For example, it has been suggested (Blundell & Rawlings 2000) that in addition to synchrotron cooling other loss mechanisms and migration of the electrons between regions of different magnetic field strengths cause simple spectral ages to be overestimates of the time elapsed since acceleration. In Chapter 3 I considered the spectral indices of the radio emission using the radio 'colour-colour' analysis of Katz-Stone et al. (1993), and could not distinguish between a JP-type (Jaffe & Perola 1973) and a KP-type (Kardashev 1962; Pacholczyk 1970) spectral ageing model, as the data did not lie on the line predicted by either model (see Figure 4.9); instead I concluded that the emission was consistent with a homogeneous distribution of relativistic electrons together with a varying magnetic field strength across the source, which was also found to be the case for Cygnus A (Katz-Stone et al. 1993). Both the JP-type and KP-type models assume a constant and known magnetic field strength; our current picture of the magnetic field variation in our targets is more consistent with models such as the 'leaky-box' model (Eilek et al. 1997; Kaiser 2005) which allows the electrons to move between regions of high and low magnetic field. This model predicts a radio spectrum above ~ 1 GHz which is dominated by the higher magnetic field regions and becomes steeper over time. This simple leaky-box model better fits the curvature of the Cygnus A data (presented by Katz-Stone et al. 1993), where the curvature of the model is dependent on the rate of diffusion of the emitting electrons (Figure 4.9). As 3C 353 has a

curvature similar to that of Cygnus A, I can conclude that the colour-colour plot could well be better described by the leaky-box model, consistent with our preferred model for the small-scale magnetic field structure.

To summarise, I have shown that the relationship between the radio synchrotron and X-ray iC emission in Pic A and 3C 353 is likely due to a strong point-to-point variation in the magnetic field strength rather than changes in the electron energy distribution. This is consistent with a leaky-box spectral ageing model, which may well be a good description of the radio colour-colour plots for 3C 353 presented in Chapter 3 (see Figure 3.13). Our results thus imply that spectral ageing models for radio galaxies in general may need to take inhomogeneous magnetic fields into account. The current generation of MHD simulations do not consider the behaviour of the magnetic fields sufficiently to confirm our results. Therefore, to further constrain the cause of these overdense, strongly polarised lobe filaments, we need detections of iC X-ray emission from these radio filaments in a greater number of radio galaxies and fully 3D MHD simulations focusing on the material within the radio lobes. Unfortunately, as the thermal bremsstrahlung dominates the iC in the X-ray of most galaxies where radio filaments have been detected, our sample is limited.

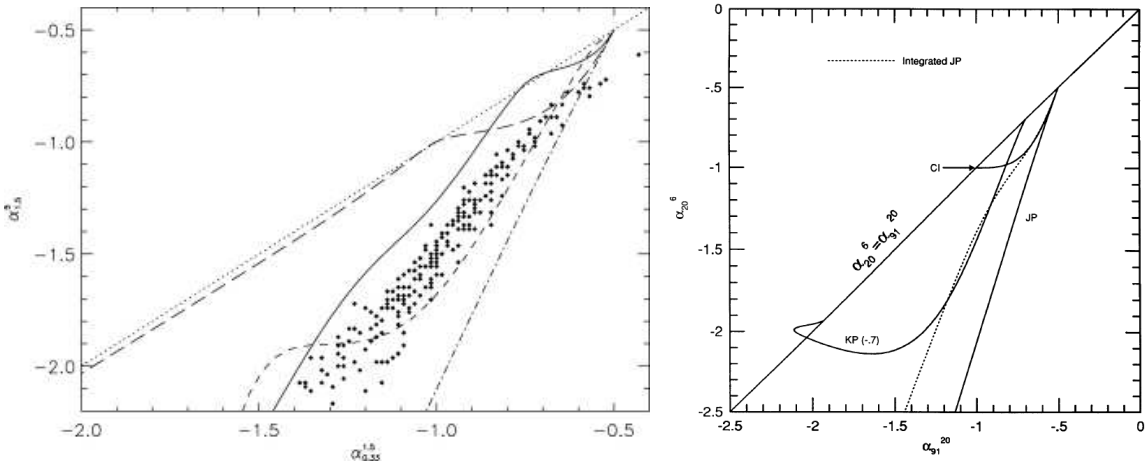

Figure 4.9: Colour-colour diagrams showing the conventional spectral ageing model predictions for the leaky box model with various diffusion rates indicated by the different line styles (Kaiser 2005) with the observational data for Cygnus A from Rudnick et al. (1994) (left panel) and the standard KP, JP and continuous injection (CI) models taken from Katz-Stone et al. (1993) (right panel).

4.7 Summary and Conclusions

In this work, I have used a point-to-point, statistical method to investigate the small-scale behaviour of the radio synchrotron and X-ray iC emission in the lobes of radio galaxies, as opposed to the studies of large-scale variation carried out in previous work. Our results can be summarised as follows:

- The radio and X-ray emission is correlated in Pic A and more significantly in 3C 353.
- A linear relationship between the radio flux density and the X-ray counts is ruled out to 99.9% confidence for both Pic A and 3C 353 suggesting that the correlation is not simply due to the geometry of the lobes, and neither is it due to a local change in the electron energy spectrum.
- I can also rule out a linearly scaling relationship between the electron and magnetic field energy densities to $>$99.9% confidence in Pic A and to 95% confidence in 3C 353, consistent with global results.
- By eliminating these relationships, I conclude that the filaments are most likely to be due to strong spatial variation of the magnetic field strength.
- It is important that varying magnetic fields be included in spectral ageing models and MHD simulations; in particular, it is apparent that ignoring this structure will introduce systematic errors into estimates of spectral ages.

Chapter 5

The Jet Knots in Centaurus A

Here I present work on the knots in the jet of Cen A, which was published in The Astrophysical Journal (Goodger et al. 2010). It incorporates nearly two decades of radio VLA and *Chandra* X-ray data including a *Chandra* Very Large Program (VLP). I used this multi-frequency data to explore the temporal behaviour of the jet knots and constrain the particle acceleration mechanisms that cause and sustain these jet knots (see Section 1.3.1). These high-surface-brightness regions are observed in a wide range of observing bands suggesting that there are very energetic processes at work in these knots. How these regions affect the energy densities of the particles and magnetic fields within the jet, and whether additional material is entrained by the jet are important questions for understanding the overall energy transfer between the jet and the lobe.

5.1 Introduction

It is generally agreed that the observed emission from Fanaroff-Riley class I (FR I; Fanaroff & Riley 1974) radio jets is due to the synchrotron process at all wavelengths, with similar jet structure observed from the radio through the optical into the X-ray (e.g. Hardcastle et al. 2002b; Harris & Krawczynski 2002). The jets of FR I radio galaxies are thought to decelerate as they move away from the core, entraining material and expanding into a plume of diffuse matter (e.g. Bicknell 1984). One of the most significant implications of the synchrotron emission model is reflected in the characteristic loss timescales: in a stable environment, the X-ray emitting electrons have lifetimes of the order of tens of years, tracing regions of current, in situ particle acceleration, while the radio emitting electrons last for hundreds of thousands of years, showing the history of particle acceleration in the jet.

In order to investigate these regions of particle acceleration we need data with sensitivity and resolution sufficient to detect jet substructure on spatial scales comparable to the synchrotron loss scales. This prompts us to look to the two closest bright FR I radio jets: M87 and Cen A. Both

of these jets have been detected in multiple frequencies from the radio through to the X-ray (e.g. Feigelson et al. 1981; Kraft et al. 2002; Hardcastle et al. 2003, 2006b; Harris & Krawczynski 2002). The proximity of these radio galaxies, 16.7 Mpc and 3.7 Mpc respectively (Blakeslee et al. 2009; Mei et al. 2007; Ferrarese et al. 2007), make them unique jet laboratories with spatial scales of 77 pc and 17 pc per arcsec respectively. The details revealed in the structure of these jets have been the focus of many recent studies (e.g. Biretta et al. 1999; Hardcastle et al. 2003; Kataoka et al. 2006; Cheung et al. 2007). Within the smooth surface brightness observed in both of these jets are clumps of bright material – the knots – embedded in diffuse material, all emitting via synchrotron emission. The precise mechanisms causing the particle acceleration responsible for the diffuse structure and the knots are still unknown.

The most surprising result of recent observations of these two systems was the radio-to-X-ray synchrotron flare of HST-1 in M87. In 2002, the X-ray flux of HST-1 increased by a factor of 2 in only 116 days (Harris et al. 2003), implying a change within an emitting volume with a characteristic size less than 0.1 pc for a stationary source (much less than the size of HST-1, ~ 3 pc). The X-ray brightness then faded in the following months only to flare again, peaking in 2005. At its brightest, this flare was higher than its 2001 level by a factor of ~ 50. The UV and radio light-curves were found to vary in step with the X-ray up to this peak (Perlman et al. 2003; Harris et al. 2006), but the subsequent decrease appeared to drop off faster in the X-ray than in either the optical or the UV, which drop off in step (Harris et al. 2009). In additional to this spectral variability, it was established with the *Hubble Space Telescope (HST)* and the NRAO Very Long Baseline Array (VLBA) that some of the knots in M87 move superluminally, including subregions of the HST-1 knot (Biretta et al. 1999; Cheung et al. 2007). Together, this suggests that we are observing synchrotron losses in addition to either beaming or compression/rarefaction of the jet fluid.

Cen A is a factor of 4.5 closer than M87 so we can resolve more details in the complicated fine structure of the jet. The originally identified features, named A-G by Feigelson et al. (1981), have since been resolved into at least 40 individual knots (Kraft et al. 2002; Hardcastle et al. 2003) with additional emission from diffuse material. Some of the diffuse emission has been described as downstream ‘tails’ of emission from the knots (Hardcastle et al. 2003) or as evidence for limb-brightening of the jet (Kraft et al. 2000). In 2003, Hardcastle et al. presented 8.4 GHz radio observations from the NRAO Very Large Array (VLA) of Cen A. That work used archival data from 1991 and new observations from 2002 to study the jet knots and investigated the offsets and relationships between the radio knots and their X-ray counterparts and vice versa. They found that only some of the radio knots appeared to have X-ray counterparts, leaving many as ‘radio-only’ knots and ‘X-ray-only’ knots. They also considered the temporal changes in the radio knots, specifically their proper motions, finding that some of the radio knots were moving. These moving knots had comparatively little X-ray emission suggesting that high-energy particle acceleration is less efficient in these regions than in the jet as a whole.

Some of the current models explaining the presence of knots within the generally smooth diffuse material of the jet include compressions in the fluid flow, collisions with obstacles in the galaxy causing local shocks, reconfinement of the jet or some other jet-wide process, and magnetic reconnection. Hardcastle et al. (2003) ruled out simple compression of the fluid as a mechanism for producing X-ray-bright, radio-faint compact knots in favour of in situ particle acceleration associated with local shocks; however, compression could still play a part in the other knots. They concluded that the most likely model to describe the majority of these knots is an interaction between the jet fluid and an obstacle such as a molecular cloud or a high mass-loss star. By exploring the temporal behaviour of the X-ray and radio emission, we can understand the evolution of the knots and constrain the various models of particle acceleration used to describe the jet features.

In this Chapter I use *Chandra* and VLA data spread over almost 20 years to measure the X-ray and radio spectral indices, flux density variations, polarisation variations, and the proper motions of the jet knots in Cen A. My aims are to detect variability in the radio and X-ray properties of the knots, either extreme variability similar to that of HST-1 in M87 or more subtle changes, and to compare these properties, which will allow me to constrain the knot formation processes at work in the jet of Cen A. The details of the radio and X-ray data reduction are discussed in Section 5.2. In Section 5.3 I discuss the details of our analysis methods and the global results for the knot population, highlighting particularly interesting features. In Section 5.4, I compare these knot properties with the predictions of various models for the formation of knots, their particle acceleration and the jet structure. Finally I outline the most likely processes for forming knots in Cen A in Section 5.5.

5.2 Data

In this work I use both new and archival VLA radio data at 4.8 GHz, 8.4 GHz and 22 GHz observed over almost 20 years. Cen A has been observed at 4.8 GHz with the VLA since 1983 and at 8.4 GHz since 1991, including 6 monitoring observations taken by us since 2002 at roughly 18 month intervals. I also present new 22 GHz data taken in 2007 as part of a multi-frequency program (AG0754, P.I. J.L.Goodger) where quasi-simultaneous observations of the jet knots were taken in these three radio frequencies timed to coincide with *Chandra* X-ray observations. The details of these radio data are shown in Table 5.1. All these data were observed with two IFs with beam widths of 50 MHz. The radio frequencies used in this paper and in Table 5.1 are the average values for the two IFs. All the radio data were reduced in AIPS using the standard methods described in Chapter 2. The data were phase-, flux- and polarisation-calibrated before being split into a single source file. As our flux calibrator, 3C 286, is resolved I followed the recommended method of using a model during the flux calibration. The core of Cen A is very bright, containing ~ 85 % of the flux density of the image, the Cen A data were calibrated with a point source model as an initial approximation, before being self calibrated in phase to the point where no further improvement was noticed. The data were then amplitude- and phase- self-calibrated and baseline calibrated using the same method as Hardcastle

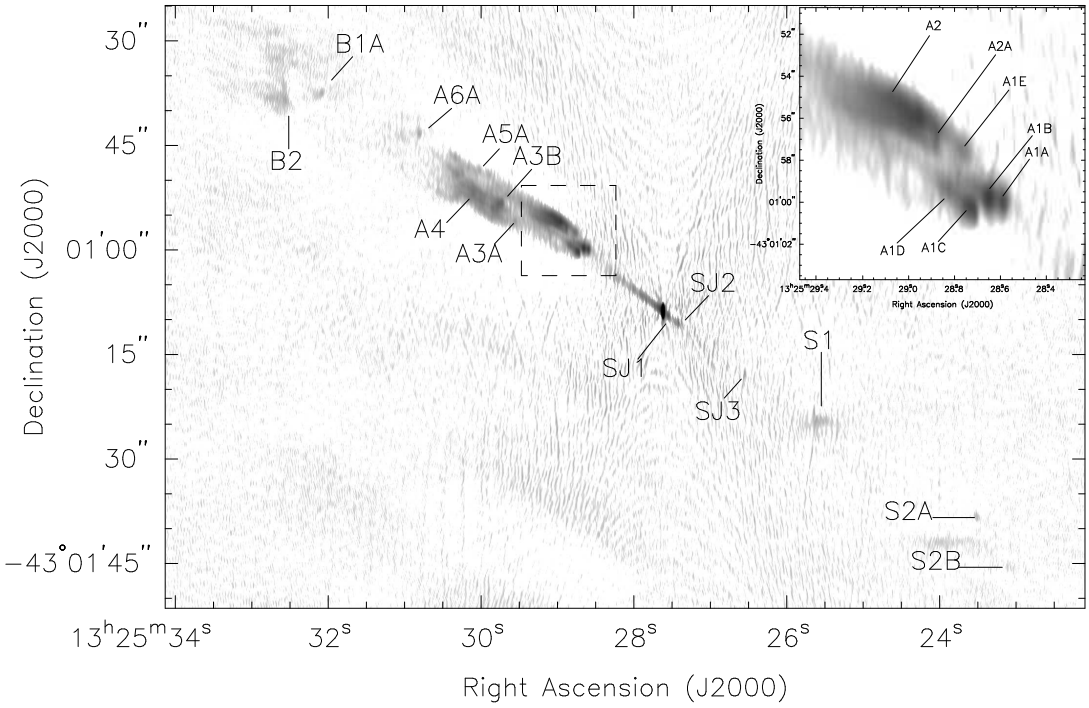

Figure 5.1: Stacked 8.4 GHz A-configuration radio image of the inner jet in Cen A showing the jet and counterjet with the 19 radio knots labelled as well as the A2 diffuse region. The dashed box indicates the location of the insert panel (top left), which shows the A1 and A2 groups of knots. In both the main image and the insert, black corresponds to 0.1 Jy beam^{-1}; however, white corresponds to 0.07 mJy beam^{-1} and 0.2 mJy beam^{-1} respectively. The beam is 0.2×0.8 arcsec.

et al. (2003). The radio data were translated to the published coordinates for the core of Cen A (Ma et al. 1998) in the uv plane using *uvfix* and *puthead*. The radio jet with all the radio knots labelled is shown in Figure 5.1; this image is the combination of all the 8.4 GHz radio images, individually scaled by the weighted mean of the rms background.

Cen A has also been observed in the X-ray with *Chandra* 10 times since 1999 (observations summarized in Table 5.2). These X-ray data span 8 years and were taken in such a way that the jet is unaffected by the chip gaps or the read-out streak of the core. With the high resolution provided by *Chandra*, these well sampled data give us a unique opportunity to study the temporal properties of the jet and its knots. The most recent data, taken in 2007, were part of a *Chandra* Very Large Program (VLP: P.I. R.P. Kraft), consisting of 6×100 ks observations, giving a combined livetime of 719 ks when merged with the earlier data. A summary of the reduction processes is given in Sivakoff et al. (2008) and Hardcastle et al. (2007b). These VLP data have been used thus far to study the X-ray binaries in Cen A (Jordán et al. 2007; Sivakoff et al. 2008; Voss et al. 2009), the properties of its hot gas (Kraft et al. 2008), its interaction with the intracluster gas (Croston et al. 2009) and of its jet (Hardcastle et al. 2007b; Worrall et al. 2008). The merged X-ray data set, in the energy range 0.4 – 2.5 keV, is shown in Figure 5.2 with the X-ray knots labelled.

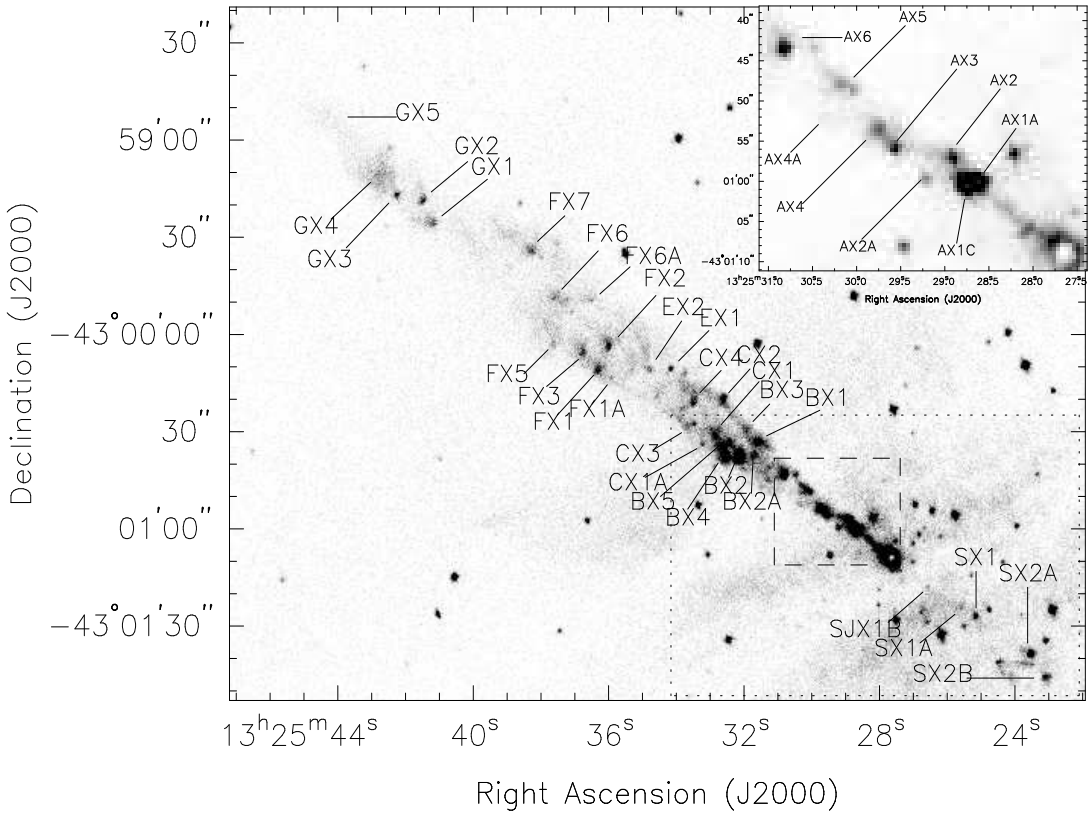

Figure 5.2: X-ray image of the jet in Cen A with all 40 detected X-ray knots labelled. The X-ray image is in the energy range 0.4 – 2.5 keV and shows only the portion of the data which includes the jet and counterjet. The dotted line indicates the extent of the radio jet shown in Figure 5.1 and the dashed line indicates the position of the insert (top left), which shows the A group of X-ray knots. In the larger image, black corresponds to 28 counts/pixel (0.4 – 2.5 keV) and in the insert, black corresponds to 150 counts/pixel (0.4 – 2.5 keV). In both images, white corresponds to 0 counts/pixel. In both images, the pixel size is 0.07 arcsec/pixel.

X-ray spectra were extracted for each of the jet knots (see Section 5.3) and the diffuse regions in the jet, using the CIAO task *specextract*, which also calculated the response files, while *psextract* was used to extract the spectra of all the point sources in the field for a comparative sample (Section 5.3.4). As some of the jet knots are clearly extended in the X-ray data (and I wanted to compare with other more extended jet features), I used *specextract* (appropriate for extended sources) for all of the jet knots for consistency; however, I used *psextract* for the comparison sample, as it consisted entirely of unresolved point sources. As the jet knots are compact sources embedded in the diffuse jet and lobe material, local, on-source annular regions were used for the background subtraction. The spectra were then binned to 20 counts per channel after background subtraction, ignoring the first 28 channels that correspond to energies below 0.4 keV. The X-ray fitting was carried out using XSPEC 11.3 in the energy range 0.4 – 7.0 keV where the *Chandra* response is well calibrated. In this analysis, *Chandra* data processing was done using CIAO version 3.4 and CALDB version 3.3.0.1.

Table 5.1: Radio Observation Details

Frequency (GHz)	VLA Config.	Date	Program ID*	Dynamic Range (arcsec)	Res. (mJy/beam)	rms Noise
4.8164	A	28-Oct 1983	AB0257	18300:1	1.23 × 0.33	0.042
4.8164	A	16-Mar 1986	AF0113	6570:1	1.41 × 0.36	0.264
4.8851	A	18-Dec 1992	AK0316	27300:1	1.63 × 0.38	0.025
4.8851	A	07-Jun 2007	AG0754	14800:1	1.58 × 0.38	0.349
8.4399	A	02-Jan 1991	AB0587	91800:1	0.78 × 0.20	0.071
8.4601	A	03-Mar 2002	AH0764	95700:1	0.76 × 0.20	0.067
8.4601	A+PT	02-Jun 2003	AH0813	32300:1	0.79 × 0.21	0.233
8.4601	A+PT	14-Dec 2004	AH0855	77300:1	0.76 × 0.19	0.082
8.4601	A+PT	18-Feb 2006	AH0892	67500:1	0.65 × 0.15	0.103
8.4601	A	04-Jun 2007	AG0754	92200:1	0.82 × 0.23	0.069
8.4061	A	20-Dec 2008	AG0798	78800:1	0.82 × 0.21	0.069
22.4851	A	16-Jun 2007	AG0754	14800:1	0.72 × 0.19	0.457
	B	21-Dec 2007				

*Observations with ID beginning AH were taken as part of a monitoring program (P.I. M.J. Hardcastle), which was continued by me (ID beginning AG).

Table 5.2: X-ray Observation Details

Obs. (#)	Date	Detector	Exposure (s)
0316	05-Dec 1999	ACIS-I	26493
0962	17-May 2000	ACIS-I	36505
2978	03-Sep 2002	ACIS-S	44589
3965	14-Sep 2003	ACIS-S	49518
7797	22-Mar 2007	ACIS-I	96888
7798	27-Mar 2007	ACIS-I	90839
7799	30-Mar 2007	ACIS-I	94783
7800	17-Apr 2007	ACIS-I	90843
8489	08-May 2007	ACIS-I	93936
8490	30-May 2007	ACIS-I	94425

5.3 Results

These radio and X-ray data allow me to analyse the temporal behaviour of the knots in Cen A's jet. I first consider whether the knots are really jet related or whether some of them are coincidentally positioned foreground or background objects (Section 5.3.1). Next, in Section 5.3.2, I examine the multi-frequency radio and X-ray data to determine whether iC emission is significant in the jet knots before establishing the proper motions of the knots in Section 5.3.3. I then consider the radio, polarisation, and X-ray variability of the knots (Sections 5.3.4 and 5.3.5). I also measure the radio spectral indices, X-ray spectral indices and X-ray/radio flux density ratio to determine the broad spectra of the knots (Sections 5.3.6 and 5.3.7). Combining these properties provides evidence to test models for particle acceleration in the jet. I also investigate whether any of the knot properties depend on the position of the knot in the jet, following up previous work by Hardcastle et al. (2007b) and Worrall et al. (2008).

I combined all of our 8.4 GHz radio data and all the X-ray observations to make deep, high dynamic range, radio and X-ray maps shown in Figures 5.1 and 5.2. These maps allowed me to make a definitive list of all the radio and X-ray knots in the jet. The 19 radio knots investigated in this work are mostly those defined by Hardcastle et al. (2003) with the addition of two knots, located downstream of the previously detected A1 knots. These knots were present in previous observations but were considered to be diffuse downstream emission. However, in the more recent observations, they appear much more compact, so have been designated A1D and A1E and are investigated in this work. In the 8.4 GHz radio maps, where the resolution is 0.8×0.2 arcsec, I find bandwidth smearing significantly affects knots beyond 140 arcsec which is beyond the F-group of X-ray knots so does not affect the radio knots in the A-configuration maps. I also note that the radio jet is within the primary beam of the VLA at all of our observed frequencies so primary beam attenuation is not corrected for. Time-averaging smearing is also not significant at these scales. I examined maps which extend to the inner edge of the inner lobes (including the B-array VLA data of Hardcastle et al. 2003) and find no evidence of additional compact radio knots beyond the B-group radio knots already detected. Bandwidth smearing does not affect these images until beyond the jet. The absence of knots at large distances from the nucleus will be discussed further in section 5.4.1.

The 40 X-ray knots used in this work are a combination of those identified by Kraft et al. (2002) and Hardcastle et al. (2003) with independently selected central coordinates. The coordinates were optimised so that a fixed radius of 3 arcsec includes the majority of the emission associated with the knot and is larger than the PSF in all observations. In the cases where the knot is close to the pointing centre this fixed radius slightly overestimates the flux from the knot including some background, although the majority of this excess is removed during the background subtraction. I compared the X-ray flux of our fixed-radius regions with the flux measured using regions with radii that were modelled using the PSF and found that the changes in the light curve reflected the changes in the PSF between observations. I therefore used fixed radii regions to eliminate this effect. I used

annular background regions to account for spatial variations in the underlying diffuse emission. I have investigated the systematic uncertainty due to variation in the surface brightness within these annular background regions and find that the contribution to the X-ray flux density is negligible (less than 1%), even in the worst affected knots. As AX1A and AX1C are very close together, manually sized regions were used, adjusted to include as much of the emission as possible, without including too much emission from the neighbouring knot. The spectral properties of all the X-ray knots are shown in Table 5.3.

5.3.1 Point Source Contamination

Kraft et al. (2002) investigated whether some of the apparent X-ray knots could be low mass X-ray binary (LMXB) in Cen A or background AGN. They simulated point sources using the first of the *Chandra* X-ray data sets used in this work (ObsID 0316) to determine whether the compact knots were point-like enough in their observations to be confused with LMXBs and found many that are consistent. They also considered the radial surface-density distribution of X-ray sources in Cen A, concluding that they expected ~ 3 of the knots or sources to be X-ray binaries within Cen A unrelated to the jet.

It has been shown (see Fabbiano (2006) for a review) that a significant fraction of LMXBs observed in early-type galaxies with *Chandra* are associated with globular clusters (GCs). It has recently been confirmed that 41 X-ray point sources in our data are associated with GCs within Cen A (Woodley et al. 2008; Jordán et al. 2007; Voss et al. 2009). I examined *Spitzer*/IRAC 3.6- and 8-μm IR maps (Hardcastle et al. 2006b) to check for IR counterparts to our jet knots, which would indicate a coincident globular cluster and found a compact IR source for GX3. I also checked the GC catalogue by Jordán et al. (2007) and found a GC coincident with GX3 only. Although we do not expect all LMXBs to reside in GCs, we can rule out any knot that has IR emission as likely to be a LMXB due to its association with a probable GC. Since $>$70% of all LMXBs identified with GCs lie in the redder GCs, those with a higher (near-solar) metal abundance (e.g., Woodley et al. 2008; Posson-Brown et al. 2009), the latter would actually be more readily detectable in the near-IR *Spitzer*/IRAC observations than in ground-based optical images.

The X-ray knots AX2A and SX1 are compact X-ray sources with no compact or diffuse radio emission, and they lie outside the boundaries of the detected radio jet and counterjet. However, the X-ray flux variability of AX2A is substantially different from that of SX1; it was undetected until 2007 when it flared to 3 nJy, and it has not varied significantly since. AX2A may therefore be a genuine new X-ray knot rather than a LMXB so is considered further in Section 5.4.

Contamination from background AGN is highly unlikely; these would appear as point sources, possibly with optical counterparts and generally with flatter X-ray spectra (typical unabsorbed X-ray AGN spectra have spectral indices 1.09 ± 0.08, Mainieri et al. 2007). I have also calculated

Table 5.3: Spectral Properties of the X-ray Knots

Knot	Flux Density† 1 keV (nJy)	Spectral Index α_X	N_H ($\times 10^{22}$ cm^{-3})
AX1A	10.65 ± 1.64	1.08 ± 0.04	0.51 ± 0.02
AX1C	21.43 ± 2.97	1.06 ± 0.04	0.52 ± 0.02
AX2	9.29 ± 0.54	0.77 ± 0.07	0.55 ± 0.04
AX2A	3.19 ± 0.96	0.56^*	0.084^*
AX3	4.02 ± 0.39	0.78 ± 0.16	0.40 ± 0.07
AX4	4.98 ± 0.28	0.94 ± 0.16	0.45 ± 0.04
AX4A	0.30 ± 0.03	0.48^*	0.084^*
AX5	6.60 ± 0.39	0.59 ± 0.09	0.59 ± 0.08
AX6	9.39 ± 0.35	0.51 ± 0.06	0.59 ± 0.05
BX1	3.69 ± 0.27	0.83 ± 0.11	0.12 ± 0.02
BX2	19.39 ± 0.97	0.63 ± 0.02	0.11 ± 0.01
BX2A	1.44 ± 0.12	0.58 ± 0.12	0.084^*
BX3	2.02 ± 0.17	1.40 ± 0.35	0.15 ± 0.10
BX4	4.94 ± 0.30	0.91 ± 0.06	0.084^*
BX5	3.06 ± 0.23	1.13 ± 0.15	0.10 ± 0.03
CX1	2.36 ± 0.20	1.23 ± 0.17	0.084^*
CX1A	0.97 ± 0.07	2.20^*	0.084^*
CX2	3.59 ± 0.37	0.79 ± 0.06	0.12 ± 0.04
CX3	0.82 ± 0.09	0.63^*	0.084^*
CX4	1.09 ± 0.18	0.54 ± 0.20	0.084^*
EX1	0.78 ± 0.14	0.60^*	0.084^*
EX2	0.58 ± 0.06	0.60^*	0.084^*
FX1	1.92 ± 0.11	0.77 ± 0.12	0.084^*
FX1A	0.34 ± 0.09	0.70^*	0.084^*
FX2	2.11 ± 0.25	1.28 ± 0.27	0.12 ± 0.09
FX3	1.36 ± 0.16	1.06 ± 0.30	0.084^*
FX5	0.52 ± 0.03	1.20^*	0.084^*
FX6	0.77 ± 0.08	1.56^*	0.084^*
FX6A	0.47 ± 0.06	1.20^*	0.084^*
FX7	1.25 ± 0.18	1.07 ± 0.17	0.084^*
GX1	1.10 ± 0.15	0.87 ± 0.19	0.084^*
GX2	1.00 ± 0.13	0.63 ± 0.14	0.084^*
GX3	1.21 ± 0.30	1.24 ± 0.50	0.15 ± 0.11
GX4	0.61 ± 0.10	1.20^*	0.084^*
GX5	0.13 ± 0.03	1.20^*	0.084^*

† weighted mean 1 keV X-ray flux density of the six 100 ks observations taken in 2007

* parameter fixed as too faint for joint fitting; the spectral index is an average of the local fitted indices and the nH is the Galactic value.

the number of AGN we expect in the jet using the background $logN - logS$ method described by Moretti et al. (2003) and find only a 33% chance of finding an AGN in our jet.

5.3.2 Emission Mechanism

Using the three frequencies of radio data observed in 2007, I fitted a synchrotron model to the radio emission from the inner A-group knots, which allowed me to predict the X-ray emission we would expect from synchrotron self-Compton emission (SSC) and from the inverse Compton scattering of the cosmic microwave background (iC/CMB) and of the galaxies optical star light (iC/SL). I used the sizes measured by Tingay & Lenc (2009) to estimate the emitting volume of the stationary knots, which appear to have compact cores, combining the volumes of the substructures in the cases of A1A and A2A. I used the radio fluxes measured from radio maps matched to the resolution of the 22 GHz data (1.80×0.40 arcsec) and the weighted mean, 1 keV X-ray flux density from the six 2007 X-ray observations. At equipartition magnetic field strengths, the observed X-ray emission is much greater than the predicted X-ray flux density, which is dominated by SSC for the stationary knots, A1A, A1C, and A2A. If we assume the SSC model is dominant in the X-ray regime, the magnetic field strengths required for the observed X-ray emission, for the stationary knots, are found to be a factor of 500 – 600 weaker than the equipartition values. This is also true for the knots that are not detected by Tingay & Lenc (2009) and that are unresolved in our data; a limit on the sizes was used to find the limits on the equipartition magnetic field strengths and the internal energies and pressures of the knots. Table 5.4 shows the radius of the emitting volume, the radio and 1 keV X-ray flux densities, the equipartition magnetic field strengths, B_{eq}, and the required magnetic field strength for SSC dominated X-ray emission, B_{SSC}, of the A-group of knots.

In other features, such as the hotspots in FR II radio galaxies, the magnetic field strengths required for the observed X-ray are only slightly less than the equipartition values (factors of 3 – 5 Hardcastle et al. 2004; Kataoka & Stawarz 2005). The much larger departure from equipartition required for iC to be significant in the Cen A knots, combined with the steepness of the spectral indices for these knots ($\alpha_X > \alpha_{iC} \sim 0.5$) suggest that iC emission is not significant in the X-ray for the majority of the jet knots. I therefore assume that the X-rays from the knots are synchrotron emission in the remainder of this work.

Using the equipartition magnetic field strengths, I was able to estimate the total energy density of the knots and find that the internal pressures of these knots are of the order of 1 nPa, which is much higher than the pressure in the surrounding diffuse material. This is also evident from the higher surface brightness of the knots, which is directly related to the internal energy of the knot material.

Table 5.4: Emission model parameters for the inner A-group knots

Knot	Radius	Flux Density				X-ray lifetime	Magnetic Field Strength		Pressure
		4.8 GHz	8.4 GHz	22 GHz	1 keV X-ray	τ_{1keV}	B_{eq}	B_{iC}	P_{int}
	(pc)	(mJy)	(mJy)	(mJy)	(nJy)	(yrs)	(nT)	(nT)	(nPa)
A1A/AX1A	2.017	20.10 ± 4.26	12.27 ± 2.04	5.32 ± 0.98	10.65 ± 1.64	5.61	69.3	0.119	0.955
A1B	<6.586	46.92 ± 5.58	29.44 ± 2.67	13.83 ± 1.28	< 19.38	17.63	32.3	≥ 0.125	0.937
A1C/AX1C	2.293	41.45 ± 5.66	25.33 ± 2.70	12.32 ± 1.30	21.43 ± 2.97	4.86	76.3	0.135	1.546
A2A/AX2	2.727	37.13 ± 5.82	15.57 ± 2.78	6.32 ± 1.33	9.29 ± 0.54	7.46	57.3	0.119	0.871
B1A/BX2	15.300	2.64 ± 0.64	0.93 ± 0.61	-	19.39 ± 0.97	30.89	22.2	0.038	0.131

5.3.3 Proper Motions

The results of Hardcastle et al. (2003) were based on only the first two epochs of radio data. With these data, they were able to establish the bulk flow speed of the jet (~ 0.5 c) and also demonstrated that some of the knots move along the jet (A1B, A2, A3B, and A4) while others were consistent with being stationary (A1A, A1C, A2A, A3A, A5A, B1A, SJ1, SJ2, SJ3, S2A, and S2B). With the multi-epoch data we can improve on the accuracy with which the proper motions are measured. I used maps with a matched resolution of 0.80×0.20 arcsec for these measurements.

The approach to fitting speeds I used was to use a modified version of the shift-and-fit method of Walker (1997), as used in a simpler form by Hardcastle et al. (2003). As I have more than two maps I attempted to fit a velocity vector, consisting of an angular speed and direction, to each knot. (More complex models are not justified by the quality of the data.) To use the shift-and-fit method I selected a reference image at a particular epoch. For a given trial value of the angular velocity vector the appropriate part of this image was then shifted (using a bicubic polynomial interpolation) to the position implied for all the other epochs, the difference of the two images was formed, and the contribution to χ^2 was calculated using estimates of the local on-source noise in both maps. The total χ^2 over all non-reference images was minimized using a Markov-Chain Monte Carlo (MCMC) algorithm (briefly described by Croston et al. 2008) which allows the efficient exploration of parameter space. A Jeffreys (scale-invariant) prior was used for the magnitude of the angular velocity vector to avoid bias towards large values. In principle this algorithm also allows an efficient determination of the uncertainties (formally the credible intervals) on the fitted parameters. However, I found that these errors were dominated by the systematic uncertainties due to the choice of reference image; in weak knots a fortuitous distortion in the reference image can give the appearance of a proper motion that is not actually present. To remedy this I carried out the fits for a given knot using each of our seven radio images in turn as the reference image. Only knots in which consistent, non-zero motions are detected for all choices of the reference image are considered to be moving. In these cases our best estimate of the speed of the motion is the median of the Bayesian estimates of the angular speed for each choice of reference image, and the range of speeds returned under different choices of the reference image gives us an estimate of the systematic uncertainties in the result. Where the velocities are inconsistent, I have taken the upper limit to be the largest velocity in this range.

This approach detected apparent motions in 6 of the radio knots as well as in the diffuse material downstream of the A2A knot (the regions downstream of A2A are labelled A2B, A2C and A2D in the following sections). To check that these motions are sensible, I verified the motion visually. I found that two of these knots, A1C and A2A are actually stationary and attribute the detected proper motion to the evolution of the knot; A1C appears to grow downstream while A2A's front edge is stationary with diffuse material appearing to break off and move downstream from this knot towards A2B, A2C and A2D [all consistent with Hardcastle et al. (2003)]. The visual checks also

rule out the apparent motion in SJ1 as its proximity to the bright core means its shape is affected by artefacts. I was left with three knots moving in the jet: A1B, A1E, and A3B (their velocities are plotted as vectors in Figure 5.3 and shown in Table 5.5 with the limits for the stationary knots). This approach is more robust that of Hardcastle et al. (2003) as it considers all seven epochs of our radio data, reducing the errors on the proper motions of the moving knots, and I have constrained the speeds of the other knots that had no previously detected proper motions.

It is worth noting here that A1B and A1E have no X-ray emission associated with them while the region A3B can be described as consisting of three sub-regions in the radio with a diffuse X-ray counterpart, possibly breaking any correlation between compact, radio-only knots and proper motions.

I have also determined the directions of travel for the well-established moving knots (Table 5.5). The axis of the inner, hundred-parsec-scale jet has a position angle (PA) of 54.1° east of north from the core and its extrapolation provides a good estimate of the axis of much of the outer jet. The moving knots all travel in directions eastward of this axis. They also all belong to the A-group of knots and, on closer inspection of this section of the jet, I find that it also deviates eastward to greater PAs. The jet axis in this region has a PA of 62.3°. Two of our three knots move in a direction consistent with this, within 3σ errors. If the jet motion was purely conical, expanding directly away from the core, the motion of the knots should be radial, but I find that the directions of motion do not match the knot PAs. The ridge line through the A-group knots may actually follow the regions of highest radio surface brightness, swinging from north of PA 54.1° at A2 to south of it at A3 and A4. In Figure 5.4, deviations of the knot PAs from 54.1° are plotted against distance from the core, clearly showing this swing in the ridge line. I can only conclude that the fluid flow along the jet is neither laminar nor in a straight line away from the core, consistent with a complex flow.

The median speeds of the remaining radio knots are generally smaller than the speed of the slowest knot with a definite detection, A1E, ($v/c \sim 0.34$), but in most cases the upper limits exceed $0.5c$, allowing the knots to be moving. Better data are required to establish whether this is the case, so for the remainder of this work, I have considered those with well established velocities to be moving, those with low median speeds ($< 0.2\,c$), and low upper limits to be stationary and I classify the others as inconclusive. In Table 5.5 these classifications are indicated by Y, N, and I respectively. I discuss the association between the motions of the knots and their other properties in Section 5.4.1.

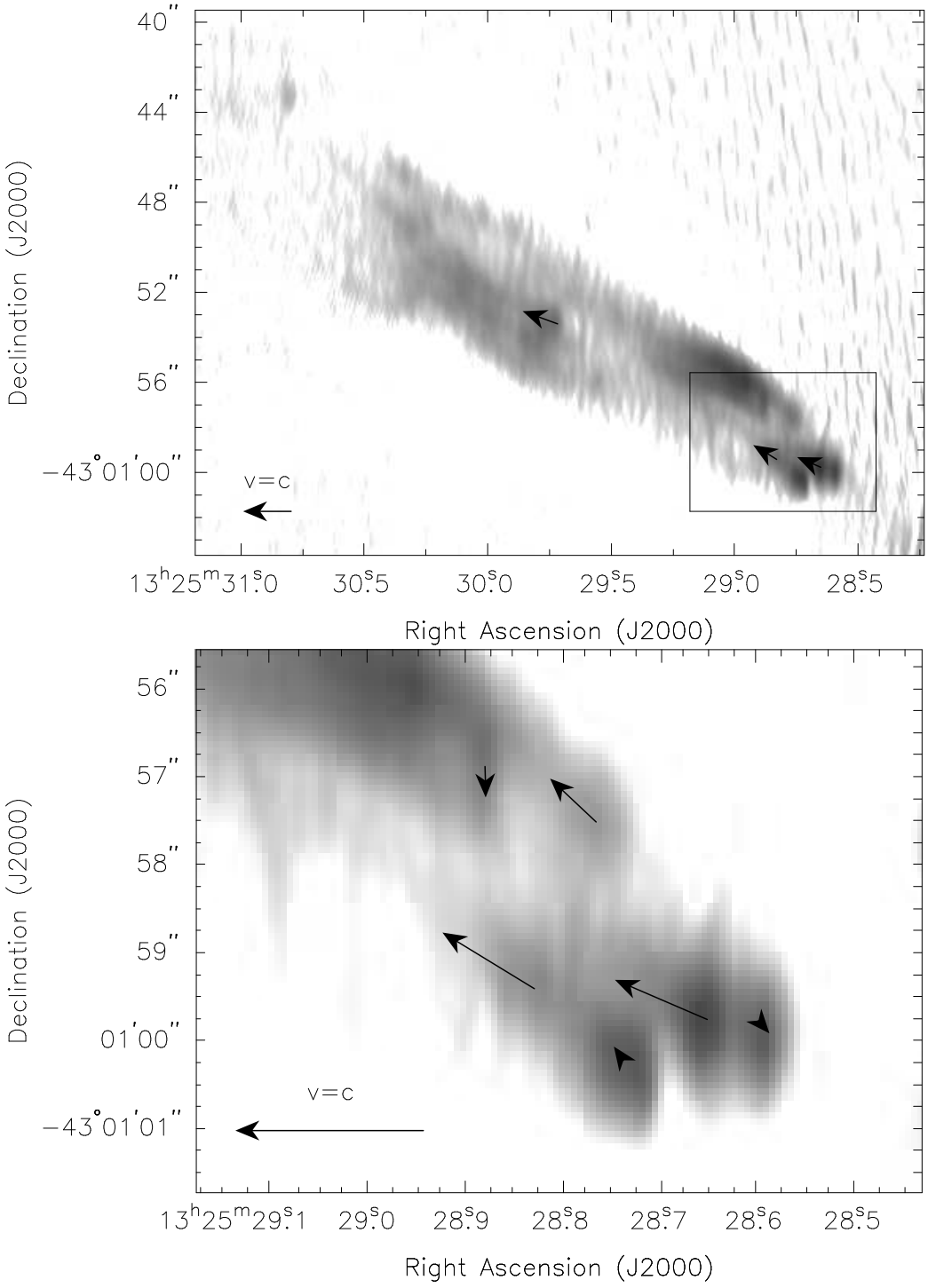

Figure 5.3: Velocity vectors for the moving knots in Cen A, with the composite 8.4 GHz radio map convolved to a resolution of 0.8×0.2 arcsec showing the well-established velocities for the A-group of radio knots (top panel) and the mean velocities of the A1 and A2 knots is shown in the bottom panel. The region included in the bottom image, is shown with the box on the top image. Black corresponds to 0.1 Jy and white corresponds to 0.1 mJy in the top panel and 0.5 mJy in the bottom panel. A velocity of $1c$ is shown in the bottom left corner of these images.

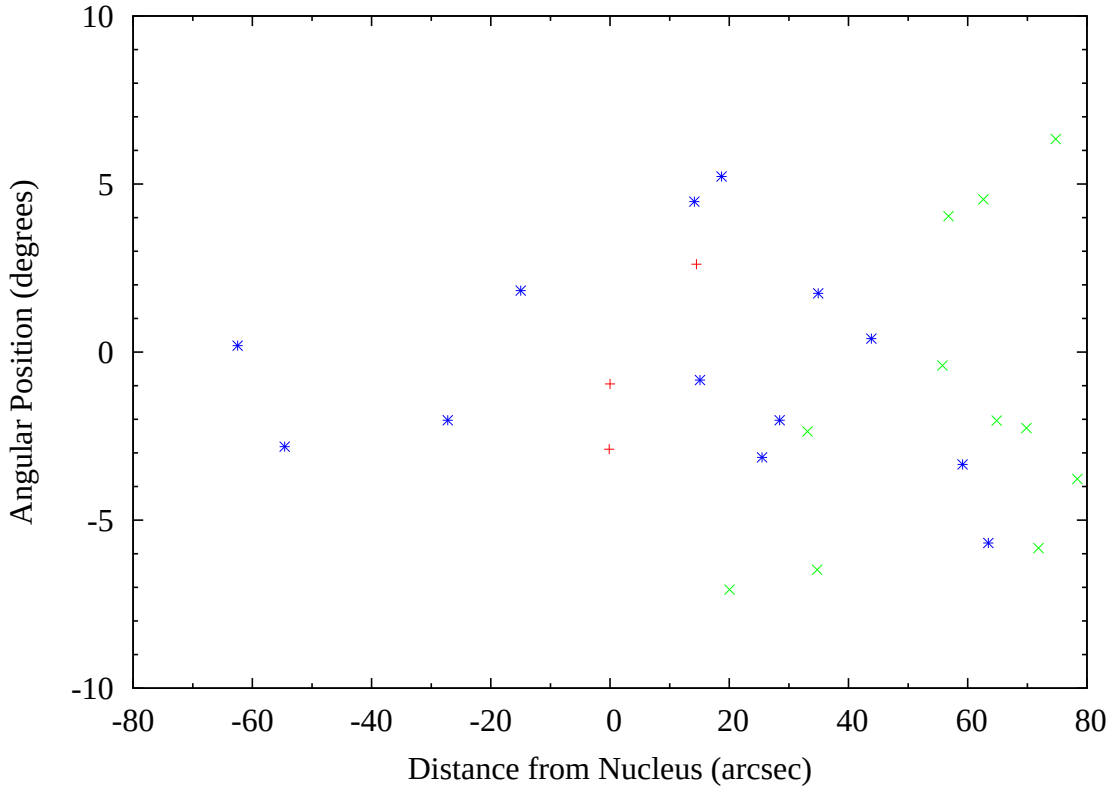

Figure 5.4: The offset between the position angle of the jet in Cen A ($54°$) and the transverse position of the radio knots (red points), X-ray knots (green points) and radio-X-ray knots (blue) as a function of the projected distance from the nucleus for the knots in the jet and counterjet (negative distances). The knots do not appear to lie at the PA $54°$ for the entire length of the jet.

5.3.4 Flux Variability

Another important property that can be measured from our multi-epoch radio and X-ray data is flux variability. Utilising the multi-epoch 8.4 GHz radio data, we have been able to monitor the radio flux variability over the last 17 years. I used radio maps of matched resolution (0.80×0.20 arcsec) for this analysis to eliminate any flux variation due to varying PSF. The initial light curves for the radio knots showed a systematic variation of up to $\pm 10\%$ common to all knots, which I attributed to differences in the flux calibration, so I normalised the radio fluxes using a weighted mean of the brightest compact knots (A1A, A1B, A1C, A2A, A3B, and A4). I chose these knots as the others are weaker and/or more diffuse, and would therefore introduce large uncertainties in our weighted mean value. I also excluded SJ1, which shows strong variation since 2004. The core was not used in this normalisation as it is known to vary. The normalised fluxes are shown in Table 5.6. I fitted a constant to these radio light curves and minimized the χ^2 to determine whether the radio fluxes are at all variable, with a reduced $\chi^2 < 2.80$ being the threshold for a constant radio light curve (99% confidence for 6 d.o.f.). I detect radio variability at this confidence level in 9 of the 19 radio knots (49.4%). The light curves of the varying radio knots that have X-ray counterparts are shown in Figures 5.5 and 5.6 and Figures 5.7 and 5.8 show the radio light curves for the radio-only knots.

The most noticeable variation is in the counterjet knot SJ1, which has increased in flux by a factor of 3 since 1991. Three of these radio variable knots show fluctuations on yearly time scales (B2, S1 and S2A), while the remaining four split into two increasing (A1C and SJ1) and two decreasing (A1B and A1D) gradually over the 17 years.

I also considered variability in the 4.8 GHz data but as I have only 4 observations over 24 years at irregular intervals, I cannot comment on any short-term variability. These light curves are all broadly consistent with the 8.4 GHz light curves, examples of which are shown in Figures 5.7 and 5.8. Accepting a reduced $\chi^2 < 3.78$ as a constant light curve (99% confidence for 3 d.o.f.) I find 6 radio knots with some degree of variability at 4.8 GHz, half of which are also variable in the 8.4 GHz data, which is not to say that those which are apparently constant do not agree with the 8.4 GHz variability. This is particularly evident in the SJ1 data, as only two observations overlap with the time baseline of the 8.4 GHz data; these data could be interpreted as decreasing while the 4.8 GHz data increases, but there are too few data to draw any conclusion from the 4.8 GHz light curves. The dynamic ranges of these 4.8 GHz data are much lower than our 8.4 GHz data so they are subject to much larger systematic errors.

I also detected long- and short-term X-ray variability. Combined with the radio variability, this allows us to search for any changes in beaming or particle acceleration properties. I carried out a joint fit to all 10 X-ray datasets for all the X-ray knots, fitting a single photon index and column density for each knot, but allowing the normalisations to vary in order for any variations in the flux to be detected. The normalisations were converted to 1 keV flux densities so the light curves could be plotted including 1σ errors. I then fitted a constant to the light curves, minimizing the χ^2 to find the best fit. I was able to carry out a joint fit for 24/40 of the X-ray knots, 22 of which have a $\chi^2_{red} < 1.10$. For the remaining knots where there were not enough counts for spectral fitting, I firstly determined whether there was a 3σ detection of the knot considering each observation separately. Where the knot was detected, I fixed the photon index to the average photon index of the nearby knots. The flux was then determined from the background subtracted counts and the model count rate from XSPEC. Where the knot was not detected, the 3σ limit was calculated.

Knots with a $\chi^2_{red} > 2.41$ (99% confidence for 9 d.o.f.) are considered variable in the X-ray. I find that 5 X-ray knots vary (12.5%) in addition to AX2A and SX1 which are candidate LMXBs (see Section 5.3.1), 3 of which have varying radio counterparts. The light curves for the X-ray varying, X-ray-only knots are shown in Figure 5.9 while those that have radio counterparts are shown in Figures 5.5 and 5.6.

To test whether the variability behaviour is consistent with, or different from that of the non-jet point sources, I also extracted spectra for the off-jet point sources. I manually checked the results of *celldetect* to remove detections of image artifacts and the jet knots before running the same fitting using annular background regions. I detected 423 point sources, only 183 of which are detectable in all observations due to changes in the pointing and roll angle of *Chandra* for each observation causing slightly different regions of the sky being imaged. Although the PSF changes across the

image for each observation, these point sources all lie within 5.5 arcmin of the core, so the changes in the PSF of each knot are not significant. However, the changes in PSF between each observation are more significant and are reflected in the light-curves causing an apparent flux variability. To remove this effect from the light-curves, I have used regions with a fixed radius of 3 arcsec for these point sources. I fitted a constant to the X-ray light curves of these point sources and found 105 show some degree of variability with 99% confidence (56.8 ± 10.3% of the point sources), a factor of 3 more than the jet X-ray knot population. In 41 instances, the background annulus contained zero counts so these were re-extracted with a larger background annulus to determine a limit. If I consider the point sources within 3.5 arcmin of the core, which limits us to the length of the jet from the core, I find that 76/141 point sources vary (53.9 ± 8.7%) and if I reduce the sample further to include only those on the East of the image, so those within 45° of the jet PA, I find that 33/71 point sources vary (46.5 ± 5.7%). The effect of the PSF is not significant in these samples and I can conclude that we are looking at a group of different objects in the jet and not just coincidentally positioned X-ray binaries in most cases.

5.3.5 Polarimetry

If there is compression/rarefaction of the plasma in the knots, we would expect changes in the polarisation, as the magnetic field is assumed to be frozen into the plasma. I can therefore use the polarisation data to investigate any link between the activity of the knots with physical changes in the plasma. The co-added, matched resolution, Q and U images at 8.4 GHz were used to make the deep magnetic field vector map shown in Figure 5.10. I made the individual Stokes Q and U maps using the AIPS task *imagr*. There are artifacts around the core for all epochs, which I attribute to the limited accuracy of the correction calculated for the 'leakage' terms determined by *pcal*; only the 2003 data set is unusable due to higher noise in these Stokes Q and U images. The overall direction of the magnetic field is down the jet, consistent with what was found by Hardcastle et al. (2003) with no obvious change in the knots.

I detected a 3σ variation in residual maps of the Q and U Stokes parameters (2007-2002) in the A1 and A2 groups. The diffuse emission further down the jet also showed evidence of low level variability, but as this was uniform across the region it was attributed to differences in the flux calibration. I proceeded to measure the fluxes in Q, U and I for these data, normalising as described in Section 5.3.4. Comparing the total intensity (I), the angle of polarisation ($\theta = \frac{1}{2}\arctan(U/Q)$, in this work I use the Q/U ratio as an approximation to this relationship) and the degree of polarisation ($p = \sqrt{Q^2 + U^2}/I$) allowed us to identify variations due to a change in the total intensity, the polarisation intensity, the polarisation position angle or those due to the proper motion of the knot.

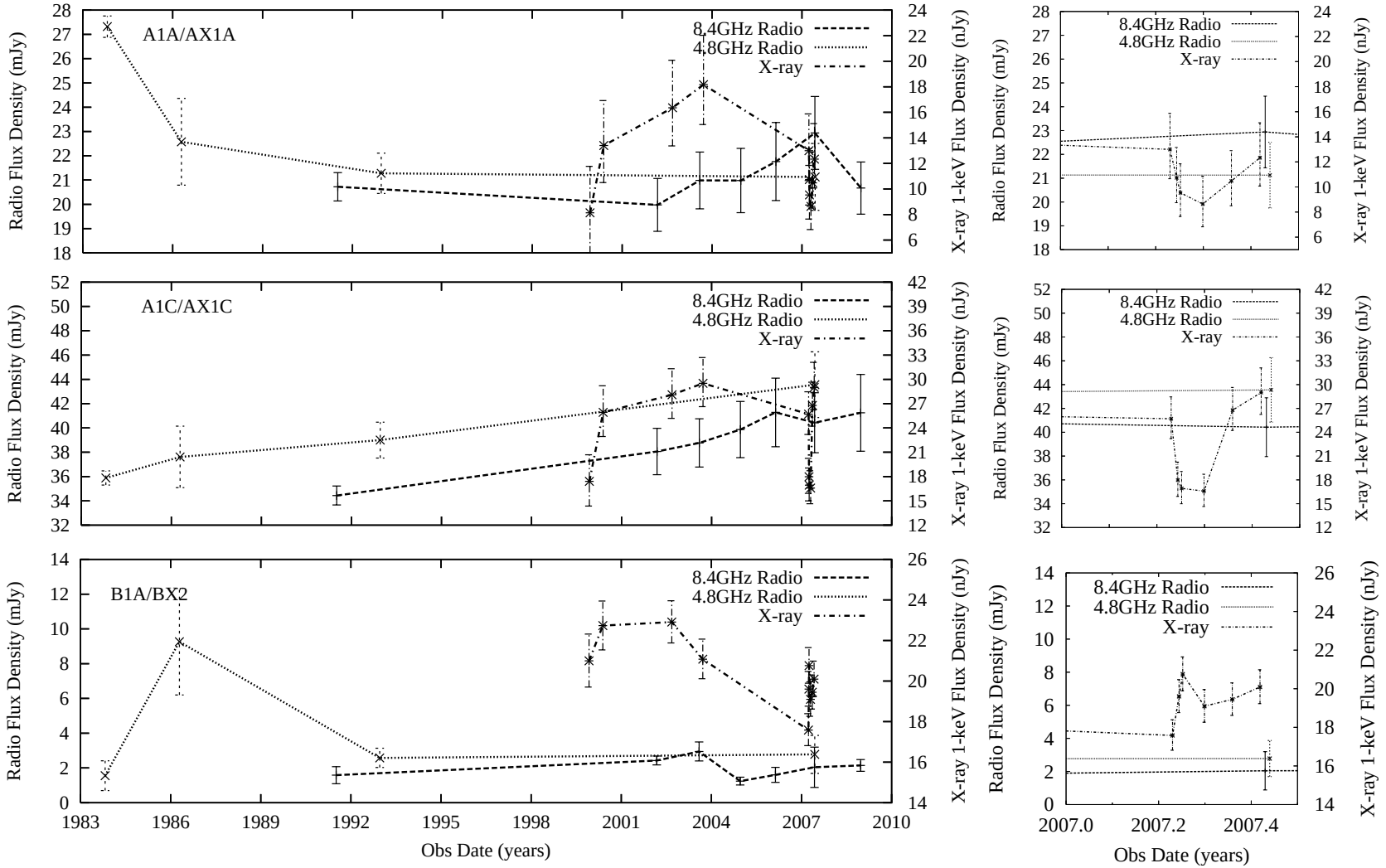

Figure 5.5: X-ray and 8.4 GHz radio light curves for the radio knots in Cen A, which show some degree of radio or X-ray variability AND have X-ray counterparts; A1C (top panel), B1A, (middle panel) and B2 (bottom panel). The right hand images are cropped to highlight changes in the X-ray flux density during the *Chandra* VLP observations.

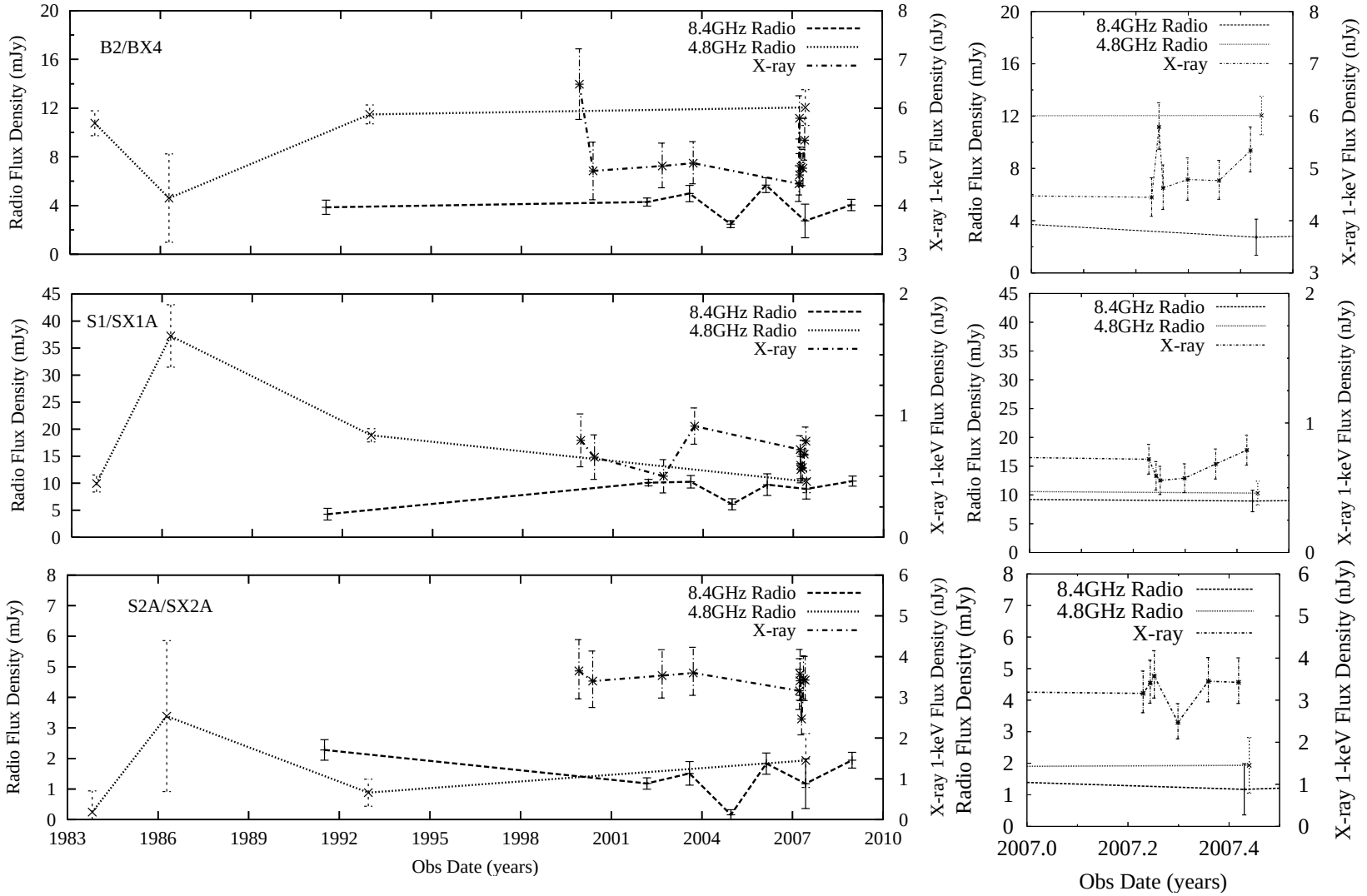

Figure 5.6: X-ray and 8.4 GHz radio light curves for the radio knots in Cen A, which show some degree of radio or X-ray variability AND have X-ray counterparts; S1 (top panel), S2A (middle panel) and S2B (bottom panel). The right hand images are cropped to highlight changes in the X-ray flux density during the *Chandra* VLP observations.

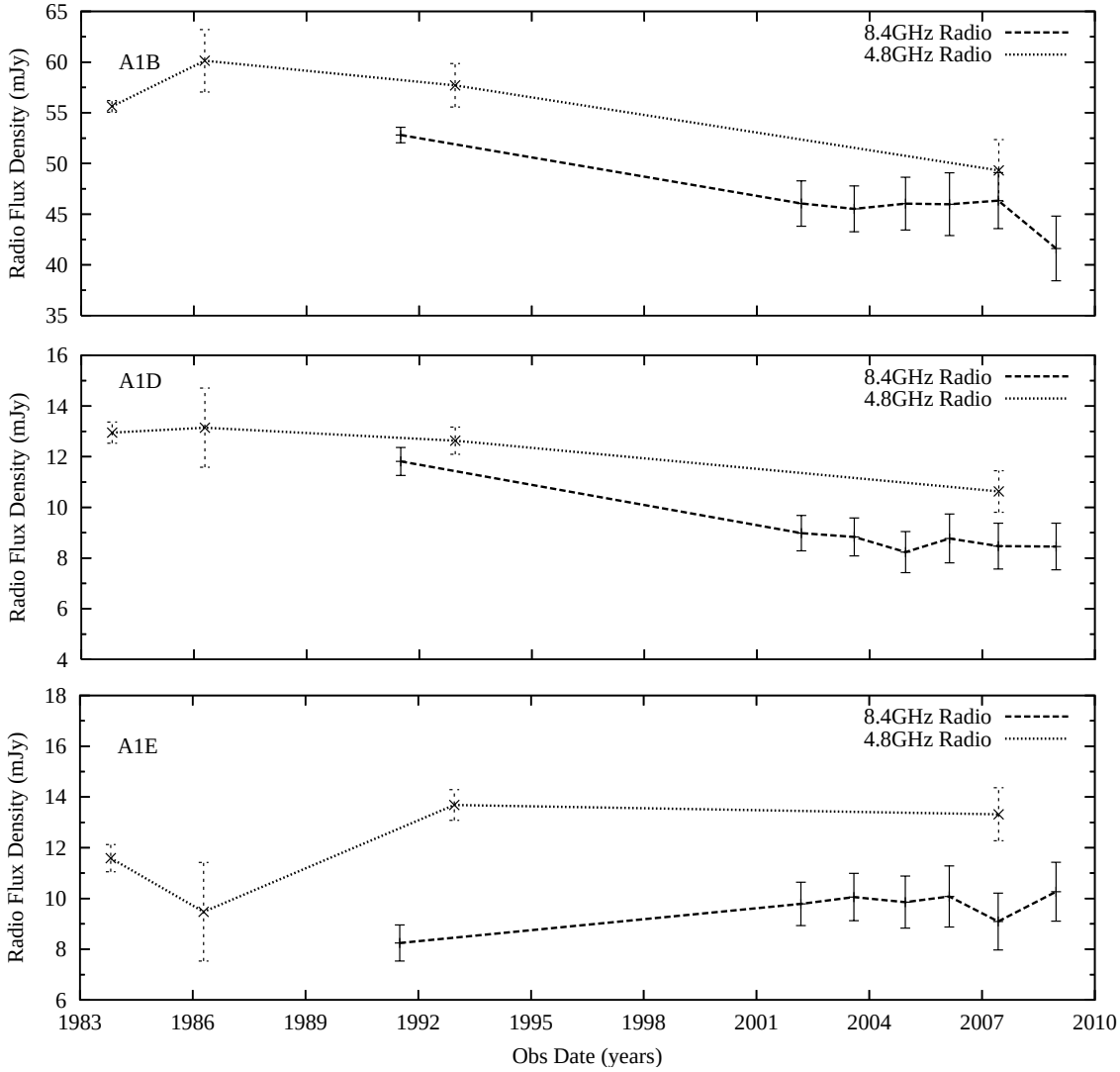

Figure 5.7: 8.4 GHz and 4.8 GHz radio light curves for the radio-only knots in Cen A; A1B (top panel), A1D (middle panel) and A1E (bottom panel).

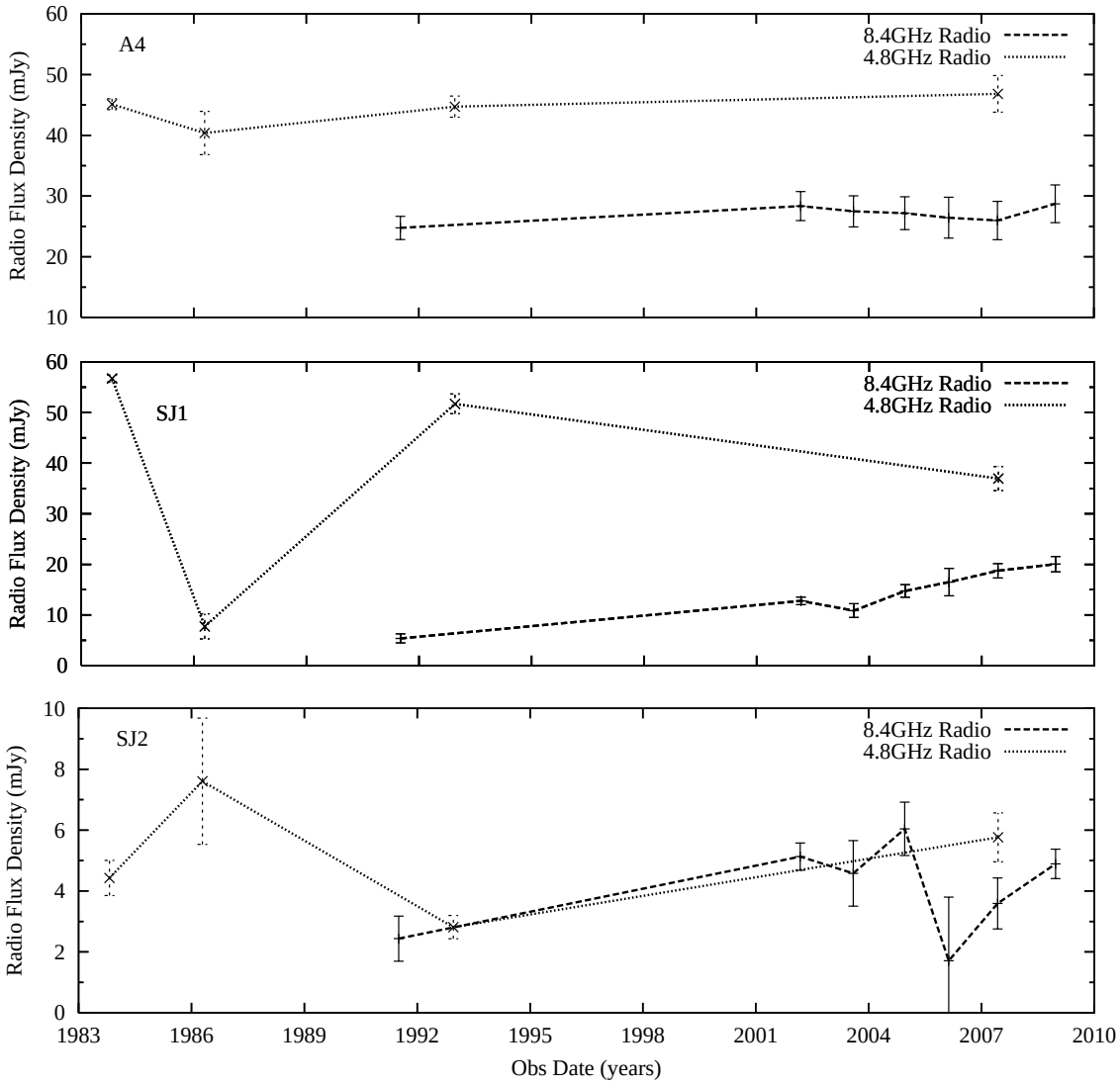

Figure 5.8: 8.4 GHz and 4.8 GHz radio light curves for the radio-only knots in Cen A; A4 (top panel), SJ1 (middle panel) and SJ2 (bottom panel).

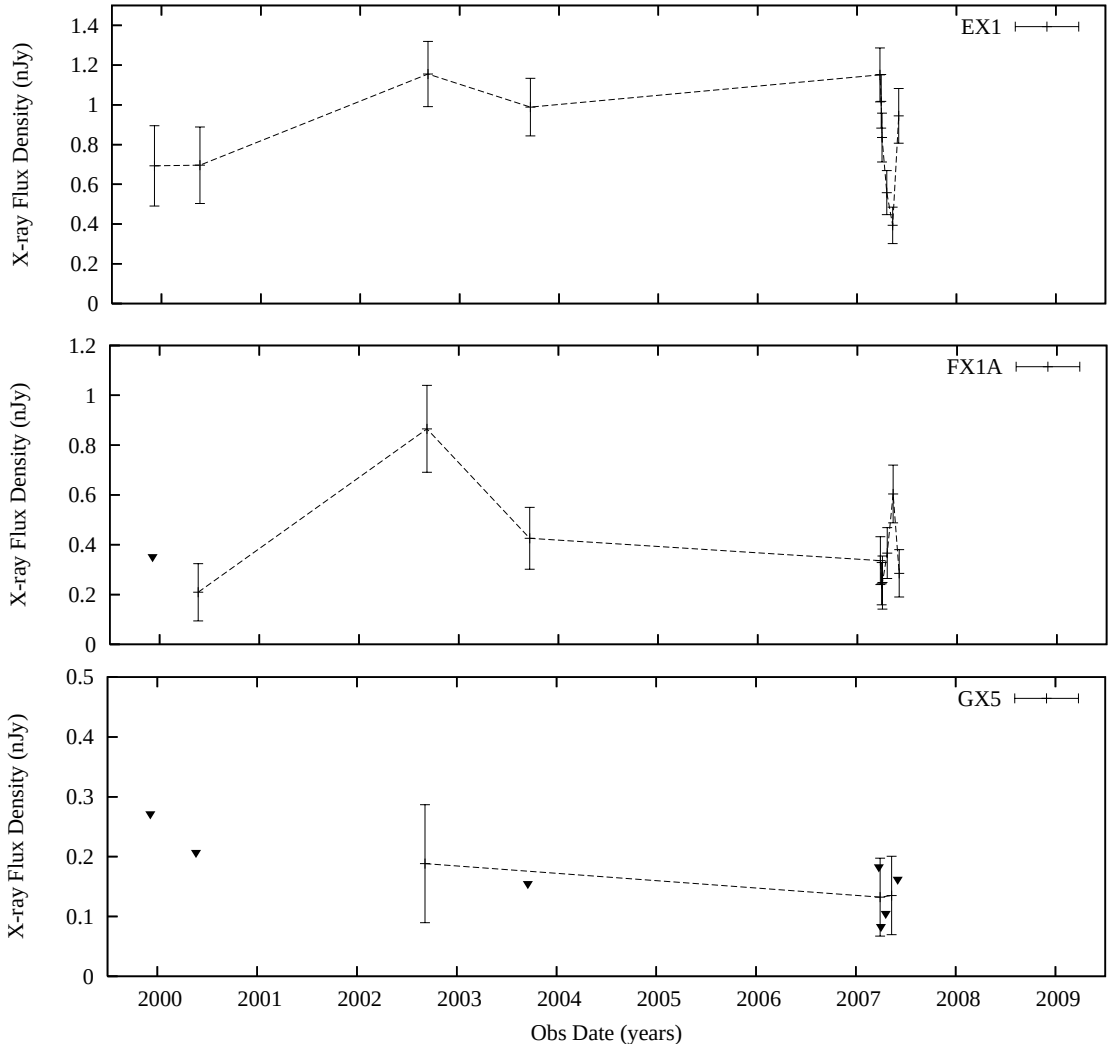

Figure 5.9: X-ray light curves for the X-ray only knots in Cen A, which show signs of variability; AX2A (top left), EX1 (top right), FX1A (bottom left) and GX5 (bottom right).

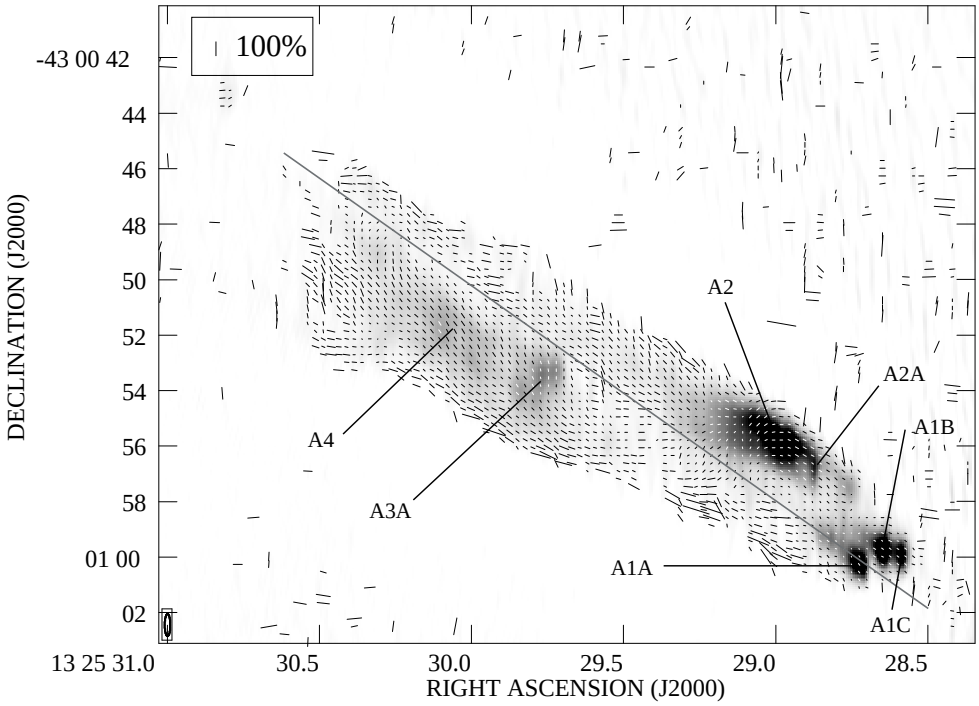

Figure 5.10: Radio polarisation in the inner jet of Cen A showing the direction of the magnetic field vectors on a composite, Stokes I, 8.4 GHz radio map. The radio image is in the range 0.1 – 0.01 Jy and a vector 0.56 arcsec long represents 100%. The solid grey line highlights a possible axis of null polarisation discussed in Section 5.3.5.

As previous described, the majority of knots show only a low level variation in total intensity; however 4/19 show changes in the degree of polarisation only; B2, SJ1, and S2B are shown in Figure 5.12, and 6/19 show changes in the angle of polarisation including two knots which show changes in both (Figure 5.13 shows the variations in polarisation angle for A1A, A1D, and A2A). It is necessary to consider that one of these knots is moving, A1B, so the observed changes in polarisation could be due to this movement. Excluding this moving knot, the number of knots varying only in the angle of polarisation is unchanged, and I have one knot, A1A, which is changing in both. These results are compared with the total radio and X-ray flux variations in Section 5.3.8.

The A2 diffuse knot (A2B, A2C, and A2D) shows a change in the Q/U ratio indicating a change in the polarisation angle across the region; however, there are no X-ray counterparts for any of these sub-regions and their radio spectral indices are consistent ($\alpha_{4.8}^{8.4} = 1.13 \pm 0.10$, 1.01 ± 0.16 and 1.22 ± 0.27 respectively). Only the central section, A2C, varies in total radio intensity but the entire region appears to be moving downstream away from A2A so this change in polarisation may be due to the motion of this diffuse material. The detected variation in the A1 group knots A1A, A1B

and A1C, cannot be attributed to motion of the knots, as only A1B is moving. In this instance, the observed polarisation variability may be explained by compression and rarefaction of the knot material. There is no perpendicular field structure across any of the knots, which might be expected in a local shock model; however, this might be masked by complicated jet polarisation structure. However, there are systematic misalignments between the jet PA and the magnetic field associated with some jet features, notably A2 and A3B, which are highlighted in Figure 5.11 which shows the difference between the polarisation angle and the PA of the jet. Clarke et al. (1992) found only a modest rotation measure (RM) in the inner lobes and jet, and only a slight change in the Faraday corrected magnetic field vectors in their 6cm (4.8 GHz) radio data, so I do not expect the effect of RM to to be significant. I will discuss the effect of various models on the polarisation of the knots further in Section 5.4.

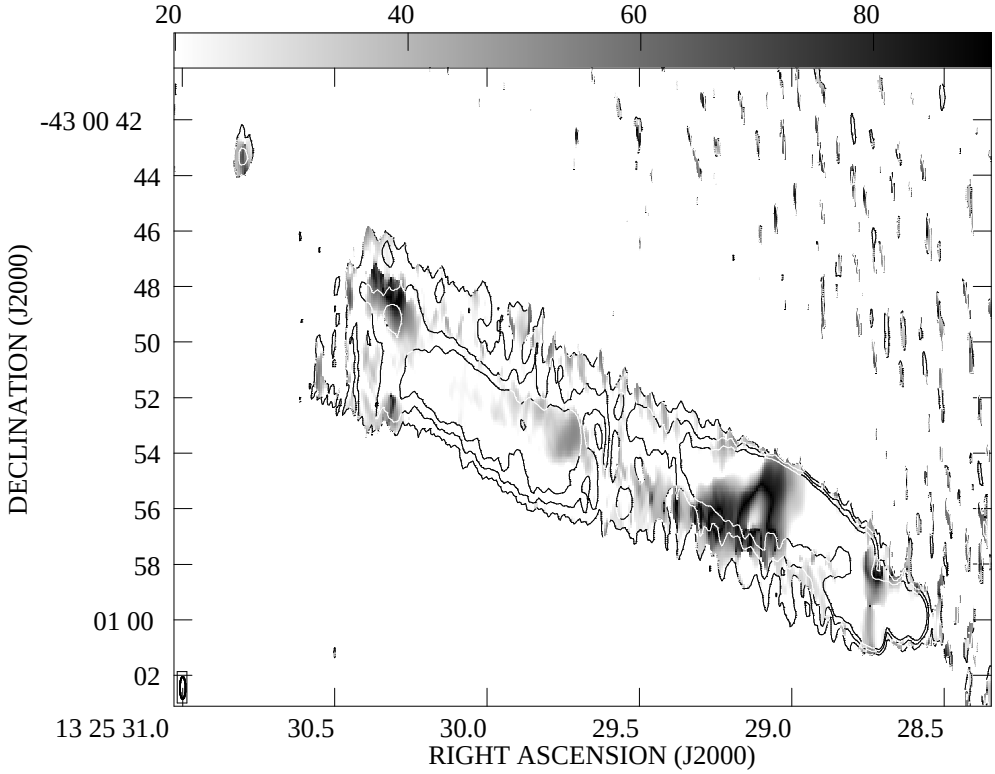

Figure 5.11: Greyscale map of the inner jet of Cen A showing the difference between the direction of the magnetic field vectors and the jet PA (51.4°) with total intensity contours at 3, 8 and 16 times the rms of the composite, Stokes I 8.4 GHz radio map, 8.23×10^{-5} Jy beam^{-1}. The greyscale image is in the range 20 – 90 degrees to emphasise structure in which the B-vectors are substantially misaligned with the jet.

It is interesting to note that there is an apparent null in the polarisation which crosses the diffuse material of the A-group region, indicated on Figure 5.10 by a grey solid line. This line extends to the core directly through the inner hundred-parsec-scale jet suggesting that it is associated with magnetic fields originating in or close to the core. This line also splits the bright A1 and A2 complexes from the A3 and A4 complexes. This could plausibly be a result of a helical jet field structure.

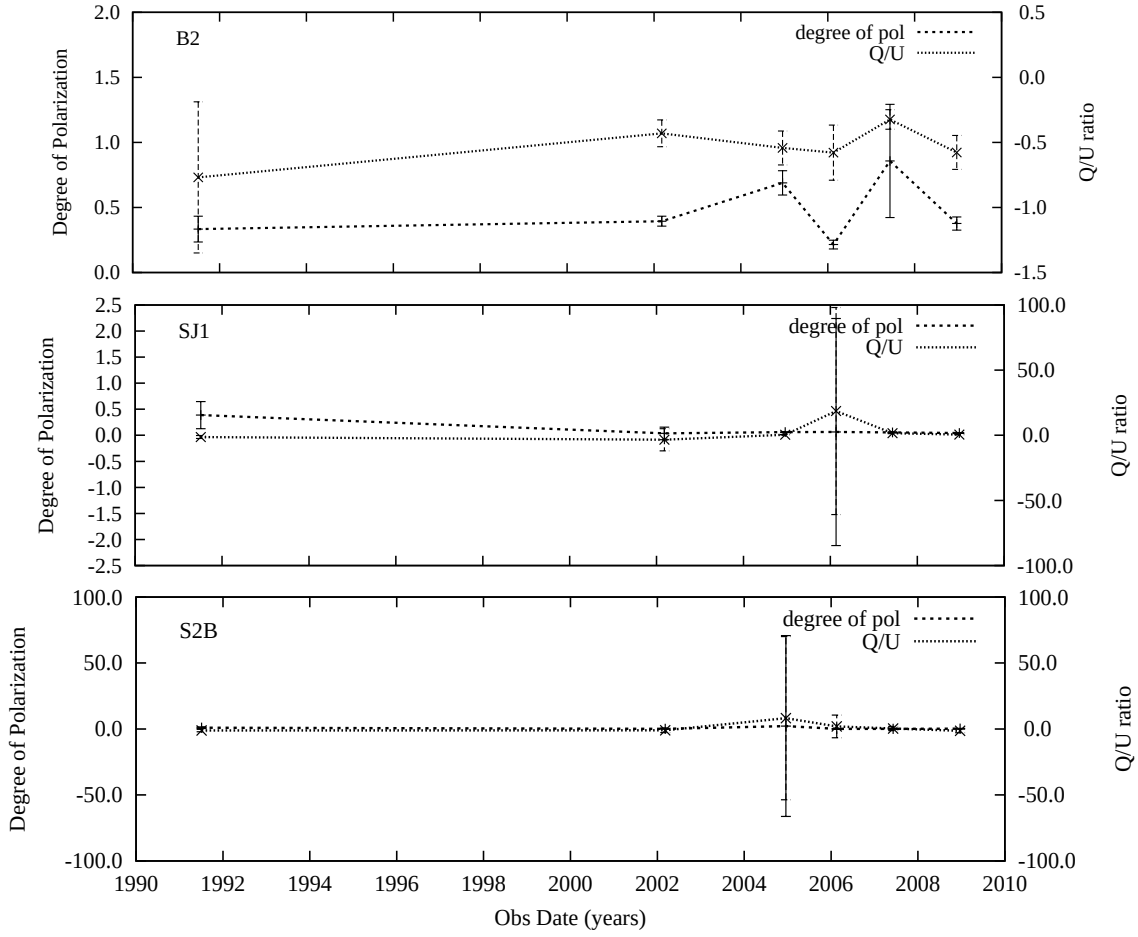

Figure 5.12: Plots for the radio knots in Cen A, which show significant variability in the degree of polarisation only with the degree of polarisation (dotted lines) and the angle of polarisation (dashed lines): B2 (top panel), SJ1 (middle panel) and S2B (bottom panel).

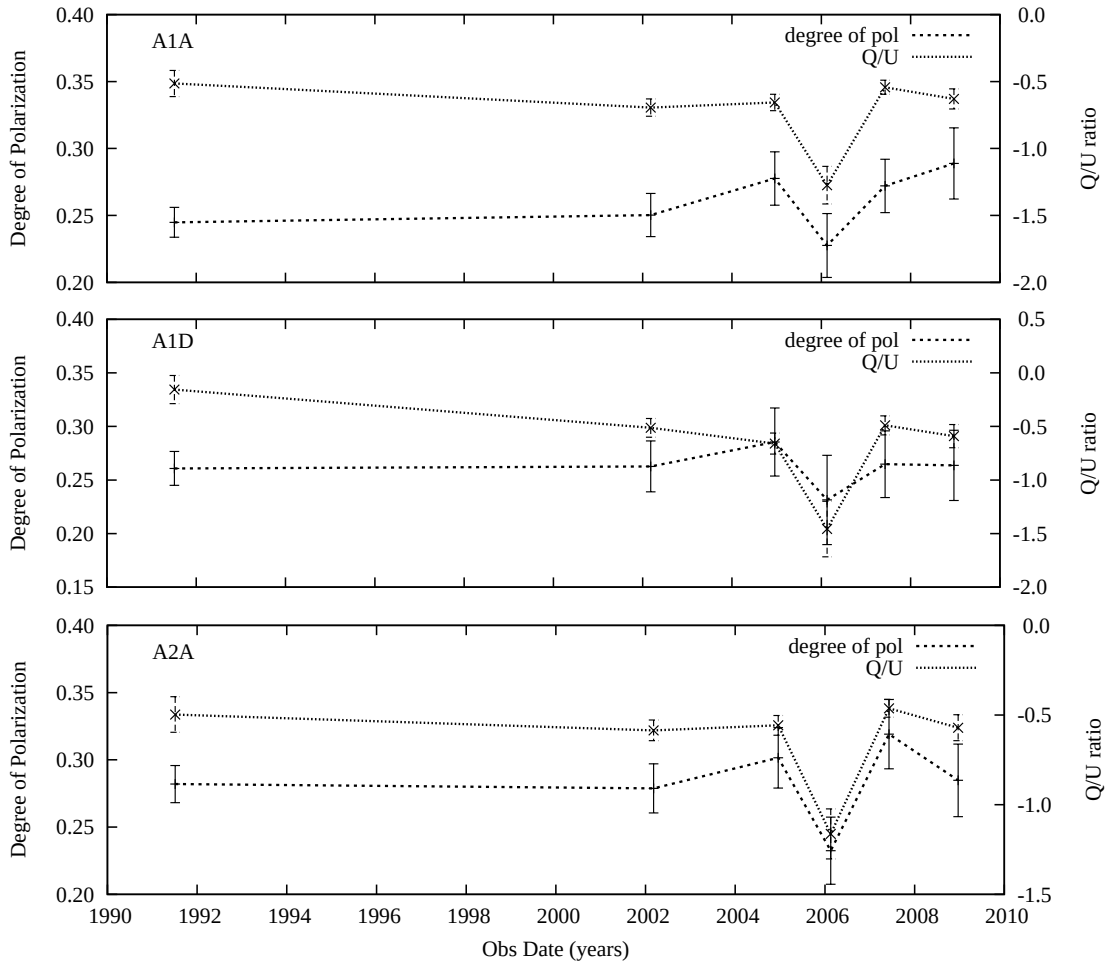

Figure 5.13: Plots for the stationary radio knots in Cen A, which show significant variability in the angle of polarisation only with the degree of polarisation (dotted lines) and the angle of polarisation (dashed lines): A1A (top panel), A1C (middle panel) and A2A (bottom panel).

5.3.6 Spectral Indices

Hardcastle et al. (2007b) and Worrall et al. (2008) investigated the X-ray spectrum of the jet in the longitudinal and transverse directions, respectively. Hardcastle et al. (2007b) showed that the inner jet is dominated by knots, consistent with local particle acceleration at shocks, while further down the jet steeper-spectrum diffuse X-ray emission is more dominant. Worrall et al. (2008) found that in the knotty region beyond the A1 and A2 complexes and within 66 arcsec of the core, the weighted X-ray spectrum of knots closer to the jets axis (the 'inner spine') is harder than that further off axis (the 'inner sheath') ($\Delta\Gamma = 0.31 \pm 0.07$). This was interpreted as evidence that the jet speed is higher closer to the axis, with more kinetic energy available for producing a harder X-ray spectrum.

Here I compare the radio and X-ray spectral indices of individual knots with their longitudinal and transverse positions. I have measured the radio spectral indices for all of the radio knots; however, only 14 have well established indices. In the X-ray, I have fitted spectral indices to 26 of the X-ray knots. I compared the X-ray spectral indices ($\alpha_X = \Gamma - 1$) of the jet-side knots, irrespective of whether they have counterparts, as a function of distance from the core (Figure 5.14), and of the offset between the angular position of the knot and the jet PA of 54.1° (Figure 5.15).

All the X-ray spectral indices were consistent with those determined by Hardcastle et al. (2007b) and consistent with synchrotron emission with $\alpha_X > 0.5$; the distances from the core of each knot were also consistent owing to the knot selection process. When I compared the measured spectral indices of all the radio and X-ray knots to the offset between the jet PA of 54.1° and the angular position of the knot (Figure 5.15), I find a continuous distribution of X-ray spectral indices with no statistically significant correlation according to both a KS and a Wilcoxon-Mann-Whitney test, although these tests do not take account of the errors on our spectral indices. I also considered the knots in each of the regions defined by Hardcastle et al. (2007b) and find no correlation in these regions either. These comparisons will be discussed further in Section 5.4.4.

I have also found the weighted mean of the spectral indices for all of the knots within the regions defined by Worrall et al. (2008) as the 'inner-spine' and 'inner-sheath', $\alpha_X = 0.62 \pm 0.01$ and $\alpha_X = 0.89 \pm 0.05$ respectively, and agree with the findings of Worrall et al. of a harder weighted X-ray spectrum in the spine than in the sheath over the same length of jet (although $N_{\rm H}$ changes by a factor of 3, the absorption is fitted so does not affect the spectral indices). Within these regions, I have fitted spectral indices for 6/7 of those in the inner-spine; AX3, AX4, AX5, AX6, BX2, and BX5, and for 3/4 or those in the inner-sheath; BX1, BX3 and BX4. Those that are not fitted; BX2a in the spine and CX1a in the sheath, are very faint knots and as discussed in Section 5.3.1. The interpretation of these measurements is discussed in Section 5.4.4.

I also calculated the radio spectral indices between 4.8 and 8.4 GHz for all the radio knots utilising our multi-frequency 2007 radio data. Due to the low dynamic range of the 22.5 GHz map, we cannot measure fluxes for many of the knots; however, for those which are resolved, the spectral index for 4.8 – 22.5 GHz, $\alpha_{4.8}^{22.5}$, is consistent with the 4.8 – 8.4 GHz spectral index ($\alpha_{4.8}^{8.4}$). The

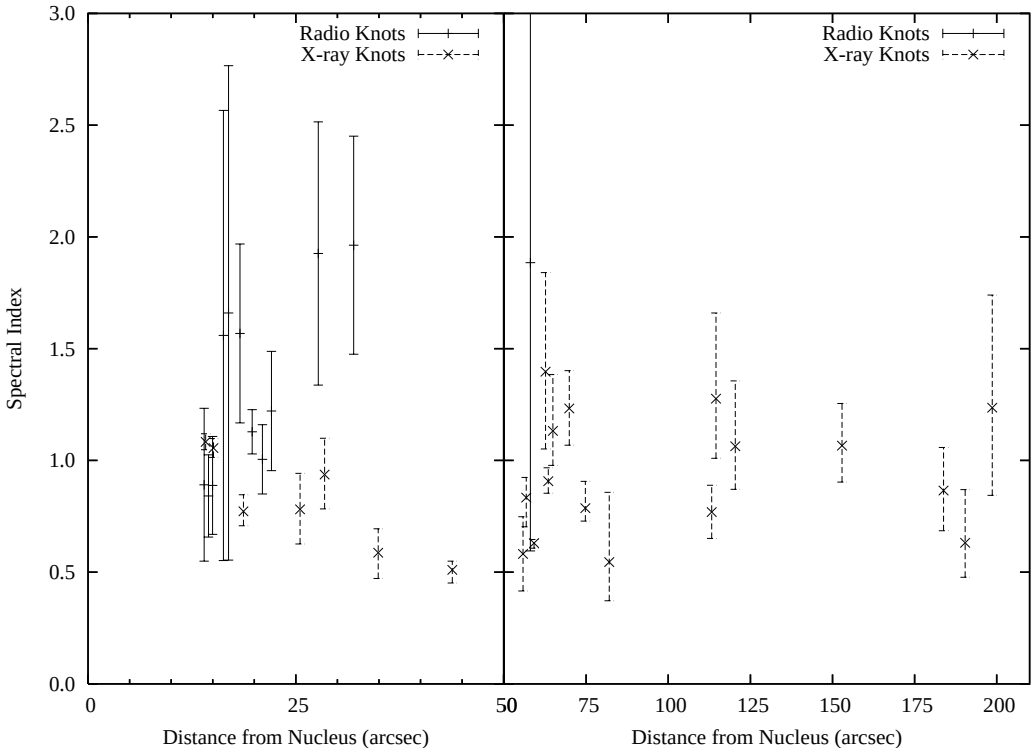

Figure 5.14: The radio spectral index, $\alpha_{4.8}^{8.4}$ (solid lines) and X-ray spectral index, α_X (dashed lines) of knots in the jet of Cen A as a function of distance from the core. The left panel shows only the inner knots (up to 50 arcsec) and the right panel shows the rest of the jet knots.

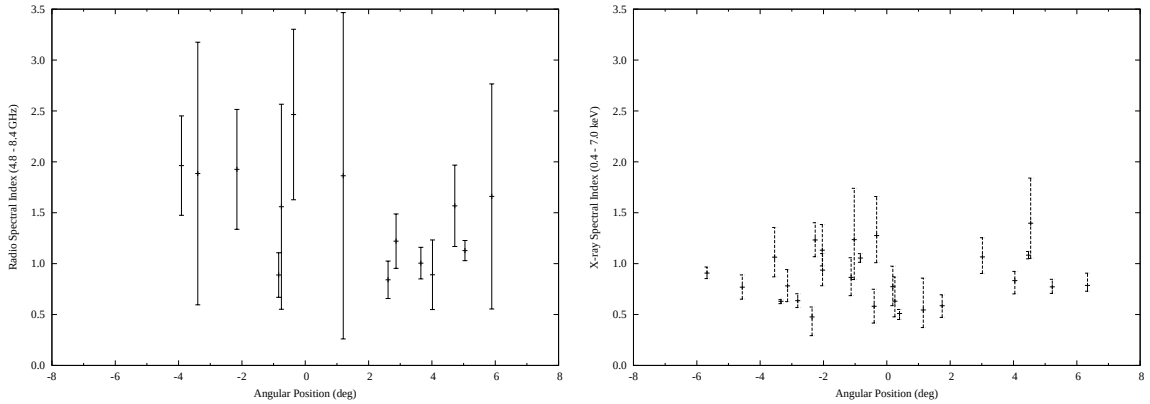

Figure 5.15: The radio spectral index, $\alpha_{4.8}^{8.4}$ (left panel, solid lines) and X-ray spectral index, α_X (right panel, dashed lines) of knots in the jet of Cen A as a function of offset between the angular position of the knot and the jet position angle of $54.1°$.

errors on these spectral index measurements are dominated by the noise in the images. These are listed in Table 5.7 with the radio and X-ray flux densities, X-ray photon indices and X-ray/radio ratios, which are discussed in Section 5.3.7.

5.3.7 Counterparts

I have identified 13 knots that are detected in both radio and X-ray: A1A and AX1A, A1C and AX1C, A2A and AX2, A3A and AX3, A3B and AX4, A5A and AX5, A6A and AX6, B1A and BX2, B2 and BX4, SJ3 and SJX1B, S1 and SX1A, S2A and SX2A, and S2B and SX2B. Each of the knots in these pairs have the same coordinates with no significant offsets; I do not consider knots with possible offset counterparts as paired, given the discussion of offsets in Hardcastle et al. (2003), who argued that the apparent offsets between the radio and X-ray knots in more distant radio galaxies are a result of an inability to resolve faint aligned radio-knot counterparts from bright downstream diffuse emission.

With the radio and X-ray data for these knots, I was able to measure the ratio of the 1 keV X-ray flux density and the 8.4 GHz radio flux density and use the median of these X-ray/radio flux density ratios to determine whether those without detected counterparts are truly without counterparts or whether the counterpart is too faint to be detected. Using the median value of the X-ray/radio flux density ratios, I predicted the flux density of the missing counterparts for the radio-only and X-ray-only knots. The median value of 1.01×10^{-6} is used rather than the mean, as the distribution of these X-ray/radio flux density ratios is not Gaussian. The measured X-ray/radio flux density ratios range from 0.07×10^{-6} to 9.44×10^{-6}. These predicted flux densities assume that all the knots have the same spectrum with consistent X-ray/radio flux density ratios. By comparing these predictions to the measured flux densities I determined whether the absent counterpart can be detected.

Out of the 6 radio-only knots, I find that all except two radio knots, A1D and A1E, should have detectable X-ray counterparts using the median X-ray/radio flux density ratio value; however, at the lower limit, only SJ1 should have a detectable X-ray counterpart. Unfortunately, SJ1 is located only 1 arcsec (~ 17 pc) from the core, so in the X-ray, the emission from the knot is contaminated by the bright core. In *Chandra* HRC observations taken in 1999 (Kraft et al. 2000), SJ1's X-ray counterpart is still unresolved from the nucleus despite the slightly higher spatial resolution. As 7/9 radio knots have detectable but unseen X-ray counterparts when the median ratio is assumed, they probably have steeper spectra than those that have detected counterparts suggesting a genuine difference in their particle acceleration properties.

When this rationale is inverted and I consider the X-ray-only knots, I find that 9/27 X-ray knots would have detectable radio counterparts at the median X-ray/radio flux density ratio and, as they are not seen, they are likely to have flatter ratios than those that do have detected counterparts. However, at the limits of the range of measured ratios, all these knots are detectable at the lower limit and not-detectable at the upper limit.

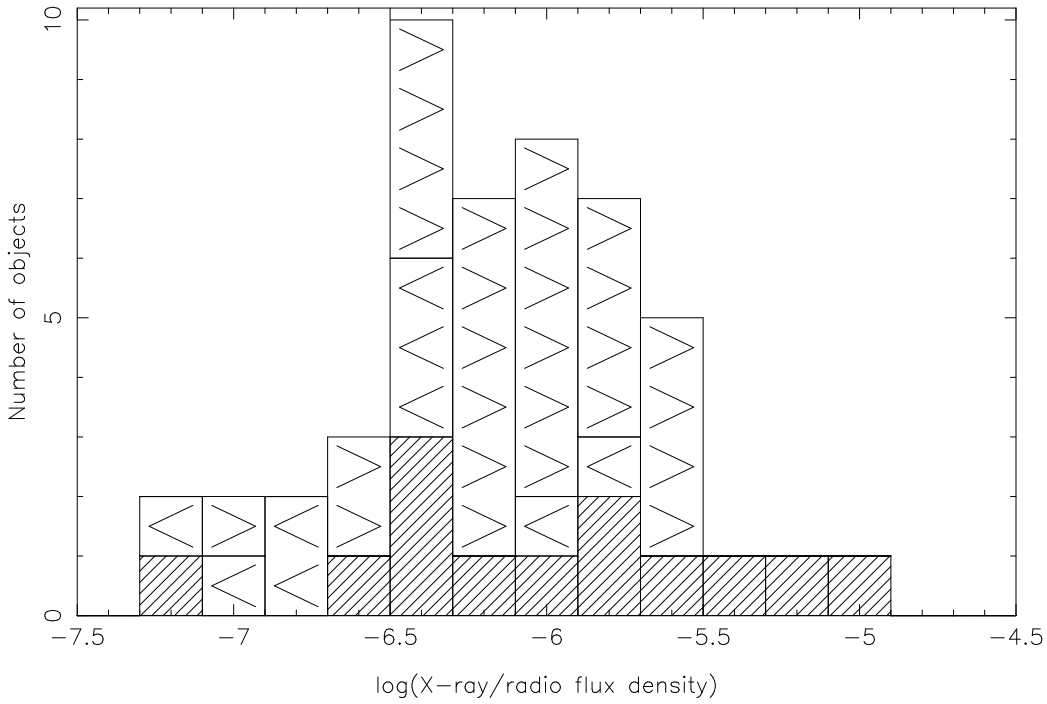

Figure 5.16: A histogram of the X-ray/radio flux density ratios for the paired knots (hashed region), the lower limits on the X-ray/radio flux density ratio for the X-ray-only knots (>), and the upper limits on the X-ray/radio flux density ratio for the radio-only knots (<) in Cen A.

If we reverse this argument and consider the X-ray/radio flux density ratio values that would be measured if the missing counterpart were at the limit of the noise in the image, I can obtain upper limits on the X-ray/radio flux density ratio for the radio-only knots and lower limits for the X-ray-only knots. In Figure 5.16, I show histograms of the X-ray/radio flux density ratios for the three populations. As the radio-only and X-ray-only knots give us limits, I find that the peaks of all three groups of knots are consistent, so I cannot rule out a single population; however, I will continue to discuss the knots in three groups and accept that many of the knots may have the same production mechanisms.

The properties of these three populations of knots are summarized in Section 5.3.8; in Section 5.4 I shall discuss current knot formation and particle acceleration models and how they explain the differences in the properties of these populations of jet knots.

5.3.8 Summary of Knot Properties

I have measured the radio and X-ray flux density variability in the knots, the polarisation variability, the proper motions and spectral properties of the 19 radio and 40 X-ray knots. Here I summarise the properties of the 13 radio knots with X-ray counterparts, the 6 radio-only knots and the 27 X-ray-only knots. The following results and groupings are summarised in Table 5.5.

Knots with Counterparts

Considering the 13 matched knots, I find that only A3B has a well determined proper motion in the radio at an apparent velocity of $v/c = 0.80^{+0.15}_{-0.02}$. Up until the radio knot A4, the knots with counterparts are likely stationary with low limits and median velocities; however, beyond A4 and in the counterjet, the velocities are inconclusive. These radio knots are generally less compact and fainter and so are more affected by artifacts.

Two knot pairs (A1C/AX1C and B1A/BX2) vary in both radio flux density at 8.4 and 4.8 GHz and X-ray flux density; of these only A1C varies in polarisation angle. The increase in radio flux density in A1C is consistent with what was seen by Hardcastle et al. (2003) and similar to the change in X-ray flux density.

None of these matched knots varies only in the X-ray, while two vary only in the 8.4 GHz radio (B2 and S2A); B2 also varies in the degree of polarisation. A1A and A3A vary in the 8.4 GHz radio data, but do not pass our requirement for significant variability in our 4.8 GHz data, while S1 varies at both 8.4 GHz and 4.8 GHz. Due to the long intervals in the 4.8 GHz data, I cannot rule out that it is consistent with the 8.4 GHz radio so only use the 4.8 GHz data to determine the spectral indices of the radio knots.

The remaining six pairs of knots vary in neither X-ray nor radio with two showing a change in the polarisation; A2A varies in the angle of polarisation and A1A varies in angle and degree of polarisation. Only two of these knot pairs are completely stable; A5A and SJ3.

Radio-only Knots

There are six radio-only knots but the motions of these are mostly inconclusive with only A1B and A1E having well established velocities ($v/c = 0.53^{+0.06}_{-0.02}$ and $v/c = 0.34^{+0.22}_{-0.15}$ respectively). The high limits on the remaining velocities cannot rule out that all of the radio-only knots are moving. Three radio-only knots are varying in 8.4 GHz radio flux density, A1B, A1D, and SJ1; SJ1 also varies in 4.8 GHz radio flux density as does A1E. With regard to the polarisation, any changes seen in the moving knots are attributed to the motion so I detect changes in the angle of polarisation of two knots (A1D and A4) and SJ1 varies in the degree of polarisation.

As mentioned in Section 5.3.7, the broad-band spectra of these knots may be steeper than those of the knots with counterparts, suggesting a difference in the particle acceleration between these knots and those with X-ray emission. However, if we consider that they may all be moving, this leaves a group of moving, radio-only knots with half showing signs of radio variability and changes in the polarisation.

The radio-only knots with well established velocities, A1B and A1E, have some degree of radio flux density variability, while the other moving knot, A3B, has a steady radio flux density and has already been described as a group of three sub-regions with only a diffuse X-ray counterpart. This X-ray emission may not be associated with the moving radio material.

X-ray-only knots

I detect 27 X-ray knots without radio counterparts and find that the X-ray light curves for 5 of them show some degree of variability in their X-ray flux densities, including AX2A and SX1, which may be LMXBs (Section 5.3.1). The vast majority of these knots therefore appear stable and many may have flatter X-ray/radio flux density ratios than those of the knots with counterparts.

I have fitted spectral indices for 14 of these X-ray-only knots and they are all consistent with synchrotron emission lying in the range 0.58 – 1.40. They are also consistent with those measured for the X-ray knots with radio counterparts (Table 5.7).

5.3.9 Inner Hundred-Parsec-scale Jet

I detect the inner hundred-parsec-scale jet in both our radio and X-ray data as a very well collimated feature extending from the core to the A1 base knots, ~ 250 pc downstream of the nucleus. I used a rectangular region to isolate the emission from this inner jet carefully positioned to include as much jet emission as possible without contamination from the core or the knots; it extends from 6.7 to 12.1 arcsec (114 – 204 pc) from the core as shown in Figure 5.17. The background emission was estimated from two regions, positioned such that they extend radially from the nucleus at the same distances as the jet region, avoiding X-ray point sources.

I measured the X-ray flux densities for each observation and jointly fitted a power-law with a spectral index of $0.63^{+0.13}_{-0.11}$ and a Galactic absorption of $0.32^{+0.05}_{-0.02} \times 10^{22}\,\mathrm{cm}^{-2}$ ($\chi^2 = 134.1$ for 133 d.o.f.). This spectral index is consistent with the spectral indices of the knots downstream; however, the Galactic absorption is higher in the knots further downstream than in this hundred-parsec-scale jet, as expected since the jet is located within the optical dust lane. I find that the X-ray to radio spectral index, $\alpha^{X}_{4.8} = 0.89 \pm 0.08$, is higher but consistent with that of the base knots while the X-ray/radio flux density ratio ($0.23 \pm 0.08 \times 10^{-6}$) is lower than those of the radio knots with X-ray counterparts but higher than the value for diffuse emission in the centre jet (Hardcastle et al. 2003, see Section 5.3.7). I detect no significant variability in the X-ray flux density; the apparent

fluctuations appear only minor with no obvious trends. However, the radio 4.8 GHz flux density increased by a factor of 2 from 1991 and shows the first indication of decreasing again in the 2008 data. I am unable to measure the radio spectral index for this region of the jet due to artifacts around the bright core. Although I detect a factor of two change in the radio flux density, I cannot make any firm conclusions on this behaviour as this section of the jet is greatly affected by artifacts from the core. These results will be discussed in Section 5.4.5.

5.4 Discussion

With all of these data we can begin to shed light on the complicated behaviour of the jet: why and where knots are formed, why we can see them and how they evolve. In this section I start by examining the many knot formation models and consider if the behaviour of any of the knots in Cen A supports them. Not one of these models can explain all of the observed properties of the knots in Cen A; however, some knots behave in a way that can be explained by one model or another. I are particularly interested to see if the different populations of knots — those with counterparts, the radio-only and the X-ray-only knots — can all be explained by these models. I then discuss the effect of relativistic beaming on the knot emission, which may explain the observed flux variability, and investigate whether the properties of the knots can be explained by a spine-sheath model of the jet. I also discuss the hundred-parsec-scale jet comparing it to the knots and to other similar jets.

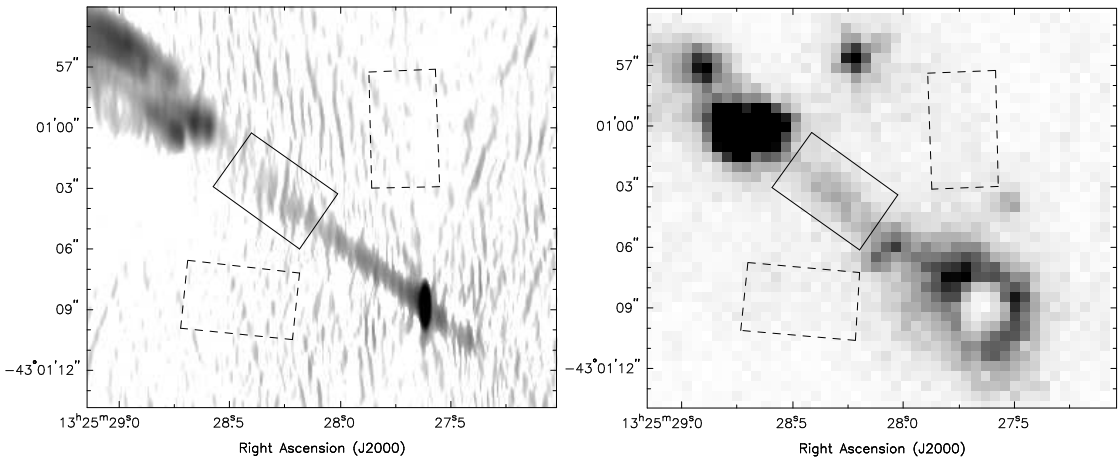

Figure 5.17: Regions used for the analysis of the hundred-parsec-scale inner jet in Cen A (discussed in Section 5.3.9) shown against the 2007 8.4 GHz radio data (left) and the combined X-ray data in the energy band 0.4 – 2.5 keV (right). The source region is shown in solid line, and the background regions in the dashed line. These regions were chosen to include as emission from only the hundred-parsec-scale inner jet, excluding the emission from the X-ray point sources near the core.

Table 5.5: Summary of X-ray and Radio Knot Behaviour

Name		Radio Varying?		Xray	Varying Polarisation		Proper Motion					
X-ray	Radio	4.8 GHz	8.4 GHz	Varying?	Degree of?	Angle of?	Y/N	median v (c)	upper limit (c)	θ_v (deg)	v_{RA} (c)	v_{dec} (c)
AX1A	A1A	Y	N	N	Y	Y	N	0.002	< 0.05		< 0.04	< 0.00
...	A1B	N	Y	-	N	N	Y	$0.534^{+0.06}_{-0.02}$		$67.40^{+3.70}_{-2.13}$	$0.50^{+0.06}_{-0.02}$	$0.21^{+0.01}_{-0.02}$
AX1C	A1C	Y	Y	Y	N	Y	N	0.076	< 0.14		< 0.14	< 0.11
...	A1D	N	Y	-	N	Y	I	0.095	< 0.58		< 0.49	< 0.30
...	A1E	Y	N	-	N	N	Y	$0.338^{+0.22}_{-0.15}$		$54.18^{+30.12}_{-25.12}$	$0.28^{+0.19}_{-0.08}$	$0.25^{+0.16}_{-0.16}$
AX2	A2A	N	N	N	N	Y	N	0.164	< 0.24		< 0.09	< 0.24
AX3	A3A	Y	N	N	N	N	N	0.031	< 0.05		< 0.03	< 0.01
AX4	A3B	N	N	N	N	N	Y	$0.802^{+0.15}_{-0.09}$		$71.17^{+11.94}_{-11.76}$	$0.79^{+0.19}_{-0.09}$	$0.27^{+0.14}_{-0.15}$
...	A4	N	N	-	N	Y	I	0.928	< 1.00		< 1.00	< 0.32
AX5	A5A	N	N	N	N	N	I	0.016	< 0.34		< 0.26	< 0.23
AX6	A6A	N	N	N	N	N	I	0.370	< 0.62		< 0.51	< 0.36
BX2	B1A	Y	Y	Y	N	N	I	0.049	< 0.74		< 0.69	< 0.27
BX4	B2	N	Y	N	Y	N	I	1.000	< 1.00		< 1.00	< 1.00
...	SJ1	Y	Y	-	Y	N	I	0.371	< 0.81		< 0.38	< 0.72
...	SJ2	N	N	-	N	N	I	0.193	< 0.59		< 0.22	< 0.55
SJX1B	SJ3	N	N	N	N	N	I	0.213	< 0.90		< 0.47	< 0.88
SX1A	S1	Y	Y	N	Y	N	I	0.238	< 0.83		< 0.79	< 0.24
SX2A	S2A	N	Y	N	N	N	I	0.250	< 0.37		< 0.30	< 0.24
SX2B	S2B	N	N	N	Y	N	I	0.305	< 0.60		< 0.55	< 0.49

AX2A, EX1, FX1A, GX5 and SX1 vary in the X-ray and do not have radio counterparts.

AX4A, BX1, BX3, BX5, CX1, CX2, CX3, CX4, EX2, FX1, FX2, FX3, FX5, FX6, FX6A, FX7, GX1, GX2, GX3 and GX4 do not vary in the X-ray and do not have radio counterparts. The knot proper motions are classified as moving (Y), stationary (N), and inconclusive (I).

Table 5.6: Normalised radio knot flux densities at 8.4 GHz with local, on-source background subtraction.

	Flux (mJy)						
Knot	1991	2002	2003	2004	2006	2007	2008
A1A	20.72 ± 0.59	19.97 ± 1.09	20.98 ± 1.17	20.98 ± 1.32	21.76 ± 1.61	22.94 ± 1.50	20.67 ± 1.68
A1B	52.80 ± 0.77	46.05 ± 2.24	45.53 ± 2.26	46.04 ± 2.61	45.98 ± 3.09	46.33 ± 2.76	41.62 ± 3.18
A1C	34.44 ± 0.78	38.06 ± 1.91	38.77 ± 1.98	39.87 ± 2.31	41.28 ± 2.83	40.43 ± 2.47	41.25 ± 3.16
A1D	11.18 ± 0.55	8.98 ± 0.70	8.83 ± 0.75	8.23 ± 0.81	8.77 ± 0.97	8.47 ± 0.91	8.46 ± 0.92
A1E	8.25 ± 0.71	9.79 ± 0.86	10.06 ± 9.31	9.86 ± 1.03	10.08 ± 1.20	9.09 ± 1.12	10.27 ± 1.16
A2A	23.99 ± 0.80	24.03 ± 1.37	23.99 ± 1.43	24.19 ± 1.62	23.33 ± 1.86	22.88 ± 1.69	23.81 ± 2.00
A3A	3.96 ± 1.29	3.75 ± 1.36	4.12 ± 1.51	3.06 ± 1.54	2.88 ± 1.98	4.05 ± 1.91	3.26 ± 1.56
A3B	22.33 ± 1.63	21.02 ± 1.96	20.64 ± 2.10	18.59 ± 2.18	16.92 ± 2.70	18.29 ± 2.59	18.46 ± 2.37
A4	24.75 ± 1.92	28.35 ± 2.39	27.48 ± 2.56	27.17 ± 2.70	26.44 ± 3.37	25.98 ± 3.16	28.72 ± 3.11
A5A	1.08 ± 0.30	1.86 ± 0.35	2.06 ± 0.34	1.23 ± 0.35	1.15 ± 0.42	0.22 ± 0.51	1.81 ± 0.43
A6A	2.85 ± 0.49	2.72 ± 0.56	3.12 ± 0.54	2.04 ± 0.57	1.19 ± 0.67	1.66 ± 0.83	2.41 ± 0.68
B1A	1.59 ± 0.49	2.43 ± 0.25	2.95 ± 0.55	1.25 ± 0.22	1.61 ± 0.43	2.04 ± 0.12	2.15 ± 0.34
B2	3.86 ± 0.59	4.29 ± 0.34	4.99 ± 0.67	2.46 ± 0.28	5.68 ± 0.61	2.74 ± 1.38	4.05 ± 0.47
SJ1	5.37 ± 0.89	12.78 ± 0.74	10.85 ± 1.36	14.76 ± 1.25	16.49 ± 2.71	18.72 ± 1.41	20.04 ± 1.51
SJ2	2.44 ± 0.74	5.13 ± 0.45	4.58 ± 0.11	6.04 ± 0.88	1.71 ± 0.21	3.59 ± 0.84	4.89 ± 0.48
SJ3	0.55 ± 0.84	1.17 ± 0.44	1.73 ± 1.20	1.53 ± 2.37	1.42 ± 0.93	0.73 ± 0.37	0.77 ± 0.39
S1	4.28 ± 1.09	10.10 ± 0.61	10.26 ± 1.16	6.11 ± 1.02	9.74 ± 2.01	8.95 ± 1.86	10.40 ± 0.93
S2A	2.28 ± 0.34	1.18 ± 0.19	1.51 ± 0.39	0.16 ± 0.17	1.83 ± 0.35	1.17 ± 0.81	1.94 ± 0.26
S2B	0.82 ± 0.34	0.55 ± 0.18	0.30 ± 0.38	0.05 ± 0.17	1.09 ± 0.34	0.43 ± 0.81	0.61 ± 0.22

Table 5.7: Spectral properties of the Radio Knots in Cen A

Name		Flux Density		S_X/S_R	Radio Spectral Index		$\alpha_{4.8}^X$	α_X	N_H
X-ray	Radio	8.4 GHz (mJy)	1 keV (nJy)	($\times 10^{-6}$)	$\alpha_{4.8}^{8.4}$	$\alpha_{4.8}^{22.5}$			($\times 10^{22}$ cm^{-2})
AX1A	A1A	22.89 ± 1.21	10.65 ± 1.64	0.46 ± 0.07	0.89 ± 0.34	0.85 ± 0.21	0.85 ± 0.14	$1.08^{+0.04}_{-0.04}$	0.51 ± 0.02
...	A1B	46.24 ± 1.08	< 19.38		0.84 ± 0.18	0.80 ± 0.07			
AX1C	A1C	40.34 ± 2.27	21.43 ± 2.97	0.48 ± 0.09	0.89 ± 0.22	0.79 ± 0.14	0.85 ± 0.23	$1.06^{+0.04}_{-0.04}$	0.52 ± 0.02
...	A1D	8.45 ± 0.77	< 3.20		1.56 ± 1.01	0.89 ± 0.41			
...	A1E	9.07 ± 1.00	< 1.41		1.66 ± 1.11	1.42 ± 0.88			
AX2	A2A	25.54 ± 1.35	9.29 ± 0.54	0.39 ± 0.04	1.57 ± 0.40	1.16 ± 0.23	0.86 ± 0.08	$0.77^{+0.07}_{-0.06}$	0.55 ± 0.04
AX3	A3A	3.12 ± 0.28	4.02 ± 0.39	1.00 ± 0.49	–	–	0.80 ± 0.14	$0.78^{+0.16}_{-0.15}$	0.40 ± 0.07
AX4	A3B	19.22 ± 1.05	4.98 ± 0.28	0.26 ± 0.04	1.93 ± 0.59	–	0.88 ± 0.08	$0.94^{+0.16}_{-0.15}$	0.45 ± 0.06
...	A4	25.92 ± 2.81	< 9.48		1.96 ± 0.49	–			
AX5	A5A	1.64 ± 0.21	6.60 ± 0.39	3.02 ± 7.01	–	–	0.61 ± 0.10	$0.59^{+0.11}_{-0.14}$	0.59 ± 0.07
AX6	A6A	2.41 ± 0.34	9.39 ± 0.35	5.64 ± 2.82	3.91 ± 2.84	–	0.70 ± 0.11	$0.51^{+0.04}_{-0.06}$	0.51 ± 0.05
BX2	B1A	2.23 ± 0.35	19.39 ± 0.97	9.44 ± 5.35	1.89 ± 1.29	–	0.67 ± 0.11	$0.63^{+0.02}_{-0.02}$	0.11 ± 0.01
BX4	B2	4.59 ± 0.46	4.94 ± 0.30	1.80 ± 0.92	4.88 ± 2.82	–	0.77 ± 0.11	$0.91^{+0.06}_{-0.02}$	0.08
...	SJ1	18.69 ± 0.97	< 46.79		-0.54 ± 0.06	–			
...	SJ2	3.58 ± 0.84	< 19.24		1.86 ± 1.60	–			
SJX1B	SJ3	1.35 ± 0.26	0.99 ± 0.12	0.65 ± 0.44	–	–	0.83 ± 0.19	0.50	0.08
SX1A	S1	9.37 ± 0.78	0.65 ± 0.06	0.07 ± 0.02	2.47 ± 0.84	–	0.96 ± 0.12	$0.48^{+0.12}_{-0.18}$	0.08
SX2A	S2A	1.17 ± 0.86	3.21 ± 0.21	1.78 ± 1.26	–	–	0.77 ± 0.58	$0.64^{+0.07}_{-0.07}$	0.15 ± 0.04
SX2B	S2B	0.43 ± 0.85	1.88 ± 0.26	4.14 ± 7.85	–	–	0.75 ± 2.21	$0.77^{+0.20}_{-0.19}$	0.13 ± 0.06
Inner pc-scale jet		32.13 ± 4.65	7.34 ± 2.41	0.23 ± 0.08	–	–	0.89 ± 0.32	$0.63^{+0.13}_{-0.11}$	0.32 ± 0.07

5.4.1 Knot Formation Models

To determine whether the current models can explain the knots observed in Cen A, here I compare the observed properties of the knots with the predicted behaviour due to changes in the fluid, namely compression or rarefaction, or changes in the particle acceleration due to processes such as reconfinement of the jet, magnetic field reconnection, or collisions with objects such as molecular clouds and high mass-loss stars.

Adiabatic Compression

If a section of the jet's diffuse material underwent adiabatic compression, the magnetic field, which is frozen into the jet plasma, would increase in strength as would the number density and energies of the emitting particles. This would be reflected in an increase in the flux density and the break frequency of the synchrotron spectrum, so we would observe a flatter X-ray to radio spectrum if compression was responsible for the knots. Hardcastle et al. (2003) calculated the required one-dimensional compression factors, $\mathcal{R}$, from the observed X-ray/radio spectrum using the break frequency ($\nu_b \propto \mathcal{R}^4$ for a tangled field geometry) and considered whether this level of compression, when applied to the surrounding diffuse material, is consistent with the observed emission properties. They found that this level of compression would cause an increase in the radio volume emissivity of the diffuse material by a factor of $\sim 10^{11}$ compared to the observed factor of ~ 2, effectively ruling out compression as a creation model for the X-ray-only knots in Cen A. Compression in more than one dimension may reduce the effect to a change in break frequency of $\nu_b \propto \mathcal{R}^2$; however, the change in volume emissivity is still much higher than the observed factor. Lesser amounts of compression may still explain the radio-only knots where the X-ray/radio flux density ratio of the diffuse material is suppressed, resulting in a X-ray counterpart too faint to be detected above the diffuse emission, but they cannot explain any knot with an X-ray counterpart. In what follows, I therefore consider only particle acceleration models as causes for radio knots with X-ray counterparts and X-ray-only knots in Cen A. It seems very likely that more than one of these particle acceleration processes is responsible; here I examine in detail the predictions of the models and the observed behaviour of the knots to identify those models which are dominant in the jet.

Impulsive Particle Acceleration

If the knots seen in Cen A are the result of impulsive particle acceleration across the entire knot region, due to a short-lived processes such as small scale magnetic field reconnection, they would fade due to synchrotron losses while others would presumably appear in order to maintain a steady state. Using the equipartition value of the magnetic field strength in the A1A knot (Section 5.3.2), we would expect a complete change in the appearance of the 1 keV X-ray jet emission in ~ 6 years; this is not seen. The X-ray synchrotron lifetimes of some of the knots that are resolved in the

radio are shown in Table 5.4. Consequently, the particle acceleration processes must be in general long-lived.

The knot HST-1 in M87 may be an impulsive event as it flared and faded to approximately its original flux in a decade. The observed fading is consistent with synchrotron losses; in addition to a general decrease in all frequencies (X-ray, UV and radio) consistent with changes in the beaming factor, the X-ray falls-off faster than the UV or radio (Harris et al. 2009). However, no knot in Cen A appears to behave like HST-1; the largest increase in flux is only a factor of 3 over the last 16 years (SJ1), much slower than the flaring of HST-1, and it has not yet begun to fade; SJ1 is better described by a collision model.

Collisions

A collision between the jet and an obstacle (Blandford & Königl 1979) would result in a local shock complex and is therefore commonly invoked to explain jet knots. In this scenario, during the initial interaction, we would see a steady increase in the luminosity of the knot relative to the diffuse background. This is a fast process relative to the lifetime of the knots, but for plausible obstacle sizes and speeds is much longer than the period of our observations and would therefore only be seen as a slight increase in flux. Once the obstacle is firmly in the path of the jet, we expect to see a prolonged period of stable particle acceleration. Eventually, the obstacle may be annihilated by the constant impact from the jet fluid; it could move transversely out of the jet, continuing on its original path; or it could be carried along the jet, which would cause a reduction in the shock strength as the obstacle accelerates. All these would result in a gradual decrease in the flux and, eventually, to the complete disappearance of the knot.

In Cen A's jet we can therefore expect to see a range of behaviours for local shocks in the jet, but the vast majority of knots in this model are expected to be in a phase of stability with X-ray and radio emission of a constant flux. The knots A1A/AX1A and A1C/AX1C are possibly local shocks due in some part to the reconfinement of the jet (see below); however, there are many other instances where there is an X-ray compact source associated with a stationary compact radio knot: A2A/AX2, A5A/AX5, B1A/BX2, and B2/BX4 in the jet and SJ3/SJX1b, S2A/SX2A and S2B/SX2B in the counterjet. There are some slight changes in the X-ray, radio or polarisation in these systems, but these are not steady, broad-band increases or decreases which could be attributed to beaming (Section 5.4.3). Their variability may be described as short-term flaring and may be due to the evolution of the interaction between the jet and the obstacle, to fluctuations in the jet's fluid flow, or to their shock being curved, which would be naturally unsteady under small perturbations of the driving flow.

The majority of the X-ray knots have no detected radio counterparts and only five of these X-ray-only knots have variability detected in the X-ray flux density, of which two are probably LMXBs (Section 5.3.1). Of the three probable jet knots, FX1A has a significant flaring event (X-ray

increases by a factor of 2 in the 2002 observation), EX1 shows evidence of a steady decrease in the 2007 VLP observations, which is consistent with predictions of synchrotron losses, and GX5, a very faint knot, is only detected in 3 of the 10 observations so that we cannot characterise its variability in detail. Despite these exceptions, the vast majority of these stationary, X-ray only, compact knots are consistent with a period of stability in the shock model where the radio counterpart is too faint to be detected in our data; the range of X-ray/radio ratios I have measured means we cannot dismiss the possibility of faint radio counterparts, and in fact there is diffuse material emitting in the radio at many of these positions.

It is still possible that the X-ray-only knots are a separate population of knots that have flatter spectra than the radio knots with X-ray counterparts; however, these knots and those with detected counterparts are consistent with collisions and shock models although we do not see any knots at a stage where the knots are fading away, which would be a very short period in the lifetime of the knot compared to their stable stage. We do see one knot, AX2A, appearing in the X-ray during the 2007, 6×100 ks observations but we do not observe a gradual brightening as there is a four-year gap in the observations prior to the 2007 observations when this may have occurred, so we cannot say for certain whether this is a new knot or a LMXB (Section 5.3.1).

The radio-only stationary knots may be explained in this scenario by a weaker shock such as would occur if the obstacle is moving downstream. As the obstacle speeds up to match the fluid flow, the shock would weaken until it was too weak to accelerate particles to X-ray emitting energies. In this model, the ratio of the numbers of radio and X-ray knots would be related to their respective lifetimes, but as the lifetime of the knots also depends on the birth rates, the times taken for the knots to move along, through or out of the jet, and the obstacle ablation or acceleration timescales, the relationship would not be a simple one. This model explains stationary and very slow moving knots but those moving at close to the mean jet speed ($v/c \sim 0.5$) cannot be explained by weak shocks, and the limits on the proper motions of the radio-only knots suggest that many knots may not be consistent with this model. A1D is an example of this with an upper limit speed of $0.58c$. Other models for the radio-only knots are discussed in more detail later in this section.

Recent 2.3 GHz very long baseline interferometry (VLBI) observations by Tingay & Lenc (2009) of the bright A-group knots do not detect our moving radio knots, A1B and A1E, or A1D while the compact cores of A1A, A1C and A2A are all resolved. These results strongly support a collision model for, at least, the stationary radio knots with X-ray counterparts, and also argue that there is an intrinsic difference between the stationary and moving knots. If the stationary knots were due to collisions with an obstacle, we would expect to detect a compact region where the interaction is occurring; whereas if the moving knots were due to a non-localised process such as compression of the fluid flow, we would not expect to detect a compact central region in the knot.

If we consider the limits on the proper motions of the stationary knots (A1A; $v/c < 0.05$, A1C; $v/c < 0.14$ and A2A; $v/c < 0.24$) it is reasonable to consider A3A, with a limit of $v/c < 0.05$, to also be stationary and therefore we can predict that in principle it should be detectable with VLBI.

The limits on the other knots are all significantly higher and in two cases, unconfined (A4 and B2) so if these knots have compact cores that can be detected with VLBI they could be independently identified as either moving or stationary knots. This is particularly interesting in the case of SJ1 as it has a measured velocity of $v/c = 0.42^{+0.39}_{-0.27}$, but this apparent velocity due to the effect of artefacts on the observed shape of the knot. An X-ray counterpart cannot be resolved due to its proximity to the core (0.95 arcsec = 17 pc), so detecting a compact peak in the radio with VLBI might give us an independent method of constraining its motion and therefore the reason for its development.

Tingay & Lenc (2009) also detect sub-structure in the knots A1A and possibly A2A. (The larger-scale structure of these knots is not detected by the VLBI observations due to the lack of short baselines.) If we consider A1A, which Tingay & Lenc (2009) divide into two compact sources A1Aa and A1Ab, we find that Tingay & Lenc (2009) only detect approximately half of the flux at 2.3 GHz (from both of these substructures) that would be expected based on our observations and assuming a power-law spectrum. We must assume that the remaining half of the emission is coming from more diffuse material on the scale of 0.1–0.2 arcsec. However, the observations of a compact core reduce the possible size of the obstacle to an area comparable to the size of the region detected (0.5 – 2.5 pc), which suggests an obstacle such as O/B stars, which are much more common, rather than more extreme systems such as Wolf-Rayet stars as suggested by Hardcastle et al. (2003).

As discussed in Section 5.3, I find that many of the X-ray knots with radio counterparts, and all of the radio-only knots, lie within the inner arcmin (~ 1 kpc), while beyond this I find a complete absence of compact radio knots, even though there is diffuse radio emission extending to the north inner lobe at ~ 190 arcsec. It is at ~ 1 arcmin that we also detect a change in the absorbing column as the jet emerges from the dust lane. Given the constraints on the geometry of the dust features seen in emission at 8μm with *Spitzer* IRAC (Quillen et al. 2006, 2008), it seems unlikely that the jet is interacting with the dust disk directly beyond the A1 group of knots. However, it remains plausible that there are a greater number of knots in this inner region due to collisions with high-mass-loss stars or clumps of cold gas, both of which will be more common in the central regions of the galaxy. If I consider the distribution of stars in Cen A (van den Bergh 1976; Mellier & Mathez 1987) and compare this with the decreasing number of knots with distance from the core, I find that the number of stars per unit length in the jet steadily increases with distance from the nucleus. This argues that the obstacles are not distributed like normal stars in the galaxy, but does not rule out the model in which the obstacles are high mass-loss stars or gas clouds associated with the central regions of the galaxy.

Further out, there is a decrease in the spatial density of knots which is consistent with a predominantly diffuse particle acceleration mechanism and at ~ 190 arcsec the environment may change again, as the radio emission expands into a lobe and there is an X-ray surface brightness discontinuity (Kraft et al. 2008).

I conclude that the majority of knots in the jet of Cen A can be described as due to the interaction between the jet and an obstacle, including knots with no detected X-ray or radio counterparts, the exceptions being those radio-only knots which are moving (Section 5.4.1); however, this assumes that the missing counterparts exist below the noise level. If there are really no counterparts, we require another model to explain the existence of X-ray-only knots.

Reconfinement of the Jet

It has been suggested (e.g. Sanders 1983) that where the jet moves from a well-collimated hundred-parsec-scale jet to a complex, knotty kpc-scale jet, the supersonic fluid encounters a less dense environment. It expands into this ambient material and is therefore likely to cause a reconfinement shock near the boundary of the jet. This could also be the case if there is a change in the internal pressure or state of the gas, or because of a change in the external sound speed or density with no change in the external pressure, which could occur if the jet is within a relativistic bubble.

At ~ 250 pc the inner jet expands from a well-collimated beam to a diffuse cone of material. This is indicative of a change in the ambient pressure which would be consistent with the conditions for a reconfinement shock. The base knots A1A/AX1A and A1C/AX1C are therefore prime candidates for reconfinement shocks. They are also stationary in the jet, and A1C is evolving downstream consistent with this model. Unfortunately, the presence of the moving knot, A1B, between two base knots is difficult to explain in a simple reconfinement model; it would require an unstable knot complex, possibly ringed, with a shock region that could have been disrupted by A1B as it moves along the jet.

The knot HST-1 in M87 has also been investigated in terms of a reconfinement shock model by Stawarz et al. (2006) and has many traits similar to A1A and A1C. It is believed that the stationary, compact, variable and overpressured flaring region is located immediately downstream of the point where the reconfinement shock reaches the jet axis. Stawarz et al. (2006) also associate the downstream, superluminal features of HST-1 with a diverging reflected shock. If we compare this to Cen A's A1 grouping, then A1A and A1C are consistent with the flaring region of HST-1 and the fainter downstream components A1D and A1E, which are moving down the jet, can be compared to the reflection components.

To summarise, the location of these knots at the point where the jet widens and the fact that, collectively, they span the width of the jet are in favour of a reconfinement shock model; however, the fact that there are two of them and that A1B is apparently moving between them makes this model harder to accept.

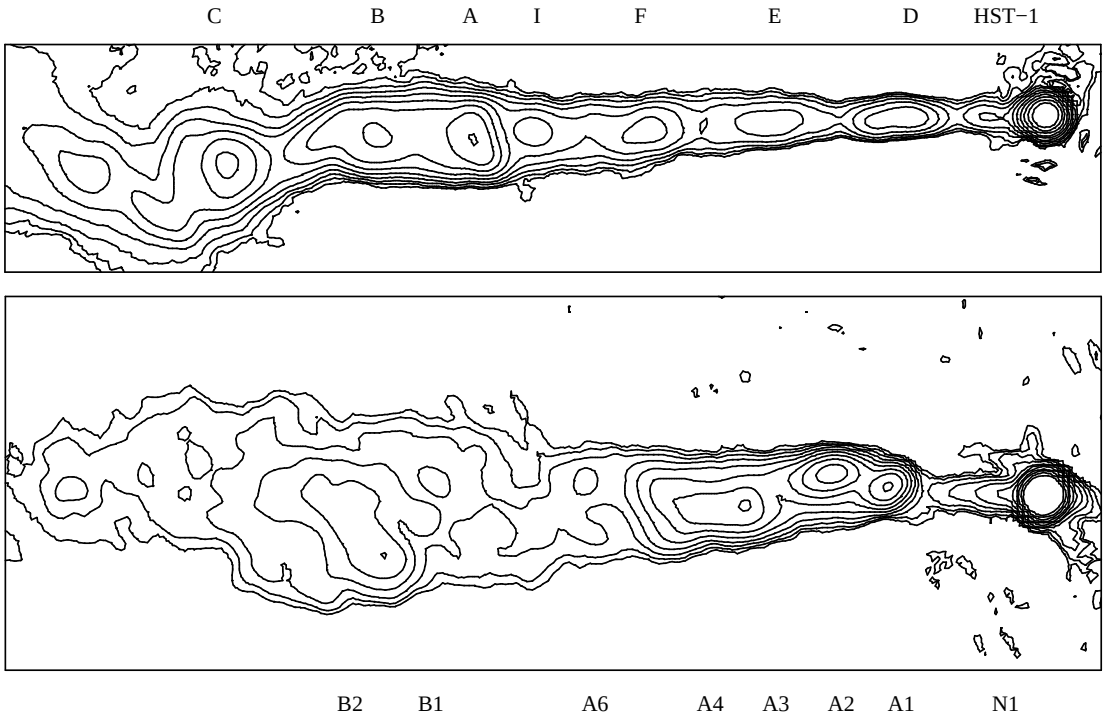

Figure 5.18: M87 (top) and Cen A (bottom) scaled to a common spatial resolution of 33 pc showing the inner 1.85 kpc of both jets (projected) so that the distances of the knots in each jet can be compared. The Cen A image is our 2002 A+B 8.4 GHz radio data and the M87 map is at 5 GHz (Hines et al. 1989). The contours are logarithmic increasing by a factor 2 at each step.

Moving Knots

The moving radio knots fit into none of the models discussed previously as all these models describe a situation in which the fluid undergoes a change at a stationary point in the jet. I also have to consider that there are no compact X-ray counterparts to the moving radio knots, A1B and A1E, as well as the diffuse radio emission downstream of A2A; A2B ($v/c = 0.57$), A2C ($v/c = 0.25$) and A2D ($v/c = 0.46$). The remaining moving knot, A3B is associated with a clumpy region in the radio jet rather than a single compact radio knot and has X-ray emission associated with it, although this could be a projection effect or emission from a nearby stationary X-ray knot unrelated to the radio knot. It is also important to note that all of the radio-only knots have either well-established or inconclusive proper motions so it may be that all of the radio-only knots are moving.

Knots that are moving at speeds comparable to the bulk jet flow speed cannot be due to collisions with a stationary or slow-moving obstacle, and, as we have argued above there is independent evidence from VLBI observations that there is an intrinsic difference between the moving and stationary knots in the A group. To describe the moving knots we require a scenario in which the jet undergoes a change resulting in a knot of either higher particle density, higher particle energy, or higher magnetic field, which moves freely along the jet with the fluid flow. This would be provided

by moderate compression of the jet fluid.

Information on X-ray motions of the other knots in the jet will be invaluable to this problem as the radio-only moving knots may not be as different as this work suggests, but X-ray proper motions will not be available for some time. Our current data spans a sufficient time frame for motions to be detected; however, the signal-to-noise of the earlier observations is not good enough to accurately measure the position of the knots, so that our *Chandra* data do not provide useful constraints.

5.4.2 Particle Acceleration Efficiency

In models in which the X-ray emission from the knots is synchrotron emission produced as a result of the interaction between the jet and an obstacle, the X-ray luminosity places some constraints on the efficiency of high-energy particle acceleration. Using the constraints on the knot sizes provided by the VLBI observations (5.4.1) I can calculate the fraction of the jet power intercepted by the knots. Some fraction of this (which cannot exceed 100%) goes to power the emission at X-ray and other bands. If I assume that the knots are in a steady state and that the incident energy produces electrons with a power-law energy spectrum that balances the radiative losses, then I can form an inequality: the ratio of the energy in the X-ray-emitting electrons to that in the whole electron population must be greater than the ratio of the energy emitted in the X-rays to the fraction of jet energy intercepted by the knot. For the unrealistic assumption of 100% efficient energy transfer of the absorbed jet energy to relativistic electrons, I find that the electron energy spectrum has an index, $p \leq 2.44$ when I consider the lowest energy electrons to have $\gamma = 1$. If I assume that the energy transfer to the electrons is 10% efficient, then the electron energy index decreases, $p \leq 2.27$ and at 1% the spectrum is constrained to have $p \leq 2.06$. However, if the minimum γ is increased to $\gamma = 100$, these indices steepen so, for example, 1% efficient energy transfer has an electron energy index of $p \leq 2.13$. These calculations use the cross-section and X-ray emission of the knot AX1A as its size is well constrained (Tingay & Lenc 2009). These indices put some constraints on the nature of the particle acceleration in the jet; I note that $p > 2.0$, the value expected for standard acceleration at a non-relativistic strong shock, is possible unless the efficiency of energy transfer to the electron population falls below $\sim 1\%$.

5.4.3 Beaming

If there are changes in the beaming factor in the knots, due to a change in the velocity or direction of the fluid flow, we would observe in-step changes in the X-ray and radio flux densities, assuming all the emission is synchrotron, as beaming to first order is independent of frequency. This may occur in stationary or moving knots as the movement of the fluid through the knot is responsible for changes in the beaming factor, not the motion of the knot itself. Although the flaring of HST-1 may be explained as a reconfinement shock or the result of impulsive particle acceleration, it fades

in a manner best described by beaming combined with synchrotron losses (Harris et al. 2009); the emission fades slowly in all frequencies, but appears to drop-off faster in the X-ray compared to the UV and radio. Compared to the factor 50 increase in X-ray emission of M87's HST-1, we observe no flaring events of similar intensity in either our radio or X-ray data. The largest increase we observe is in the radio knot SJ1, which increases in radio emission by a factor of 3.5 over the last 17 years. This is the only knot showing variability in the inner hundred-parsec-scale jet region suggesting it has different physics from the knots further down the jet and it is better described by a collision and shock model.

Smaller increases are seen in other stationary radio knots, increasing in step in the radio and X-ray although only A1C/AX1C shows a significant change in both. In the radio, A1C increases steadily while in the X-ray we see short-term variability with a dip in the flux density in the middle of 2007 (Figure 5.7). This is consistent with the short-term variability observed in HST-1, which also shows slight dips in the X-ray flux density during an overall increase. The knots A1A/AX1A and S1/SX1A also fit these conditions; however, the subtle increase in flux ($\sim 10\%$) is below the significance limit described in Section 5.3.4.

I conclude that although we see in-step changes in the radio and X-ray flux densities in several of the knots, beaming is not the dominant effect as other mechanisms can explain the observed behaviours.

5.4.4 Spine-Sheath Model

Current models of FRI jets (Laing & Bridle 2002) propose that the jets have a non-uniform radial velocity profile in which the speed decreases with increasing radius. Because of early polarisation results that seemed to point to a two-fluid structure, this is often discussed in the literature in terms of a fast-moving 'spine' and slower 'sheath' of the jet. The almost entirely parallel magnetic field seen in this work and in polarisation maps by Hardcastle et al. (2003) provides no evidence in itself either for or against 'spine-sheath' models, since modern versions of models with velocity structure do not predict a transition to a central perpendicular field in all cases. Some evidence for models with velocity structure might be provided by the observed localised edge-brightening in the diffuse material (Kataoka et al. 2006), if this is predominantly due to variations in the Doppler enhancement of different layers of the jet material. However, this limb-brightening is not seen along the entire jet; where it is seen, it lies downstream of a compact knot and could be described as a knot tail. Similar structures are seen behind many of the knots, for example A2A, and are consistent with a shock model with downstream advection Hardcastle et al. (2003). Kataoka et al. (2006) also suggest that at the edges there is a slight hardening of the X-ray emission suggesting the spectrum changes.

To investigate if this is seen in our deeper X-ray data, Worrall et al. (2008) fitted a joint spectrum to all the X-ray knots that reside in the 'inner-spine' and 'inner-sheath' regions (at a distance of 21 to 66 arcsec from the core with position angles of $51.2^\circ - 57.8^\circ$ for the spine and $49^\circ - 51.2^\circ$ and

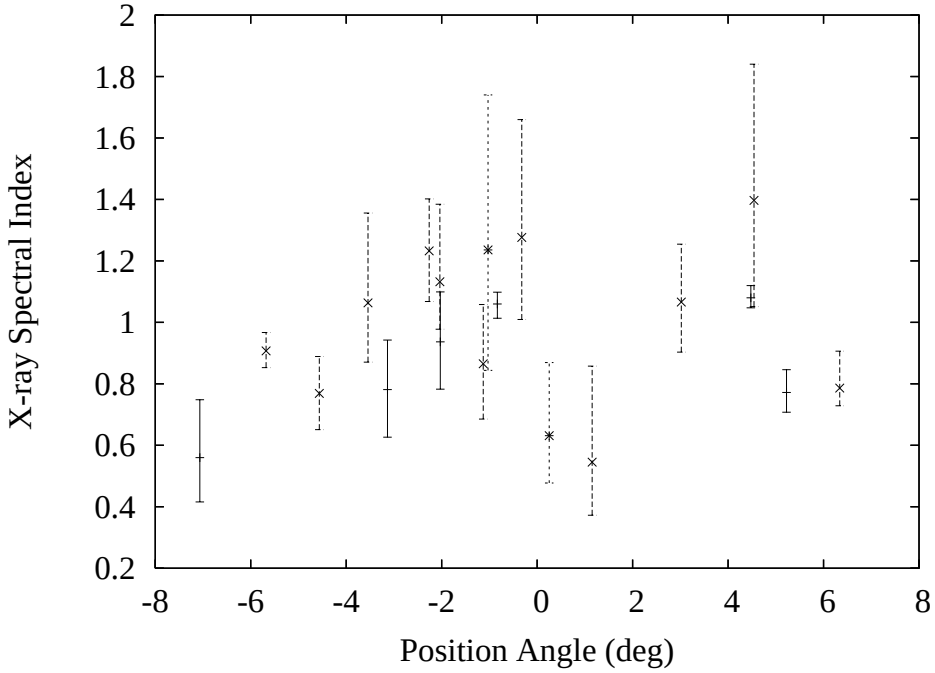

Figure 5.19: The X-ray photon index of knots in the jet of Cen A as a function of angular position measured from the centre of the jet at a position angle of $54.0°$, from the core to 60 arcsec (solid line), from 60 – 190 arcsec (dashed line) and further than 190 arcsec from the core (dotted line).

$57.8°$ – $60°$ for the sheath[1]). As described in Section 5.4.4, I have spectral fits for 6 of the 7 X-ray knots in the inner-spine and 3 of the 5 X-ray knots in the inner-sheath regions defined by Worrall et al. (2008). The weighted mean of the spectral indices I measured for the X-ray knots in these regions are $\alpha_{spine} = 0.62 \pm 0.01$ and $\alpha_{sheath} = 0.89 \pm 0.05$ respectively, which are consistent with the results of Worrall et al. but not with each other. On closer inspection of the individual knot spectral indices, we find that the inner-spine spectral index is dominated by the bright X-ray knot BX2 ($\alpha_X = 0.67 \pm 0.11$). Given the small number statistics and the dominance of individual knots, it is difficult to draw conclusions about the behaviour of either knot population.

As discussed in Section 5.3.3, we see no dependence of the velocities on the angular position of the knots, nor on the distance of the knots from the core, although our sample is too small for a statistical analysis. I have considered the directions of motion and find that they are consistent with following the fluid flow, appearing to move toward the downstream regions of bright material. The directions of motion are not consistent with moving exactly parallel to the jet axis but we argue that the ridge line through the jet is not at a constant positional angle and that the fluid flow is complicated and not a simple laminar flow directed away from the core. I therefore cannot comment further on the possibility of a faster moving spine in the jet of Cen A nor on the possible migration of the knots towards or away from the jet axis.

[1]Worrall et al. (2008) define these pie sections from a base position of 13:25:26.98 -43:01:14.06 (not the core)

5.4.5 Inner Hundred-Parsec-scale Jet

I found that the spectrum of the inner hundred-parsec-scale jet of Cen A is flatter in the X-ray than the base knots and the diffuse material (Hardcastle et al. 2003) but consistent in the radio to X-ray spectral index. These measurements are also consistent with the values for knots further along the jet. The X-ray/radio flux density ratio is lower for the inner hundred-parsec-scale jet than for any of the knots, except S1/SX1A; however, it is higher than the X-ray/radio flux density ratio of the diffuse material further down the jet suggesting that the inner jet is more efficient at making X-rays for a given amount of radio than the diffuse emission further up the jet. This is consistent with what is seen in other FR I jets such as that in 3C 66B (Hardcastle et al. 2001).

5.5 Summary and Conclusions

Our results can be summarized as follows:

- I rule out impulsive particle acceleration in the knots of Cen A as I detect no extreme variability in the X-ray knots, in contrast to what is seen in knot HST-1 in M87. Essentially the same distribution of X-ray knots are observed in our most recent observation as was seen in the earliest *Chandra* observations in 1999. This would not be the case if the knots were impulsive as they would fade due to synchrotron losses indicating long-lived particle acceleration in the knots of Cen A.

- For those radio knots with X-ray counterparts, the most likely formation mechanism is a collision between the jet and an obstacle, resulting in a local shock. I see no significant variability in many of these knots, suggesting a long-lived, stable stage of particle acceleration during the interaction between the jet and the obstacle.

- The formation of knots at the point where the inner hundred-parsec-scale jet broadens abruptly suggests that these base knots (A1A and A1C) may be reconfinement shocks; however, this is complicated by the presence of a radio-only knot (A1B) moving downstream between the possible confinement-shock knots.

- I detect a factor of 3 increase in radio flux density of the counterjet knot SJ1. This knot lies only 17 pc from the nucleus so is unresolved in the X-ray; however, it was still increasing in flux in the most recent observation (Dec 2008) so I plan to continue to monitor its radio behaviour with the VLA.

- I detect proper motions in three of our radio knots; two of which have no compact X-ray counterparts and a third which has only diffuse X-ray emission associated with it. Studies of the distribution of the moving knots are inconclusive due to the low number of well-established

proper motions; however, that the direction of motion of the knots may not be directly parallel to the jet axis which appears to vary along the jet. Their motions are all downstream and they show no dependence on the position of the knot within the jet.

The most likely cause of knots in the jet is collisions; if the X-ray-only knots have faint radio counterparts and the radio-only knots are seen only during the latter stages of the collision when the interaction is weaker, then only the moving knots are a separate population. These may include all the radio-only knots but our proper motion measurements are inconclusive for many of these. I argue that these moving knots are due to compressions in the fluid flow that do not result in particle acceleration to X-ray emitting energies. It is possible, however, that the X-ray-only knots are also a separate population with flatter X-ray to radio spectra than those with counterparts, in which case we currently have no model for their formation.

Compared to other FR I jets, Cen A is atypical, with an obscuring dust lane extending out to 1 kpc from the core which may affect the jet and its knots. Other galaxies where dust has been detected, such as 3C31 and 3C449, have much smaller disks, which cannot affect even the innermost regions of the observed X-ray jet. If we can attribute the knot dominated particle acceleration of the inner kpc to the presence of this disk then we can postulate that the X-ray jet emission seen in other FR I galaxies should be comparable to the dominant diffuse particle acceleration that dominates further out in the Cen A jet. I would then predict that knot-dominated structure will not be seen in other FR I galaxies.

Chapter 6

An XMM Sample of Groups of Galaxies

In the previous Chapters, I have presented work that focuses on the lobes and jets of radio galaxies. The final section of this thesis is focused on the hot gas of the intragroup medium (IGM). Groups of galaxies are physically smaller than clusters so their evolution and response to heating and cooling are much faster than that of clusters. Groups of galaxies are therefore useful to test ideas relating to how the scaling relations of different gas properties change over time with heating and cooling. As radio-source heating may play an important part in galaxy formation, the impact of radio sources on the gas properties of the environment is also considered here.

Here, I use *XMM-Newton* data to characterise the surface brightness profiles and temperatures of a subset of groups of galaxies from the Group Evolution Multiwavelength Study (GEMS) group sample (Osmond & Ponman 2004) that were originally selected to investigate the potential effect of radio-source heating on the group gas properties by Croston et al. (2005a), in order to better constrain the relationship between the distributions of gas and dark matter in these systems and to relate this to their radio properties.

6.1 Introduction

In isothermal systems, we expect the velocity dispersion of the galaxies in the system to be related to the temperature as $\sigma_{opt} \propto T_X^{1/2}$ and the ratio of specific energy in the galaxies to specific energy in the gas to be unity ($\beta \sim 1$) (e.g. White et al. 1997, see Section 1.5). Both σ and T_X are probes of the gravitational potential of the system, while the luminosity L_X is a measure of the total mass of gas in the system. Hierarchical models of structure formation in a standard cold dark matter (ΛCDM) universe predict self-similar scaling so that $L_X \propto T_X^2$ (Kaiser 1986; Evrard & Henry 1991). However, observations suggest that this relationship for clusters is steeper still ($L_X \propto T_X^3$; White et al. 1997). It has also been suggested that the relationship for groups is even steeper with relationships of $L_X \propto T_X^{8.2}$ and $L_X \propto T_X^{4.9}$ (Ponman et al. 1996; Helsdon & Ponman

2000, respectively); however, Mulchaey & Zabludoff (1998) found that a single relationship could adequately fit the data for groups and clusters ($L_X \propto T_X^{2.8}$).

Observations of groups and clusters therefore suggest that these systems are not self-similar and are not consistent with basic hierarchical scenarios. However, the dark matter distribution scales self-similarly as predicted by hierarchical galaxy formation (e.g. Pointecouteau et al. 2005; Vikhlinin et al. 2006).

Because the luminosity probes the gas mass and the temperature is related to the gravitational potential, the $L_X - T_X$ relationship can reveal how the gas and dark matter are related, and whether there are differences in the gas properties of systems that have AGN feeding energy back into the environment. Work by Croston et al. (2003, 2005a) on elliptical dominated groups observed by *ROSAT* showed that there was a significant difference in the $L_X - T_X$ relationship for groups with and without radio activity. This was confirmed using *Chandra* data by Jetha et al. (2007).

Current models suggest that in radio galaxies, the expansion of the lobes displaces gas thereby dissipating energy into the environment (Böhringer et al. 2002). There is also evidence for shock heating due to the supersonic expansion of the lobes including both weak shock structures in the intracluster medium (ICM) (e.g. Fabian et al. 2003; Forman et al. 2005) and much stronger shocks observed at the edge of the radio lobes (e.g. Kraft et al. 2003; Croston et al. 2009). But these mechanisms feed energy mainly into the outer kpc-scale regions of the environment, rather than into the core where the material is being accreted so that they cannot affect the central gas properties.

As well as measuring the $L_X - T_X$ relationship, Jetha et al. (2007) also fitted X-ray temperature, gas density, gas pressure and gas entropy profiles to the emission from these groups and found that all of these profiles follow modified self-similar scaling, as discussed by Voit & Ponman (2003). Additional cooling, feedback, merging and perhaps conduction (Voit et al. 2002) within the central regions should result in an isentropic core at the level of the entropy floor (see Section 1.5). However, in clusters (Ponman et al. 2003) and in the *Chandra* data studied by Jetha et al. (2007), there are no detections of an isentropic core.

In this work, I use *XMM-Newton* archival data on 20 elliptical-dominated groups previously studied by Croston et al. (2005a) (including 13/15 of the groups studied by Jetha et al. 2007). These *XMM-Newton* data are more sensitive than the *ROSAT* and *Chandra* data used in these previous studies and have higher resolution than *ROSAT* so that the PSF can be better accounted for. Although the *Chandra* data used by Jetha et al. (2007) are more sensitive and have better resolution than the *ROSAT* data, the field of view does not include all of the group gas emission (unlike these *XMM-Newton* data). I use these data to test independently whether there is a dichotomy in the $L_X - T_X$ relationship associated with the presence of a radio source. I also fit temperature profiles, which reveal cool cores in the central regions of the majority of these groups, and use the $L_X - \sigma_v$ relationship to understand their positions in the $L_X - T_X$ plots. In many cluster studies, cool cores are associated with AGN so it is difficult to detangle the effects of these two features; this work should reveal whether they are linked in groups.

6.2 Sample

This analysis is a continuation of the work by Croston et al. (2005a) based on the Group Evolution Multiwavelength Study (GEMS) group sample, presented by Osmond & Ponman (2004, hereafter OP04). Osmond & Ponman collated optical data on 4320 groups from 10 previously published optical catalogues and compared it to the *ROSAT* observation log. They then selected groups with X-ray observations of at least 10 ks, pointed no more than 20 arcmin from the groups position, and with recessional velocities in the range $1000 < v < 3000$ km s^{-1}. These constraints guaranteed good X-ray data as the group emission was within the field of view (so not too close) and it was close enough that the group X-ray emission could be detected. Only 45 groups met these criteria. Osmond & Ponman also included 13 groups previously studied by Helsdon & Ponman (2000) and two Hickson compact groups, HCG 4 and HCG 40, which have good optical data. The purpose of their sample of 60 groups was to have a wide range of group properties rather than to have a statistically complete sample.

Croston et al. (2005a) reduced the GEMS sample to 30 groups by selecting groups that had a large elliptical galaxy as their brightest group galaxy (BGG), rejecting those with spiral or S0 BGG, as the spiral-dominated groups are unlikely to contain a strong radio galaxy. When the spiral-dominated groups were excluded, Croston et al. (2005a) found that the scatter in the $L_X - T_X$ relation was significantly reduced, as spiral-dominated groups probably have different gas properties to those with a large elliptical. In addition, they excluded the groups where no X-ray emission was detected by OP04 as the purpose of their work, like mine, was to investigate the X-ray properties of radio-loud and radio-quiet groups.

I use the same sample as Croston et al. (2005a), but analyse the available *XMM-Newton* archive data, which is more sensitive and has higher resolution than the data used in the work by OP04 and Croston et al. (2005a) who used *ROSAT*, and Jetha et al. (2007), who used *Chandra* data. These *XMM-Newton* data also have a large enough field of view to detect all of the X-ray emission associated with the group. I found that 24 of these groups have been observed by *XMM-Newton* and are available in the archive. These *XMM-Newton* X-ray data were processed using the SAS version 7.0.0 using the standard pattern filtering described in Chapter 2. Several of these data were affected by flares so GTI filtering was applied to remove flares with greater than $\pm 20\%$ variation from the lightcurve as measured in the 12–14 keV (pn) or 10-12 keV (MOS) energy range where the effective area for X-rays is negligible. Unfortunately, no thermal emission was detected from HCG 90 as its spectrum was dominated by a central AGN. The X-ray observation details of the groups successfully analysed in this work are shown in Table 6.1.

Croston et al. (2005a) classified the groups into radio-loud and radio-quiet groups by checking the NASA/IPAC extragalactic data base (NED), and NVSS (NRAO VLA Sky Survey) and FIRST (Faint Images of the Radio Sky at Twenty cm) for any that were not identified in NED, for radio sources which are associated with the group. Croston et al. then defined three cut-offs in the radio

luminosity to split the groups into radio-loud and radio-quiet. The cut $c0$ allows any groups with any detected radio emission to be classed as radio-loud; however, the other cuts, $c1$ and $c2$, were based on the radio luminosity density of NGC 3665, which is the lowest luminosity source in the sample that is an extended radio galaxy rather than a very small central source. I should still be able to detect extended, low-luminosity radio galaxies using these thresholds; $c1$ classed groups as radio loud if $L_{1.4}^{cut} = 1.2 \times 10^{21}\,\mathrm{W\,Hz^{-1}}$, which corresponds to $L_{NGC3665}/10$, and cut $c2$ uses a threshold of $L_{1.4}^{cut} = 6.0 \times 10^{21}\,\mathrm{W\,Hz^{-1}}$, which corresponds to $L_{NGC3665}/2$. These cut-offs account for the NVSS flux limit of 2.3 mJy so that with the threshold of $c2$, radio emission could be detected in all of the groups. In this work I used the $c2$ threshold as this is likely to be a minimum for extended radio emission at the redshifts of these groups. Using this cut-off, I have nine radio-loud groups and 10 radio-quiet groups, which should give me good enough statistics for an independent comparison. Croston et al. (2005a) found no significant difference between the results of the comparisons made using the three cut-off values, and Jetha et al. (2007) also used the $c2$ cut-off. I discuss the effect of choosing this cut-off in Section 6.5.2.

6.3 Analysis

The *XMM-Newton* X-ray data were reduced using the standard pipelines and method described in Chapter 2. I followed the method of Croston et al. (2008a) to make images showing the extended X-ray emission (shown in Figure 6.1) and to extract spectra corrected for both particle and instrument background. These methods are summarized here.

6.3.1 Imaging and Spectral Analysis

To make images of the extended X-ray emission from the groups in our sample, I extracted images in the 0.5 – 5.0 keV energy range from all the datasets and each camera for each group using the SAS tool *evselect*. These data were then used to produce images using the method described in Section 2.2.3. These images are only used in the analysis to define regions of interest, the location of point sources in the field of view, and for measurements such as the approximate location of the group centre for centroiding. Where the central galaxy was a known AGN, I used an annular source region so that the spectral fitting excludes the AGN contribution. These chip-gap corrected combined images are shown in Figure 6.1.

As discussed in Section 2.2.6, for the spectral analysis, I had to remove initially the contribution from particles and the instruments from the spectra and so a double subtraction method was required. To do this I used closed filter-wheel observations, which are data taken with the closed filter in place preventing X-rays from the sky being detected. These data provide high signal-to-noise spatial information on the particle and instrument background. To account for differences in the level of particle background between our observations and these closed filter-wheel data, I scaled the

Table 6.1: X-ray observation details

Group	Redshift	N_H (10^{20} cm^{-2})	Ang. Scale (kpc/arcsec)	ObsID	Date	Filtered Livetime MOS1,MOS2,pn (s)
HCG 62	0.0146	3.01	0.298	0112270701	15-Jan 2003	12407,12418,809
				0504780501	26-Jun 2007	99226,98089,99211
				0504780601	29-Jun 2007	33261,32020,22279
NGC 383	0.0169	5.39	0.346	0551720101	01-Jul 2008	26827,21663,12610
NGC 533	0.0181	3.01	0.368	0109860101	31-Dec 2000	38348,37779,0
				0109860201	01-Jan 2001	5791,5792,1687
NGC 720	0.0059	1.54	0.122	0112300101	13-Jul 2002	29027,29250,17206
NGC 741	0.0179	4.56	0.364	0153030701	03-Jan 2004	8581,8489,4977
NGC 1052	0.0049	3.07	0.101	0093630101	15-Aug 2001	15550,15553,11861
NGC 1407	0.0057	5.24	0.118	0404750101	11-Feb 2007	39328,38915,28035
NGC 3607	0.00411	1.48	0.085	0099030101	22-Nov 2000	17411,18134,17765
NGC 3665	0.00692	2.06	0.142	0052140201	02-Dec 2001	32108,31523,20024
NGC 3923	0.00459	6.21	0.095	0027340101	03-Jan 2002	36702,37230,29858
NGC 4065	0.0235	2.39	0.474	0112270601	02-Jan 2003	6469,6431,2609
				0112271001	09-Jun 2003	7403,8274,0
				0112271101	30-Jun 2003	4659,4869,3022
NGC 4073	0.0204	1.89	0.413	0093060101	21-Dec 2001	0,13974,9347
NGC 4261	0.00785	1.55	0.161	0056340101	16-Dec 2001	26657,28362,20792
				0502120101	16-Dec 2007	85634,83316,63995
NGC 4325	0.0252	2.24	0.507	0108860101	24-Dec 2000	20858,20861,15955
NGC 4636	0.00565	1.81	0.117	0111190701	05-Jan 2001	58225,58938,50316
NGC 5044	0.00820	4.93	0.169	0037950101	13-Jan 2003	21853,22018,12655
NGC 5129	0.0232	1.76	0.468	0108860701	07-Jul 2002	16379,16073,12263
NGC 5322	0.00702	1.81	0.145	0071340501	24-Dec 2001	18493,18329,13313
NGC 5846	0.0063	4.26	0.130	0021540101	25-Jan 2001	0,0,25634
				0021540501	26-Aug 2001	13930,13129,7841
IC 1459	0.00569	1.18	0.117	0135980201	30-Apr 2002	28637,28339,23416

background events by the ratio of the high energy (10–12 keV for MOS and 12–14 keV for pn) count rates of the observed and closed filter-wheel data, using a large annular region positioned around the group. The particle background scale factors were high (> 2) in four of the groups (HCG 42, HCG 97, NGC 4697 and NGC 5171) so these groups could not be used in the remainder of this analysis because the uncertainties on the background would be too high.

When I extracted the spectrum from a region in the observed data, I also extracted the spectrum from this region from the corresponding closed filter-wheel data. These observed and closed spectra were grouped together using *fungroup* to a minimum of 20 counts per bin after background subtraction. The grouped data also ignored the first 20 bins in the MOS data and the first 50 in the pn data which corresponds to energies below 0.4 keV. The X-ray fitting was carried out using XSPEC 11.3 in the energy range 0.4 – 7.0 keV where the *XMM-Newton* response is well calibrated.

To account for Galactic and cosmic X-ray background emission local to the source, I extracted a spectrum from an annular, local background region located beyond the edge of the group emission. The local background emission from this region was modelled as a double *apec* model, to account for emission from the Galactic bubble, and a power-law model absorbed by the Galactic N_H in the direction of the target (Lumb et al. 2002), which was fixed at a value taken from H I radio observations (Dickey & Lockman 1990). I then scaled the normalisations of this model, to account for the difference in area between the source region and the local background region, and included this background spectral fit in the source spectrum model. The group emission was fitted as an absorbed *apec* model from which the global temperature and abundance was measured. In the cases where there is complicated temperature structure in the group, e.g. NGC 4325, a double absorbed *apec* model was used to confirm multiple component thermal emission from the group. Where the abundance was not well constrained, a fixed value of $0.3 Z_{\odot}$ was used (NGC 383, NGC 1052, NGC 3923 and NGC 5322). The spectral fits are shown in Table 6.2.

To confirm whether there was temperature structure within the groups with poor global temperature fits, I first checked the literature for evidence of bubbles, cavities and shocks within the group gas, and then fitted temperature profiles to the group gas. I used the radial surface brightness profiles described in Section 6.3.2 to define annular regions, from which I extracted the spectra and fitted the same model as for the global fitting. In cases where the data quality prevented the fitting of abundances to the annular spectra, I fixed the abundance to that measured during the global spectral fitting. The temperature profiles with fixed abundances are shown in Figures 6.2 and 6.3. The temperature measurements are discussed further in Section 6.4.1.

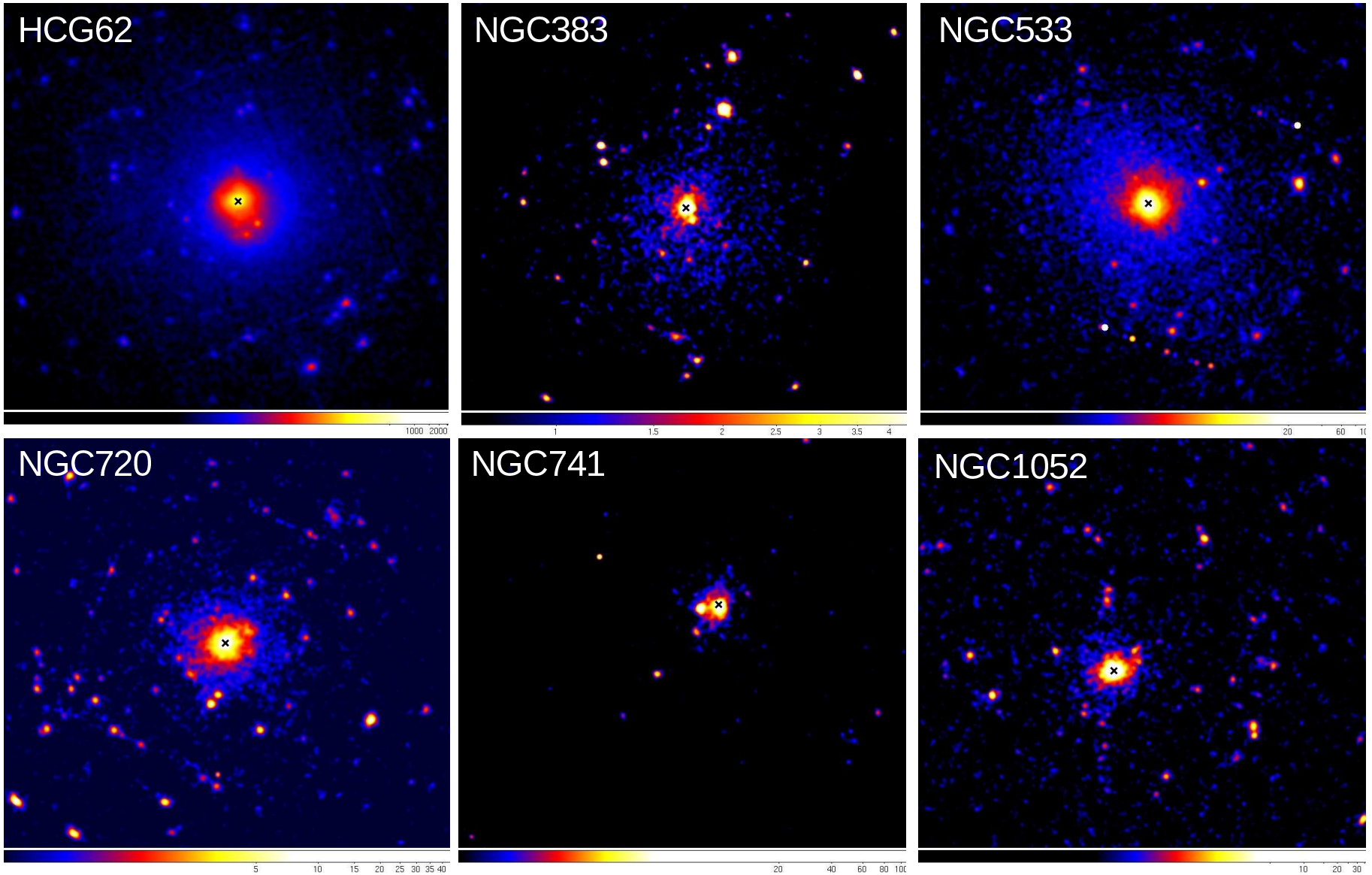

Figure 6.1: Exposure-corrected images for the groups in this sample, smoothed with a Gaussian of 6 pixels (9 arcsec) using DS9. The position of the group as determined by OP04 are shown by the crosses.

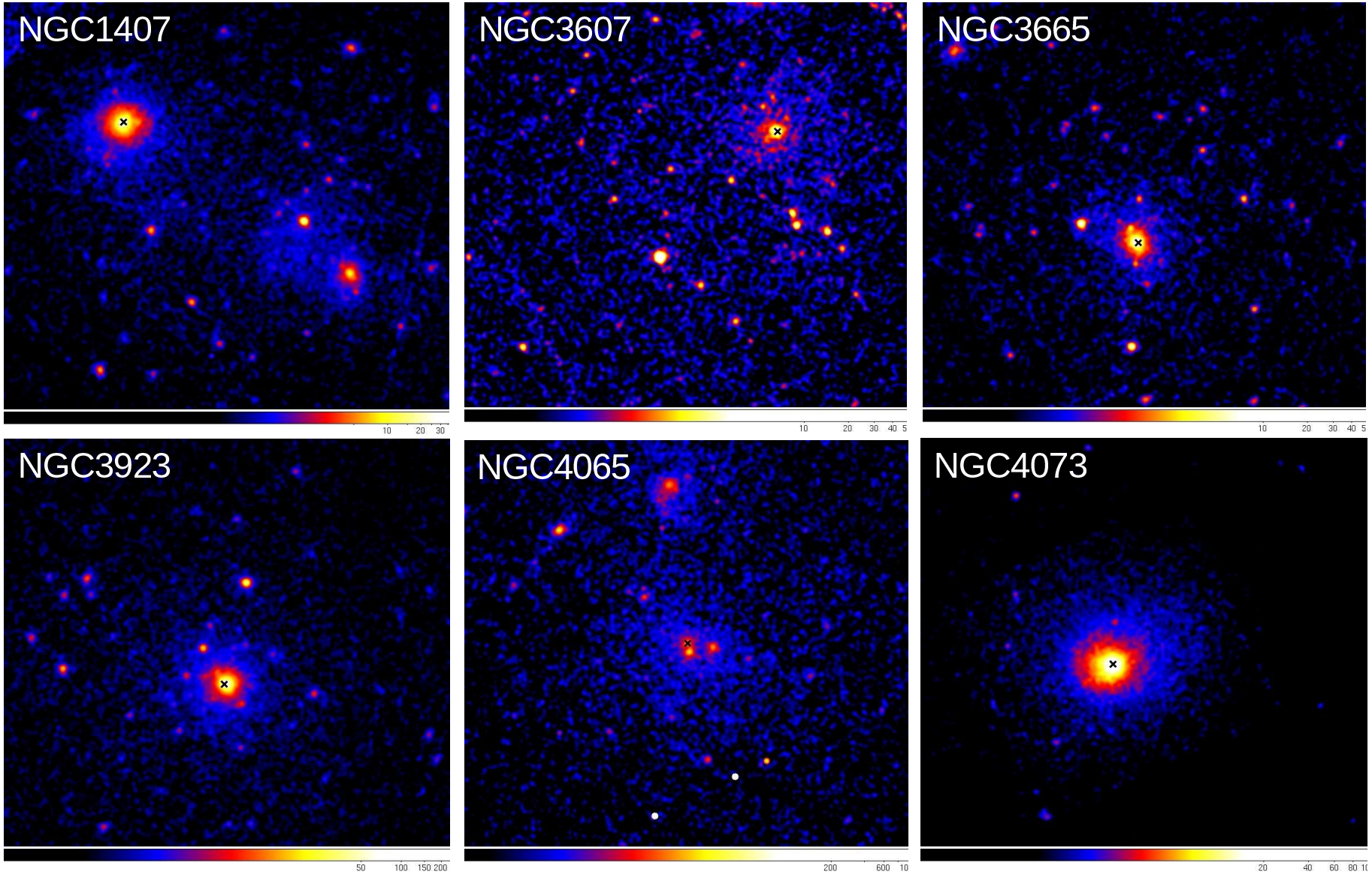

Figure 6.1 continued

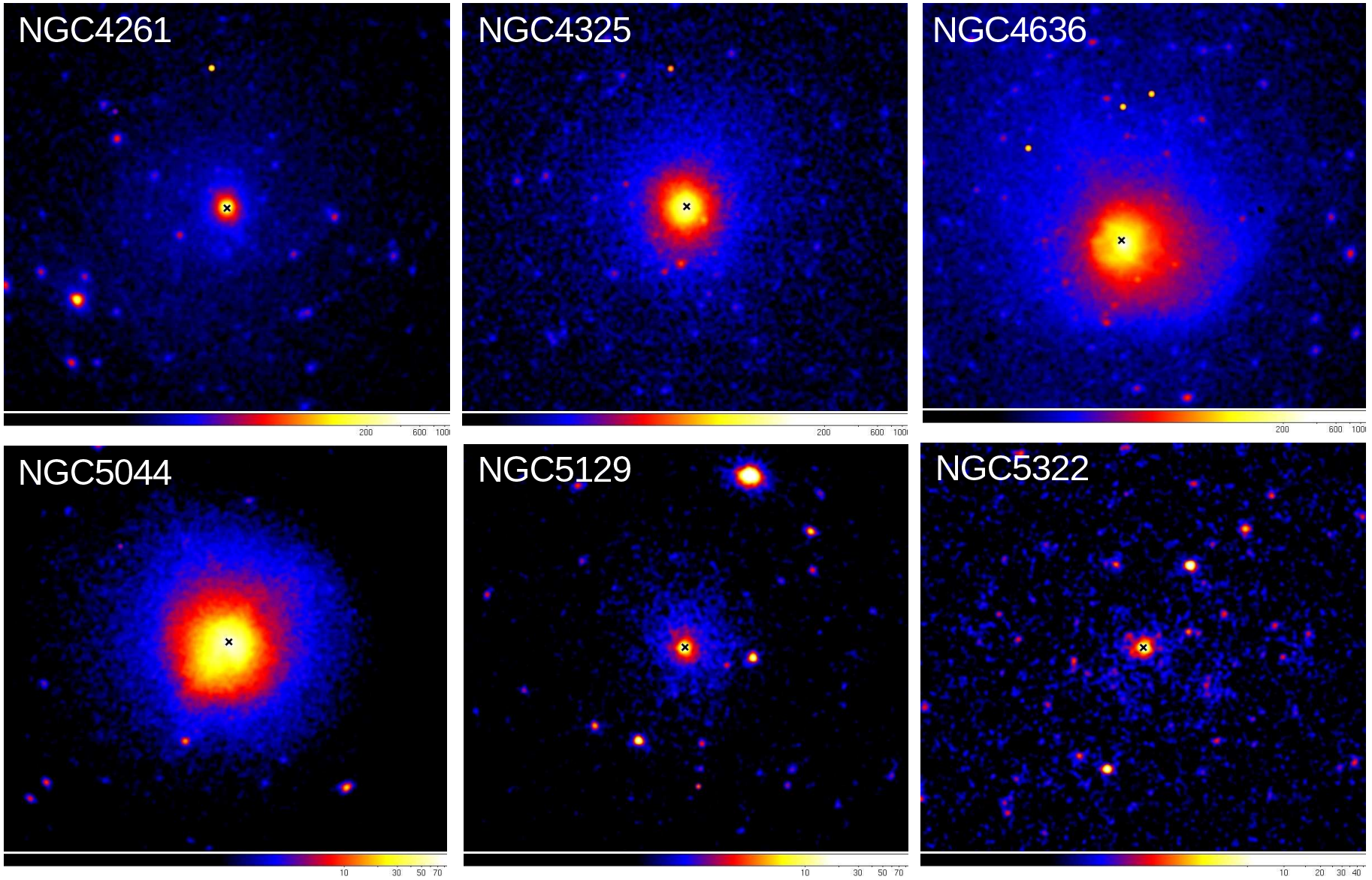

Figure 6.1 continued

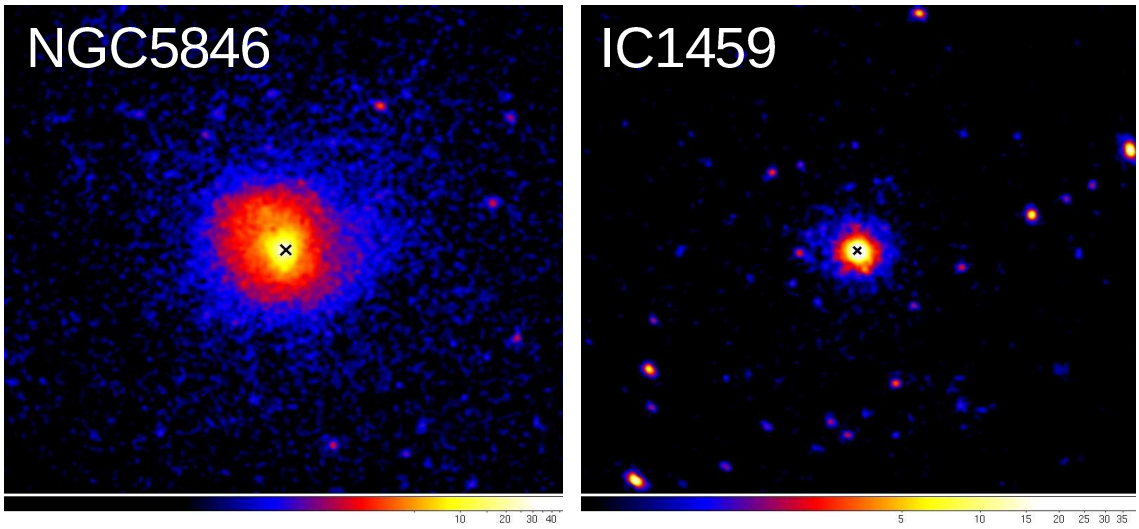

Figure 6.1 continued

6.3.2 Spatial Analysis

I analysed the group gas distribution using radial surface brightness profiles as discussed in Section 1.5, extracted from concentric annular regions with the point sources and chip gaps masked out. For these surface brightness profiles, the central AGN were not excluded from the profiles but modelled as a point source during the analysis. Vignetting correction and double background subtraction were performed as for the spectral analysis. The profiles for each camera in each observation were scaled by the livetime and combined to a single profile for each group. These combined profiles were convolved with the PSF and fitted with models including point-source components, a single β model (e.g. Birkinshaw & Worrall 1993) (Equation 1.13) and in some cases a projected double-β model (Croston et al. 2008a), which is defined as the projected line-of-sight sum of two β models in gas density (Equation 1.15).

I used the Markov-Chain Monte Carlo (MCMC) method described by Croston et al. (2008a) to explore the parameter space of these models and thus find the Bayesian estimates of the core radii (r_c) and β values which are shown in Table 6.3, as well as the maximum likelihood model for each group, which is overplotted on the surface brightness profiles shown in Figure 6.4. This MCMC method uses the Metropolis-Hastings algorithm in a manner similar to the METRO code by Hobson & Baldwin (2004), but implemented to run on a cluster of multiple processors using the Message Passing Interface (MPI)[1]. Plausible ranges for the core radii, normalisations and β values were estimated and set as priors for the MCMC method. The uncertainties corresponding to 1σ errors for 2 or 4 interesting parameters, consistent with Table 6.3, for the β and projected double-β models respectively were determined using 1-dimensional projections of the minimal n-dimensional volume that encloses 68 per cent of the posterior probability distribution as returned by the MCMC code. This code was also used to measure the luminosities discussed in Section 6.4.3.

[1] see Hardcastle et al. (2009b) for more details

The first profile shown in Figure 6.4 is for HCG 62 (top left panel) and is an example of a β-model fit and NGC 383 (top right panel of this figure) is an example of a projected double-β model. The residuals shown beneath the surface brightness profile and the reduced χ^2 suggest that these are poor fits; however, this is likely due to the high quality of the data and would thus be reduced if the profile was smoothed further. These residuals in the surface brightness profiles also reflect the complicated structures seen in many of these groups. For example, NGC 4636 has ripples in the surface brightness that are clearly seen in the residuals. The reliability of these fits is discussed further in Section 6.4.2.

In Section 6.6, I present summaries of the previous work on the groups in this sample, which includes the β-model fits by OP04. They fitted the standard β-model described by Equation (1.13) to all of the surface brightness profiles, including additional free parameters for the ellipticity and position angle of the group gas. In the cases where the fit was inadequate, they added a second component and constrained the first component to an zero ellipticity. The combinations of OP04's different approach to multiple components and the additional ellipticity and position angle information makes a comparison to these previous results difficult and so when I discuss the results of the individual groups in Section 6.6, I have only considered whether a second component was required and not OP04's specific fit values.

Table 6.2: Comparison of the spectrally fitted temperature, those determined from the temperature profiles.

Group	kT_{spec}	Z	χ^2_{red} (dof)	Integrated Temperature (keV)			Radial Range	R_{500}
	(keV)	$Z_\odot$		mean kT_m	weighted mean kT_{wm}	truncated kT_{twm}	R (arcsec)	(kpc)
HCG 62	$0.983^{+0.004}_{-0.004}$	$0.25^{+0.006}_{-0.006}$	3.47 (1120)	0.98 ± 0.18	0.93 ± 0.05	1.23 ± 0.10	150 – 675	438.95
NGC 383	$1.36^{+0.006}_{-0.006}$	0.3	1.61 (1568)	1.47 ± 0.01	1.44 ± 0.06	1.44 ± 0.01	50 – 600	538.88
NGC 533	$1.212^{+0.008}_{-0.008}$	$0.36^{+0.013}_{-0.013}$	2.33 (550)	1.17 ± 0.21	1.13 ± 0.06	1.38 ± 0.10	100 – 547	495.83
NGC 720	$0.584^{+0.005}_{-0.005}$	$0.33^{+0.021}_{-0.034}$	1.37 (302)	0.62 ± 0.11	0.62 ± 0.01	0.61 ± 0.01	25 – 1656	324.25
NGC 741	$1.576^{+0.062}_{-0.078}$	$0.37^{+0.08}_{-0.07}$	1.13 (401)	1.49 ± 0.29	1.46 ± 0.28	1.55 ± 0.18	100 – 553	577.22
NGC 1407	$1.040^{+0.007}_{-0.008}$	$0.27^{+0.01}_{-0.01}$	1.73 (878)	1.00 ± 0.40	1.00 ± 0.04	1.24 ± 0.03	75 – 1720	276.87
NGC 3607	$0.569^{+0.013}_{-0.012}$	$0.27^{+0.06}_{-0.04}$	1.54 (280)	0.49 ± 0.32	0.48 ± 0.06	0.39 ± 0.05	100 – 2358	297.71
NGC 3665	$0.442^{+0.025}_{-0.016}$	$0.26^{+0.17}_{-0.06}$	1.49 (384)	0.46 ± 0.09	0.48 ± 0.05	0.42 ± 0.01	25 – 1407	277.12
NGC 3923	$0.489^{+0.014}_{-0.024}$	0.3	1.71 (899)	0.58 ± 0.13	0.58 ± 0.01	0.55 ± 0.02	50 – 2113	294.36
NGC 4065	$1.214^{+0.080}_{-0.187}$	$0.18^{+0.03}_{-0.08}$	1.67 (396)	0.94 ± 0.07	0.94 ± 0.07	0.94 ± 0.07	0 – 425	487.43
NGC 4073	$1.810^{+0.032}_{-0.032}$	$0.55^{+0.03}_{-0.03}$	1.26 (211)	1.87 ± 1.21	1.85 ± 0.06	2.00 ± 0.04	75 – 487	624.39
NGC 4261	$1.719^{+0.070}_{-0.013}$	$0.44^{+0.04}_{-0.03}$	1.66 (1218)	1.28 ± 0.47	1.05 ± 0.14	1.97 ± 0.07	100 – 1242	603.07
NGC 4325	$0.927^{+0.003}_{-0.003}$	$0.47^{+0.01}_{-0.01}$	2.21 (615)	0.93 ± 0.81	0.93 ± 0.02	0.99 ± 0.02	70 – 397	428.15
NGC 4636	$0.949^{+0.003}_{-0.003}$	$0.59^{+0.01}_{-0.01}$	5.91 (731)	0.83 ± 1.02	0.99 ± 0.08	0.91 ± 0.01	125 – 186	419.12
NGC 5044	$0.957^{+0.002}_{-0.001}$	$0.46^{+0.005}_{-0.005}$	6.37 (905)	0.98 ± 0.30	0.98 ± 0.04	1.33 ± 0.08	200 –1189	432.09
NGC 5129	$0.882^{+0.011}_{-0.011}$	$0.38^{+0.04}_{-0.03}$	1.43 (445)	0.85 ± 0.17	0.85 ± 0.03	0.92 ± 0.02	50 – 430	414.47
NGC 5322	$0.382^{+0.057}_{-0.042}$	0.3	1.18 (348)	0.47 ± 0.05	0.49 ± 0.10	0.37 ± 0.02	50 – 1387	254.93
NGC 5846	$0.737^{+0.003}_{-0.003}$	$0.42^{+0.003}_{-0.003}$	1.89 (489)	0.80 ± 0.18	0.79 ± 0.04	1.37 ± 0.10	300 – 1544	372.63
IC 1459	$0.564^{+0.021}_{-0.017}$	$0.81^{+3.57}_{-0.83}$	2.13 (512)	3.80 ± 5.33	3.82 ± 0.78	0.70 ± 0.02	50 – 1708	317.80

Table 6.3: Bayesian estimated best-fitting model results for the β and projected double-β model fits. Errors are 1σ errors for two interesting parameters irrespective of the model as the extended and central values are not correlated.

Group	Extended		Central	
	r_{core} (kpc)	β_{fit}	r_{core} (kpc)	β_{fit}
HCG 62	$27.32^{+21.64}_{-17.33}$	$0.99^{+0.21}_{-0.02}$	$1.23^{+4.08}_{-0.75}$	$0.46^{+0.04}_{-0.08}$
NGC 383	$141.10^{+82.71}_{-11.36}$	$0.82^{+0.48}_{-0.16}$	$1.05^{+0.37}_{-0.51}$	$0.59^{+0.04}_{-0.10}$
NGC 533	$206.90^{+184.51}_{-41.47}$	$0.69^{+0.15}_{-0.39}$	$1.85^{+0.47}_{-0.18}$	$0.54^{+0.01}_{-0.03}$
NGC 720	$1.39^{+0.13}_{-0.11}$	$0.50^{+0.02}_{-0.02}$	n/a	n/a
NGC 741	$0.50^{+0.39}_{-0.27}$	$0.40^{+0.02}_{-0.02}$	n/a	n/a
NGC 1052	$0.21^{+0.11}_{-0.05}$	$0.51^{+0.17}_{-0.05}$	n/a	n/a
NGC 1407	$0.84^{+0.12}_{-0.11}$	$0.49^{+0.02}_{-0.02}$	n/a	n/a
NGC 3607	$64.38^{+20.58}_{-7.99}$	$0.44^{+0.04}_{-0.14}$	$0.14^{+0.01}_{-0.06}$	$0.49^{+0.01}_{-0.04}$
NGC 3665	$0.80^{+0.16}_{-0.13}$	$0.49^{+0.04}_{-0.03}$	n/a	n/a
NGC 3923	$0.32^{+0.10}_{-0.09}$	$0.53^{+0.02}_{-0.02}$	n/a	n/a
NGC 4065	$2251.05^{+737.29}_{-30.42}$	$0.60^{+0.09}_{-0.30}$	$4.82^{+1.14}_{-0.83}$	$0.57^{+0.03}_{-0.05}$
NGC 4073	$176.09^{+184.48}_{-9.46}$	$0.70^{+0.17}_{-0.40}$	$1.70^{+1.38}_{-0.24}$	$0.44^{+0.02}_{-0.04}$
NGC 4261	$61.78^{+19.69}_{-15.16}$	$0.80^{+0.32}_{-0.19}$	$0.99^{+0.37}_{-0.04}$	$0.66^{+0.06}_{-0.02}$
NGC 4325	$9.17^{+0.51}_{-0.50}$	$0.59^{+0.01}_{-0.01}$	n/a	n/a
NGC 4636	$6.92^{+1.16}_{-1.52}$	$0.71^{+0.05}_{-0.13}$	$0.45^{+0.78}_{-0.12}$	$0.65^{+0.02}_{-0.25}$
NGC 5044	$28.80^{+1.70}_{-15.16}$	$0.93^{+0.37}_{-0.19}$	$5.87^{+1.90}_{-0.63}$	$0.52^{+0.02}_{-0.02}$
NGC 5129	$70.54^{+69.31}_{-16.33}$	$0.69^{+0.21}_{-0.25}$	$0.95^{+0.12}_{-0.48}$	$0.52^{+0.01}_{-0.15}$
NGC 5322	$0.19^{+0.16}_{-0.11}$	$0.51^{+0.08}_{-0.03}$	n/a	n/a
NGC 5846	$18.33^{+0.69}_{-0.23}$	$1.17^{+0.03}_{-0.01}$	$1.61^{+0.65}_{-0.19}$	$1.01^{+0.19}_{-0.01}$
IC 1459	$4.24^{+0.07}_{-0.54}$	$0.70^{+0.01}_{-0.04}$	$0.14^{+0.01}_{-0.03}$	$0.96^{+0.05}_{-0.11}$

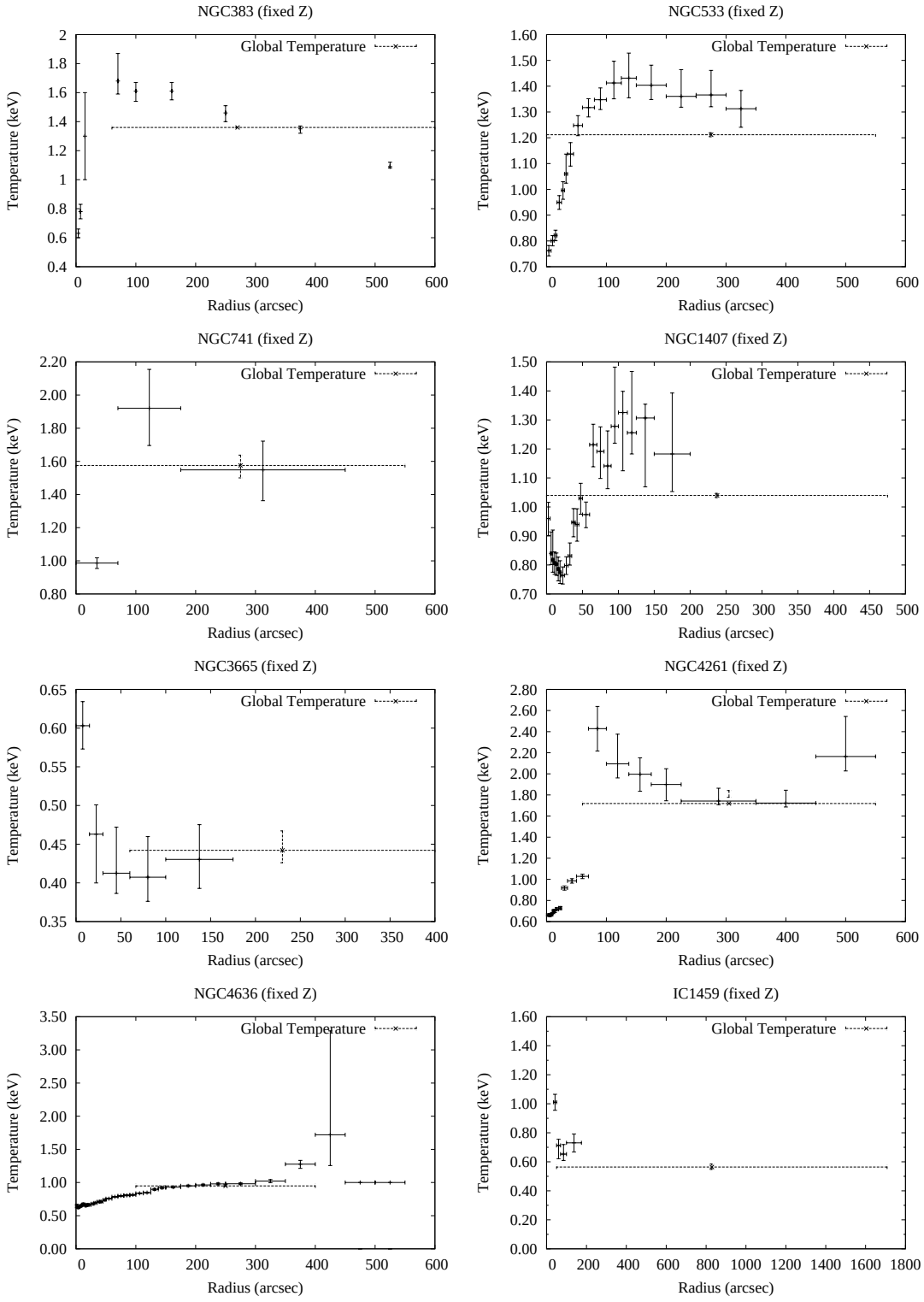

Figure 6.2: Temperature profiles for the radio-loud groups with abundances fixed at the globally fitted values. The spectrally measured global temperatures and the corresponding source region radial coverage is shown by the dashed points. NGC 1052 is also radio-loud, but its X-ray emission is dominated by the central AGN so no profile could be made.

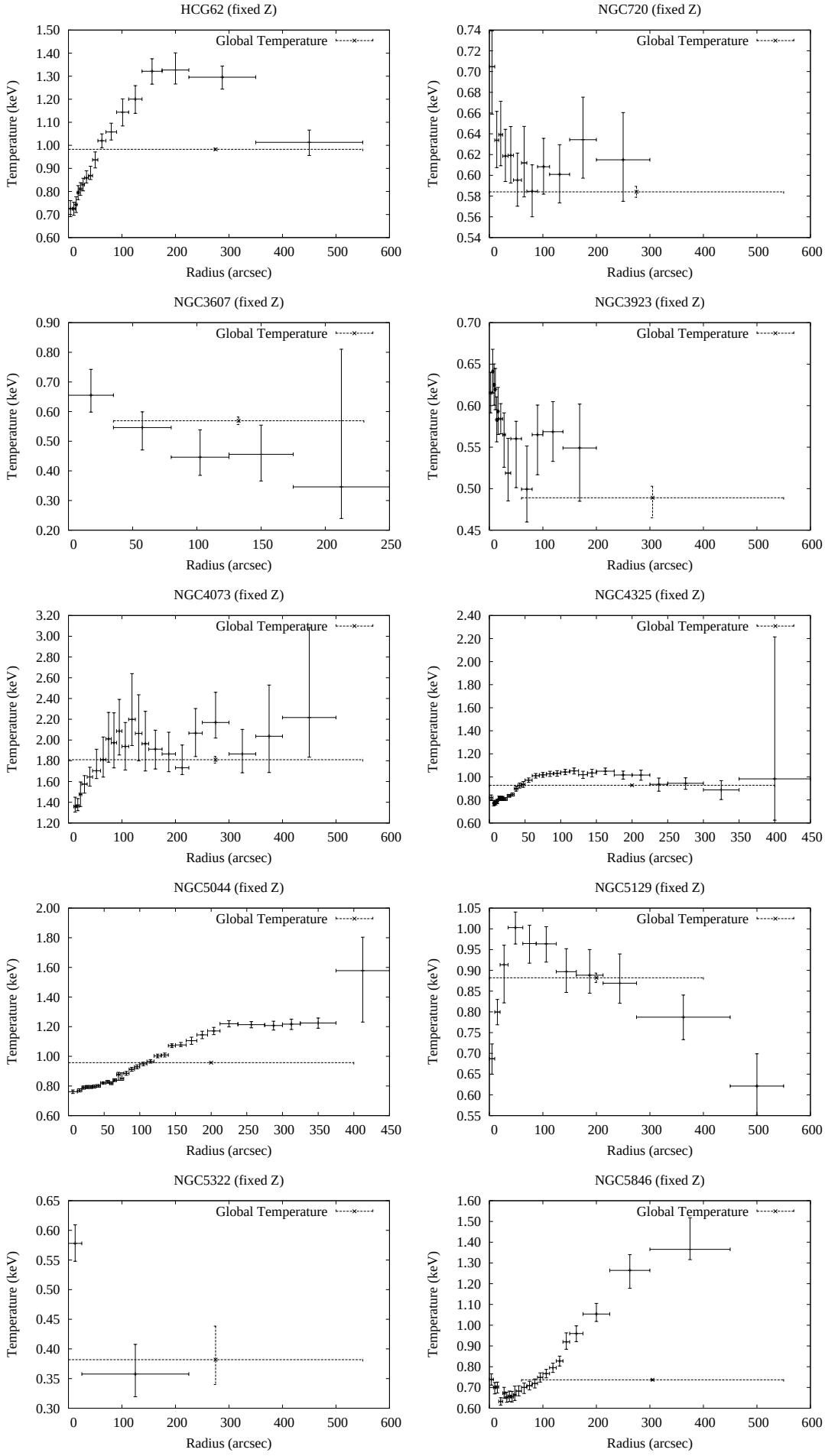

Figure 6.3: Temperature profiles for the radio-quiet groups with abundances fixed at the globally fitted values. The spectrally measured global temperatures and the corresponding source region radial coverage are shown by the dashed points.

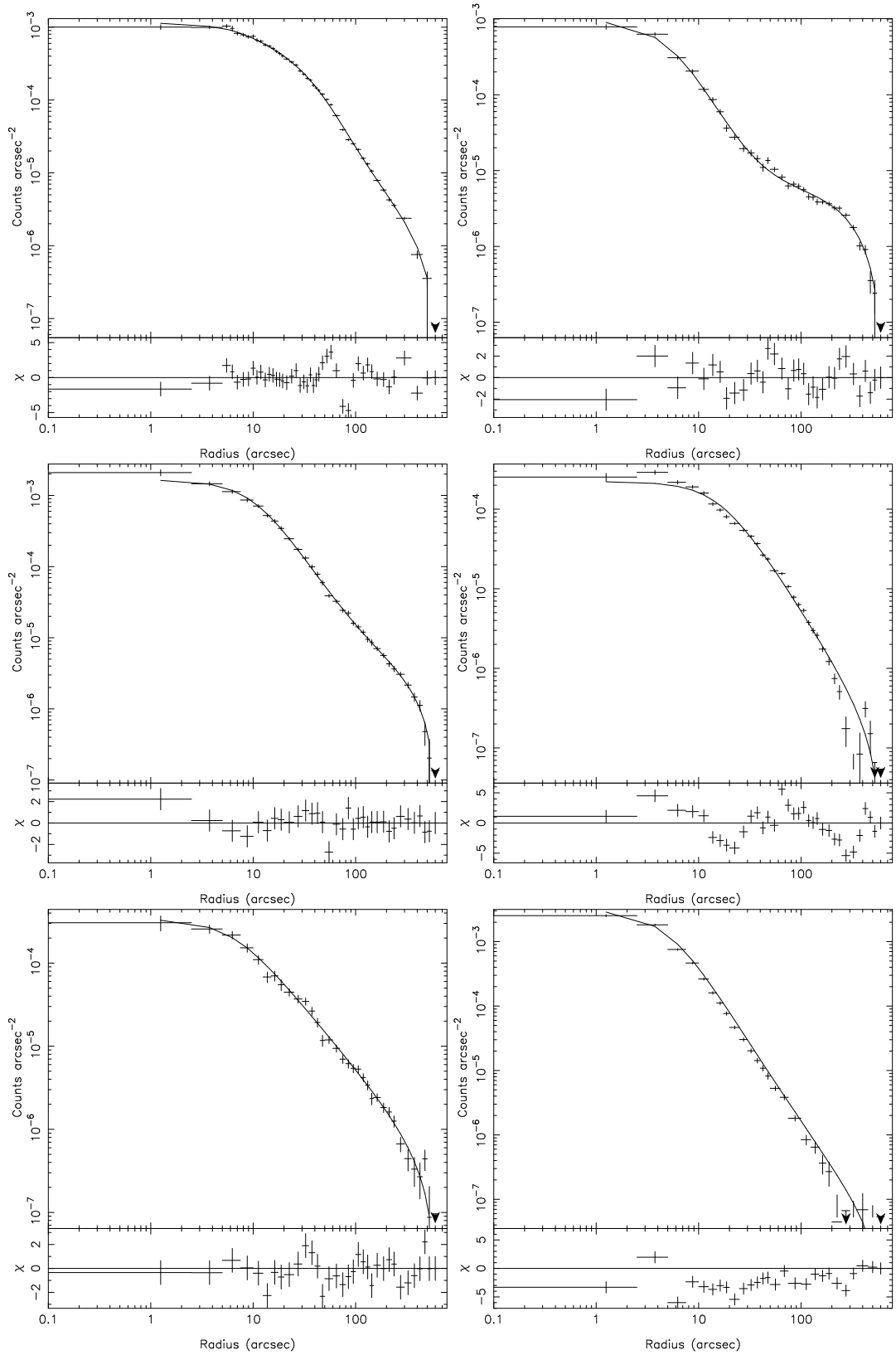

Figure 6.4: Surface brightness profiles for the radio-loud groups with the maximum likelihood fits overplotted. From left to right are the surface brightness profiles of HCG 62 and NGC 383 on the top row, NGC 533 and NGC 720 on the middle row, and NGC 741 and NGC 1052 on the bottom row.

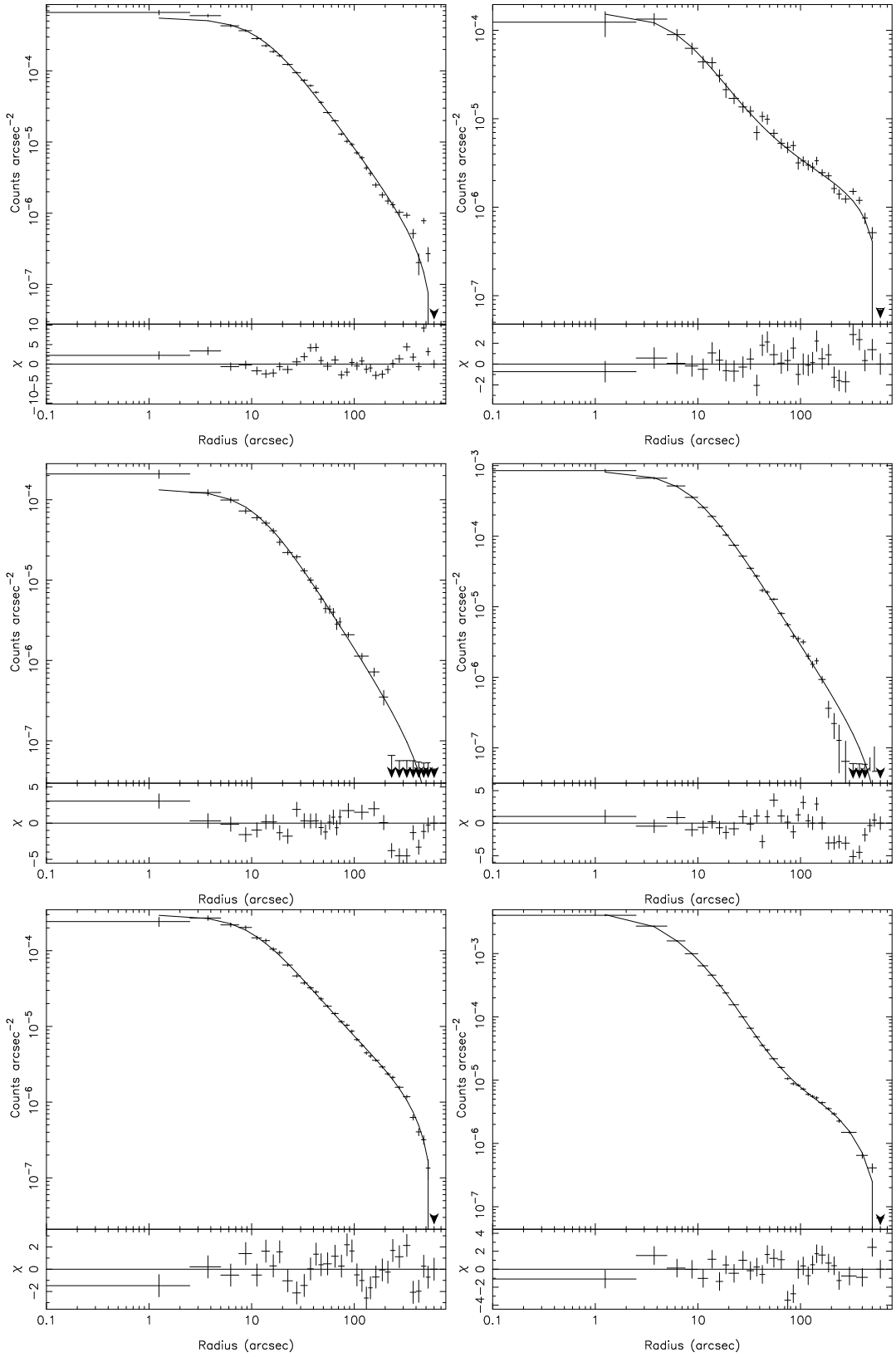

Figure 6.4 continued. From left to right are the surface brightness profiles of NGC 1407 and NGC 3607 on the top row, NGC 3665 and NGC 3923 on the middle row, and NGC 4073 and NGC 4261 on the bottom row.

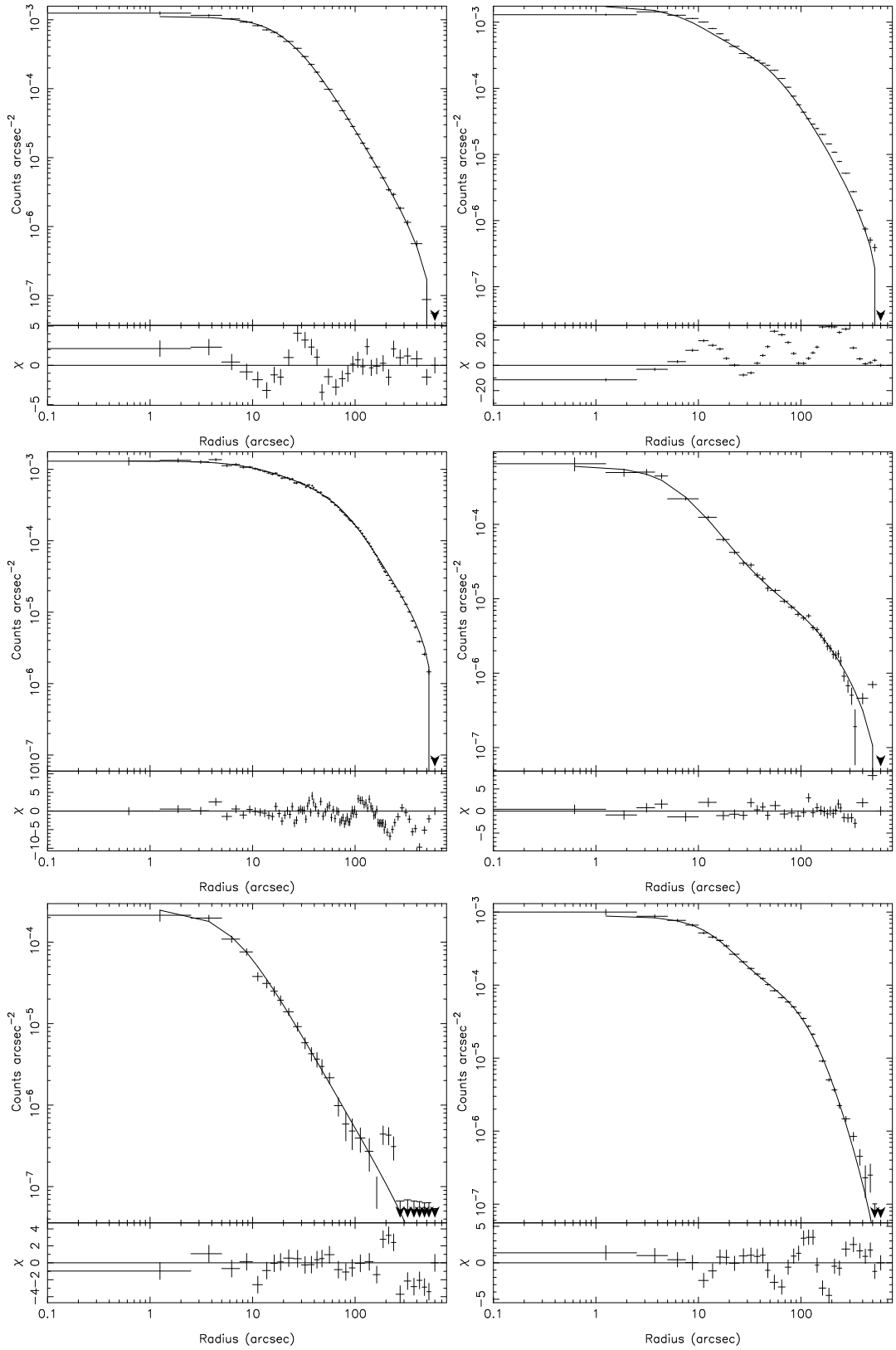

Figure 6.4 continued. From left to right are the surface brightness profiles of NGC 4325 and NGC 4636 on the top row, NGC 5044 and NGC 5129 on the middle row, and NGC 5322 and NGC 5846 on the bottom row.

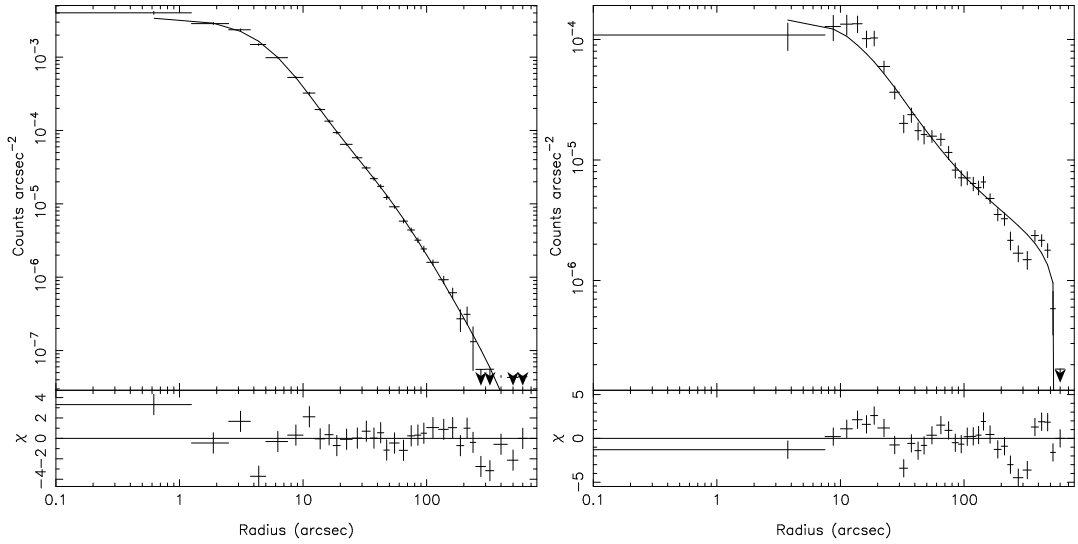

Figure 6.4 continued. The surface brightness profiles of IC 1459 (left) and NGC 4065 (right).

6.4 Results

6.4.1 Global Temperatures

In this work, I measured the global temperatures of the group gas directly from our *XMM-Newton* data using circular source regions, except where there was an AGN in the core of the group in which case I used an annular source region (Section 6.3.1). In the majority of cases, the absorbed *apec* model was a good fit to the source spectrum (14/20 groups have fits with $\chi^2_{red} < 2.0$). In the six cases where the fit was not acceptable, there are previous reports of complicated temperature structures, such as bubbles, cavities, filaments and shock features (see Section 6.6 for summaries of the structures and previous work on the groups in this sample). These spectrally measured global temperatures, T_{sp}, are consistent within 1σ of the OP04 *ROSAT* results for only seven of these groups (see left panel of Figure 6.5, blue points), which I attribute to *ROSAT*s poorly constrained PSF and to the fact that the regions used may include contamination from unresolved point sources, AGN, and hot ISM gas within the core of the BGG. These sources would contribute additional spectral components to the X-ray emission which would result in an incorrect temperature being fitted to the gas; point sources, such as X-ray binaries (XRBs), should be modelled out as a power-law, an AGN would also need power-law model(s) and an additional thermal component for the hot ISM gas within the core to model them separately. There is, however, no systematic difference between these spectrally fitted temperatures and the OP04 results. A regression fit of this comparison shows that these results are not significantly different ($T_{sp} = (0.98^{+0.05}_{-0.07})T_{OP} - 0.04^{+0.07}_{-0.05}$).

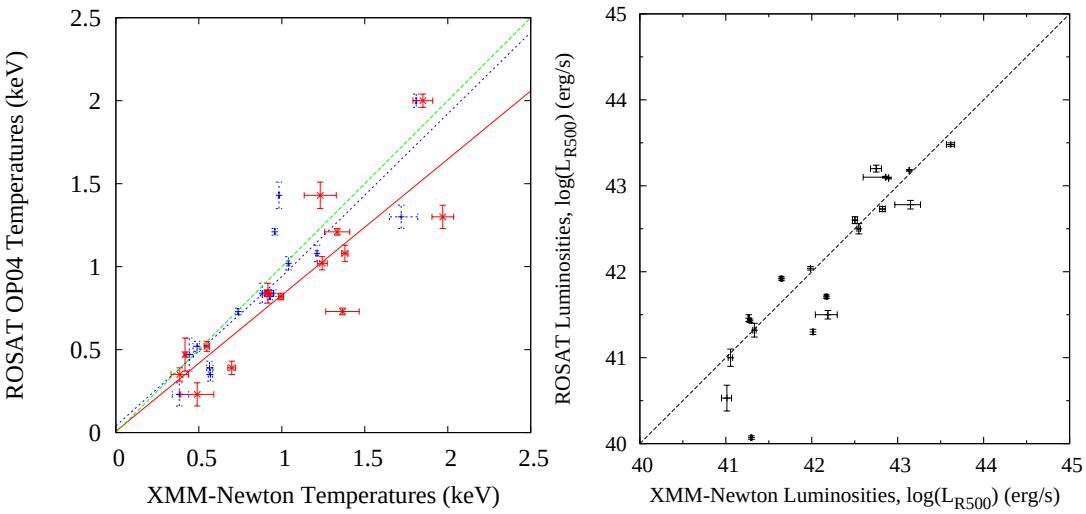

Figure 6.5: Comparison between these *XMM-Newton* temperatures (left panel) and luminosities (right panel) and the *ROSAT* results by Osmond & Ponman (2004). In the temperature comparison, the spectral temperatures are shown in blue, and the profile temperatures in red with the corresponding regression line fits plotted in the same colours. The green line is a line of equality.

I was able to measure the temperature profiles for all except one of our groups, NGC 1052, where the gas emission was dominated to the edge of observed group emission by a central AGN (See Note 6.6.6). The spectrally fitted global temperature was therefore used for NGC 1052 in my luminosity-temperature relationship analysis (Section 6.5). I used the surface brightness profiles to determine the radial bins for the temperature profile. The surface brightness annuli were combined until there were more than 600 background subtracted counts in each radial bin for the majority of the groups; in the case of NGC 5044, the annuli were binned to more than 4000 background subtracted counts per temperature bin due to the high quality of these data. The high number of background subtracted counts per radial bin assured there were sufficient data to group the spectrum and fit the temperature using XSPEC.

These temperature profiles supported the complicated temperature structure explanation for those groups with poor spectral temperature fits and also confirmed the presence of cool-cores (CCs) in many of the groups (11/20 groups have CCs). Using these temperature profiles, I calculated a mean and weighted mean temperature for each of the groups (Table 6.2) to determine whether the spectrally fitted temperatures were affected by the presence of a CC. I weighted the fitted temperature for each annular region by its normalisation so that the combined temperature mimics the XSPEC method of fitting the temperatures.

In order to compare the same physical volume of the group gas, we considered truncating the integrated temperature to 10% and 20% of R_{500} for each group and also to the same physical radius of 200 kpc; R_{500} is the radius where the gas density is 500 times the critical density of the Universe.

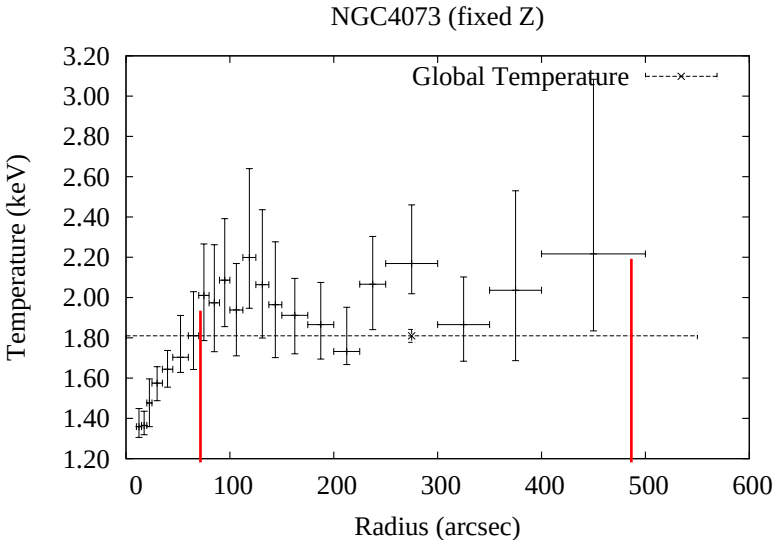

Figure 6.6: Integrated temperature radial limits for the group NGC 4073 based on eliminating the contribution from the cool core and a 200 kpc outer limit. The limits are shown by the red, bold lines demonstrating how the integrated temperature of NGC 4073 was limited to the range 75 – 487 arcsec (31 – 200 kpc).

I have used the physical radius of 200 kpc as the outer limit of my integrated temperatures, which lies within the detected limit of the profiles and is not dependent on the temperature measurement.

In many cases, the profile was not detected to large enough radii for these limited radial ranges to make a significant difference to the integrated temperatures. I calculated the R_{500} radii using the definition of Arnaud et al. (2005); for a radius of δ times the critical density, R_δ, Arnaud et al. determined that

$$h(z)R_\delta = B_\delta \left(\frac{kT}{5keV}\right)^\beta \tag{6.1}$$

where $h(z) = (1+z)\sqrt{1+z\Omega_m + \Omega_\Lambda/(1+z)^2 - \Omega_\Lambda}$ and kT is the groups global temperature (in keV). For R_{500}, they found $B_{500} = 1104 \pm 13$ kpc and $\beta = 0.57 \pm 0.02$. The R_{500} radii are dominated by 5% errors due to the systematic error of the calculation. I used the spectrally fitted global temperatures to determine R_{500}, which is then used to determine the mean temperatures so the calculation becomes quite circular. This is why I have used an outer limit of 200 kpc.

As cool cores affect the spectral temperature fits of the group gas almost as much as the presence of an AGN, I decided to also limit the inner radius as I aim to measure the group gas temperature. The inner cut-off radius was decided by eye, choosing the point where the profile levels out beyond either the drop due to a cool core or the peak due to an AGN. This is demonstrated using the temperature profile of NGC 4073 in Figure 6.6.

My truncated, weighted-mean temperatures, T_p are not systematically higher or lower than the spectrally fitted temperatures or those measured using the whole profile, but this is expected due to the truncation of the profile clipping high temperatures due to central AGN, and low temperatures due to cool cores. These profile temperatures are shown in the left panel of Figure 6.5 with red

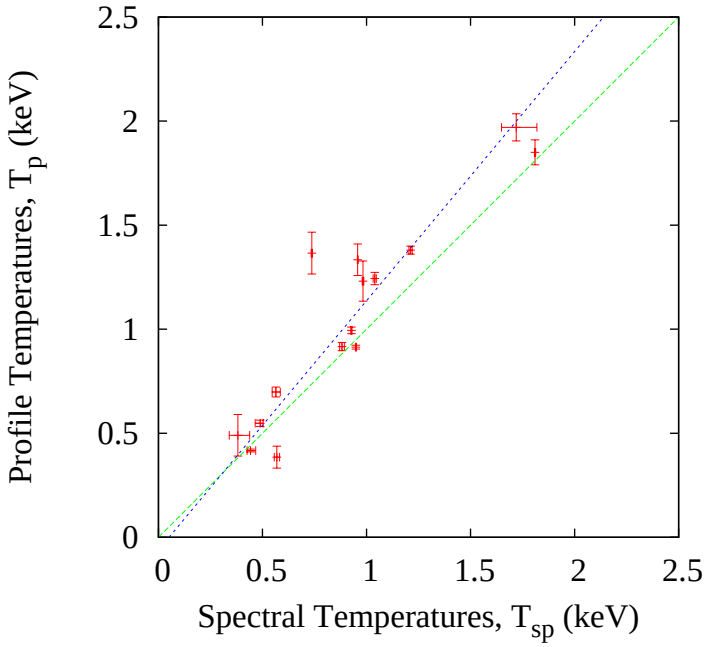

Figure 6.7: Comparison between the spectral temperatures and profile temperatures measured in this work. The green line is an equality line and the blue line is the fitted regression line.

points in a comparison to the temperatures measured by OP04 from the *ROSAT* data and I found that these temperatures are slightly hotter than the *ROSAT* spectrally measured temperatures in most cases, which is likely due to the exclusion of contributions from cool cores in this work; a regression fit supports this, $T_p = 0.82^{+0.03}_{-0.06} T_{OP} + 0.01^{+0.05}_{-0.05}$.

I also fitted a line of regression to compare the spectral- and profile-derived temperatures and found that these temperatures are also consistent with a higher profile-derived temperature; $T_{sp} = 0.84^{+0.02}_{-0.03} T_p + 0.05^{+0.03}_{-0.03}$. These data are shown in Figure 6.7.

6.4.2 Surface Brightness Profiles

As discussed in Section 6.3.2, I fitted single-β and projected double-β models to the combined surface brightness profiles for all of the groups in this sample; the maximum likelihood fits are shown overplotted on the surface brightness profiles in Figure 6.4 and the Bayesian estimates are shown in Table 6.3. For the majority of the groups (13/15) I agree with the model selection of OP04; however for NGC 5846 and IC 1459, I have better constraints using a projected double-β model. I have successfully fitted models for two additional groups, NGC 1052 and NGC 5322, and although I have a reasonable projected double-β-model fit for NGC 4636, a triple-β model would likely better fit these data, but this is beyond the scope of this work as it is not necessary for obtaining a reliable luminosity measurement. Although the results of OP04 are a good initial comparison, they also fitted the ellipticity of the group emission and the PSF of *ROSAT* is not well known so could not be accurately accounted for in their fits.

As mentioned in Section 6.3.2, the reduced χ^2 values for these model fits are not formally good, but I believe this is a consequence of the high quality of the data and real physical deviations in the gas distribution rather than a genuine poor fit. Similar residuals have been found using other models for fitting the temperature and densities simultaneously (Sanderson & Ponman 2010), and it was suggested in that work that less viralised systems that are more likely to have interacting galaxies would have distorted morphologies, which are not well modelled by these models as they assume spherical symmetry.

6.4.3 Luminosities

My luminosities were determined by integrating each of the surface brightness fits modelled in the MCMC code, extrapolating out to R_{500}. I used the truncated, weighted-mean temperatures, as described in Section 6.4.1, in these calculations and I converted the surface brightness count rates into flux using a conversion factor determined using the bolometric flux of the best fitting spectral model and the sum of the model count-rates of each dataset. In the comparisons with previous results and with the temperatures, I use the Bayesian estimated luminosities. My luminosities are all slightly higher than those measured by OP04 (Figure 6.5), which is likely due to the difference in our definitions of luminosities. In this work I have calculated the bolometric luminosities, extrapolating the X-ray fluxes (from 0.5 – 5.0 keV) to a luminosity between 0.01 keV to 100 keV. Although I have also integrated the luminosity out to a radius of R_{500}, as I used the temperature to determine this distance, my calculations of R_{500} may also be different, which would also add to a discrepancy in the luminosities.

I considered the contribution to the X-ray luminosity from the BGG low-mass X-ray binary (LMXB) population. Using the relationship between the integrated stellar luminosity in the optical band, L_B, and the LMXB X-ray luminosity, L_{LMXB} (Kim & Fabbiano 2004), I found that the majority of our groups X-ray luminosities exceeded L_{LMXB} by at least an order of magnitude. The worst affected group is NGC 5322, where the difference in $\log(L_X/L_{LMXB}) = 0.80$. The effect of LMXB on my luminosity measurements is therefore not significant and is not accounted for in the following analysis.

6.5 Luminosity-Temperature Relationship

In Figure 6.9 I have plotted the truncated, weighted-mean, *XMM-Newton* temperatures against the Bayesian estimated luminosities for all of the groups, except NGC 1052 where the spectrally fitted global temperature is used (see Section 6.4.1). I have also included on this plot, four previously observed relationships for the $L_X - T_X$ relation;

(i) the cluster relation (White et al. 1997)

$$\log(L_X) = (2.98)\log(T) + (42.67) \tag{6.2}$$

(ii) the group relation by Helsdon & Ponman (2000),

$$\log(L_X) = (4.9 \pm 0.8)\log(T) + (42.98 \pm 0.08) \tag{6.3}$$

(iii) the radio-loud group relation (Croston et al. 2005a),

$$\log(L_X) = (5.15 \pm 0.52)\log(T) + (42.27 \pm 0.07) \tag{6.4}$$

(iv) the radio-quiet group relationship (Croston et al. 2005a)

$$\log(L_X) = (4.42 \pm 0.51)\log(T) + (42.63 \pm 0.08) \tag{6.5}$$

By eye, it is difficult to tell if any of these relationships are a good fit to these data so I fitted my own regression line to these data using a Bayesian code developed by Hardcastle et al. (2009b), based on the MCMC algorithm, which takes account of both the errors and upper limits and determines the slope and intercept. I found that:

$$\log(L_X) = (5.06^{+0.05}_{-0.04})\log(T) + (42.44^{+0.01}_{-0.01}) \tag{6.6}$$

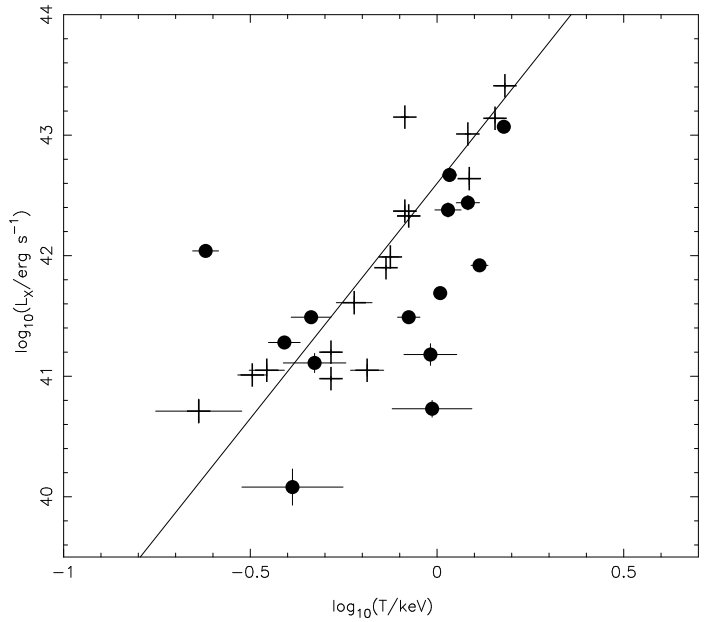

Figure 6.8: Luminosity-temperature relationships for the original group sample using *ROSAT* data (Croston et al. 2005a, Figure 2, bottom panel). The plus symbols are the radio-quiet groups and the filled circles are the radio-loud groups with the best fitting radio-quiet relationship, overplotted.

This relationship is consistent with the previously published relationships for groups but steeper than the cluster relationship (Equation 6.2). As the regression method can have a significant effect on the best fitting lines, I also fitted my own lines to the *ROSAT* data used by Croston et al. (2005a). I found the following expressions for the *ROSAT* data for all of the groups, the radio-loud groups and the radio-quiet groups respectively:

$$\log(L_X) = (4.71^{+0.48}_{-0.68})\log(T) + (42.56^{+0.07}_{-0.10}) \tag{6.7}$$

$$\log(L_X) = (4.64^{+0.64}_{-1.09})\log(T) + (42.21^{+0.11}_{-0.11}) \tag{6.8}$$

$$\log(L_X) = (4.57^{+0.41}_{-0.82})\log(T) + (42.82^{+0.12}_{-0.11}) \tag{6.9}$$

which are consistent with those fitted by Croston et al..

I also compare my results to the previously published relationships by defining the parameter, x, which takes account of the differences between the observed luminosities and temperatures and those expected from these relationships. I initially shifted the data so that the relationship intercepted the y-axis, L_X, at zero, and then I rotated the frame so that the relationship was the y-axis. What was previously the perpendicular distance of the data from the relationship is now the x-value, displayed on the x-axis. The values of x calculated using each relationship are shown in Figure 6.10.

The scatter in the L-T offset (x) for each relationship is not significantly different but the median value is closest to zero for the group relationship (Equation 6.3).

What is immediately obvious is the positions of the radio-loud and radio-quiet groups in this comparison, which is discussed in the next Section. In Section 6.5.3, I look at the effect of a cool core in the group to see if the scatter in my $L_X - T_X$ relationship is due to different populations of groups.

6.5.1 Radio Loud Groups

In 2005, Croston et al. used the measurements of luminosity and temperature by OP04 to determine whether the $L_X - T_X$ relationship of groups agrees with previous data for clusters. They found a steeper relationship for groups, but they also found that the radio-loud groups are hotter, for a given luminosity, than the radio-quiet groups (Figure 6.8).

Out of this sample of 20 groups, 9 are radio-loud groups and 11 are radio-quiet groups using the $c2$ cut-off; the effect of changing this cut-off is explored in Section 6.5.2. In all of the comparisons between these data and the previously published relationships, the L-T offset for radio-loud groups (the red data in Figure 6.10) is typically higher than for radio-quiet groups, which suggests that the radio-loud groups are hotter than the radio-quiet groups at a given luminosity. This is consistent with the suggestion by Croston et al. (2005a), that these elliptical dominated groups have different gas properties due to the short-term effects of radio-source heating in the radio loud groups. These elliptical-dominated groups have had similar numbers of radio-galaxy outbursts averaged over the group lifetime, causing a temporary temperature increase and less easily detectable long-term effects on the group luminosity and surface brightness profile.

To explore this further, I tested the L-T offsets of the radio-loud and radio-quiet groups with a 1D Kolmogorov-Smirnov (KS) test to determine whether the radio-loud and radio-quiet groups

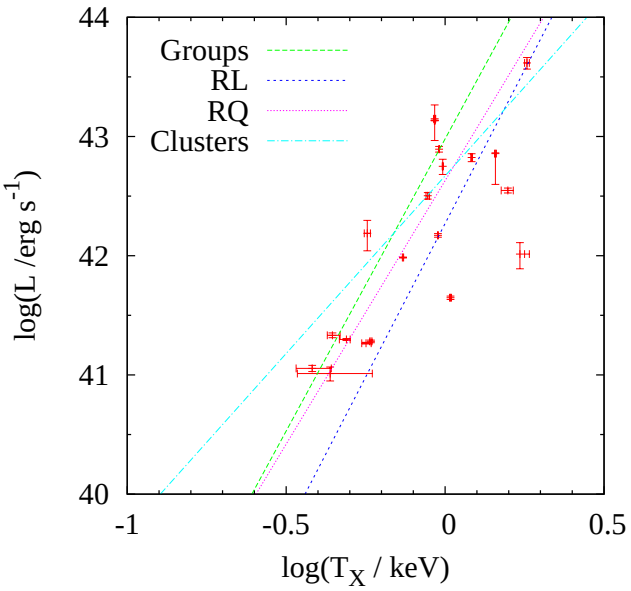

Figure 6.9: Luminosity-temperature relationships for all the groups using the truncated, weighted-mean profile temperatures (T_p) and the Bayesian estimated luminosity. The relationship for clusters (Equation 6.2) is shown with the cyan dashed-dotted line, Equation 6.3 for groups is shown with the green long-dashed line, the relationship for radio-loud groups (Equation 6.4) is shown with the blue dashed line and the relationship for radio-quiet groups (Equation 6.5) is shown in the magenta dotted line.

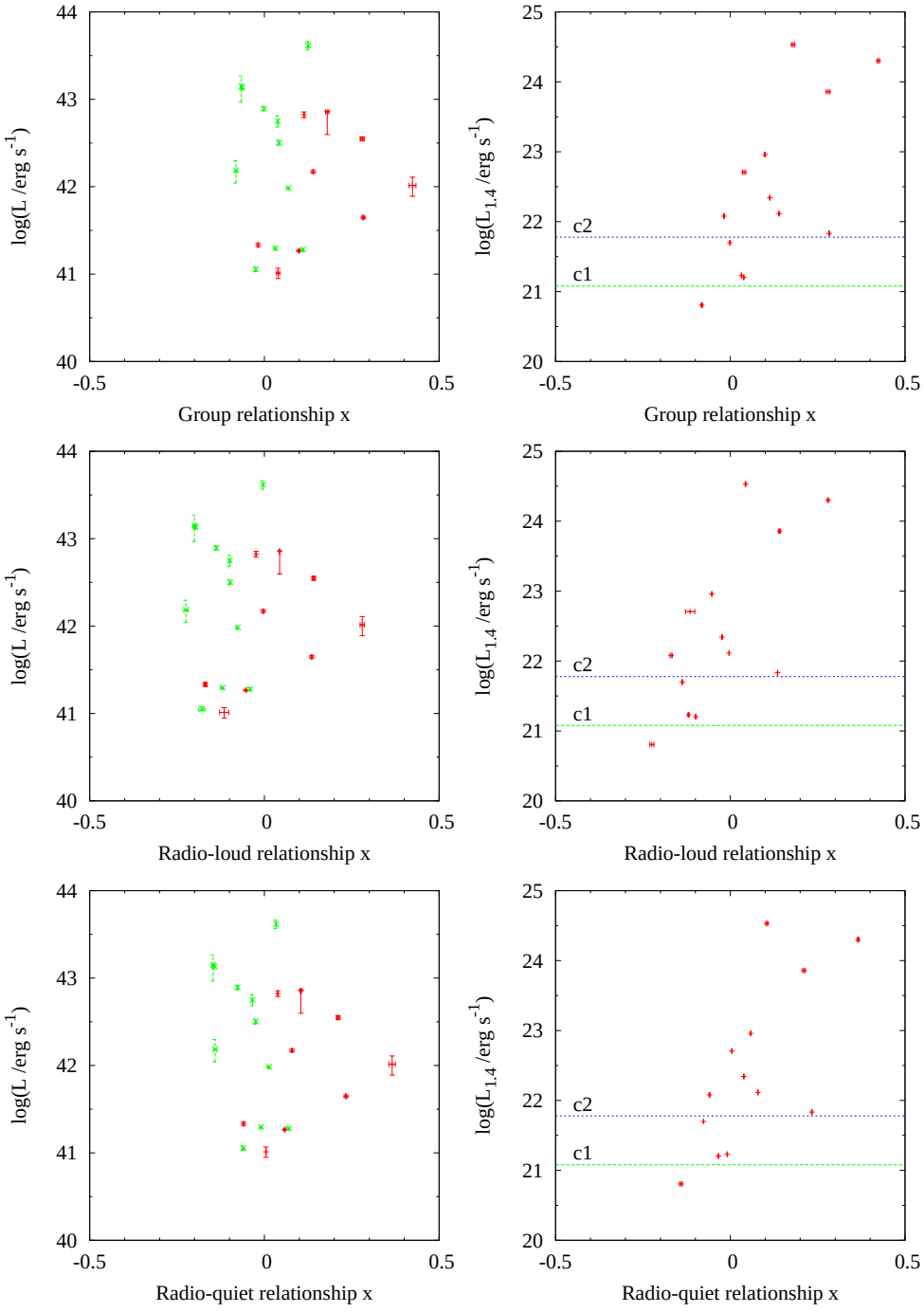

Figure 6.10: Plots of x, a measure of the difference between the expected correlation and the observations, against X-ray luminosity (left panels) and against using the 1.4 GHz radio luminosities for the groups relationship (top panels), radio-loud groups (middle panels) and radio-quiet groups (bottom panels). The radio-loud groups are shown in red and the radio-quiet groups are in green. In the right-hand panels, the radio-loud cut-offs are also shown; $c1$ in green and $c2$ in blue.

are from the same parent population of indistinguishable groups. A summary of the KS statistic values and probabilities for all the cuts are shown in Table 6.5. For this sample (using the $c2$ radio-loud threshold) the probabilities are less than 1 per cent for all the relationships, which supports the notion that the radio-loud and radio-quiet groups display different gas properties as suggested by Croston et al. (2005a).

In the right-hand panels of Figure 6.10, I show the L-T offset for the group, radio-loud and radio-quiet relationships plotted against the radio luminosity, $L_{1.4}$. The $c1$ and $c2$ cuts are also plotted. I used the Spearman rank correlation test to determine the strength of the correlation between the L-T offset parameter and the radio luminosity and found that there are significant correlations for each of the relationships plotted in the right hand panels, to 99 % confidence.

As discussed in Croston et al. (2005a), the radio luminosity can be used as a proxy of the jet kinetic energy, although other factors are also important such as the source size, the source age, and the particle content, which are in most cases unknown. They compared the radio luminosity to the heat capacity, C, determined using the density profile ($C = (3/2)Nk$, where N is the total number of particles), and the energy required to increase the observed temperature from the temperature predicted by their radio-loud and radio-quiet relationships. They found that the energy required is strongly correlated to the radio luminosity and that this is not due to an underlying $L_{1.4} - L_X$ correlation nor is it due to the heat capacity, as both of these correlations are much weaker. By this reasoning, this radio-luminosity – L-T offset correlation strongly supports a model where an AGN is heating the group gas, increasing the observed temperatures in radio-loud groups.

I also fitted regression lines to the $L_X - T_X$ data for all the groups and the radio-loud and radio-quiet subsamples, using the MCMC regression method described in Section 6.5, and found that their best fitting lines are not significantly different:
for radio-loud groups:

$$\log(L_X) = (3.16^{+0.06}_{-0.06}) \log(T) + (42.16^{+0.01}_{-0.02}) \tag{6.10}$$

for radio-quiet groups:

$$\log(L_X) = (5.98^{+0.07}_{-0.08}) \log(T) + (42.64^{+0.01}_{-0.01}) \tag{6.11}$$

These trends are inconsistent with each other and steeper than all of the previously published relationships.

6.5.2 Radio-Quiet Threshold

As mentioned in Section 6.2, I chose to use the $c2$ radio-loud threshold defined as $L_{1.4} = 6.0 \times 10^{21}\,\mathrm{W\,Hz^{-1}}$, which corresponds to $L_{NGC3665}/2$ as suggested by Croston et al. (2005a). This threshold means that large-scale radio structures can be detected at all the redshifts observed. Below this threshold, we also run the risk of the radio-loud set being contaminated by star-burst galaxies.

If I use the $c1$ cut-off ($L_{1.4GHz} = 1.2 \times 10^{21}\,\mathrm{W\,Hz^{-1}}$), the number of radio-quiet groups is reduced from 10 to 7, so there are 12 radio-loud groups, and using $c0$ reduces the numbers to six radio-quiet and 13 radio-loud. The $c0$ cut-off is also dependant on the flux limit of the SDSS survey so does not represent a physical cut-off in radio luminosity. This change increases the probabilities of the groups having a single parent population so that they can no longer be ruled out; the probabilities increase to < 10 per cent for $c1$ and < 30 per cent for cut-off $c0$.

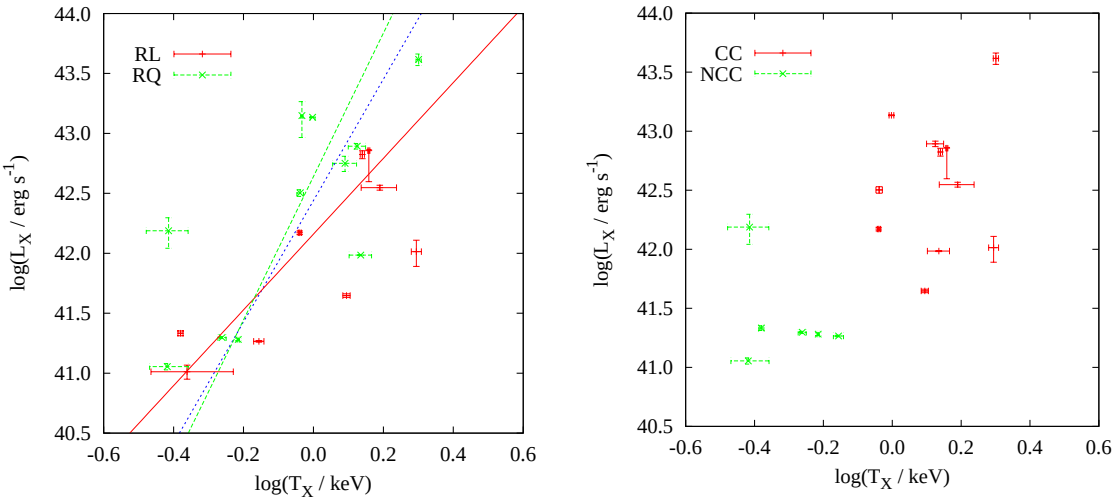

Figure 6.11: Luminosity-temperature relationships for the radio-loud groups (red solid lines) and radio-quiet groups (green dashed lines) in the left panel with the best-fitting regression lines over-plotted in the same colours for these populations and for the all of the groups in blue. The cool-core groups (red solid lines) and non cool-core groups (green dashed lines) are shown in the right panel as defined from the temperature profiles (Figure 6.2). NGC 1052 is not included in the CC/NCC comparison as its bright core prevents us from measuring its temperature profile and NGC 4065 is also excluded because it is too faint to construct a temperature profile.

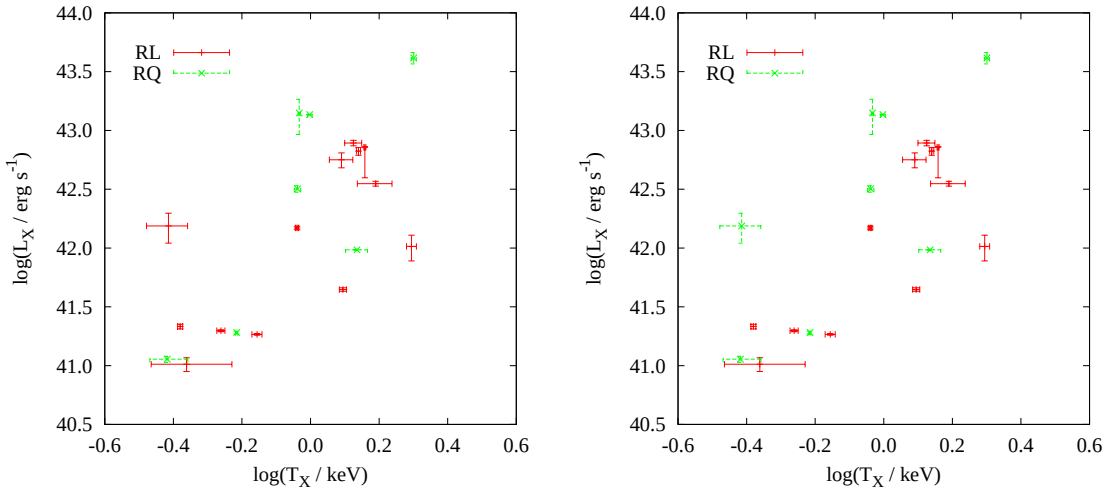

Figure 6.12: Luminosity-temperature relationships for radio-loud (red) and radio-quiet (green) groups using $c0$ in the left panel and $c1$ in the right panel.

6.5.3 Cool-core Groups

I also considered whether the presence of a cool core directly affects the temperature of the groups and found that the groups are clearly separated at $T_p \sim 0.8$ keV (Figure 6.11). In this work I have defined a cool-core group as one that has a sharp decline in the inner regions of its temperature profile. A more definitive method may be to consider groups with a ratio of the mean group gas temperature between 0.1 – 0.3R_{500} to the mean core temperatures of the inner region of the temperature profile between 0.0 and 0.05R_{500}, which is used in the work on groups and clusters by Johnson et al. (2009). If the mean outer temperature is greater than the mean inner temperature, then the group has a positive temperature gradient in the inner regions. Unfortunately, only 5 of my groups have more than 2 bins with more than 600 background subtracted counts within the central 0.05R_{500} of the group's temperature profile, so we cannot measure the spectral temperature of the inner region. Another method, used by Sun et al. (2009), is to put a limit of the central isochoric cooling time. I have not calculated these cooling times but using the ratio of mean temperatures, there is no change to my classifications.

The divide of CC and NCC in the $L_X - T_X$ comparison is not the same split as in the radio-loud split so suggests that the presence of a cool core is not related to the radio brightness of the group and that CC and NCC groups cannot be compared in the same way as RL and RQ groups. The fact that the NCC groups in this sample have lower temperatures and lower X-ray luminosities than the cool core groups is consistent with the results of Johnson et al. (2009) who also used *XMM-Newton* data of groups in the GEMS sample (including 11 of the groups studied here) as well as some groups from the Two-Dimensional *XMM-Newton* Group Survey (2dXGS).

In Figure 6.13, I have replotted the L-T offset comparisons against X-ray luminosity and radio luminosity and these show that the CC groups are typically above the group relationship (Equation 6.3) with higher X-ray luminosities than the NCC groups, and that the NCC groups are not correlated with radio luminosity although with the $c2$ cut-off, only two of the radio-loud groups in this sample are NCC systems. This suggests that the NCC groups have cooler outer temperatures for a given luminosity than those with cool cores.

By comparing the velocity dispersions, σ_v (measured by OP04), to my luminosity measurements (Figure 6.14), I find that the NCC groups have lower velocity dispersions than the CC groups. I also split these data into radio-loud and radio-quiet to demonstrate that the radio loud classification is not related to the X-ray luminosity nor to the velocity dispersion. Following the argument of current group formation models (Miles et al. 2004), the lower dispersion velocities suggest increased deceleration due to dynamical friction in these NCC groups, which is consistent with a less relaxed state. If the NCC are not fully relaxed systems, it is possible that there are more mergers in these groups; however, as we see a similar split in the $L_X - T_X$ relationship, it is more likely that these splits are due to non cool-core groups being lower-mass systems.

Further evidence for the difference between CC and NCC groups is required to determine why there is such a sharp division in the $L_X - T_X$ comparison. By comparing the entropy profiles of CC and NCC groups, I will be able to judge if the differences in gas properties that are detected in clusters are also present in groups and thus draw stronger conclusions on the evolutionary differences between these two system populations (see Chapter 7).

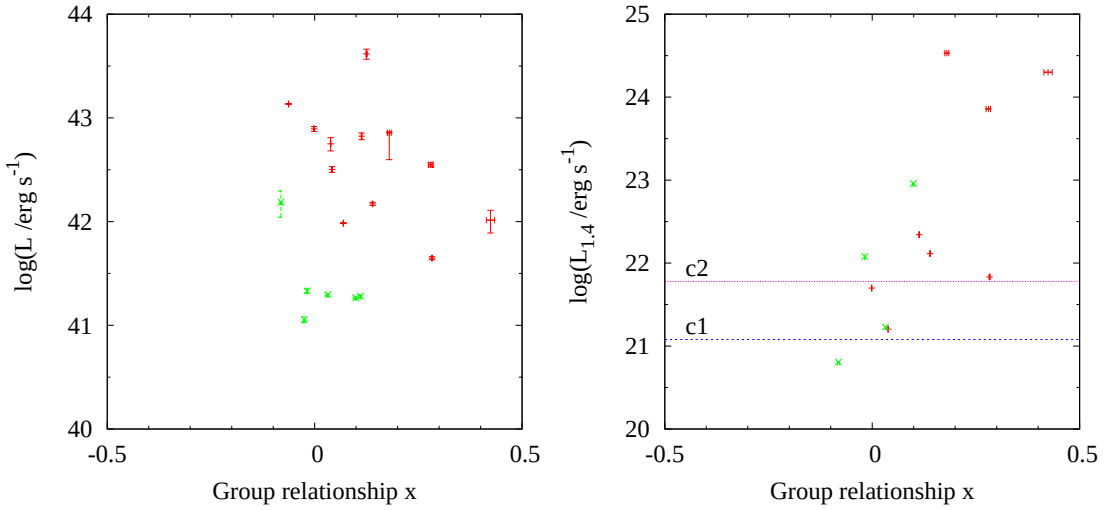

Figure 6.13: Plots of the L-T offset, x, against X-ray luminosity (left panel) and 1.4 GHz radio luminosity (right panel) showing the cool core groups in red and the non cool core groups in green.

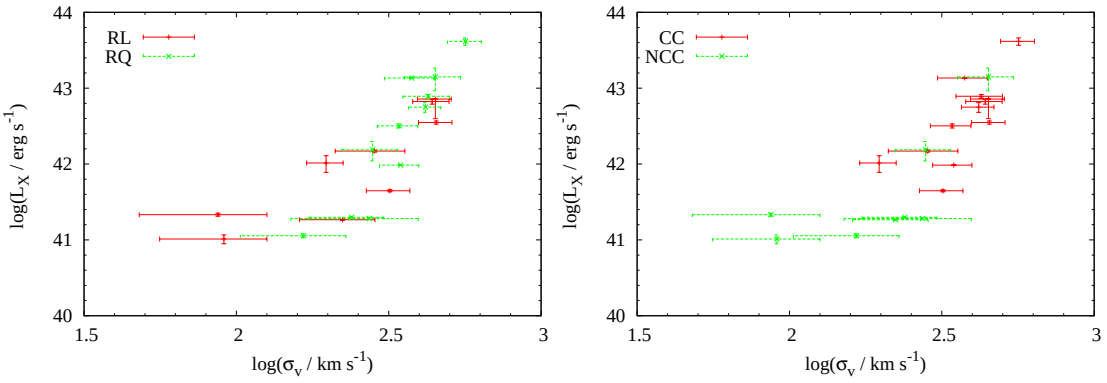

Figure 6.14: Luminosity-σ_v relationships for radio-loud (red) and radio-quiet (green) groups in the left panel and CC (red) and NCC (green) in the right panel.

Table 6.4: Spatial Results

Group	My XMM-Newton results		OP04 ROSAT results	
	T_X (keV)	$\log_{10} L_X$ (erg s^{-1})	T_X (keV)	$\log_{10} L_X$ (erg s^{-1})
HCG 62	1.23 ± 0.10	42.75 ± 0.06	1.43 ± 0.08	43.14 ± 0.04
NGC 383	1.44 ± 0.01	42.86 ± 0.01	1.51 ± 0.06	43.07 ± 0.01
NGC 533	1.38 ± 0.10	42.82 ± 0.03	1.08 ± 0.05	42.67 ± 0.03
NGC 720	0.61 ± 0.01	41.28 ± 0.01	0.52 ± 0.03	41.20 ± 0.02
NGC 741	1.55 ± 0.18	42.55 ± 0.02	1.21 ± 0.09	42.44 ± 0.01
NGC 1052	0.44 ± 0.13	41.01 ± 0.06	0.41 ± 0.15	40.08 ± 0.15
NGC 1407	1.24 ± 0.03	42.65 ± 0.02	1.02 ± 0.04	41.69 ± 0.02
NGC 3607	0.39 ± 0.05	42.19 ± 0.13	0.35 ± 0.04	41.05 ± 0.05
NGC 3665	0.42 ± 0.01	41.33 ± 0.02	0.47 ± 0.10	41.11 ± 0.08
NGC 3923	0.55 ± 0.02	41.30 ± 0.01	0.52 ± 0.03	40.98 ± 0.02
NGC 4065	0.93 ± 0.07	43.15 ± 0.14	1.22 ± 0.08	42.64 ± 0.05
NGC 4073	2.00 ± 0.04	43.62 ± 0.05	1.52 ± 0.09	43.41 ± 0.02
NGC 4261	1.97 ± 0.07	42.01 ± 0.01	1.30 ± 0.07	41.92 ± 0.03
NGC 4325	0.99 ± 0.02	43.13 ± 0.01	0.82 ± 0.02	43.15 ± 0.01
NGC 4636	0.91 ± 0.01	42.17 ± 0.02	0.84 ± 0.02	41.49 ± 0.02
NGC 5044	1.33 ± 0.08	42.89 ± 0.01	1.21 ± 0.02	43.01 ± 0.01
NGC 5129	0.92 ± 0.02	42.50 ± 0.02	0.84 ± 0.06	42.33 ± 0.04
NGC 5322	0.37 ± 0.02	41.06 ± 0.03	0.23 ± 0.07	40.71 ± 0.10
NGC 5846	1.37 ± 0.10	41.98 ± 0.01	0.73 ± 0.02	41.90 ± 0.02
IC 1459	0.70 ± 0.02	41.27 ± 0.01	0.39 ± 0.04	41.28 ± 0.04

Table 6.5: Results of the 1D KS test

	$c0$		$c1$		$c2$	
Relationship	Statistic	Probability	Statistic	Probability	Statistic	Probability
(i) Cluster	0.396	0.377	0.458	0.192	0.636	0.019
(ii) Group	0.385	0.412	0.500	0.123	0.596	0.034
(iii) Radio-loud	0.385	0.412	0.500	0.123	0.596	0.034
(iv) Radio-quiet	0.396	0.377	0.458	0.192	0.687	0.009

6.5.4 Optical Properties of the Groups

In clusters, the brightest cluster galaxy (BCG) is more likely to be radio-loud than other galaxies of the same luminosity and stellar mass (von der Linden et al. 2007). If this is also the case in groups of galaxies, the number of galaxies within the group and the respective luminosities of the brightest group members may affect the luminosity-temperature relationship for radio-loud and radio-quiet groups.

Croston et al. (2005a) considered whether the radio-loud and radio-quiet groups are at a different stage of evolution by comparing the distribution of the number of galaxies, N_{gal}, and the luminosity ratio of the BGG and the second brightest galaxy, L_{12}. In heirarchical galaxy formation, older, more relaxed groups have fewer galaxies as the BCG would be much larger and brighter than field galaxies of a similar age as they would have undergone many mergers. They found that there is no significant difference in the distributions of the two subsamples so that there is no evidence of a difference in their evolutionary stages.

To determine whether the number of galaxies or the relative brightness of the brightest galaxies is related to the radio luminosity and could thus contribute to the difference in the luminosity-temperature relationship, I compared the radio luminosity to the number of galaxies and to L_{12}, which was calculated by OP04 (see Figure 6.15). To reduce the inhomogeneity in the number of galaxies determined in the original catalogues (Hickson 1982; Garcia 1993; Nolthenius 1993; Ledlow & Owen 1996; Ramella et al. 1997; Mulchaey & Zabludoff 1998), OP04 redefined the number of galaxies associated with the group, including all galaxies within a projected radius of R_{500} of the group position and within the velocity range of $v \pm 3\sigma_v$. They also considered the number of galaxies above an optical luminosity cutoff of $L_{cut} = 5.28 \times 10^8 L_{\odot}$. I have compared all three of these N_{gal} values to the radio luminosity (see Figure 6.16).

Spearman rank correlation tests show that these data are not significantly correlated in any of these comparisons. I also tested these data with a K-S test and confirm the results of Croston et al. (2005a) where no difference is detected in the distributions of the number of galaxies or the L_{12} ratio for the radio-loud and radio-quiet groups. Eight of the radio-quiet groups have radio luminosities beneath the observation limit of NVSS so are not plotted. Although there is no formal correlation in these data, in all of the comparisons to the number of galaxies, the most luminous groups all have quite large values for N_{gal}. This suggests that although radio galaxies are not guaranteed in rich groups, we are unlikely to find a very powerful radio source unless it is a moderately large group (Best 2004).

The fact that there is no evidence for a difference in the optical properties of the BGG and the number of member galaxies in the radio-loud and radio-quiet groups supports my earlier conclusion that the difference in the $L_X - T_X$ relationship of groups is due to radio-source heating and not due to differences in the optical properties.

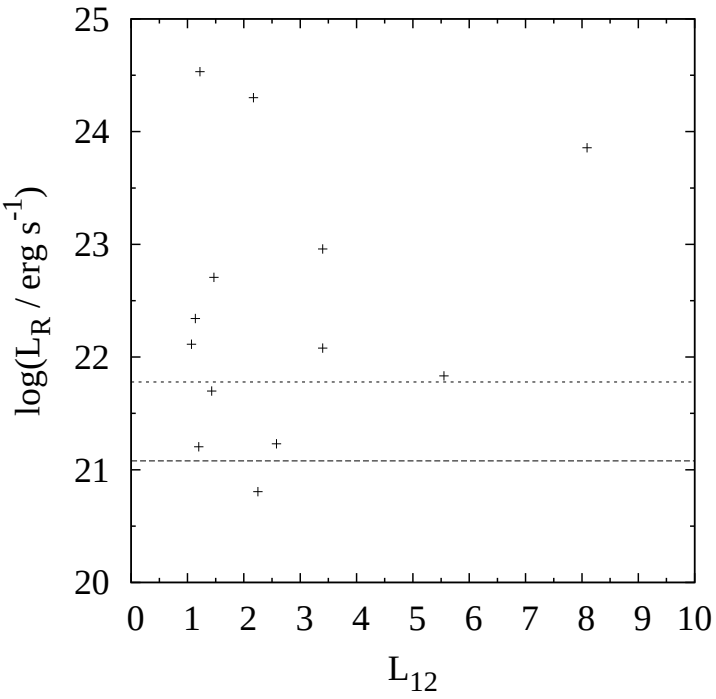

Figure 6.15: Comparison of radio luminosity at 1.4 GHz and the ratio of luminosities of the BGG and the second brightest galaxy, L_{12}.

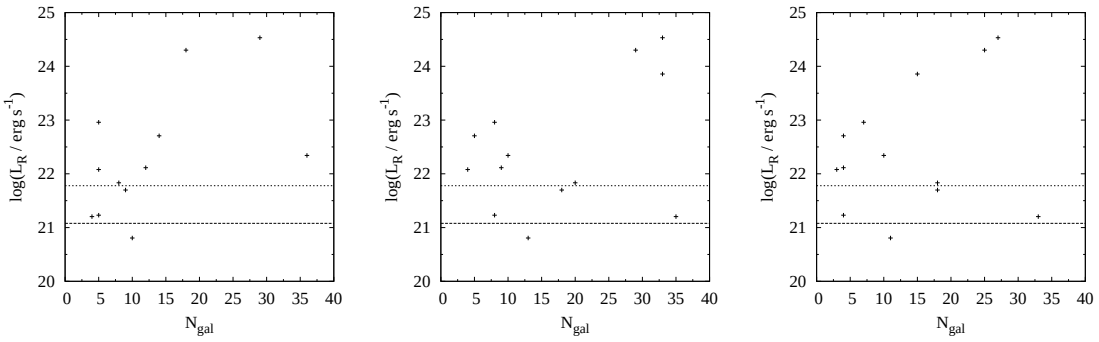

Figure 6.16: Comparison of the 1.4 Ghz radio luminosity and number of galaxies from the original catalogues (left panel), and from OP04 before and after their optical luminosity cut at $L > 2.73 \times 10^{41}$ erg s^{-1} (middle and right panels respectively).

6.6 Discussion of Individual Groups

Osmond & Ponman (2004) have published temperature and surface brightness profile results for all of the groups in this sample. Their temperatures were determined from spectra extracted in regions to r_{500}. They then fitted a single-component *mekal* hot plasma model and a multiplicative absorption component with the neutral hydrogen column density at the H I values determined by Dickey & Lockman (1990). They did not model nor subtract a background component from their spectra but they did exclude the core in sources with a central AGN.

The method used by Osmond & Ponman to determine the shape of the surface brightness profile is discussed in Section 6.3.2.

6.6.1 HCG 62

This group consists of 63 galaxies within the central 50 arcmin (900 kpc), 4 of which dominate the core. Two ghost cavities were detected within the hot gas (Vrtilek et al. 2002; Morita et al. 2006). HCG 62 has a radio luminosity of $1.6 \times 10^{23}\,\mathrm{W\,Hz^{-1}}$ so is radio-loud irrespective of the cut-off used (Croston et al. 2005a); however none of the central galaxies are X-ray bright AGN so the core region is not excluded from the spectral fit of the global temperature.

HCG 62 is also classified as a cool-core group with a well studied temperature profile (Finoguenov & Ponman 1999; Buote 2000; Morita et al. 2006; Johnson et al. 2009). The temperature rises from 0.7 – 1.4 keV within 200 arcsec (60 kpc) then drops steadily with radius. The global temperature was measured by OP04 using *ROSAT*, $kT = 1.43 \pm 0.08$ keV, which is consistent with the mid-value of the temperature profile. My temperature profile is consistent with these previous measurements and my final gas temperature of $kT = 1.23 \pm 0.10$ keV is also within the range of the previous results.

Previous surface brightness fits have been attempted; OP04 fitted a double-β model with a primary spherical component of radius, $r_c = 2.44 \pm 0.26$ kpc and $\beta = 0.48 \pm 0.01$, and a second component with a radius of 10.75 ± 0.60 kpc, 1.00 ± 0.05) and ellipticity, $e = 1.12 \pm 0.03$. The radii of these components were confirmed by Morita et al. (2006) who successfully fitted a triple-β model with $r_c = 2, 10$ and 160 kpc, fitting an additional 'very-extended' component to the group emission, but without the ellipticity included by OP04. I also fitted a dual component, projected-β model with β values consistent with OP04; my central component has $r_c = 1.23^{+4.08}_{-0.75}$ and $\beta = 0.46^{+0.04}_{-0.08}$ and the extended component has $r_c = 27.32^{+21.64}_{-17.33}$ and $\beta = 0.99^{+0.21}_{-0.02}$.

6.6.2 NGC 383

This group has 33 galaxies, dominated by NGC 383, which hosts the AGN, 3C 31, which is a twin-jet FR I radio galaxy (e.g. Burch 1977; Fomalont et al. 1980). The temperature of the extended emission from this group was measured by OP04 as $kT = 1.51 \pm 0.06$ keV and the surface brightness profile was characterised by a double-β model with a spherical component with a radius of $r_c = 2.11 \pm 0.21$ kpc and $\beta = 0.36 \pm 0.00$, and a second component of radius 0.41 ± 0.43 kpc, $\beta = 0.60 \pm 0.15$, and ellipticity $e = 1.08 \pm 0.03$. The second component is in agreement with previous fits; $r_c = 460 \pm 60$ arcsec (159 ± 21 kpc), with $\beta = 0.61 \pm 0.06$ (Trussoni et al. 1997), and the spherical component is consistent with the model fitted by Komossa & Böhringer (1999) ($r_c = 73$ kpc with $\beta = 0.38$). These models both use ROSAT data so are affected by the poorly modelled PSF. More recent measurements using *Chandra* data (Hardcastle et al. 2002b) used a model consisting of a central point source, an extended β model fixed at the Komossa & Böhringer (1999) measurements and a free-β model, with best fitting parameters of $r_c = 3.6 \pm 0.7$ arcsec and $\beta = 0.73 \pm 0.07$.

I fitted a spectral temperature of $kT = 1.36 \pm 0.01$ keV, which is lower than OP04's result, and a gas temperature from the temperature profile of $kT = 1.44 \pm 0.01$ keV, which is consistent with OP04 likely because the central AGN was excluded from the analysis. The surface brightness profile measured in this work was characterised by a projected double-β model with a central component that is smaller than the previous fits ($r_c = 1.05^{+0.37}_{-0.51}$ with $\beta = 0.59^{+0.04}_{-0.10}$), but my extended component is consistent with the results of Trussoni et al. (1997); $r_c = 141.10^{+82.71}_{-11.36}$ with $\beta = 0.82^{+0.48}_{-0.16}$
.

6.6.3 NGC 533

This cool-core group has 28 member galaxies (Mulchaey & Zabludoff 1998) and previous measurements of the temperature have shown a global temperature between $kT = 0.99 \pm 0.11$ keV (Mulchaey & Zabludoff 1998) and $kT = 1.08 \pm 0.05$ keV (OP04) determined using *ROSAT* data. As a cool-core group, a temperature profile reveals an increase from 0.67 – 1.35 keV within 50 kpc of the core. My temperature profile agrees with these measurements and I find a gas temperature at the top end of this range at $kT = 1.38 \pm 0.10$ keV.

Osmond & Ponman also fitted a two component β model to these data with spherical component of radius $r_c = 2.21 \pm 1.68$ and $\beta = 0.42 \pm 0.01$, with a second component with a radius of 2.52 ± 0.83 kpc, $\beta = 0.59 \pm 0.06$, and an ellipticity of $e = 1.50 \pm 0.03$. My central component, $r_c = 1.85^{+0.47}_{-0.18}$ kpc and $\beta = 0.54^{+0.01}_{-0.03}$, is in agreement with both these components as they are themselves consistent in radius within the errors. I also fit an extended component of $r_c = 206.90^{+184.51}_{-41.47}$ kpc and $\beta = 0.69^{+0.15}_{-0.39}$.

6.6.4 NGC 720

Although NGC 720 has been included in many previous statistical studies of groups, the surface brightness has also been studied as an isolated elliptical showing strong evidence for a dark matter halo that cannot be explained by dark matter models (Buote & Canizares 1998). It is a radio-loud group (Croston et al. 2005a) with 4 group members (Garcia 1993).

Buote et al. (2002) measured the global temperature at $kT \sim 0.6$ keV between 0.7 – 2.0 keV, which is consistent with the later results by OP04 ($kT = 0.52 \pm 0.03$ keV). Both of these works also characterised the surface brightness profiles; Buote et al. (2002) measured a core radius of $r_c = 0.56$ kpc with $\beta = 0.42$ and OP04 determined the best-fitting β model to have a radius $r_c = 1.15 \pm 0.20$ kpc with $\beta = 0.47 \pm 0.01$ and $e = 1.21 \pm 0.06$.

My spectral temperature measurement, $kT = 0.58 \pm 0.01$ keV agrees with the previous measurements; however, the gas temperature measured from the temperature profile, $kT = 0.61 \pm 0.01$ keV is higher than OP04 but still consistent with Buote et al. (2002). My beta model fits also agree with OP04; $r_c = 1.39^{+0.13}_{-0.11}$ kpc and $\beta = 0.50^{+0.01}_{-0.01}$.

6.6.5 NGC 741

With 41 group members, this is a radio-loud group with no reported structure within the gas. Previous temperature measurements using *ROSAT* data put the global temperature between $kT = 1.06 \pm 0.20$ keV (Mulchaey & Zabludoff 1998) and $kT = 1.21 \pm 0.09$ keV (OP04). A temperature profile was measured in the *Chandra* observations (Sun et al. 2009) showing a cool core and an increase from 0.8 – 2.0 keV within 40 kpc of the core. My temperature profile agrees broadly with the previous measurements and the gas temperature of 1.55 ± 0.18 keV is within this range.

Osmond & Ponman fitted a β model to the *ROSAT* surface brightness profile finding the best fit core radius, $r_c = 2.30 \pm 0.18$ kpc with $\beta = 0.44 \pm 0.01$ and $e = 1.30 \pm 0.09$. My β model fit is for a more compact component with $r_c = 0.50^{+0.39}_{-0.27}$ kpc with $\beta = 0.40 \pm 0.02$. Jetha et al. (2008) also fitted a single-β model to these *XMM-Newton* data with $\beta = 0.428 \pm 0.005$ and core radius $r_c = 2.1 \pm 0.2$ kpc by smoothing the surface brightness profile. Their analysis of the *Chandra* data does however reveal an X-ray cavity between 10 kpc and 40 kpc from the core.

6.6.6 NGC 1052

This faint group is dominated by the emission from the LINER NGC 1052, the X-ray spectrum of which contains an absorbed power-law component from a torus and a thermal component due to the jet interacting with the ISM. Due to this dominance, the temperature profile of this group could not be measured (Kadler et al. 2004; Croston et al. 2005a). The group temperature cannot be separated from the jet-ISM interaction with our *XMM-Newton* data.

OP04 were unable to fit a surface brightness profile to the emission from NGC 1052 so I have a new result of $r_c = 0.21^{+0.11}_{-0.05}$ kpc with $\beta = 0.51^{+0.17}_{-0.05}$.

6.6.7 NGC 1407

The dominant E0 galaxy contains a weak AGN making this group a radio-loud, cool-core group (Romanowsky et al. 2009). The temperature rises from $kT = 0.76 \pm 0.11$ in the inner regions to $kT = 0.95 \pm 0.13$ keV at 10 kpc (Fukazawa et al. 2006); however, the global fit by OP04 is higher with $kT = 1.02 \pm 0.04$ keV. My temperature profile shows a strong cool core with a central peak. These previous measurements are consistent with the range measured in my temperature profile and the gas temperature lies towards the upper limits, 1.24 ± 0.03 keV.

Osmond & Ponman also fitted a β model with an unconstrained core radius of $r_c = 0.08 \pm 0.15$ kpc, $\beta = 0.46 \pm 0.01$ and $e = 1.22 \pm 0.06$. I constrained the profile with a β-model of $r_c = 0.83 \pm 0.12$ kpc and $\beta = 0.49 \pm 0.01$.

6.6.8 NGC 3607

The BCG is a lenticular LINER galaxy (NGC 3607) with two other giant ellipticals nearby (NGC 3605 and NGC 3608) and is thus a radio-loud group. Previous studies of the X-ray emission have detected no AGN (Terashima et al. 2002) and attribute the extended X-ray emission to discrete sources in the host (Matsushita et al. 2000).

Matsushita et al. (2000) measured the temperature of the extended emission using ASCA data at $kT = 0.53 \pm 0.04$ keV including a hard bremsstrahlung component for the point sources in their fits, while OP04 found a global temperature of $kT = 0.53 \pm 0.04$ keV with their ROSAT data. My temperature profile is centrally peaked so the gas temperature, which removes this emission, is lower at $kT = 0.39 \pm 0.05$ keV.

Osmond & Ponman also fitted a two-component β model with a spherical component with a radius of $r_c = 1.98 \pm 0.93$ and $\beta = 0.39 \pm 0.02$, and a second component with a radius $r_c = 5.16 \pm 2.73$ kpc with $\beta = 0.60 \pm 0.21$ and $e = 2.06 \pm 0.18$. My projected double-β model fitted a much more extended component and a much smaller central component to the gas; $r_c = 64.38^{+20.58}_{-7.99}$ and $0.14^{+0.01}_{-0.06}$ kpc with $\beta = 0.44^{+0.04}_{-0.14}$ and $0.49^{+0.01}_{-0.04}$ respectively.

6.6.9 NGC 3665

This group has only 6 member galaxies (Finoguenov et al. 2006) and is radio-loud due to its BCG, NGC 3665. Previous temperature measurements have placed the global temperature around 0.45 keV; Mulchaey et al. (2003) used ROSAT data and measured $kT = 0.40 \pm 0.05$ keV and

OP04 agrees ($kT = 0.47 \pm 0.10$ keV). More recent studies of the *XMM-Newton* data (Finoguenov et al. 2006) has confirmed these results, with $kT = 0.40 \pm 0.02$ keV within a radius of $30h_{70}^{-1}$ kpc and $kT = 0.54 \pm 0.16$ keV within $0.1R_{500}$. I measured a central peak in the temperature profile with a temperature consistent with the results of Finoguenov et al. and my gas temperature of $kT = 0.42 \pm 0.05$ keV agrees with the previous temperature measurements for the more extended gas.

Osmond & Ponman also fitted a single β model to the surface brightness profile with an unconfined core radius of $r_c = 1.08 \pm 1.31$ kpc with $\beta = 0.47 \pm 0.03$ and $e = 1.67 \pm 0.04$. My fit constrains the core radius to $r_c = 0.80^{+0.16}_{-0.13}$ kpc with $\beta = 0.49^{+0.04}_{-0.03}$, which does agree with OP04's fit.

6.6.10 NGC 3923

This radio-loud group has 8 galaxy members (Osmond & Ponman 2004), the BGG is the early-type galaxy, NGC 3923. Previous global temperatures were measured by Mulchaey et al. (2003) ($kT = 0.51 \pm 0.13$ keV) and confirmed by OP04 ($kT = 0.52 \pm 0.03$ keV). My gas temperature agrees with these results; $kT = 0.55 \pm 0.02$ keV.

Osmond & Ponman also constrained a β-model fit to a core radius of $r_c = 0.63 \pm 0.06$ kpc with $\beta = 0.55 \pm 0.01$ and $e = 0.18 \pm 0.08$. My β-model fit found a smaller core radius of $0.32^{+0.10}_{-0.09}$ kpc but has a consistent β value of $\beta = 0.53 \pm 0.01$.

6.6.11 NGC 4065

Previous ROSAT temperatures of this group are consistent; Mulchaey et al. (2003) measured $kT = 1.20 \pm 0.15$ keV and Osmond & Ponman (2004) found $kT = 1.22 \pm 0.08$ keV. These measurements agree with my *XMM-Newton* spectral temperature result, $kT = 1.24 \pm 0.07$ keV; however, my profile temperature, which in this case is a measured from a single, smaller region as this group is too faint to fit a temperature profile, is lower at $kT = 0.93 \pm 0.07$ keV

These two collaborations also found a double-β model is the best fit for this groups surface brightness profile but with inconsistent results; Mulchaey et al. (2003) found a core radius of $r_c = 2.52 \pm 0.50$ and $r_c < 0.1$ arcsec for the extended emission, with $\beta = 0.46 \pm 0.01$ and 0.31 ± 0.01 respectively, while OP04 found radii of $r_c = 3.08 \pm 0.51$ kpc and 6.68 ± 7.86 kpc with $\beta = 0.36 \pm 0.01$ and 0.37 ± 0.03. I also fitted a projected double-β model with a central component with a core radius of $r_c = 4.82^{+1.14}_{-0.83}$ kpc with $\beta = 0.57^{+0.03}_{-0.05}$ and an extended component with radius $r_c = 2.25^{+0.74}_{-0.03}$ Mpc and $\beta = 0.60^{+0.09}_{-0.30}$.

6.6.12 NGC 4073

Previous results with ROSAT data find consistent temperatures, $kT = 1.75 \pm 0.20$ keV (Mulchaey et al. 2003) and $kT = 1.52 \pm 0.09$ keV (Osmond & Ponman 2004). Surface brightness profiles fitted in these works, however, were inconsistent; (Mulchaey et al. 2003) found a core radius of $r_c < 0.1$ arcsec and $r_c = 0.61 \pm 0.04$ kpc for the extended emission with $\beta = 0.43 \pm 0.01$ and 1.00 respectively, and OP04 determined the best fitting double β model with a spherical component with a radius of $r_c = 4.42 \pm 2.89$ and $\beta = 0.43 \pm 0.01$, and a second component with a radius of 3.72 ± 1.50 kpc, $\beta = 0.53 \pm 0.07$ and ellipticity of $e = 1.20 \pm 0.03$.

My spectrally fitted temperature agrees with Mulchaey et al. ($kT = 1.81 \pm 0.03$) keV); however, my gas temperature is much higher than previous measurements at $kT = 2.00 \pm 0.04$ keV. This is likely due to the cool core revealed in our temperature profile, which is excluded from the gas temperature measurement. The central component of my projected double-β model fit to the surface brightness profile is consistent with the OP04 result ($r_c = 1.70^{+1.38}_{-0.24}$ kpc and $\beta = 0.44 \pm 0.03$); however, I fit an extended component at a much larger radius, $r_c = 176.09^{+184.48}_{-9.46}$ kpc and $\beta = 0.70^{+0.17}_{-0.40}$.

6.6.13 NGC 4261

This radio-loud group is dominated by the type-2 LINER, NGC 4261 (a.k.a. 3C 270), which has radio jets and lobes but no broad line emission lines that would indicate AGN activity (Zezas et al. 2005). Previous temperature measurements have found $kT = 0.65 - 1.37$ keV (Mulchaey et al. (2003) measured $kT = 0.91 \pm 0.05$ keV, and OP04 found $kT = 1.30 \pm 0.07$ keV). Croston et al. (2008a) used the same *XMM-Newton* data as I have in this work and measured $kT = 1.45^{+0.23}_{-0.01}$ keV when they fitted a *mekal* model with an abundance of $0.26^{+0.15}_{-0.04}$ times solar. My gas temperature is higher than these results ($kT = 1.97 \pm 0.07$), but in the first two cases, this is likely due to the presence of a cool core in this group, which drops to temperatures of $kT \sim 0.65$ keV in the centre (Croston et al. (2008a) found a central temperature of $kT = 0.65^{+0.01}_{-0.01}$ keV with a fixed abundance of 0.5 times solar).

Osmond & Ponman constrained a β-model fit of the surface brightness profile to a core radius $r_c = 0.63 \pm 0.06$ kpc with $\beta = 0.55 \pm 0.01$ and $e = 1.17 \pm 0.12$. Croston et al. (2008a) also fitted a projected double-β model which agrees with my best fit, which was with a projected double-β model with much larger radii; $r_c = 0.99^{+0.37}_{-0.04}$ kpc and $r_c = 61.78^{+19.69}_{-15.16}$ kpc with $\beta = 0.66^{+0.06}_{-0.02}$ and $\beta = 0.80^{+0.32}_{-0.19}$ respectively for the core and extended components.

6.6.14 NGC 4325

This radio-quiet, cool-core group (Gastaldello et al. 2007; Sun et al. 2009) contains 18 galaxies (OP04) and has two cavities, East and West of the core, suggesting a previous AGN burst (Russell et al. 2007). The temperature measured by OP04, $kT = 0.82 \pm 0.02$ keV is at the lower end of the profile range detected by Russell et al. (2007) and Sun et al. (2009). My gas temperature ($kT = 0.99 \pm 0.02$ keV) is much higher than this as it excludes the low temperature core.

The surface brightness profile was fitted by OP04 with core radius, $r_c = 27.56 \pm 4.97$ kpc, $\beta = 0.58 \pm 0.02$ and $e = 1.16 \pm 0.05$. Although my fit has a consistent beta ($\beta = 0.59 \pm 0.01$), the core radius is much smaller, $r_c = 9.17^{+0.51}_{-0.50}$ kpc.

6.6.15 NGC 4636

This group is dominated by a LINER BCG so an annular source region was used in this work during the global temperature subtraction. There is an extended hot gas halo with temperature and abundance gradients (Awaki et al. 1994; Trinchieri et al. 1994; Buote 2000). The temperature increased from 0.5 – 0.8 keV (Baldi et al. 2009) with changes in temperature detected with *Chandra* coincident with the edges of three bubbles. The global temperature measured by OP04 is consistent with the higher temperature, 0.84 ± 0.02 keV. This group is classified as a cool-core group (Peres et al. 1998), which is confirmed by these previously published temperature profiles; however our gas temperature, $kT = 0.91 \pm 0.01$ keV, is higher. Jones et al. (2002) present *Chandra* data showing armlike structures that are likely produced by shocks, driven by symmetric off-centre outbursts, which are accompanied by a temperature increase of $\sim 30\%$.

Osmond & Ponman found a double-β model fitted the surface brightness well, with spherical component with a radius of $r_c = 0.30 \pm 0.06$ kpc and $\beta = 0.47 \pm 0.00$, and a second component with a radius of 2.67 ± 0.25 kpc, $\beta = 0.79 \pm 0.04$ and $e = 1.08 \pm 0.02$. My projected double-β model fit (a compact component of $r_c = 0.45^{+0.05}_{0.13}$ kpc and $\beta = 0.65^{0.02}_{0.25}$ and an extended component with $r_c = 6.92^{+1.16}_{1.52}$ kpc and $\beta = 0.71^{0.05}_{0.13}$) does not agree with this previous fit but with a reduced $\chi^2 = 83.43$, I found that the complicated structure of this group was not well fitted with a projected double-β model. Baldi et al. (2009) describes the surface brightness profile noting that there is no central peak and is quite flat in the centre; then it starts to decline monotonically at ~ 5 arcsec from the centreq, showing another plateau at $25 < r < 60$ arcsec. This is consistent with the *Chandra* image which shows complicated structures.

6.6.16 NGC 5044

This is a hot cool-core group (Sanderson et al. 2006), with previously measured temperatures of $kT > 2$ keV (Reiprich & Böhringer 2002). With 16 members, it also has a complicated structure

with holes and filaments within 10 kpc (Gastaldello et al. 2009) and a surface brightness discontinuity at 67 kpc, which affect the temperature and metallicity of the group (Buote et al. 2003a,b).

Buote et al. (2003a) determined a multiphase temperature structure for NGC 5044, with a cool component with $T_c = 0.7$ keV, consistent with the kinetic energy of the stars, and a hotter component with $T_h = 1.4$ keV, consistent with the viral temperature of the halo (with a mass $\sim 10^{13}$ M$_\odot$. The global temperature fitted by OP04 is consistent with the hotter component ($kT = 1.21 \pm 0.02$ keV) and so is my gas temperature, $kT = 1.33 \pm 0.08$ keV.

Buote et al. (2003a) fitted a single beta model to the surface brightness profile of this group ($r_c = 61.9 \pm 0.4$ kpc and $\beta = 0.58 \pm 0.001$) while OP04 fitted a double-β model with a spherical component of radius $r_c = 5.96 \pm 0.16$ kpc with $\beta = 0.51 \pm 0.00$, and a second component with a radius of $r_c = 11.04 \pm 0.66$ kpc with a β value of 0.80 ± 0.06 and $e = 1.04 \pm 0.01$. I was also able to fit a projected double-β model with a central component with radius $r_c = 5.87^{+1.90}_{-0.63}$ kpc and $\beta = 0.52^{+0.02}_{-0.02}$ and an extended component with radius $r_c = 28.80^{+1.70}_{-15.16}$ kpc and $\beta = 0.93^{+0.37}_{-0.19}$.

6.6.17 NGC 5129

This radio-quiet group has 23 galaxy members, the BCG being the elliptical, NGC 5129. There is evidence of a cool core, with temperatures rising from ~ 0.7 keV to ~ 1.0 keV within 20 kpc of the core (Johnson et al. 2009; Sun et al. 2009). Due to this temperature variation, ROSAT temperature measurements lie in the middle of this range; Mulchaey et al. (2003) measured $kT = 0.81 \pm 0.10$ keV with a fixed abundance of $Z = 0.3 Z_\odot$ and this was confirmed by OP04 who found $kT = 0.84 \pm 0.06$. My gas temperature is consistent with this ($kT = 0.92 \pm 0.02$).

The surface brightness profile was best fit with a single-β model by Osmond & Ponman who constrained the core radius to $r_c = 3.14 \pm 1.71$ kpc with $\beta = 0.43 \pm 0.02$ and $e = 1.18 \pm 0.18$. I found a projected double-β model was a better fit with a central component with $r_c = 0.95^{+0.12}_{0.48}$ kpc and $\beta = 0.52^{+0.01}_{-0.15}$ and an extended component of $r_c = 70.54^{+69.31}_{-16.33}$ kpc and $\beta = 0.69^{+0.21}_{-0.25}$.

6.6.18 NGC 5322

The temperature of the gas within this radio-quiet group has been measured from ROSAT data at $kT = 0.33 \pm 0.15$ keV at a constant abundance of $Z = 0.3 Z_\odot$ by Mulchaey et al. (2003) and $kT = 0.23 \pm 0.07$ keV by OP04 who fixed the abundance to $Z = 0.00 \pm 0.02$. Previous attempts to fit the surface brightness profile have not been successful.

I measured a gas temperature of $kT = 0.37 \pm 0.02$ keV, which is consistent with the previous measurements. I also constrained the surface brightness profile with a β model with a radius of $r_c = 0.19^{+0.16}_{-0.11}$ kpc and $\beta = 0.51^{+0.08}_{-0.03}$.

6.6.19 NGC 5846

This radio-quiet group consists of 25 group members dominated by the elliptical NGC 5846. Previous ROSAT temperature measurements find $kT \sim 0.72$ keV (Mulchaey et al. 2003; Osmond & Ponman 2004) and our spectrally fitted temperature agrees; however, I find a much higher gas temperature from our profile, $kT = 1.37 \pm 0.10$ keV, as this removes the lower temperature contribution from the cool core.

Osmond & Ponman constrained the surface brightness profile to a β model with a core radius $r_c = 2.19 \pm 0.26$ kpc with $\beta = 0.51 \pm 0.01$ and $e = 1.13 \pm 0.04$, which agrees with Mulchaey et al. (2003). However, I found a projected double-β model is a better fit with a central component with a radius $r_c = 1.61^{+0.65}_{-0.19}$ and $\beta = 1.01^{+0.19}_{-0.01}$, and an extended component with $r_c = 18.33^{+0.69}_{-0.23}$ and $\beta = 1.17^{+0.03}_{-0.01}$.

6.6.20 IC 1459

This radio-quiet group is dominated by a LINER surrounded by hot ISM emission at $kT \sim 0.6$ keV (Fukazawa et al. 2006). The temperature measured by Mulchaey et al. (2003) agrees with this; however, Osmond & Ponman excluded the core emission and measured a temperature of $kT = 0.39 \pm 0.04$ keV. The surface brightness profile is unconfined in ROSAT data (OP04).

Our gas temperature also excludes the central AGN component but agrees with Mulchaey et al. (2003), $kT = 0.70 \pm 0.02$. I was also able to fit the surface brightness profile with a projected double-β model with radii of $r_c = 0.14^{+0.01}_{-0.03}$ and $4.24^{+0.07}_{-0.54}$ with $\beta = 0.96^{+0.05}_{-0.11}$ and $\beta = 0.70^{+0.01}_{-0.04}$ respectively.

6.7 Summary and Future Work

The results of the work presented in this Chapter can be summarized as follows:

- I independently measure the temperatures of the groups' gas removing the contamination from central AGN and of cool cores.
- I find that radio-loud and radio-quiet groups in this sample of 20 groups do not come from the same parent population using the results of a 1D KS test and the luminosity-temperature relationship.
- I find that the radio-loud classification is not correlated to whether the group has a cool core.
- I find that there is no significant correlation between the optical properties of the groups and their radio luminosities.
- I find that the L-T offset is correlated with the radio luminosity.

The next stage of this work is initially to increase the sample so that the statistics are enough to reduce the scatter on my best fitting lines and thus allow me to distinguish better between the radio-loud and radio-quiet groups. This can be done by either applying for new *XMM-Newton* observations for the groups that had high particle background (HCG 42, HCG 92, NGC 4697 and NGC 5171) and for those that have not been observed (NGC 524, NGC 1587, NGC 3557, NGC 4589, and NGC 5930), which would increase the sample to 14 radio-loud groups and 14 radio-quiet groups, or I could expand the sample to other groups from the GEMS group sample that are also elliptical dominated and were not included in the work of OP04 and Croston et al. (2003) because the group emission was not detected in the *ROSAT* data (HCG 4, 48 and 58 and NGC 1808, 3640, 3783, 4151, 4193, 6338 and 7714). There are currently archival data for 5 of these additional groups although three are Seyfert galaxies whose nuclear emission may complicate the analysis.

In addition to the work done here on the luminosity-temperature relationship of groups, I also intend to deproject the surface brightness profiles that I have fitted and convert them into density, pressure and entropy profiles so I can compare the profiles of radio-loud and radio-quiet groups thereby testing the scaling relations. It was suggested by Jetha et al. (2007) that there is no difference in the inner entropy profile of radio-loud and radio-quiet groups which indicated that AGN heating is not a factor in the entropy problem. I can also compare the CC and NCC groups to a similar end.

I will also be able to compare our group results with clusters such as those in the REXCESS (Representative *XMM-Newton* Cluster Structure Survey) sample (e.g. Böhringer et al. 2007; Croston et al. 2008a; Pratt et al. 2009), which also uses *XMM-Newton* data for clusters selected based on their luminosities with no bias toward any particular morphology.

Chapter 7

Discussion and Future Work

The purpose of this work was to explore the features of radio galaxies and their environments to determine how energy is stored and transferred from the central engine to the environment via the jet and the lobes of active galaxies. This work can be split into three themes and in this Chapter I summarise my results and discuss potential future work.

7.1 Jets

7.1.1 Retrospect

In Chapter 5, I presented work on the jet in Cen A, the closest FR I active galaxy to us. By concentrating on the temporal, spatial and spectral changes of the knots in the radio and X-ray, I determined the most likely mechanisms for the formation of the knots.

I combined information on the changing radio and X-ray fluxes, radio polarisation and positions of the knots within the jet to rule out impulsive particle acceleration in the knots. Essentially the same distribution of X-ray knots is seen in the most recent observation as was seen in the earliest *Chandra* observations in 1999. This would not be the case if the knots were impulsive as they would fade due to synchrotron losses. The lack of fading indicates long-lived particle acceleration in the knots of Cen A.

For those radio knots with X-ray counterparts, the most likely formation mechanism is a collision between the jet and an obstacle, resulting in a local shock. I found no significant variability in many of these knots, suggesting a long-lived, stable stage of particle acceleration during the interaction between the jet and the obstacle. The formation of knots at the point where the inner hundred-parsec-scale jet broadens abruptly suggests that these base knots (A1A and A1C) may be reconfinement shocks; however, this is complicated by the presence of a radio-only knot (A1B) moving downstream between the possible confinement-shock knots. I detect proper motions in

three of the radio knots: two of these have no compact X-ray counterparts and a third has only diffuse X-ray emission associated with it. My analysis of the distribution of the moving knots was inconclusive due to the low number of knots with well-established proper motions; however, the direction of motion of the knots may not be directly parallel to the jet axis. The knot motions are all downstream and they show no dependence on the position of the knot within the jet. I argue that the moving knots are due to compressions in the fluid flow that do not result in particle acceleration to X-ray emitting energies. It is possible, however, that the X-ray-only knots are also a separate population with flatter X-ray to radio spectra than those with counterparts, in which case we currently have no model for their formation.

7.1.2 Future Work

My work on jets has thus far been concentrated on the jet in Cen A. Although I have compared my results to the jet in M87, I would like to compare them to other FR I jets as Cen A is atypical, with an obscuring dust lane extending out to 1 kpc from the core which may affect the jet and its knots. Other galaxies where dust has been detected, such as 3C 31 and 3C 449, have much smaller disks, which cannot affect even the innermost regions of the observed X-ray jet. If we can attribute the knot dominated particle acceleration of the inner kpc to the presence of this disk then we can postulate that the X-ray jet emission seen in other FR I galaxies should be comparable to the dominant diffuse particle acceleration that dominates farther out in the Cen A jet. I would then predict that knot-dominated structure will not be seen in other FR I galaxies. By increasing my sample of FR I jets, I would also be able to determine whether the flaring of M87's HST-1 knot was a chance case of impulsive particle acceleration. By continuing to monitor the jet knots in Cen A, I will detect any future impulsive flaring events in Cen A as well as better constraining the velocities of the moving knots. Further monitoring observations with *Chandra* are in progress.

Knots are also seen in radio and X-ray in the jets of the FR II radio galaxies, such as 3C 353 which was studied in Chapter 3 (Swain et al. 1998; Kataoka et al. 2008). In recent work by Kataoka et al., 31 distinct X-ray sources were detected with WAVDETECT (Vikhlinin et al. 1995), of which five were closely aligned with the radio knots identified by Swain et al. (1998) (shown in Figure 7.1). These knots can also be split into a population with X-ray counterparts; J1/EJ1, J4/EJ2, CJ2/WJ1 as well as two X-ray knots associated with the hotspots, EJ3 with the eastern hotspot and WJ2 with the western hotspot, and a population without X-ray counterparts; J2, J3 and CJ1. Although this is a much more powerful jet, it has similar jet features and may therefore have similar jet formation mechanisms as in the less powerful FR I jets. Monitoring of this FR II jet would allow me to perform similar temporal analyses as for Cen A so that I can determine whether there are common particle acceleration mechanisms at work; however, the background of 3C 353 is complicated by the nearby merging cluster so other FR II galaxies may be better suited to this analysis. Recently, a temporal study of Pic A by Marshall et al. (2010) revealed a two possible knot flaring events with lifetimes

of years. They suggest that the X-ray emission must be from a small knot substantially smaller than the jet cross section of 700 pc and that the local magnetic field must be substantially larger than the average over the jet. They go further to suggest that expansion of the jet fluid could be a plausible explanation; however, VLBI observations and further monitoring are required to further constrain the knot formation mechanisms. This is an encouraging result for future temporal studies of FR II jet knots.

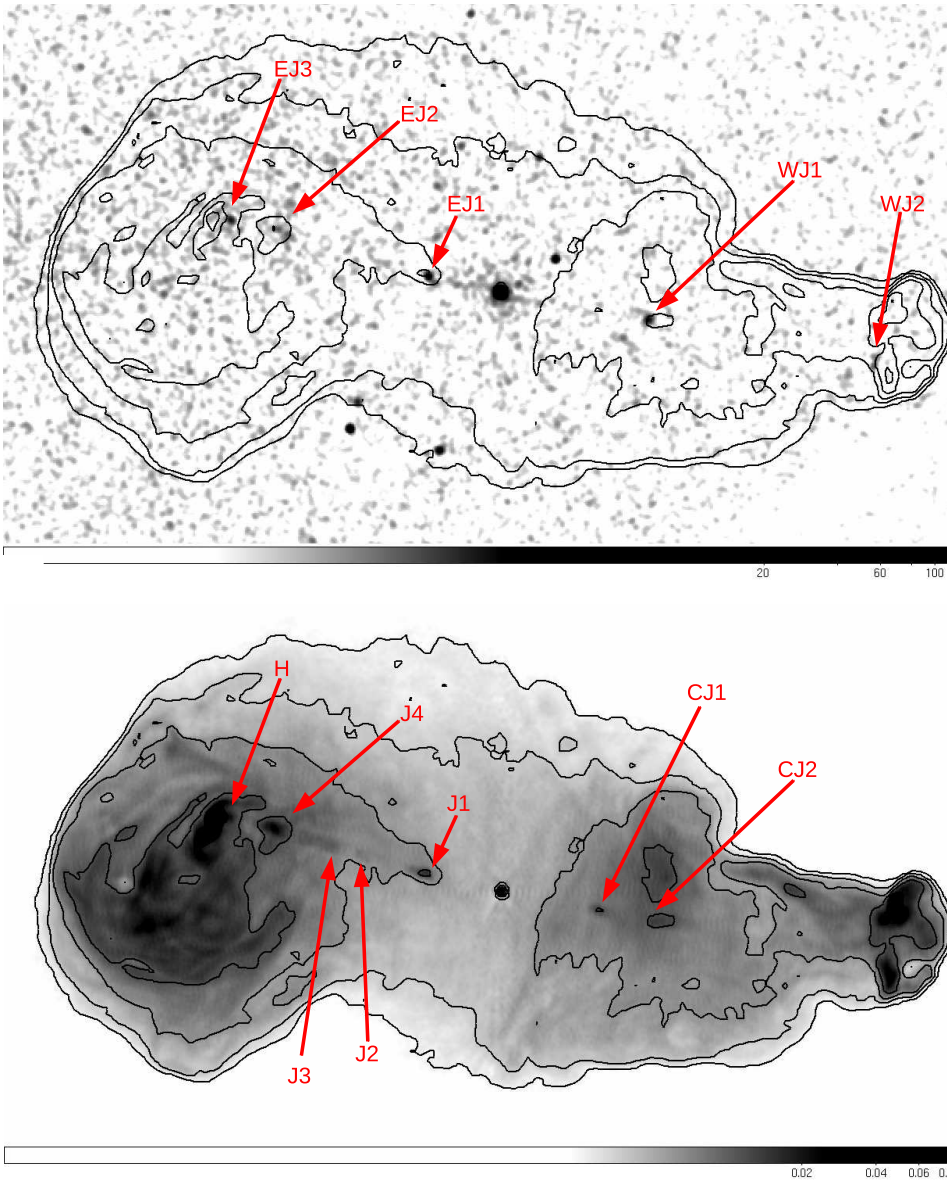

Figure 7.1: In the top panel is the chip-gap corrected X-ray image of 3C 353 smoothed with a Gaussian with a kernel of 3 pixels (1.5 arcsec), and in the bottom panel is the 1.4 GHz radio image (res 0.492 arcsec). Both are overlaid with 1.4 GHz radio contours at 0.001, 0.002, 0.005, 0.01, 0.02, 0.05 and 0.1 Jy beam^{-1}. The X-ray knots defined by Kataoka et al. (2008) are labelled in the top panel and the radio knots defined by Swain et al. (1998) are labelled in the bottom panel.

7.2 Lobes

7.2.1 Retrospect

When I studied the lobes of the FR II radio galaxy 3C 353 in Chapter 3, I found that the radio spectrum steepened with distance from the hotspots into the intralobe region. I examined the changing ratio of X-ray to radio flux densities and determined that the X-ray emission must be inverse-Compton scattering of the CMB and that the variation in the spectral index requires a changing magnetic field strength and may not require an additional spatially changing electron energy distribution. This agreed with the results of a similar analysis using Pic A (Hardcastle & Croston 2005); however, Hardcastle & Croston had better X-ray data so were also able to rule out a scenario where the magnetic field strength alone is responsible.

On smaller scales, I was also able to rule out a change in both the magnetic field strength and electron energy distribution, using a new statistical method that considers the distribution of X-ray counts as a function of radio flux density (Chapter 4). I compared the observed distributions of the radio and X-ray lobe emission from 3C 353 and Pic A with simulations of simple relationships between the magnetic field and electron energy densities and I was able to rule out all but a spatially changing magnetic field as the cause of the changes in surface brightness. This suggests that the filamentary structure seen in the lobes are likely regions of overpressured, higher magnetic field strength material.

In Cen A, we detect discontinuities in temperature and gas density at the inner edge of the lobes (Kraft et al. 2007) and as these lobes are expanding supersonically ($\mathcal{M} \sim 8$; Kraft et al. 2003) we also detect shocks which are accelerating particles and emitting X-ray synchrotron at the driving edge of the lobe (Croston et al. 2009). The lobes of Cen A are clearly overpressured; however, in 3C 353, we found no evidence of discontinuities or shocks so we assumed pressure balance in these lobes and thus found these lobes to be electron dominated (but consistent with equipartition in the West Lobe). In Cen A, we see direct evidence of energy being transferred from the lobe to the environment; however, in the absence of a shock, the energy is likely transferred during the expansion of the lobe via compression of the external material.

I was also able to put a limit on the radial distance of 3C 353 from the cluster centre as, unlike the majority of galaxies, 3C 353 lies on the edge of the cluster. The difference in the external pressure on each of the lobes, nearly a factor of two, may explain the striking difference in their appearance. In addition, the cluster itself consists of two sub-clusters which are slowly and non-violently merging. 3C 353 may be on the edge of the cluster because of a previous merger which could have disturbed its path around the core, and it may be the BCG despite its location, as there have been no other massive galaxies detected in the centre of either sub-cluster. Iwasawa et al. (2000) detected three galaxies associated with the southern sub-cluster and more recent surveys (2MASS and 6dFGS) have revealed four more, but none are in the centre (Figure 7.2).

7.2.2 Future Work

An obvious progression of this work would be to extend the sample of galaxies where this analysis can be carried out. An ideal place to start would be with a sample of close ($z < 0.1$) double-lobed radio-loud galaxies and a search for VLA archive data and complementary X-ray data from *XMM-Newton* and/or *Chandra*. This sample would allow us to judge whether either Pic A or 3C 353 are special cases or whether all radio galaxies are subject to spatial changes in their magnetic field strengths.

It would also be interesting to get deeper optical imaging of the cluster with which 3C 353 is associated to clarify if there are a significant number of small, low surface brightness galaxies in this cluster, and using microlensing techniques (e.g. Mahdavi et al. 2007), I could also investigate whether the dark matter is disturbed which would suggest that 3C 353 is the BCG.

Much of my work on radio galaxies uses iC from the low-energy electron population combined with synchrotron emission from the higher-energy electron population. However, with new facilities operating in lower radio frequencies, and broad bands throughout the radio regime, we will better understand the radio emission from radio galaxies. With the additional information available at low frequencies provided by LOFAR, we will be able to detect the synchrotron emission from the low-energy electron population that is responsible for the X-ray iC emission. This low-energy electron synchrotron emission can be directly compared to the higher-energy electron synchrotron emission to get information on the relative behaviour of these electron populations. (I am thus involved in a project to test spectral ageing models in classical double radio galaxies using the new broad-bandwidth capabilities of the EVLA.) To test the behaviour of the synchrotron spectrum at low radio frequencies, I intend to observe 3C 353 with the new facilities and thus constrain the low-radio synchrotron spectrum.

7.3 Environments

7.3.1 Retrospect

In Chapter 6 I considered the gas properties of a sample of galaxy groups, extending the work of Croston et al. (2005a) and Jetha et al. (2007). Croston et al. found a difference in the luminosity-temperature relationship for radio-loud and radio-quiet groups. Using *XMM-Newton*, which is more sensitive than *Chandra* and *ROSAT* and has a large enough field of view to detect all of the gas emission, I was able to measure the gas temperatures, temperature profiles and luminosities of 19 groups of galaxies from the sample selected by Croston et al. (2005a). I was also able to rule out a single parent population for radio-loud and radio-quiet groups by defining a parameter that takes account of the difference in both luminosity and temperature between the observed values and the expected values from the previously published luminosity-temperature relationships; however, this

depends on the assumed radio luminosity cut-off used to classify groups as radio-loud or radio-quiet. I would ideally like *XMM-Newton* data for more of the groups as five were lost to high background levels and many have not been observed with *XMM-Newton*. These extra groups would strengthen my statistics and would solidify my conclusion that radio-loud groups are hotter for a given luminosity suggesting that AGN heating is at work in these groups. I also found that the

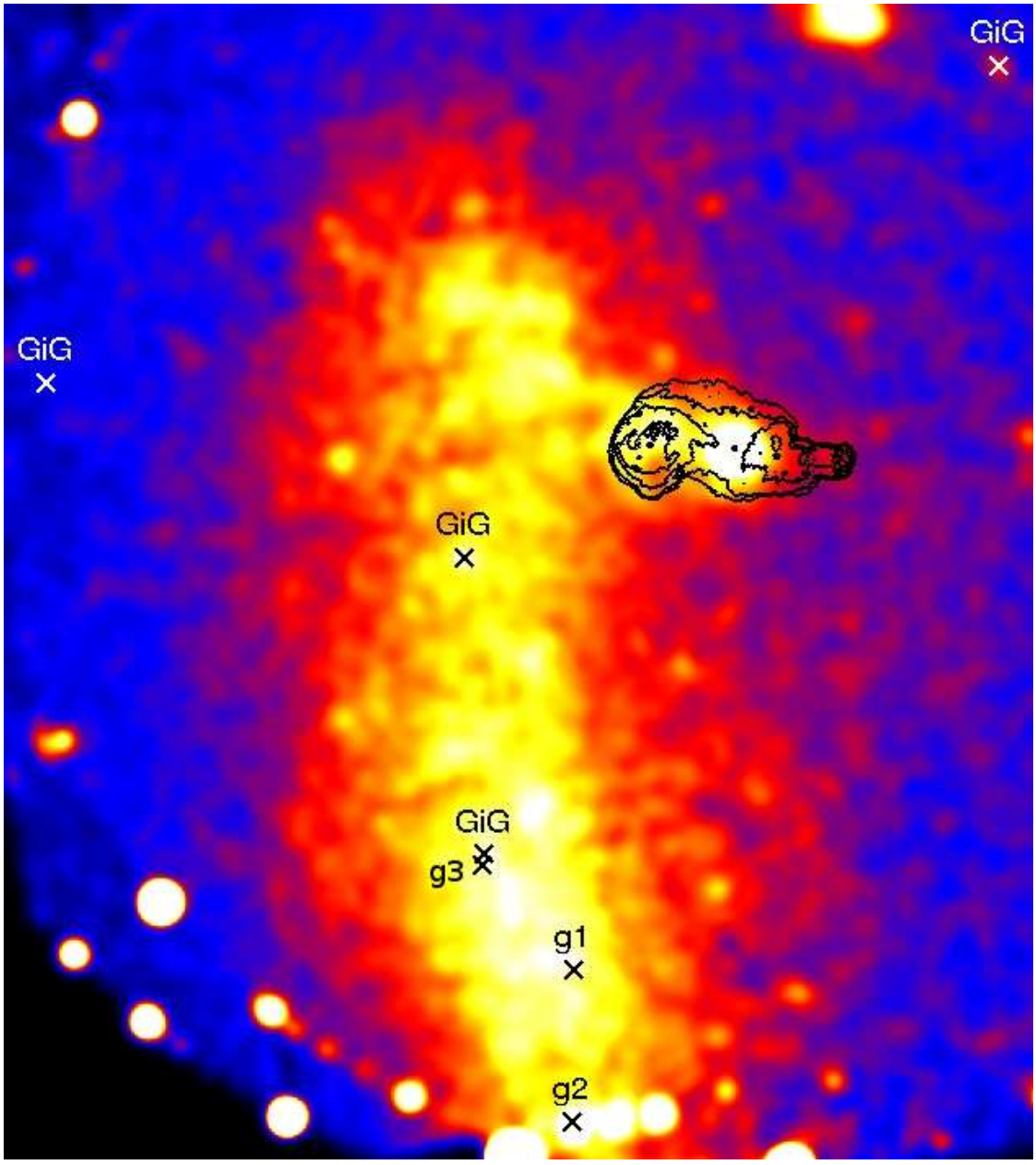

Figure 7.2: Exposure corrected X-ray image of the cluster Zw 1718.1-0108 smoothed with a Gaussian of 10.4 arcsec overlaid with the 1.4 GHz radio contours of 3C 353 at 0.001, 0.002, 0.005, 0.01, 0.02, 0.05 and 0.1 Jy beam^{-1}. The galaxies associated with the group are shown with crosses, those identified by Iwasawa et al. (2000) are labelled g1 – g3, and the additional galaxies identified by the 2MASS and 6dFGS are labelled GiG.

L-T offset from the previously published relationships depends on the radio luminosity, providing further support for radio-source heating as an explanation for the split in the $L_X - T_X$ relationship.

I also used my temperature profiles to independently classify our groups as those with a cool core and those without and found that those without cool cores have lower gas temperatures and lower luminosities than those with cool cores. These groups also have lower velocity dispersions, which suggests that these groups are less relaxed and have lower masses than those with cool cores.

7.3.2 Future Work

In the immediate future, I plan to convert my surface brightness profiles into density, pressure and entropy profiles to investigate the scaling of these properties. In the previous work by Jetha et al. (2007), there was no detected difference in the inner entropy profile of radio-loud and radio-quiet groups which suggests that there is no extra energy being injected into the core by current radio source heating, but systems with jets may be transferring energy to larger radii. With the field of view of *XMM-Newton* we would be able to test this further.

I also intend to extend the sample to initially include as many of the elliptical-dominated groups within the GEMS sample as possible by applying for observations of those groups whose particle background was too high for my analysis, and those that do not currently have *XMM-Newton* data available in the archive. I would also like to re-analyse the available *Chandra* data to test my methods for fitting the surface brightness profiles; this would allow me to improve the inner regions of my temperature profile so that I can measure the temperature at smaller radii and thus use the standard temperature comparisons to identify my cool-core groups. This will also allow me to compare my profiles with those presented by Jetha et al. (2007).

To better compare the properties of clusters and groups, I would also like to select groups in a consistent way to the REXCESS cluster sample (Pratt et al. 2007; Croston et al. 2008c; Pratt et al. 2010), which is an unbiased, X-ray selected cluster subsample of the REFLEX survey catalogue (Böhringer et al. 2004). However, studying groups in this way is difficult because of the long observation times required to map the group extended emission out to large radii.

Bibliography

Abdo, A. A., Ackermann, M., Ajello, M., et al. 2009, ApJ, 707, 55

Aharonian, F., Akhperjanian, A., Beilicke, M., et al. 2003, A&A, 403, L1

Aharonian, F., Akhperjanian, A. G., Anton, G., et al. 2009, ApJL, 695, L40

Aharonian, F., Akhperjanian, A. G., Bazer-Bachi, A. R., et al. 2006, Science, 314, 1424

Allen, S. W., Dunn, R. J. H., Fabian, A. C., Taylor, G. B., & Reynolds, C. S. 2006, MNRAS, 372, 21

Allen, S. W., Schmidt, R. W., & Fabian, A. C. 2001, MNRAS, 328, L37

Antonucci, R. R. J. & Miller, J. S. 1985, ApJ, 297, 621

Antonucci, R. R. J. & Ulvestad, J. S. 1985, ApJ, 294, 158

Archibald, E. N., Dunlop, J. S., Jimenez, R., et al. 2002, MNRAS, 336, 353

Arnaud, M., Majerowicz, S., Lumb, D., et al. 2002, A&A, 390, 27

Arnaud, M., Pointecouteau, E., & Pratt, G. W. 2005, A&A, 441, 893

Awaki, H., Mushotzky, R., Tsuru, T., et al. 1994, PASJ, 46, L65

Baade, W. & Minkowski, R. 1954, ApJ, 119, 215

Baldi, A., Forman, W., Jones, C., et al. 2009, ApJ, 707, 1034

Baldi, R. D. & Capetti, A. 2008, A&A, 489, 989

Band, D. L. & Grindlay, J. E. 1985, ApJ, 298, 128

Barthel, P. D. 1989, ApJ, 336, 606

Belsole, E., Worrall, D. M., & Hardcastle, M. J. 2006, MNRAS, 366, 339

Belsole, E., Worrall, D. M., Hardcastle, M. J., Birkinshaw, M., & Lawrence, C. R. 2004, MNRAS, 352, 924

Bennett, A. S. 1962, MmRAS, 68, 163

Benson, A. J., Bower, R. G., Frenk, C. S., et al. 2003, ApJ, 599, 38

Best, P. N. 2004, MNRAS, 351, 70

Best, P. N., Kauffmann, G., Heckman, T. M., et al. 2005, MNRAS, 362, 25

Bicknell, G. V. 1984, ApJ, 286, 68

Bicknell, G. V. 1995, ApJS, 101, 29

Biretta, J. A., Sparks, W. B., & Macchetto, F. 1999, ApJ, 520, 621

Birkinshaw, M. & Worrall, D. M. 1993, ApJ, 412, 568

Blakeslee, J. P., Jordán, A., Mei, S., et al. 2009, ApJ, 694, 556

Blandford, R. D. & Königl, A. 1979, ApL, 20, 15

Blandford, R. D. & Rees, M. J. 1974, MNRAS, 169, 395

Blundell, K. M. & Rawlings, S. 2000, AJ, 119, 1111

Blundell, K. M. & Rawlings, S. 2001, ApJL, 562, L5

Blundell, K. M., Rawlings, S., & Willott, C. J. 1999, AJ, 117, 677

Böhringer, H., Matsushita, K., Churazov, E., Ikebe, Y., & Chen, Y. 2002, A&A, 382, 804

Böhringer, H., Schuecker, P., Guzzo, L., et al. 2004, A&A, 425, 367

Böhringer, H., Schuecker, P., Pratt, G. W., et al. 2007, A&A, 469, 363

Bondi, H. 1952, MNRAS, 112, 195

Bower, R. G., Benson, A. J., Malbon, R., et al. 2006, MNRAS, 370, 645

Bridle, A. H. 1982, in IAU Symposium, Vol. 97, Extragalactic Radio Sources, ed. D. S. Heeschen & C. M. Wade, 121–128

Bridle, A. H. & Perley, R. A. 1984, ARAA, 22, 319

Brookes, M. H., Lawrence, C. R., Keene, J., et al. 2006, ApJL, 646, L41

Browne, I. W. A. 1983, MNRAS, 204, 23P

Brunetti, G. 2000, Astroparticle Physics, 13, 107

Brunetti, G., Comastri, A., Setti, G., & Feretti, L. 1999, A&A, 342, 57

Brunetti, G., Setti, G., & Comastri, A. 1997, A&A, 325, 898

Buote, D. A. 2000, ApJ, 539, 172

Buote, D. A. & Canizares, C. R. 1998, in Astronomical Society of the Pacific Conference Series, Vol. 136, Galactic Halos, ed. D. Zaritsky, 289–+

Buote, D. A., Jeltema, T. E., Canizares, C. R., & Garmire, G. P. 2002, ApJ, 577, 183

Buote, D. A., Lewis, A. D., Brighenti, F., & Mathews, W. G. 2003a, ApJ, 594, 741

Buote, D. A., Lewis, A. D., Brighenti, F., & Mathews, W. G. 2003b, ApJ, 595, 151

Burbidge, G. R. 1956, ApJ, 124, 416

Burch, S. F. 1977, MNRAS, 181, 599

Butcher, H. R., van Breugel, W., & Miley, G. K. 1980, ApJ, 235, 749

Carlstrom, J. E., Holder, G. P., & Reese, E. D. 2002, ARAA, 40, 643

Cheung, C. C. & Fermi-LAT collaboration. 2010, in AAS/High Energy Astrophysics Division, Vol. 11, AAS/High Energy Astrophysics Division, 3007

Cheung, C. C., Harris, D. E., & Stawarz, Ł. 2007, ApJL, 663, L65

Chiaberge, M., Capetti, A., & Celotti, A. 2002, A&A, 394, 791

Clark, B. G. 1999, in Astronomical Society of the Pacific Conference Series, Vol. 180, Synthesis Imaging in Radio Astronomy II, ed. G. B. Taylor, C. L. Carilli, & R. A. Perley, 1–+

Clarke, D. A., Burns, J. O., & Norman, M. L. 1992, ApJ, 395, 444

Cleary, K., Lawrence, C. R., Marshall, J. A., Hao, L., & Meier, D. 2007, ApJ, 660, 117

Cole, S., Norberg, P., Baugh, C. M., et al. 2001, MNRAS, 326, 255

Collaboration, T. F.-L. 2010, Science, science.1184656

Croston, J. H., Arnaud, M., Pointecouteau, E., & Pratt, G. W. 2006, A&A, 459, 1007

Croston, J. H., Hardcastle, M. J., & Birkinshaw, M. 2005a, MNRAS, 357, 279

Croston, J. H., Hardcastle, M. J., Birkinshaw, M., & Worrall, D. M. 2003, MNRAS, 346, 1041

Croston, J. H., Hardcastle, M. J., Birkinshaw, M., Worrall, D. M., & Laing, R. A. 2008a, MNRAS, 386, 1709

Croston, J. H., Hardcastle, M. J., Harris, D. E., et al. 2005b, ApJ, 626, 733

Croston, J. H., Hardcastle, M. J., Kharb, P., Kraft, R. P., & Hota, A. 2008b, ApJ, 688, 190

Croston, J. H., Kraft, R. P., & Hardcastle, M. J. 2007, ApJ, 660, 191

Croston, J. H., Kraft, R. P., Hardcastle, M. J., et al. 2009, MNRAS, 395, 1999

Croston, J. H., Pratt, G. W., Böhringer, H., et al. 2008c, A&A, 487, 431

Croton, D. J., Springel, V., White, S. D. M., et al. 2006, MNRAS, 365, 11

Curtis, H. D. 1918, Pub. Lick. Obs., 13, 31

Dickey, J. M. & Lockman, F. J. 1990, ARAA, 28, 215

Dreher, J. W. & Feigelson, E. D. 1984, Nature, 308, 43

Dumont, A., Collin-Souffrin, S., & Nazarova, L. 1998, A&A, 331, 11

Dunlop, J. S. & Peacock, J. A. 1990, MNRAS, 247, 19

Edelson, R. A. & Malkan, M. A. 1986, ApJ, 308, 59

Edge, D. O., Shakeshaft, J. R., McAdam, W. B., Baldwin, J. E., & Archer, S. 1959, MmRAS, 68, 37

Eilek, J. A., Melrose, D. B., & Walker, M. A. 1997, ApJ, 483, 282

Ekers, R. D., Goss, W. M., Wellington, K. J., et al. 1983, A&A, 127, 361

Erlund, M. C., Fabian, A. C., Blundell, K. M., Moss, C., & Ballantyne, D. R. 2007, MNRAS, 379, 498

Evrard, A. E. & Henry, J. P. 1991, ApJ, 383, 95

Fabbiano, G. 2006, ARAA, 44, 323

Fabian, A. C. 1994, ARAA, 32, 277

Fabian, A. C. 1999, MNRAS, 308, L39

Fabian, A. C., Sanders, J. S., Crawford, C. S., et al. 2003, MNRAS, 344, L48

Falle, S. A. E. G. 1991, MNRAS, 250, 581

Fanaroff, B. L. & Riley, J. M. 1974, MNRAS, 167, 31P

Feigelson, E. D., Laurent-Muehleisen, S. A., Kollgaard, R. I., & Fomalont, E. B. 1995, ApJL, 449, L149+

Feigelson, E. D., Schreier, E. J., Delvaille, J. P., et al. 1981, ApJ, 251, 31

Ferland, G. J., Peterson, B. M., Horne, K., Welsh, W. F., & Nahar, S. N. 1992, ApJ, 387, 95

Ferrarese, L. & Merritt, D. 2000, ApJL, 539, L9

Ferrarese, L., Mould, J. R., Stetson, P. B., et al. 2007, ApJ, 654, 186

Finoguenov, A., Davis, D. S., Zimer, M., & Mulchaey, J. S. 2006, ApJ, 646, 143

Finoguenov, A. & Ponman, T. J. 1999, MNRAS, 305, 325

Fomalont, E. B., Bridle, A. H., Willis, A. G., & Perley, R. A. 1980, ApJ, 237, 418

Fomalont, E. B., Ebneter, K. A., van Breugel, W. J. M., & Ekers, R. D. 1989, ApJL, 346, L17

Forman, W., Nulsen, P., Heinz, S., et al. 2005, ApJ, 635, 894

Fukazawa, Y., Botoya-Nonesa, J. G., Pu, J., Ohto, A., & Kawano, N. 2006, ApJ, 636, 698

Gaibler, V., Krause, M., & Camenzind, M. 2009, MNRAS, 400, 1785

Garcia, A. M. 1993, A&AS, 100, 47

Gastaldello, F., Buote, D. A., Humphrey, P. J., et al. 2007, ApJ, 669, 158

Gastaldello, F., Buote, D. A., Temi, P., et al. 2009, ApJ, 693, 43

Georganopoulos, M., Sambruna, R. M., Kazanas, D., et al. 2008, ApJL, 686, L5

Giacconi, R., Gursky, H., Paolini, F. R., & Rossi, B. B. 1962, Physical Review Letters, 9, 439

Gonzalez-Serrano, J. I., Carballo, R., & Perez-Fournon, I. 1993, AJ, 105, 1710

Goodger, J. L., Hardcastle, M. J., Croston, J. H., Kassim, N. E., & Perley, R. A. 2008, MNRAS, 386, 337

Goodger, J. L., Hardcastle, M. J., Croston, J. H., et al. 2010, ApJ, 708, 675

Govoni, F., Falomo, R., Fasano, G., & Scarpa, R. 2000, A&A, 353, 507

Grandi, P., Malaguti, G., & Fiocchi, M. 2006, ApJ, 642, 113

Greenstein, J. L. & Schmidt, M. 1964, ApJ, 140, 1

Haas, M., Müller, S. A. H., Bertoldi, F., et al. 2004, A&A, 424, 531

Hardcastle, M. J., Birkinshaw, M., Cameron, R. A., et al. 2002a, ApJ, 581, 948

Hardcastle, M. J., Birkinshaw, M., & Worrall, D. M. 1998, MNRAS, 294, 615

Hardcastle, M. J., Birkinshaw, M., & Worrall, D. M. 2001, MNRAS, 326, 1499

Hardcastle, M. J., Cheung, C. C., Feain, I. J., & Stawarz, Ł. 2009a, MNRAS, 393, 1041

Hardcastle, M. J. & Croston, J. H. 2005, MNRAS, 363, 649

Hardcastle, M. J., Evans, D. A., & Croston, J. H. 2006a, MNRAS, 370, 1893

Hardcastle, M. J., Evans, D. A., & Croston, J. H. 2007a, MNRAS, 376, 1849

Hardcastle, M. J., Evans, D. A., & Croston, J. H. 2009b, MNRAS, 396, 1929

Hardcastle, M. J., Harris, D. E., Worrall, D. M., & Birkinshaw, M. 2004, ApJ, 612, 729

Hardcastle, M. J., Kraft, R. P., Sivakoff, G. R., et al. 2007b, ApJL, 670, L81

Hardcastle, M. J., Kraft, R. P., & Worrall, D. M. 2006b, MNRAS, 368, L15

Hardcastle, M. J., Sakelliou, I., & Worrall, D. M. 2005, MNRAS, 359, 1007

Hardcastle, M. J. & Worrall, D. M. 2000, MNRAS, 319, 562

Hardcastle, M. J., Worrall, D. M., Birkinshaw, M., Laing, R. A., & Bridle, A. H. 2002b, MNRAS, 334, 182

Hardcastle, M. J., Worrall, D. M., Kraft, R. P., et al. 2003, ApJ, 593, 169

Harper, Jr., D. A. & Low, F. J. 1973, ApJL, 182, L89+

Harris, D. E., Biretta, J. A., Junor, W., et al. 2003, ApJL, 586, L41

Harris, D. E., Cheung, C. C., Biretta, J. A., et al. 2006, ApJ, 640, 211

Harris, D. E., Cheung, C. C., Stawarz, Ł., Biretta, J. A., & Perlman, E. S. 2009, ApJ, 699, 305

Harris, D. E. & Krawczynski, H. 2002, ApJ, 565, 244

Heckman, T. M., Smith, E. P., Baum, S. A., et al. 1986, ApJ, 311, 526

Helsdon, S. F. & Ponman, T. J. 2000, MNRAS, 315, 356

Herbert, P. D., Jarvis, M. J., Willott, C. J., et al. 2010, ArXiv e-prints

Hickson, P. 1982, ApJ, 255, 382

Hill, G. J. & Lilly, S. J. 1991, ApJ, 367, 1

Hine, R. G. & Longair, M. S. 1979, MNRAS, 188, 111

Hines, D. C., Eilek, J. A., & Owen, F. N. 1989, ApJ, 347, 713

Hobson, M. P. & Baldwin, J. E. 2004, Appl. Opt., 43, 2651

Högbom, J. A. 1974, A&AS, 15, 417

Hota, A. & Saikia, D. J. 2006, MNRAS, 371, 945

Huang, J., Glazebrook, K., Cowie, L. L., & Tinney, C. 2003, ApJ, 584, 203

Hubble, E. P. 1936, Realm of the Nebulae (Yale University Press)

Isobe, N., Tashiro, M., Makishima, K., et al. 2002, ApJL, 580, L111

Iwasawa, K., Ettori, S., Fabian, A. C., Edge, A. C., & Ebeling, H. 2000, MNRAS, 313, 515

Jackson, C. A. & Wall, J. V. 1999, MNRAS, 304, 160

Jackson, N. & Rawlings, S. 1997, MNRAS, 286, 241

Jaffe, W. J. & Perola, G. C. 1973, A&A, 26, 423

Jester, S. 2003, New Astronomy Review, 47, 427

Jetha, N. N., Hardcastle, M. J., Babul, A., et al. 2008, MNRAS, 384, 1344

Jetha, N. N., Ponman, T. J., Hardcastle, M. J., & Croston, J. H. 2007, MNRAS, 376, 193

Johnson, R., Ponman, T. J., & Finoguenov, A. 2009, MNRAS, 395, 1287

Jones, C., Forman, W., Vikhlinin, A., et al. 2002, ApJL, 567, L115

Jordán, A., Sivakoff, G. R., McLaughlin, D. E., et al. 2007, ApJL, 671, L117

Kadler, M., Kerp, J., Ros, E., et al. 2004, A&A, 420, 467

Kaiser, C. R. 2005, MNRAS, 360, 176

Kaiser, C. R. & Alexander, P. 1997, MNRAS, 286, 215

Kaiser, C. R. & Best, P. N. 2007, MNRAS, 381, 1548

Kaiser, C. R., Dennett-Thorpe, J., & Alexander, P. 1997, MNRAS, 292, 723

Kaiser, N. 1986, MNRAS, 222, 323

Kardashev, N. S. 1962, Soviet Astronomy, 6, 317

Kassim, N. E., Lazio, T. J. W., Erickson, W. C., et al. 2007, ApJS, 172, 686

Kataoka, J. & Stawarz, Ł. 2005, ApJ, 622, 797

Kataoka, J., Stawarz, Ł., Aharonian, F., et al. 2006, ApJ, 641, 158

Kataoka, J., Stawarz, Ł., Harris, D. E., et al. 2008, ApJ, 685, 839

Katz-Stone, D. M., Rudnick, L., & Anderson, M. C. 1993, ApJ, 407, 549

Keel, W. C., White, III, R. E., Owen, F. N., & Ledlow, M. J. 2006, AJ, 132, 2233

Khachikian, E. Y. & Weedman, D. W. 1974, ApJ, 192, 581

Kim, D. & Fabbiano, G. 2004, ApJ, 611, 846

Knight, P. A. & Ponman, T. J. 1997, MNRAS, 289, 955

Komossa, S. & Böhringer, H. 1999, A&A, 344, 755

Kormendy, J. 2001, in Astronomical Society of the Pacific Conference Series, Vol. 230, Galaxy Disks and Disk Galaxies, ed. J. G. Funes & E. M. Corsini, 247–256

Kormendy, J. & Richstone, D. 1995, ARAA, 33, 581

Kraft, R. P., Forman, W., Jones, C., et al. 2000, ApJL, 531, L9

Kraft, R. P., Forman, W. R., Jones, C., et al. 2002, ApJ, 569, 54

Kraft, R. P., Hardcastle, M. J., Sivakoff, G. R., et al. 2008, ApJL, 677, L97

Kraft, R. P., Kregenow, J. M., Forman, W. R., Jones, C., & Murray, S. S. 2001, ApJ, 560, 675

Kraft, R. P., Nulsen, P. E. J., Birkinshaw, M., et al. 2007, ApJ, 665, 1129

Kraft, R. P., Vázquez, S. E., Forman, W. R., et al. 2003, ApJ, 592, 129

Krause, M. & Alexander, P. 2007, MNRAS, 376, 465

Laing, R. 1982, in IAU Symposium, Vol. 97, Extragalactic Radio Sources, ed. D. S. Heeschen & C. M. Wade, 161–+

Laing, R. 1989, in Lecture Notes in Physics, Berlin Springer Verlag, Vol. 327, Hot Spots in Extragalactic Radio Sources, ed. K. Meisenheimer & H.-J. Roeser, 27–43

Laing, R. A. & Bridle, A. H. 2002, MNRAS, 336, 328

Laing, R. A., Jenkins, C. R., Wall, J. V., & Unger, S. W. 1994, in Astronomical Society of the Pacific Conference Series, Vol. 54, The Physics of Active Galaxies, ed. G. V. Bicknell, M. A. Dopita, & P. J. Quinn, 201–+

Laing, R. A., Parma, P., de Ruiter, H. R., & Fanti, R. 1999, MNRAS, 306, 513

Leahy, J. P. 1991, Interpretation of large scale extragalactic jets (Cambridge University Press, Cambridge (UK)), 100–+

Leahy, J. P. & Williams, A. G. 1984, MNRAS, 210, 929

Ledlow, M. J. & Owen, F. N. 1996, AJ, 112, 9

Liedahl, D. A., Osterheld, A. L., & Goldstein, W. H. 1995, ApJL, 438, L115

Lilly, S. J. & Prestage, R. M. 1987, MNRAS, 225, 531

Lind, K. R. & Blandford, R. D. 1985, ApJ, 295, 358

Longair, M. S. 1994, High energy astrophysics. Volume 2. Stars, the Galaxy and the interstellar medium. (Cambridge University Press, Cambridge (UK))

Lonsdale, C. J. & Barthel, P. D. 1986, AJ, 92, 12

Lumb, D. H., Warwick, R. S., Page, M., & De Luca, A. 2002, A&A, 389, 93

Lynden-Bell, D. 1969, Nature, 223, 690

Ma, C., Arias, E. F., Eubanks, T. M., et al. 1998, AJ, 116, 516

Mackay, C. D. 1973, MNRAS, 162, 1

Madau, P., Ferguson, H. C., Dickinson, M. E., et al. 1996, MNRAS, 283, 1388

Mahdavi, A., Hoekstra, H., Babul, A., Balam, D. D., & Capak, P. L. 2007, ApJ, 668, 806

Mainieri, V., Hasinger, G., Cappelluti, N., et al. 2007, ApJS, 172, 368

Manolakou, K. & Kirk, J. G. 2002, A&A, 391, 127

Marconi, A. & Hunt, L. K. 2003, ApJL, 589, L21

Marshall, H. L., Hardcastle, M. J., Birkinshaw, M., et al. 2010, ApJL, 714, L213

Mason, A., Morrison, P., & Sadun, A. C. 1988, Nature, 333, 640

Matsushita, K., Ohashi, T., & Makishima, K. 2000, PASJ, 52, 685

Mei, S., Blakeslee, J. P., Côté, P., et al. 2007, ApJ, 655, 144

Mellier, Y. & Mathez, G. 1987, A&A, 175, 1

Mewe, R., Gronenschild, E. H. B. M., & van den Oord, G. H. J. 1985, A&AS, 62, 197

Mewe, R., Lemen, J. R., & van den Oord, G. H. J. 1986, A&AS, 65, 511

Miles, T. A., Raychaudhury, S., Forbes, D. A., et al. 2004, MNRAS, 355, 785

Moretti, A., Campana, S., Lazzati, D., & Tagliaferri, G. 2003, ApJ, 588, 696

Morganti, R., Fanti, R., Gioia, I. M., et al. 1988, A&A, 189, 11

Morita, U., Ishisaki, Y., Yamasaki, N. Y., et al. 2006, PASJ, 58, 719

Mulchaey, J. S., Davis, D. S., Mushotzky, R. F., & Burstein, D. 2003, ApJS, 145, 39

Mulchaey, J. S. & Zabludoff, A. I. 1998, ApJ, 496, 73

Muxlow, T. W. B. & Garrington, S. T. 1991, Observations of large scale extragalactic jets, 52–+

Narayan, R. 2005, New Journal of Physics, 7, 199

Navarro, J. F., Frenk, C. S., & White, S. D. M. 1995, MNRAS, 275, 720

Nolthenius, R. 1993, ApJS, 85, 1

Norberg, P., Cole, S., Baugh, C. M., et al. 2002, MNRAS, 336, 907

O'Neill, S. M., Tregillis, I. L., Jones, T. W., & Ryu, D. 2005, ApJ, 633, 717

Orr, M. J. L. & Browne, I. W. A. 1982, MNRAS, 200, 1067

Osmond, J. P. F. & Ponman, T. J. 2004, MNRAS, 350, 1511

Owen, F. N. & Laing, R. A. 1989, MNRAS, 238, 357

Pacholczyk, A. G. 1970, Radio astrophysics. Nonthermal processes in galactic and extragalactic sources (Freeman)

Pearson, T. J. 1996, in Astronomical Society of the Pacific Conference Series, Vol. 100, Energy Transport in Radio Galaxies and Quasars, ed. P. E. Hardee, A. H. Bridle, & J. A. Zensus, 97–+

Peres, C. B., Fabian, A. C., Edge, A. C., et al. 1998, MNRAS, 298, 416

Perley, R. A., Dreher, J. W., & Cowan, J. J. 1984, ApJL, 285, L35

Perley, R. A., Fomalont, E. B., & Johnston, K. J. 1980, AJ, 85, 649

Perley, R. A., Roser, H., & Meisenheimer, K. 1997, A&A, 328, 12

Perlman, E. S., Harris, D. E., Biretta, J. A., Sparks, W. B., & Macchetto, F. D. 2003, ApJL, 599, L65

Peterson, J. R., Kahn, S. M., Paerels, F. B. S., et al. 2003, ApJ, 590, 207

Phinney, E. S. 1985, Astrophysics of Active Galaxies and Quasi-Stellar Objects (Oxford University Press, Oxford (UK)), 453–496

Pointecouteau, E., Arnaud, M., & Pratt, G. W. 2005, A&A, 435, 1

Ponman, T. J., Bourner, P. D. J., Ebeling, H., & Böhringer, H. 1996, MNRAS, 283, 690

Ponman, T. J., Cannon, D. B., & Navarro, J. F. 1999, Nature, 397, 135

Ponman, T. J., Sanderson, A. J. R., & Finoguenov, A. 2003, MNRAS, 343, 331

Posson-Brown, J., Raychaudhury, S., Forman, W., Donnelly, R. H., & Jones, C. 2009, ApJ, 695, 1094

Pratt, G. W. & Arnaud, M. 2002, A&A, 394, 375

Pratt, G. W., Arnaud, M., Piffaretti, R., et al. 2010, A&A, 511, A85+

Pratt, G. W., Böhringer, H., Croston, J. H., et al. 2007, A&A, 461, 71

Pratt, G. W., Croston, J. H., Arnaud, M., & Böhringer, H. 2009, A&A, 498, 361

Prestage, R. M. & Peacock, J. A. 1988, MNRAS, 230, 131

Quillen, A. C., Bland-Hawthorn, J., Green, J. D., et al. 2008, MNRAS, 384, 1469

Quillen, A. C., Brookes, M. H., Keene, J., et al. 2006, ApJ, 645, 1092

Ramella, M., Pisani, A., & Geller, M. J. 1997, AJ, 113, 483

Rawlings, S. & Saunders, R. 1991, Nature, 349, 138

Read, A. M. & Ponman, T. J. 2003, A&A, 409, 395

Rees, M. J., Netzer, H., & Ferland, G. J. 1989, ApJ, 347, 640

Reimer, A., Protheroe, R. J., & Donea, A. 2004, A&A, 419, 89

Reiprich, T. H. & Böhringer, H. 2002, ApJ, 567, 716

Romanowsky, A. J., Strader, J., Spitler, L. R., et al. 2009, AJ, 137, 4956

Rudnick, L., Katz-Stone, D. M., & Anderson, M. C. 1994, ApJS, 90, 955

Russell, P. A., Ponman, T. J., & Sanderson, A. J. R. 2007, MNRAS, 378, 1217

Rybicki, G. B. & Lightman, A. P. 1979, Radiative processes in astrophysics (Wiley-Interscience, New York)

Sadler, E. M., Jackson, C. A., Cannon, R. D., et al. 2002, MNRAS, 329, 227

Sakelliou, I., Peterson, J. R., Tamura, T., et al. 2002, A&A, 391, 903

Salpeter, E. E. 1964, ApJ, 140, 796

Sambruna, R. M., Eracleous, M., & Mushotzky, R. F. 1999, ApJ, 526, 60

Sanders, R. H. 1983, ApJ, 266, 73

Sanderson, A. J. R. & Ponman, T. J. 2010, MNRAS, 402, 65

Sanderson, A. J. R., Ponman, T. J., & O'Sullivan, E. 2006, MNRAS, 372, 1496

Sarazin, C. L. 1986, Reviews of Modern Physics, 58, 1

Scheuer, P. A. G. 1974, MNRAS, 166, 513

Scheuer, P. A. G. & Readhead, A. C. S. 1979, Nature, 277, 182

Schlegel, D. J., Finkbeiner, D. P., & Davis, M. 1998, ApJ, 500, 525

Schmidt, M. 1963, Nature, 197, 1040

Seyfert, C. K. 1943, ApJ, 97, 28

Shakura, N. I. & Sunyaev, R. A. 1973, A&A, 24, 337

Shapiro, S. L., Lightman, A. P., & Eardley, D. M. 1976, ApJ, 204, 187

Silk, J. & Rees, M. J. 1998, A&A, 331, L1

Simpson, C., Ward, M., Clements, D. L., & Rawlings, S. 1996, MNRAS, 281, 509

Sivakoff, G. R., Kraft, R. P., Jordán, A., et al. 2008, ApJL, 677, L27

Smith, R. K., Brickhouse, N. S., Liedahl, D. A., & Raymond, J. C. 2001, ApJL, 556, L91

Stawarz, Ł., Aharonian, F., Kataoka, J., et al. 2006, MNRAS, 370, 981

Stawarz, Ł., Sikora, M., & Ostrowski, M. 2003, ApJ, 597, 186

Sun, M., Voit, G. M., Donahue, M., et al. 2009, ApJ, 693, 1142

Sunyaev, R. A. & Truemper, J. 1979, Nature, 279, 506

Swain, M. R. 1996, PhD thesis, The University of Rochester

Swain, M. R., Bridle, A. H., & Baum, S. A. 1998, ApJL, 507, L29

Tadhunter, C., Robinson, T. G., González Delgado, R. M., Wills, K., & Morganti, R. 2005, MNRAS, 356, 480

Tashiro, M., Kaneda, H., Makishima, K., et al. 1998, ApJ, 499, 713

Tashiro, M., Makishima, K., Iyomoto, N., Isobe, N., & Kaneda, H. 2001, ApJL, 546, L19

Tasse, C., Best, P. N., Röttgering, H., & Le Borgne, D. 2008, A&A, 490, 893

Telesco, C. M. & Harper, D. A. 1980, ApJ, 235, 392

Terashima, Y., Iyomoto, N., Ho, L. C., & Ptak, A. F. 2002, ApJS, 139, 1

Tingay, S. J. & Lenc, E. 2009, AJ, 138, 808

Tozzi, P. & Norman, C. 2001, ApJ, 546, 63

Tregillis, I. L., Jones, T. W., & Ryu, D. 2004, ApJ, 601, 778

Trinchieri, G., Kim, D., Fabbiano, G., & Canizares, C. R. C. 1994, ApJ, 428, 555

Trussoni, E., Massaglia, S., Ferrari, R., et al. 1997, A&A, 327, 27

Urry, C. M. & Padovani, P. 1995, PASP, 107, 803

van Breugel, W. & Fomalont, E. B. 1984, ApJL, 282, L55

van den Bergh, S. 1976, ApJ, 208, 673

Vikhlinin, A., Forman, W., Jones, C., & Murray, S. 1995, ApJ, 451, 542

Vikhlinin, A., Kravtsov, A., Forman, W., et al. 2006, ApJ, 640, 691

Vikhlinin, A., Markevitch, M., Murray, S. S., et al. 2005, ApJ, 628, 655

Voit, G. M. 2005, Reviews of Modern Physics, 77, 207

Voit, G. M., Bryan, G. L., Balogh, M. L., & Bower, R. G. 2002, ApJ, 576, 601

Voit, G. M. & Ponman, T. J. 2003, ApJL, 594, L75

von der Linden, A., Best, P. N., Kauffmann, G., & White, S. D. M. 2007, MNRAS, 379, 867

Voss, R., Gilfanov, M., Sivakoff, G. R., et al. 2009, ApJ, 701, 471

Vrtilek, J. M., Grego, L., David, L. P., et al. 2002, APS Meeting Abstracts, 17107

Walker, R. C. 1997, ApJ, 488, 675

White, D. A., Jones, C., & Forman, W. 1997, MNRAS, 292, 419

White, S. D. M. & Rees, M. J. 1978, MNRAS, 183, 341

Williams, A. G. & Gull, S. F. 1985, Nature, 313, 34

Woltjer, L. 1959, ApJ, 130, 38

Woodley, K. A., Raychaudhury, S., Kraft, R. P., et al. 2008, ApJ, 682, 199

Worrall, D. M. & Birkinshaw, M. 2000, ApJ, 530, 719

Worrall, D. M., Birkinshaw, M., Kraft, R. P., et al. 2008, ApJL, 673, L135

Zezas, A., Birkinshaw, M., Worrall, D. M., Peters, A., & Fabbiano, G. 2005, ApJ, 627, 711